

THE UNIVERSITY OF SHEFFIELD

DOCTORAL THESIS

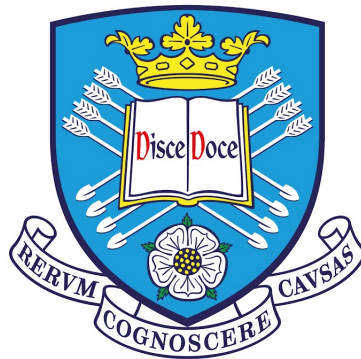
**Channelling Current in FAST Processed
Titanium Alloys to Generate Uniquely
Tailored Microstructures in a Single Step**

Author:

James PEPPER

Supervisor:

Martin JACKSON



*A thesis submitted in fulfilment of the requirements
for the degree of Doctor of Philosophy*

in the

STAR Research Group
Department of Materials Science and Engineering

April 24, 2024

Declaration of Authorship

I, James PEPPER, declare that this thesis titled, “Channelling Current in FAST Processed Titanium Alloys to Generate Uniquely Tailored Microstructures in a Single Step” and the work presented in it are my own. I confirm that:

- This work was done wholly or mainly while in candidature for a research degree at this University.
- Where any part of this thesis has previously been submitted for a degree or any other qualification at this University or any other institution, this has been clearly stated.
- Where I have consulted the published work of others, this is always clearly attributed.
- Where I have quoted from the work of others, the source is always given. With the exception of such quotations, this thesis is entirely my own work.
- I have acknowledged all main sources of help.
- Where the thesis is based on work done by myself jointly with others, I have made clear exactly what was done by others and what I have contributed myself.

Signed:

Date:

“People say nothing is impossible, but I do nothing every day”

A. A. Milne

THE UNIVERSITY OF SHEFFIELD

Abstract

Faculty of Engineering

Department of Materials Science and Engineering

Doctor of Philosophy

Channelling Current in FAST Processed Titanium Alloys to Generate Uniquely Tailored Microstructures in a Single Step

by James PEPPER

The clear impact that intensifying the electric current density has on the sintering process has been observed previously in several works, through the addition of insulation, coatings, and across a range of material systems. In this thesis it is investigated, and demonstrated, that the impact of not only intensifying, but also spatially directing this current to generate tailored thermal distributions, has a significant and useful resulting impact on final microstructures. This is analysed using prior β grain size in super-transus Ti-6Al-4V sintered samples as a marker for thermal history, and TiB metal matrix composites where in situ reactions demonstrate the thermal gradients.

A finite element analysis (FEA) model was created using experimentally gathered data to examine, and predict any internal thermal profiles, proving to be spatially accurate and validated within 5% error. Using this, the electric flow was controlled through the precise addition of insulating boron nitride (BN) to the graphite foil surrounding the powder region, redistributing the current density, and thus the regions of highest resistive heating. Relative densities for 20 mm Ti 6Al-4V samples were demonstrated to vary by up to 15% and showed gradients matching projected thermal histories from the FEA model. MIPAR image analysis software was then

utilised to examine the microstructure and provide a quantitative measure for further validation of the simulation and its predictive capacity. It was observed that the addition of these shaped insulation inserts resulted in temperature gradients over $1^{\circ}\text{C} / \text{mm}$ during sintering with a directly correlated impact on prior β grain size and material properties. This effect, up to $150 \mu\text{m}$ average grain diameter difference over 40 mm, was also determined to be more pronounced within a processing window for dwell times shorter than 5 mins due to temperature dependant resistive limitations with the insulating material and thermal equilibrium in smaller samples. Longer dwells have also been demonstrated for different material systems with similarly large thermal gradients through the generation of TiB needles in a thermally sensitive reaction.

These needles were formed in large scale production of metal matrix Ti + TiB composites functionally graded 250 mm plates using FAST, a scale previously not seen, and the current control technique was applied to demonstrate the potential impact of thermal gradients at scale in a real world situation. The sintered composite plate then performed better than standard Ti-6Al-4V military standards highlighting the effectiveness of the FAST technique. The thermal sensitivity was then demonstrated, through an additional plate produced through the current control technique with an intentionally lower ballistic performance originating from the extreme differences in thermal gradients experienced during processing.

Acknowledgements

I'd like to thank my supervisor Prof. Martin Jackson who has provided consistent support and confidence during the project, enabling me to take an equally confident stance on my work and results. The Defence Science Technology Laboratories (DSTL) along with the EPSRC need mentioning for generously funding the project through the Advanced Materials Systems CDT.

Additional thanks to Ben Thomas for his significant contribution to troubleshooting the creation and development of our initial simulations. I would still be lost in sub menus without his guidance. Simon Graham, Oliver Levano Blanch, and Sam Lister must also be acknowledged for all their help with sample prep and, unfortunately, regular machine alarms and tooling breakages.

Thanks also to the other members of the Sheffield Titanium Alloy Research (STAR) group over the years, specifically Nick Weston, Daniel Suarez, Bea Fernandez, and Tom Childerhouse for their advice on any number of complications. Not forgetting the technicians, especially Nigel Adams, for the arduous preparation involved in the larger sample creations which would have been intimidating to tackle alone.

Finally, a special thank you to my parents and close friends for reminding me there is a world outside the university and occasionally dragging me into it...

Contents

Declaration of Authorship	iii
Abstract	vii
Acknowledgements	ix
1 Introduction	1
1.1 Background	1
1.1.1 Thesis Overview	3
2 Literature Review	5
2.1 Titanium	5
2.1.1 Titanium Alloys	6
α alloys	8
$\alpha + \beta$ alloys	8
β alloys	9
2.1.2 Strengthening Mechanisms	9
Grain Boundary Strengthening	9
Solid Solution Strengthening	10
2.1.3 Selected Alloys	10
Ti-6Al-4V	10
Ti-3Al-2.5V	12
2.2 Titanium Powder Characterisation/Creation	12
2.2.1 Powder Production Routes	12
Atomisation and PREP	12
Hydride-dehydride	14
2.3 Titanium Matrix Composites	14

2.3.1	Titanium Boron System	16
2.3.2	In Situ Formation Of Titanium Boride	17
	TiB Crystal Structure	17
2.3.3	Boron Impact On β Transus	18
2.3.4	TiB Strengthening Mechanisms	18
2.3.5	Manufacture Of TiB Composites	19
2.4	Mechanical Alloying	19
2.5	Consolidation	21
2.5.1	Consolidation Theory	22
2.5.2	Hot Consolidation	23
2.5.3	Alternatively Available Sintering Techniques	25
	Conventional Sintering	25
	Hot Isostatic Pressing	26
2.6	Field Assisted Sintering Technique	27
2.6.1	Naming Schemes	28
2.6.2	FAST Materials	30
	Functionally Graded Materials	30
2.6.3	FAST Equipment Development	31
	Manufacturing From Powder	32
2.6.4	Temperature Control	34
	Thermal Measurements	34
	Heating Rate / Dwell	35
	Temperature Effects/Gradients	36
	Thermal Distributions	38
2.6.5	Electrical Effects	39
	Joule Heating	40
	Peltier Effect	41
	Atomic Diffusion	42
2.6.6	Atmospheric Effects	43
2.7	Computational Techniques For FAST	45
2.7.1	Atomistic Simulations	45
2.7.2	DEM	46

2.7.3	FEM	46
	Meshing	47
	Boundary Conditions	49
2.7.4	Powder Porosity In FEM	51
2.8	Summary	53
3	Experimental Techniques	55
3.1	Introduction	55
3.2	Powders Studied	56
	3.2.1 Gas Atomised and Hydride De-Hydride Powders	56
	3.2.2 Cold Milling	59
3.3	Powder Processing	59
	3.3.1 FAST Sintering Machine HP D 25	59
	3.3.2 FAST Sintering Machine H-HP D 250	63
3.4	Metallographic Preparation and Imaging	64
	3.4.1 Sample Preparation	64
	3.4.2 Optical, Scanning Electron Microscopy, and X-EDS	64
	Electron Backscatter Diffraction	65
	3.4.3 Vickers Hardness Testing	66
3.5	Computational Techniques	66
	3.5.1 FEM Software	66
	2D Axisymmetric	66
	3.5.2 MIPAR	69
3.6	Graphite Physical Property Testing	70
	3.6.1 Thermo-Mechanical Compression and Flexural testing	71
	Compression Testing	71
	Flexural Strength Testing	72
	3.6.2 Conductivity Testing	74
	Electrical	74
	Thermal	75
	Specific Heat Capacity	76
	3.6.3 Coefficient of Thermal Expansion Testing	77

4	Current Control Trials	79
4.1	Introduction	79
4.1.1	FEM 'Twin'	84
	2D Axisymmetric Restrictions	84
4.2	Methods	85
4.2.1	Practical Sintering	87
4.3	Results	92
4.4	Discussion	96
5	Predictive Sintering	99
5.1	Introduction	99
5.2	Methods	105
5.2.1	FEM Simulation	105
5.2.2	Resistance Measurements	107
5.2.3	Sample Creation	107
5.2.4	Image Analysis	109
5.3	Results	110
5.3.1	Characterisation	112
5.4	Discussion	117
5.5	Conclusions	124
6	Current Control At Scale	127
6.1	Introduction	127
6.2	Methods	131
6.2.1	Powder Production	132
6.2.2	Sample Sintering	133
6.3	Microstructure Optimisation	135
6.3.1	Process Mapping	135
6.3.2	Scaled Sample Profiling	138
	Layer Boundary Microstructures	139
6.3.3	Layer Microhardness	140
	Discussion	143
6.3.4	Scaled Plates	144

6.3.5	FEM Simulation	145
6.3.6	Microstructure Analysis	147
	Microhardness	150
6.4	Ballistic Trials	153
6.4.1	Microstructure Analysis	160
	Crack Propagation Mechanisms	163
6.5	Further Analysis	168
	X-ray Energy Dispersive Spectroscopy	168
	Electron Backscatter Diffraction	169
6.6	Conclusions	171
7	Conclusions and Further Work	173
7.1	Conclusions	173
7.1.1	FEM digital twin production	173
7.1.2	Current Control Thermal Gradients	174
	Microstructural Validation	175
7.1.3	TiB System And Ballistic Trials	175
7.2	Further Works	176
7.2.1	Further Ti-6Al-4V Work	176
7.2.2	Dissimilar Materials	177
7.2.3	Additional TiB MMC V ₅₀ Optimisation	177
A	Appendix	179
A.1	Graphite Data	179
A.1.1	Thermal Conductivity	179
B	Appendix	183
B.1	MIPAR Recipe	183
B.2	Python Scripts	184
B.2.1	MIPAR grain size heat map processing	185
	Bibliography	187

List of Figures

2.1	Schematic illustration of the α HCP and β BCC titanium unit cell crystal structures [9]	7
2.2	A pseudo binary phase diagram for titanium with stabilising additions adapted from [8]	8
2.3	Optical microscope images of Ti-6Al-4V common microstructures from [14]. (a) mill annealed; (b) bimodal; (c) fully equiaxed; and (d) fully lamellar	11
2.4	Schematic diagrams of both the GA method (left) and PA method (right) for powder production taken from carpenter additive [21]	13
2.5	Secondary Electron Powder surface images (a) GA Ti-6Al-4V powder and (b) HDH Ti-6Al-4V Eckhart powder used in this work	14
2.6	The Titanium Boron Phase Diagram adapted from [25]	16
2.7	Schematic illustration of (a) the primitive cell crystal structure of TiB_2 , (b) the orthorhombic unit cell of TiB, and (c) the expanded boron-boron (grey) chain of the TiB structure obtained after reaction with titanium (white).	17
2.8	Schematic of the basic mechanical alloying process demonstrating the interaction between the milling balls and powder under Centrifugal Force (CF)	20
2.9	Schematic illustration of the stages of the necking process between two particles during sintering (i) Initial Contact (ii) Early Growth (iii) Late Stage Necking (iv) Fully Coalesced	24
2.10	Schematic illustration of dissolution in the titanium oxide layer and common transport mechanisms available during the sintering process, adapted from [45]	25

2.11	Diagram of the Powder Hot Isostatic Pressing process, from canning to final component, sourced from [49]	26
2.12	Schematic of a simplified FAST tooling layout highlighting the current driven nature of the process	27
2.13	Number of publications for the process over the last 23 years labelled as Spark Plasma Sintering - from Web of Science	29
2.14	(i) A CAD model of the designed geometry (ii) Corresponding image of the sintered component from [66]	33
2.15	FEM model demonstrating the impacts of the impact of die design on thermal distribution within the tooling for Alumina samples from Achenani et al. [83]	39
2.16	Diagram of the Peltier Effect creating a thermal gradient at the junction of dissimilar conductors	41
2.17	Arrhenius diagram of the diffusivities of alloying elements in titanium in both α and β phases, adapted from [4]	43
2.18	COMSOL 2D-axisymmetric slice showing the end result of the simulation (left), the variation in meshing within the FEM model to suit the geometry (centre), and a closer view of a.) the free triangular method used and b.) the free quad method (right)	48
3.1	Secondary electron images of the HDH Ti-6Al-4V (left) and 9 wt.% TiB powders (right)	56
3.2	Gas atomised powder secondary electron surface image of Ti-6Al-4V powder (a) and BSE Microstructure (b)	57
3.3	FCT HP D 25 FAST machine pictured (left) External view of the machine, (right) Internal view of the vacuum chamber with 20 mm graphite tooling	60
3.4	Image and Schematic cut away of the FAST graphite tooling at 20 mm scale demonstrating the internal lay up and symmetrical openings for the optical pyrometer	61
3.5	Photograph of the FAST Sintering Machine H-HP D 250 and accompanying 250 mm diameter graphite tooling	63

3.6	(A) Graphite tooling photograph (B) Simplified 2D Axisymmetric slice used in COMSOL simulations for computational efficiency	67
3.7	A plot of temperature vs distance from centre of the sample for varying mesh maximum element size on a 80 mm diameter simulation demonstrating convergence	69
3.8	(a) Machine drawing of graphite sample geometry for TMC testing and (b) photograph of the machine the grades were tested on	71
3.9	Compression strength results from the TMC graphite testing, showing particularly high strength on the Y552 grade in use	72
3.10	(a) Machine Drawing of the sample geometry for 4 point bend testing and (b) photograph of the set up used	73
3.11	Flexural Strength results from the graphite testing in MPa	74
3.12	Electrical Conductivity results for the graphite grades highlighting the excellent conductivity of the material	75
3.13	Thermal Conductivity results displayed for the relevant graphite grades tested Y-552 and Y-542 due to the additional size of the dataset from testing at temperature	76
3.14	Heat Capacity results displayed for the relevant graphite grades tested Y-552 and Y-542	77
3.15	Thermally dependent Coefficient of Thermal Expansion for grades Y-542 and T-552	78
4.1	Initial current and voltage plots against sintering time for both experimental and simulated results demonstrating good qualitative matches, though with a disparity in voltage from simulated direct current simplification without adjustment	81
4.2	Schematics of the 2D axial slice view of the graphite tooling stack with focused schematics (right) demonstrating the Full BN spray concept pattern for testing and simulation.	83
4.3	Schematics of all the 2D axial slice views of the focused schematics demonstrating the initial BN spray concept patterns for testing and simulation.	84

4.4	Threshold images of the sprayed graphite foils for resistivity testing . . .	86
4.5	Plots demonstrating the rise in resistance to the normal flowing current as the surface % of graphite foil coated with Boron Nitride (A) increases. For circles with approximately 85 % or higher coverage, there was a sharp increase in total resistance.	87
4.6	A mosaic micrograph of the control sample which has been cropped and processed (left) and the python output density heat map (right) with calculated average density	88
4.7	A mosaic micrograph of the aperture sample which has been cropped and processed (left) and the python output density heat map (right) with calculated average density demonstrating impact on consolidation of current control	89
4.8	The resulting density heat maps from the 20 mm diameter 975°C processed samples for the Control (top left), Aperture(top right), Reverse Aperture (bottom left), and Full (bottom left) showing increase in overall density.	90
4.9	Bar graph displaying the impact of increasing the electrical insulation reducing the required energy to reach dwell temperature.	91
4.10	The resulting density heat maps from the 20 mm diameter 995°C processed samples for the Control (top left), Aperture (top right), Reverse Aperture (bottom left), and Full (bottom left) showing increase in overall density.	93
4.11	The resulting density heat maps from the 20 mm diameter 1015°C processed samples for the Control (top left), Aperture(top right), Reverse Aperture (bottom left), and Full (bottom left) showing increase in overall density.	93
4.12	The resulting density heat maps from the 20 mm diameter 1075°C processed samples for the Control (top left), Aperture(top right), Reverse Aperture (bottom left), and Full (bottom left) showing increase in overall density.	95

4.13	Cross polarised micrographs taken at 100x magnification of (a) the 1075°C control sample, (b) the 1075°C aperture sample, and (c) the 1075°C full microstructure.	96
5.1	Left: Photograph of 80 mm graphite tooling in the FAST vacuum chamber / Right: Labelled Schematic of the 2D uniaxial slice of the FAST tooling stack.	102
5.2	Left: Simplified 2D uniaxial slice of the simulated 80 mm graphite tooling stack. Right: The primary region of interest highlighted and enlarged, showing A - Control B - Aperture C - Reverse Aperture D - Full Insulation.	103
5.3	Ti-6Al-4V Puris Powder Size Distribution (PSD), averaged over several runs. Insert - Secondary electron micrograph image (20 kV accelerating voltage) of the powder's topography	108
5.4	Left - Temperature cross sections of simulated region of interest at maximum temperature for BN insulation (blue) configurations. Right - 2D axisymmetric display of the sample regions thermal distributions in both Z and R for A - Control , B - Aperture, C - Reverse Aperture, D - Full samples	112
5.5	Right: Sample transus line separating equiaxed α particles (A) and prior β regions (B). Right: grain structure visible on the etched Aperture sample (examples highlighted) with a qualitatively similar angle in simulation.	113
5.6	Insert: Overlay of the detected grains from MIPAR onto the original image (Top Right). Main: The associated histogram of output data from the measurements of the insert image, creating an average value and a range.	115
5.7	Top: A cropped mosaic micrograph of higher resolution images from the Aperture Sample 5min Dwell. Bottom: MIPAR results plotted as raw data. Each square displays the average diameter of the grains detected within that micrograph from the mosaic above.	116

- 5.8 Control (Sample centre left (i) and edge right (ii)) - Raw (a) and processed (b) grain size distributions compared to the predicted temperature profiles (c) from Figure 5.4 demonstrating the correlation between heating and resulting grain size. Unexpected spots of grain size variance approximately $30\ \mu\text{m}$ in scale. 118
- 5.9 Aperture (Sample centre left (i) and edge right (ii)) - Raw (a) and processed (b) grain size distributions compared to the predicted temperature profiles (C) from Figure 5.4 demonstrating the correlation between heating and resulting grain size. This shows a very accurate overall trend, though the expected line of transus falls 7 mm short of its predicted location. 119
- 5.10 Reverse Aperture (Sample centre left (i) and edge right (ii)) - Raw (a) and processed (b) grain size distributions compared to the predicted temperature profiles (c) from Figure 5.4 demonstrating correlation between heating and grain size. This accurately predicted the temperatures being too low to cause significant grain growth in the majority of the sample. 120
- 5.11 Full (Sample centre left (i) and edge right (ii)) - Raw (a) and processed (b) grain size distributions compared to the predicted temperature profiles (c) from Figure 5.4 demonstrating the correlation between heating and resulting grain size. The trend again appears to fit the profile very well with the most homogenous large grain growth at the sample edges. 121
- 5.12 Ti-6Al-4V sintered super transus grain growth plotted as average grain size against highest predicted temperature for a 5 minute Dwell. The sampling was done pseudo randomly and shows a good fit linear trend. 122
- 6.1 Secondary Electron SEM image of the TiB_2 un-milled powder. 132
- 6.2 BSE image of (a) the HDH Ti-3Al-2.5V with 6 wt.% TiB_2 milled powder; (i) HDH Ti-3Al-2.5V particle unseeded and; (ii) HDH Ti-3Al-2.5V particle seeded with TiB_2 133

6.3	Diagram schematic of the as sintered layers of the FGM Ti-3Al-2.5V + TiB ₂ system powders in this 80 mm diameter sample with a final height of 12.5mm.	134
6.4	(Backscattered electron images of TiB needles produced at 1200°C in the 6 wt. % TiB ₂ milled powder with the HDH Ti-3Al-2.5V alloy, close to the boundary layer	135
6.5	Backscattered electron images of the 0-6 wt.% TiB ₂ boundary layer with increasing energy conditions.	136
6.6	Graph of needle growth for the process mapping of the Ti-3Al-2.5V + TiB ₂ powder system, demonstrating the limited increase in these features with additional processing.	138
6.7	Backscatter electron images of the 80 mm microstructure at the 0 / 6 wt.% TiB ₂ and the 6 / 9 wt.% TiB ₂ boundary regions for the 1200°C 10-minute sample (A,B) and the sample produced at 1300°C for 1 hour (C,D).	139
6.8	Grouped bar plots of the microhardness measured from 3 Ti-3Al-2.5V + 0-6 wt.% TiB ₂ samples at 900°C (grey), 1200°C (blue), and 1400°C (black)	141
6.9	Microhardness plot of the 1200°C 10 min sample from the 9 wt.% TiB ₂ edge to the Ti-3Al-2.5V layer of the 80 mm sample (Fig 6.3).	142
6.10	Microhardness plot of the 1300°C 1 hr sample from the hard 9 wt.% TiB ₂ edge to the Ti-3Al-2.5V layer of the 80 mm sample with a marked improvement in consistency from Fig 6.9	142
6.11	Top: Schematic of the design for the powder grading in the 250 mm samples. Bottom: Photograph of both plates produced post sinter with Control (Left) and Aperture (Right). Faces were labelled to ensure correct attack face tested	145
6.12	FEM simulations of the thermal gradients at dwell for the 250 mm diameter plates during sintering demonstrating the differing thermal gradients created	146

6.13	A 250 mm diameter aperture plate produced (Left), and backscattered electron images of internal microstructures of the 6 wt.% layer demonstrating microstructural variation.	147
6.14	Backscattered electron images of the microstructure at increasing radial distances from the centre of both TiB FGM (Control) and TiB FGM (Aperture) samples post firing	148
6.15	Micro-hardness of each layer at diagonally spaced points on a line from the attack face to the rear face of both Aperture (grey / white) and Control (black / blue) samples	151
6.16	30-60 AP M2 hardened steel slug data sheet (left), photograph of the core, and full schematic (right) images, adapted from RBSL documentation	153
6.17	A visual schematic of the equipment used for the ballistic test, referenced with permission from [203]	154
6.18	Photographs of the impact faces taken after each shot into the 250 mm diameter control plate, as well as the final shot rear face demonstrating the scabbing failure mechanisms	155
6.19	Galanov's model diagram adapted from Zhang et al. [204] (a) and an overlaid photograph of the impact of Shot 1 from Fig 6.18(b) displaying the impact cavity region, as well as the visible pulverised area of front spallation.	155
6.20	Photographs of the impact face taken after each shot into the 250 mm diameter aperture plate, with shot 6 demonstrating critical failure of the plate.	157
6.21	(a) Photograph of the hardened steel slugs fired at the metallic target plate (top) and the ceramic plates (bottom). (b) Impact (pass) on ceramic attack face. (c) Impact (fail) on metallic face	158
6.22	Relative V_{50} , results normalised to military specification (Mil Spec) titanium alloys for the same thickness and firing conditions	160

6.23	Backscatter electron images of ballistically induced cracks in 1350°C 2 hr processed Ti-TiB MMC plates, arresting at the interfaces of the functionally graded Ti-6Al-4V + TiB layers with features highlighted in white: crack tip deflection (CTD) in c and d, crack face bridging (CFB) in a, b and c, particle de-bonding (PDB) in c and d, and crack branching (CB) in a and b.	164
6.24	Backscatter electron imaging of cracks interacting with individual TiB needles during propagation showing de-bonding and deflection in white with examples of needle cracking in red. Images a and c are taken from the control, and b and d from the aperture Ti-TiB MMC plate, processed at 1350°C for 2 hr	167
6.25	X-ray Energy Dispersive Spectroscopy (X-EDS) showing displacement of Al from needles and distribution of elements in the edge aperture sample, displaying the inhomogeneous effect of poor processing	169
6.26	Electron Back Scatter Diffraction (EBSD) of the Ti-6Al-4V + 3 wt.% TiB ₂ interface demonstrating extreme grain pinning from the TiB ₂ and TiB ceramic particles on the growth of the titanium alloy prior β grains	170
6.27	Pole figures showing the lack of texture discovered in Fig 6.26 above, consistent through both regions	170
A.1	Thermal Conductivity of TDX-1 grade ISO Graphite	179
A.2	Thermal Conductivity of TDX-2 grade ISO Graphite	179
A.3	Thermal Conductivity of TDX-3 grade ISO Graphite	180
A.4	Thermal Conductivity of TDX-4 grade ISO Graphite	180
A.5	Thermal Conductivity of TDX-5 grade ISO Graphite	180
A.6	Thermal Conductivity of TDX-6 grade ISO Graphite	181
B.1	Python script for generation of grain size heat maps in chapter 5	185

List of Tables

3.1	Powder chemistry determined prior to processing for titanium alloy powders used in this work. *Typical values that the powder supplier produces	58
3.2	Mesh refined simulation parameters for the reported models at all scales utilised later in chapters 4, 5, and 6.	68
5.1	Data comparison between experimental runs and associated models demonstrating a 2-6% match on the current and voltages with a remarkable 1-2% match for the resistances.	111
6.1	PSD results of the analysed powders for sample creation demonstrating large variance in size and oversized nature of the rough topography powders	133
6.2	Ballistic results from range firing using hardened steel slugs. Indicative V_{50} (*) noted where insufficient shots for a more accurate determination were possible due to impact ablation and structural damage.	159

List of Abbreviations

PM	Powder Metallurgy
HIP	Hot Isostatic Pressing
HIP	Hot Pressing
SPS	Spark Plasma Sintering
FAST	Field Assisted Sintering Technology
AM	Additive Manufacturing
FEM	Finite Element Modelling
FEA	Finite Element Analysis
DEM	Discrete Element Modelling
VIM	Vacuum Induction Melting
HCP	Hexagonal Close Packed
BCC	Body Centred Cubic
CP	Comercially Pure
PSD	Powder Size Distribution
PA/GA	Plasma Atomised Gas Atomised
(P)REP	(Plasma) Rotating Electrode Process
HDH	Hydride De-Hydride
CIP	Cold Isostatic Pressing
TMC	Titanium Matrix Composite
MMC	Metal Matrix Composite
MA	Mechanical Alloying
RS	Rapid Solidification
ISO	ISOstatically Molded Graphite
PPC	Plasma Pressure Compaction
PECS	Pulsed Electric Current Sintering

PAS	Plasma Activated Sintering
EPAC	Electric Pulse Assisted Consolidation
ECAS	Electric Current Activated Sintering
FGM	Functionally Graded Material
CAD	Computer Aided Design
TC	ThermoCouple
PID	Proportional Integral Derivative
AC	Alternating Current
DC	Direct Current
MD	Molecular Dynamics
KMC	Kinetic Monte Carlo
FKM	Fleck Kuhn Meeking
GTN	Gurson Tvergaard Needleman
DPC	Drucker Prager Cap
SEM	Scanning Electron Microscopy
EBSD	Electron BackScatter Diffraction
X-EDS	X-ray Energy Dispersive Technology
XCT	X-ray Computational Tomography
TMC	Thermo Mechanical Compression
SEI	Secondary Electron Imaging
XRF	X-Ray Fluorescence
CFC	Carbon Fibre Composite
EPMA	Electron Probe Micro Analysis
TKD	Transmission Kikuchi Diffraction
CTE	Coefficient of Thermal Expansion
BC	Boundary Condition
PDE	Partial Differential Equation

*Dedicated to my parents and friends, without whom I most
certainly would have gone completely mad.*

Chapter 1

Introduction

1.1 Background

The production of titanium (Ti) components has long been an expensive and time consuming pursuit, with the Kroll Process [1] producing most of the worlds titanium through a six step intensive process. This might suggest the material is rare, belying its position as the fourth most common structural metal on earth, making up 0.6% of the planet's crust; however it is commonly relegated to relatively niche applications where the strong, lightweight properties are absolutely necessary. For example, aerospace industries, where more than half of this metal ends up in the form of alloys such as the most common Ti-6Al-4V, accounting for more than 50% of the Ti tonnage in the world, or Ti-5553, often found in the landing gear of commercial aircraft for its high strength and toughness.

Ti-6Al-4V was one of the first alloys developed and is an $\alpha + \beta$ system with excellent physical and mechanical properties, able to be manipulated through the microstructures evolved during thermomechanical processing. These alloys offer high strength to weight ratios, as well as high level corrosion resistance, allowing them to be used in a wide variety of industries, from chemical applications to medical inserts. Many of these components have very complex geometries, requiring significant machining from traditionally produced billets. Commonly, as much as 90% of the initial material, already challenging and expensive to produce, is machined away in this shaping process resulting in significant waste and time expenditure. The costs involved have historically limited titanium to high end markets, however,

certain Powder Metallurgy (PM) production techniques over the last few decades have revealed disruptive processing routes which could change this entirely.

The two most commonly touted options have been Hot Isostatic Pressing (HIP) and Spark Plasma Sintering (SPS), also known as Field Assisted Sintering Technology (FAST). These provide the capability to consolidate surplus additive manufacturing (AM) titanium powders or waste materials from machining, such as swarf, without the need for melting, maintaining the required complex microstructures for purpose. Both processes use sintering, a technique where powder materials are compacted into solid-state objects using heat and pressure below the melting point of the respective materials. The particles are bonded through atomic transport mechanisms, and driven by the reduction of enthalpy through reducing specific surface area, or recrystallisation. Further particle growth then causes any remaining voids to be expelled and complete the consolidation.

Sintering, and specifically FAST, has been investigated for use in titanium part production, alongside other metallic systems [2] and often ceramics [3]; however, whilst challenges with sintering non conductive ceramics led to the creation of a few techniques to more efficiently control the electric current involved, such as Flash Sintering, this variable has, debatably, been overlooked for more conductive metal systems. A finer understanding and control on this fundamental part of the process will enable the design and creation of unique thermal gradients, and provide a previously unavailable degree of flexibility to the technique.

This is, however, a very challenging undertaking as the FAST process itself is a 'black box', meaning it is opaque to internal analysis, with only surface thermocouples and a pyrometer capable of providing untampered information on the ongoing process. To gain an understanding of the internal workings of the FAST process and methods to control the current, Ohmic heating in the tooling, and their impact on the final produced samples a simulation is required. The scale of lab samples, let alone industrial requirements, makes multi-particle simulations too computationally intense to provide a full picture of the machine. Finite Element Analysis (FEA),

resolves this challenge with its scaling capabilities and compatibility with the coupling of multiple physical systems, allowing us to approach the problem from fundamental equations, creating a model akin to a digital twin.

Simulated models will, of course, need validation through comparison to the physical systems they are modelling and here 2 alloy systems were chosen. Firstly, Ti-6Al-4V with its clearly detectable β transus and temperature dependence of its grain size will allow us to attain these validations whilst also demonstrating the technique's utility for the most commonly utilised titanium alloy. Secondly, Ti - TiB₂ MMC systems provide additional thermal dependencies and another, practical demonstration through its ballistic resistances.

With this in mind, the aims of this research are: (i) to develop a validated simulation capable of modifying electrical current control and predicting the thermal outcomes at a range of scales, and then (ii) demonstrate the effectiveness and utility of such a tool for the improvement of the FAST process, further enabling the industry readiness of the technique to promote low cost titanium components in a range of sectors.

1.1.1 Thesis Overview

This thesis is divided into six chapters following this introductory chapter, a literature review on the field goes over the fundamental knowledge required to understand this work and papers referenced in later chapters.

Chapter 3 contains the methodologies used in this work as well as the gathering of graphite material data required for accurate simulation results in chapters 4, 5, and 6.

Chapters 4 and 5 cover the creation of the simulation used for prediction of thermal gradients and the initial consolidation and microstructure results. Chapter 5 in particular, is based on a paper published in the Journal of Materials Science titled

"Channelling electric current during Field-Assisted Sintering Technique (FAST) to control microstructural evolution in Ti-6Al-4V" authored by Pepper et al. This focuses on a demonstration of the current control technique developed to prove its predictive capabilities at larger scales and the resolutions possible.

Chapter 6 draws from two papers published on the production of titanium metal matrix composite plates, demonstrating the practical impact of this current control addition to the FAST process through its impact on ballistic properties of a TiB functionally graded material.

Finally, chapter 7 is a conclusion of the thesis, concluding the work and suggesting paths for future work which could be taken.

Chapter 2

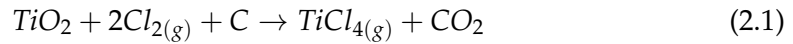
Literature Review

2.1 Titanium

Titanium is found naturally in the ores, rutile (TiO_2) and ilmenite ($FeTiO_3$), and comprises 0.6% of the planet's crust. This makes it the ninth most common metal and fourth most common structural metal on earth and has huge importance as a lightweight metal in industry. With high strength to weight ratios and an exceptional corrosion resistance, it is commonly used in challenging environments such as the biomedical implants, surgical tools, or offshore parts. The majority of titanium alloys however, are used in the aerospace sector due to its comparatively high specific strength to weight ratio. This is required in aero-engine compressor discs and landing gear, making up to 15%, by weight, of commercial aircraft such as the Boeing 787 airframe [4].

It has less of a history than other metals with it only being manufactured into its pure form in 1910 by Mathew Hunter [5] when he heated $TiCl_4$ and sodium at 700-800°C. This was then replaced three decades later when Wilhelm Kroll [1] created a commercially viable process for producing titanium, lasting to this day. In the Kroll process the ore is reacted with carbon and chlorine gas, producing titanium tetrachloride ($TiCl_4$) seen in Eq. 2.1. This, then needs to be purified to remove any remaining iron chloride before it is combined with liquid magnesium under an argon atmosphere at 800-850°C producing titanium sponge through Eq. 2.2. The 'sponge' is named for its incredible porosity and friability at this stage, containing gases which need to be expelled before it is crushed, compressed and electron beam

welded onto an electrode. All this prior to the vacuum induction melting (VIM) used to create the ingots that are broken down into billets and bars using multiple hot forging steps. Often additional thermomechanical steps are also required to remove impurities and ensure a uniform product, adding to the cost of the titanium.



All of these steps are incredibly time consuming and the process is limited to batch production, making it inefficient and costly. However, in spite of this and other efforts [6] to disrupt the process it still remains the primary processing route, responsible for the majority of the world's titanium. This titanium does, however, need to undergo several more thermomechanical steps to reach the chemical and mechanical requirements for use [7], and it is here where the largest individual cost involved in titanium production arises. This challenge presents a tempting opportunity for a disruptive process to reduce processing time and costs and is, in large part, responsible for this growing field of study.

2.1.1 Titanium Alloys

As an allotropic alloy titanium is capable of existing in two crystalline forms: the alpha (α) phase with an hexagonal close packed (hcp) structure, and the beta phase with its body centred cubic (bcc) phase. The two are thermodynamically stable within their own temperature ranges, separated in pure titanium at 882°C by the β transus temperature. The β phase is stable above this temperature, the the α below, and it is this transformation which governs the metallurgical properties of this metal and its alloys [8].

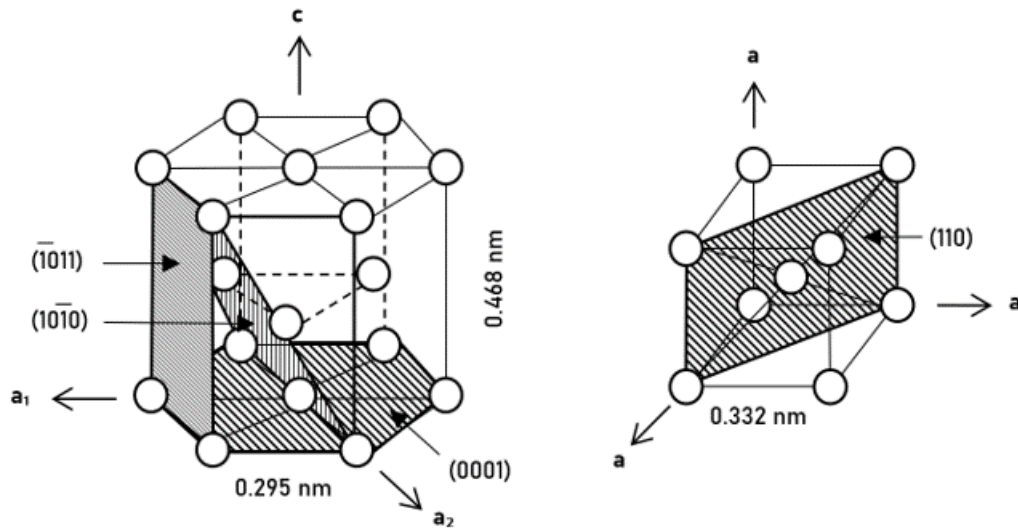


FIGURE 2.1: Schematic illustration of the α HCP and β BCC titanium unit cell crystal structures [9]

There are several alloying elements commonly found in service alloys which have a strong impact on this transformation temperature when dissolved in titanium. They are categorised by their impact on this temperature, with elements raising it being referred to as α stabilisers, and those that lower it as β stabilisers. Titanium is a transition metal and as such has an outer electron d sub-shell that is partially filled. This plays the largest role in which elements conform to which category, with those containing 4 electrons in their outer shell, like titanium, commonly stabilising the β phase. When these stabilising elements have this same outer shell configuration (V, Mo, Nb) and can form a solid solution they stabilise the alloy through substitution. Whereas when not isomorphous they form a eutectoid reaction (Fe, Cr, Ni, Mn) and stabilise the alloy as interstitials. This is not always the case as these eutectoid alloying elements may also form intermetallics if their concentration is high enough, and an obvious exception can be found in hydrogen. There are also neutral stabilisers (Sn, Zr) which do not stabilise either the α or β phase but can offer solution strengthening to the alloy. These effects, shifting the β transus temperature, lead to a variety of different sweeping classifications for these alloys: α , near- α , $\alpha + \beta$, near- β , and β alloys.

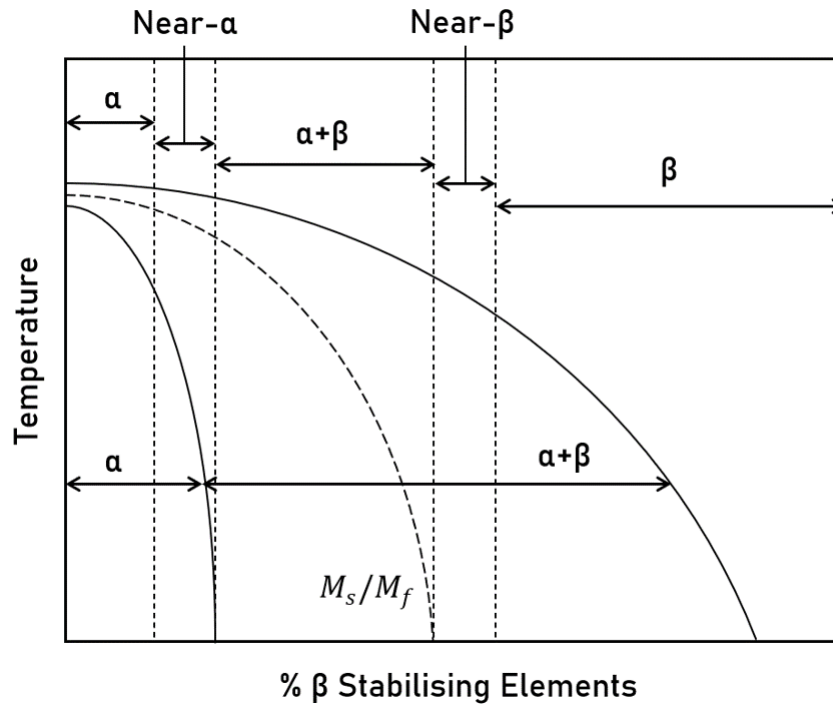


FIGURE 2.2: A pseudo binary phase diagram for titanium with stabilising additions adapted from [8]

α alloys

α alloys have a HCP crystal lattice structure and are defined as titanium alloys which are, predominantly, fully stabilised α at room temperature. The primary strengthening element here is oxygen held in solid solution and many of these alloys are found as Commercially Pure (CP) titanium, grades 1-4. These alloys can be further subdivided into α and near α , which widen the thermomechanical processing window compared to the former type. They are able to retain a small quantity of β at room temperatures, containing elements like V and Mo, though limited to 2 wt.%. On average they exhibit higher tensile strengths than pure α alloys, as well as superior creep resistance.

$\alpha + \beta$ alloys

In this classification $\alpha + \beta$ alloys have sufficient β stabilising elements, with concentrations of between 4 and 6 wt. %, to retain both structures at ambient temperatures.

The thermomechanical processing can be manipulated to provide a range of microstructural profiles, for example, quenching can allow the β phase to be retained if the rate of cooling is sufficient. Ti-6Al-4V is considered the primary alloy in this category and the main candidate through a large section of the titanium industry.

β alloys

β alloys have large enough concentrations of the stabilising elements that the β structures are retained once cooled. They can be often considered to be metastable due to the stable $\alpha + \beta$ phase extending into this region, visible in Fig. 2.2. There are also near β alloys which contain lower wt. % β stabilisers, with potential small additions of α alloying elements and they are more commonly used than pure β alloys due to the sometimes excessive amounts of β stabilisers required to create them.

2.1.2 Strengthening Mechanisms

Titanium, and specifically Ti-6Al-4V, is so commonly utilised throughout the industrial sector due to its properties, such as its high strength to weight ratio. This strength comes from two primary mechanisms which strengthen the titanium alloys which will be examined in this work through grain boundary strengthening, and solid solution strengthening.

Grain Boundary Strengthening

Grain size has a huge impact on the performance of titanium alloys, as well as many other metallic systems. This is commonly referred to as the Hall-Petch relationship which describes an inverse relationship between the yield strength and the grain size. This relationship describes the effect grain boundaries have, impeding dislocation movement within metals. This dislocation motion, and therefore the deformation, can occur along slip planes with priority in each grain. When encountering a new grain boundary the direction of the plane must reorient itself based on the

new orientation of subsequent grains in its path complicating the optimal path, and therefore requiring more energy. With a fine grain structure, more of these changes are required and thus more energy is needed to deform the material, increasing the strength [10]. This is a vital mechanism in both α and $\alpha + \beta$ titanium alloys, such as Ti-6Al-4V, as rapid cooling causes the desirable formation of very fine α grains, providing a higher strength to the alloy [11] through this Hall-Petch effect. Grain growth during sintering or heat treatments when metals are held at high temperatures for extended periods are therefore not commonly desirable and high dwell temperatures or excessive thermal gradients can result in a significant loss of strength.

Solid Solution Strengthening

The differing atomic sizes of alloying elements in titanium cause strain in the crystallographic lattice by pushing or pulling their neighbouring atoms. This is a known effect of the inclusion of alloying components and the benefits significantly outweigh the drawbacks. For smaller, and often unexpected, inclusions such as O, N, H, C, or B, their relative size allows them to occupy interstitial sites within the lattice causing tensile strain to the hosting titanium lattice. The opposite occurs with larger atoms such as Mo or V where the titanium atoms are substituted and the lattice experiences compressive strains instead. These solute alloying atoms, regardless of size, are seen to segregate around dislocations resulting in an overall reduction of strain energy meaning greater quantities are required to move dislocations, leaving the alloy with greater strength through this solid solution strengthening.

2.1.3 Selected Alloys

Ti-6Al-4V

As titanium development has primarily been pushed through the aerospace industry with its stringent requirements and high costs, there has been a common focus on the microstructural development of known alloys. Ti-6Al-4V was discovered in the 1950s and used as one of the first alloys in compressor blades for gas turbine

engines, but has since been utilised in a number of different applications such as medical and dental implants [12]. As an $\alpha + \beta$ alloy with a β transus of 995°C there are many possible microstructures to obtain with good overall properties. Some common microstructures are depicted here in Fig 2.3 as useful indicators of the materials thermomechanical history.

There are three main classes of microstructure for this alloy system; lamellar, bimodal, and equiaxed [13]. Lamella microstructures are made up of transformed β and are formed when cooling from the stable β phase at higher temperatures. The slower the cooling, the coarser the lamella plates, and this kind of structure can commonly be seen referred to as 'Widmanstätten', or β annealed titanium. A much finer lamella structure is possible if the material is quenched from above the β transus followed by annealing in the mixed phase region, forming a β quenched structure.

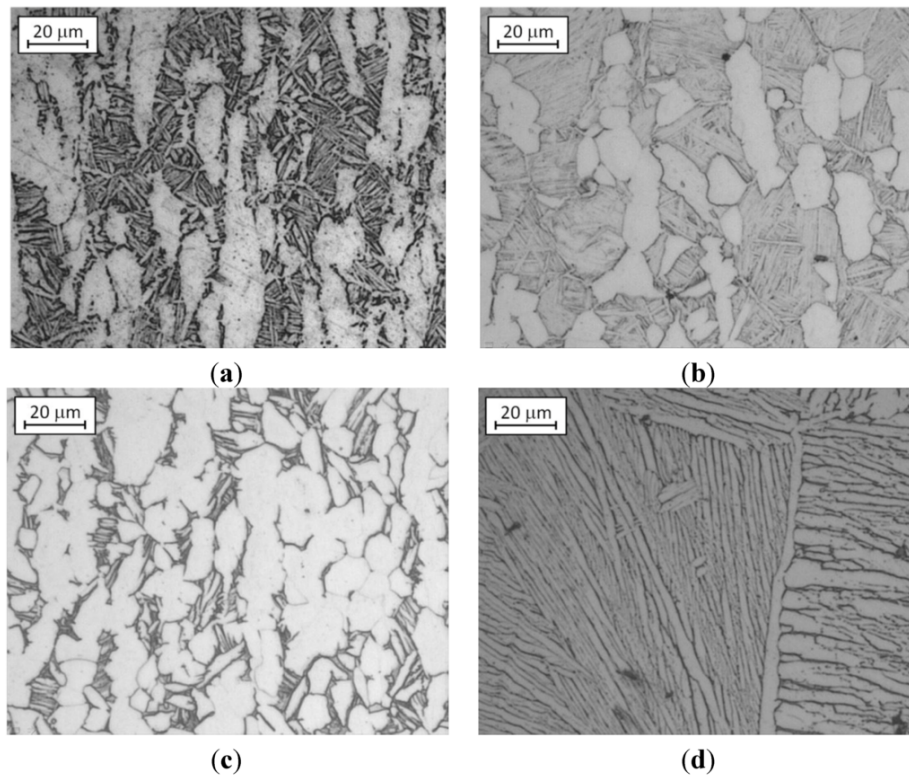


FIGURE 2.3: Optical microscope images of Ti-6Al-4V common microstructures from [14]. (a) mill annealed; (b) bimodal; (c) fully equiaxed; and (d) fully lamellar

Ti-3Al-2.5V

This alloy is also known as 'half-6-4' and is a near α titanium alloy. It sits between Commercially Pure(CP)-Ti and Ti-6Al-4V with intermediate strength and good cold formability. Originally used for aerospace hydraulic fuel tubes and foil [15], [16] though today, like Ti-6Al-4V it can also be used for dental implants and sports equipment such as tennis rackets or golf clubs [12]. The microstructures which can be developed in sintered samples of this alloy are similar to that of Ti-6Al-4V but with a β transus 60 °C lower, recipes are not interchangeable between the two.

2.2 Titanium Powder Characterisation/Creation

In this thesis, titanium alloys are primarily considered, initially in the form of powders, making it important to understand how they are characterised by their chemical, physical, and process characteristics. This includes: shape; powder size distribution (PSD); surface morphology; condition of the particles; packing, or tap density; and flowability [17], [18]. These powders and their properties are influenced by their production routes outlined below.

2.2.1 Powder Production Routes

There are several options for the creation of titanium alloy powders [19] including plasma or gas atomisation (PA/GA), the hydride-dehydride (HDH) process, and plasma rotating electrode process (PREP), as well as newer novel approaches. Apart from the novel approaches, all of these options rely on billet or ingot material from the Kroll process and have a range of associated costs and uses.

Atomisation and PREP

Rapid solidification routes involve the solidification of liquid metal at high cooling rates up to 10^5°C s^{-1} [20]. These include a variety of options such as Gas Atomisation

(GA) which uses a gas jet to atomise the molten metal stream whereas the Plasma Atomisation (PA) uses a wire feed which is simultaneously melted and atomised by a high temperature plasma. The advantage of PA is the high purity powders it produces, which comes from the liquid metal's lack of contact with refractory metals that often cause contamination prior to solidification.

The related Rotating Electrode Process (REP) uses a tungsten arc to melt feedstock and the arc Plasma Rotating Electrode Process (PREP) uses a plasma arc, but beyond this solidification happens similarly to the atomisation processes. PREP produces higher purity material with the same lack of physical contact the corresponding atomisation method boasts, and both rotating electrode processes typically produce coarser powders than when atomised. All of these techniques share a final smooth spherical morphology, meaning powders can pack to high density and readily flow. They do not compact well at low temperatures however, and as such are avoided by processes such as Cold Isostatic Pressing (CIP).

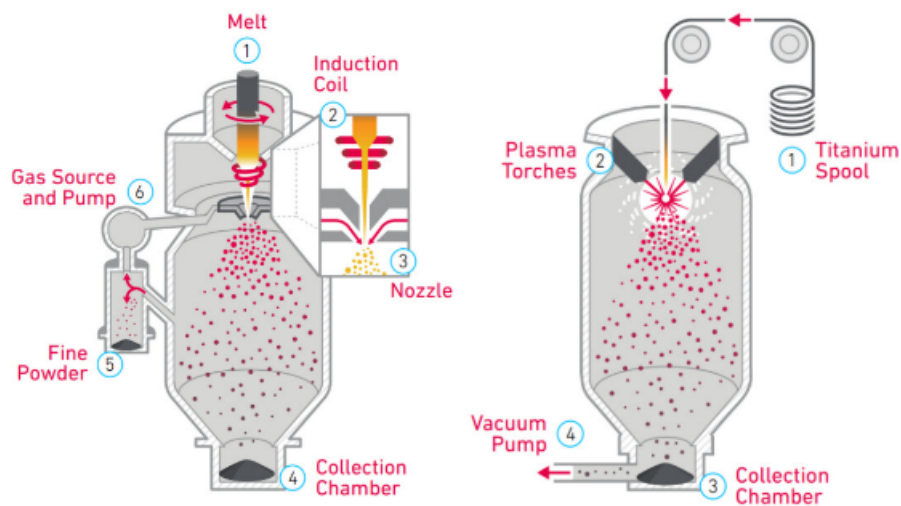


FIGURE 2.4: Schematic diagrams of both the GA method (left) and PA method (right) for powder production taken from carpenter additive [21]

Hydride-dehydride

Powder is considered to be hydride-dehydride (HDH) if made from solid titanium which has been heated to over 400°C under a environment of hydrogen. Under these conditions the atoms diffuse into the material along the grain boundaries and embrittle it, allowing it to be more easily pulverised into fine powders. When the required size, depending primarily on the grain size of the initial microstructure, has been reached the material is heated under vacuum to expel the remaining hydrogen. These powders are very angular in shape with smooth faces from the shattering visible in Fig 2.5, this can be beneficial for consolidation methods such as CIP due to interlocking of the particles. As may be expected, hydrogen is a common impurity in powders created with this route, but oxygen, iron, nickel, and chromium can also be seen from interactions with the steel reactor where the initial metal is produced.

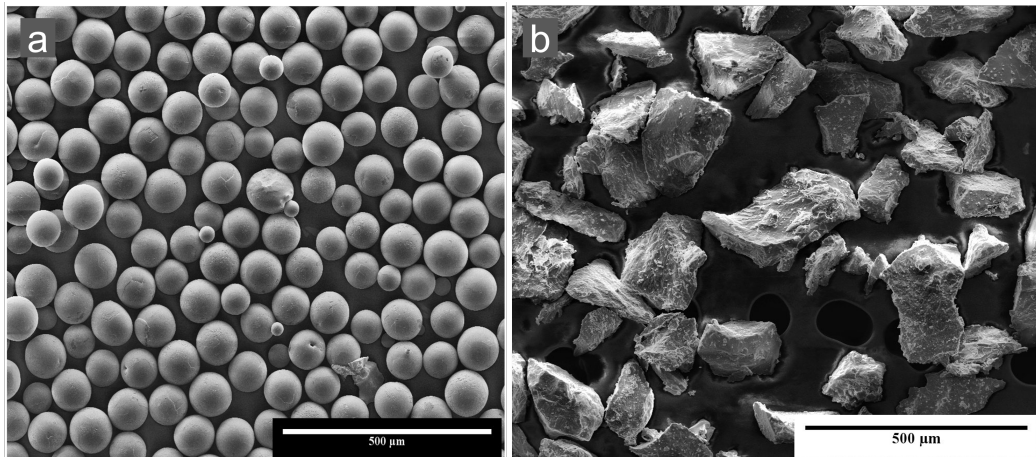


FIGURE 2.5: Secondary Electron Powder surface images (a) GA Ti-6Al-4V powder and (b) HDH Ti-6Al-4V Eckhart powder used in this work

2.3 Titanium Matrix Composites

Titanium matrix composites (TMC) are promising MMCs as they provide both significant strength, and stiffness improvements over conventional titanium alloys with potential cost reductions. For certain systems, such as Ti-TiB used here in chapter 6, there are also in situ reactions to form whisker reinforced composites and they are gaining popularity in various industries. Aerospace and automotive industries are

taking specific interest due to their ability to enhance high temperature and specific strength applications [22]. It is understood that for these industries the reinforcing material needs the following properties [23]:

- Have comparable coefficient of thermal expansion (CTE) to the matrix to prevent cracking and de-bonding
- They must be stiffer than the matrix material
- Ideally provide a low solubility, minimising inter-facial reactions in the matrix

For titanium alloys most ceramic candidates are unsuitable for reinforcement as they react with the matrix, with popular remaining options being TiB, TiC, and TiN. TiN however, has a 22% max solubility, breaking the third requirement, and therefore cannot be considered. This low solubility requirement points towards the other two options as titanium can accommodate only up to 0.4 wt.% carbon in solid solution, and less than 0.05 wt.% boron can be held in α phase titanium [24]. However, despite the higher stiffness of TiC, its CTE discrepancy compared to TiB and Ti, combined with difficulty forming the reinforcement in-situ, makes TiB the primary reinforcement option for this TMCs.

2.3.1 Titanium Boron System

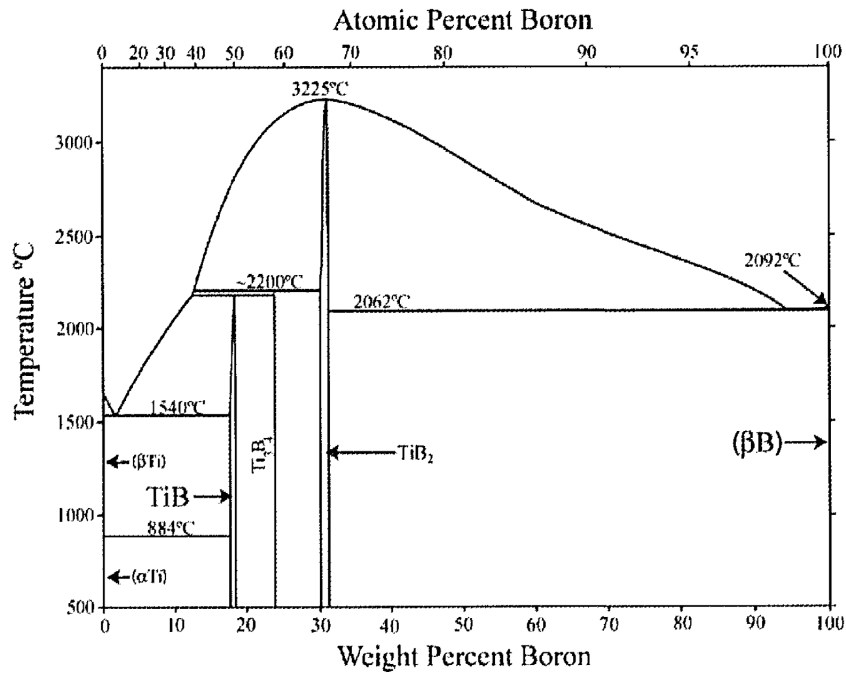


FIGURE 2.6: The Titanium Boron Phase Diagram adapted from [25]

The phase diagram of this system (Fig 2.6) shows that B cannot exist in solid solution within titanium. However it can in fact hold up to 0.05 wt.% boron in both α and β phases up to melting point where it becomes completely soluble. It also demonstrates that of the three compounds able to present at equilibrium, TiB is the most stable and will form if there is low atomic % boron in the material. When mixed with either boron or TiB₂, TiB will form via a reaction in-situ wherever excess titanium is present [26]. Some other points of note are that there are no equilibrium phases between Ti and TiB meaning no inter-facial reaction in the composite, resulting in very stable and clear interfaces [27]. The narrow wt.% range of TiB formation also means that the stoichiometry of the reinforcement will be the same across the whole material and therefore the mechanical properties will be consistent for each TiB whisker. This will then also be true for the bulk material assuming even dispersion throughout the matrix. Additionally, TiB and TiB₂ both have great thermal stability within the titanium processing window, making it useful for high temperature applications with near zero reactivity between reinforcement and matrix.

2.3.2 In Situ Formation Of Titanium Boride

Previous work by Brandstötter and Lengauer [28] observed TiB needles developing from the TiB₂ particles in their work with no Ti₃B₄ at the interface confirming the direct transformation expected. TiB is orthorhombic in structure and is formed by the diffusion of boron atoms through the titanium matrix forming which form 'zigzag' chains of boron atoms [29] surrounded by titanium atoms. The reaction for this is described below in eq 2.4.

TiB Crystal Structure

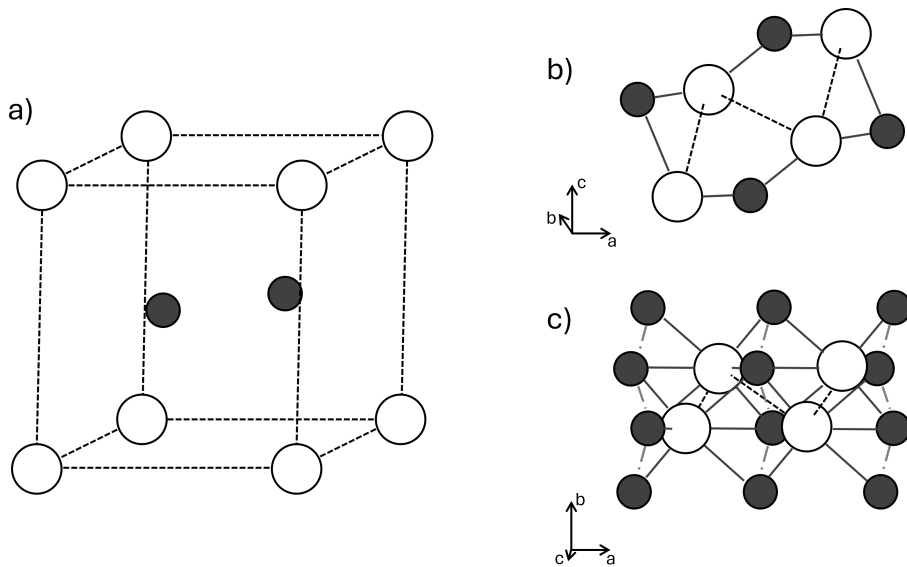


FIGURE 2.7: Schematic illustration of (a) the primitive cell crystal structure of TiB₂, (b) the orthorhombic unit cell of TiB, and (c) the expanded boron-boron (grey) chain of the TiB structure obtained after reaction with titanium (white).

This atomic structure seen in Fig 2.7 forms in-situ with reaction between the titanium matrix and TiB₂ with a needle shaped morphology, sometimes also referred to as a whisker. A high temperature annealing phase is often required to fully convert all the material, however, due to the diffusion dependency of the process, it can vary depending on boron content and concentration.





The most common reactions to form these compounds in this technique are above. All three process used are known to be spontaneous ($\Delta_r G < 0$), as well as exothermic ($\Delta_r H < 0$) when temperatures exceed 1200 K [30]. This in situ conversion is possible as long as these conditions are reached and will be utilised in this work.

2.3.3 Boron Impact On β Transus

When included as an alloying element in titanium, boron is an α stabiliser, but because of its low solubility not much actually enters solution, meaning a negligible effect on titanium without additional processing [31]. Whang et al. [32] report achieving this with up to 10% boron solubility using rapid solidification of between 10^5 and 10^7 K s^{-1} . Alloying with this level of boron would certainly increase the β transus, although the paper does not report an exact value. Tamirisakandala et al. [33] saw a 60°C increase in this transus temperature for a Ti-6Al-4V-1.7B powder from this boron inclusion, achieved through GA under 'inert' conditions. Therefore, even though the reported solubility is low in titanium, it is believed that the β transus will be raised slightly with the inclusion of this reinforcement. The exact temperature increase depends on many additional factors such as the purity of the constituent materials, the oxygen content of titanium, or the powder processing method.

2.3.4 TiB Strengthening Mechanisms

The reason for overcoming the challenges of manufacture for this MMC material is the significant improvement in mechanical properties which it can provide. There are two main explanations which can be given for these enhancements: the load-transferring, and matrix-transferring mechanisms. Load transferring mechanisms are often considered to be the primary source of this strengthening, with Li et al. [34] focusing their research on the reinforcement effects of TiC-TiB composites and Chandravanshi et al. [35] theorising that their increased creep resistance was owing

to the lack of deformation in the whiskers.

Other researchers have demonstrated through a yield strength model that the grain refinement of the matrix from the presence of the TiB is responsible for the increase in said composite yield strength [36]. Though the true dominant effect remains unclear, it is apparent that both aspects play a role in the improvement of material properties and the material holds high potential for armour and aerospace applications.

2.3.5 Manufacture Of TiB Composites

Two main methods to manufacture these TiB composites are: rapid solidification (RS) [32], [37] and mechanical alloying (MA) [38], [39]. It has been demonstrated that a more well distributed mixture of boron is seen when RS is used and finer TiB has been observed. However, the RS technique's prohibitive cost makes it challenging for many practical uses and directs many to alternative processes such as MA. As this work is aimed at potential practical armour applications this mechanical alloying is the route selected here.

2.4 Mechanical Alloying

Originally developed to produce nickel based superalloys, mechanically alloying material is a solid state technique where a ball mill is used to combine the constituent phases through mixing at high energies resulting in alloying [40]. This is schematically depicted below in Fig 2.8.

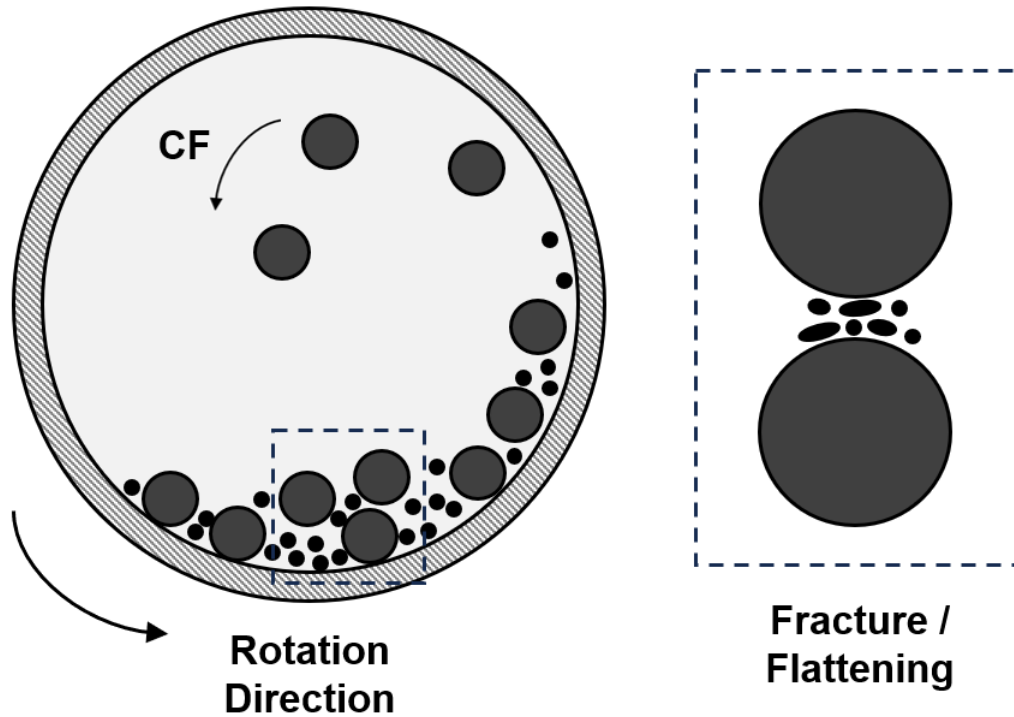


FIGURE 2.8: Schematic of the basic mechanical alloying process demonstrating the interaction between the milling balls and powder under Centrifugal Force (CF)

Initially for mechanical alloying, the components are combined through milling as in Fig 2.8 and layering occurs as the particles become trapped in-between the host powder. This milling ideally process then continues until the layers system becomes a homogeneous distribution of the elements with the new alloy composition. This technique has become extensively used for Al reinforced SiC composites [41] since its inception but the results vary depending on the ductility of the source materials.

Given its hard and brittle nature it has been determined [38] that even with long milling times, it is not possible to get this even distribution of boron or TiB_2 in the titanium matrix using MA. The boron distribution in the titanium matrix is likely instead to resemble the layered structure rather than a homogeneous distribution. With differing powder size distributions it may also result in a boron seeded powder with small inclusions cold welded into the powders as used in chapter 6 of this work.

With more ductile powders, the alloying is achieved as specified through deformation, fracture and cold welding and the process is as expected. However, with more brittle powders, where powder fracture and welding dominate, some assisting process control agents may be utilised to limit particle agglomeration. TiH_2 can be used for titanium alloys due to its embrittling effect, however, the material requires degassing post milling to remove the hydrogen.

2.5 Consolidation

Consolidation itself is used to describe compaction of a powder to the maximum possible, or theoretical, density of the material. Compaction, specifically here, can often be used to describe an incomplete consolidation of the material instead, For titanium this is commonly from the oxide layer on the powder surface acting as a barrier between particles preventing full joining. It is possible to compact a powder to near full density without breaking this oxide layer, however, this will leave an 'unconsolidated' material which is near 100% dense but poorly bonded [42], as is the case with some powder extrusion. For many materials, titanium being no exception, heat and pressure are required to overcome this final barrier and achieve full consolidation. Sintering is the most common commercial method to achieve this for titanium, if traditional casting is not considered, though there are other avenues such as alternative powder metallurgy (PM) techniques, or additive manufacturing (AM) routes for alloys and MMCs.

The drive for the advancement of these sintering techniques is strong due to the multiple advantages of powder metallurgy routes can have over the classic cast, or wrought products:

- Near-net shaping is possible in the consolidation step reducing waste with a range of product sizes
- This leads to more cost-effective and potentially green components

- Fine thermal control allows for grain size targeting to suit desired properties
- More isotropic properties are possible to achieve
- Highly alloyed or functionally graded components are also more easily achievable than from ingot metallurgy

2.5.1 Consolidation Theory

The final density of powder produced components is a critical property and one which determines whether the sintering has been successful or not. It has a great influence on the physical, mechanical and functional properties of these metallic parts and can be influenced by several parameters of the consolidation process. Increasing the densification is the same as reducing the porosity of a sample which often brings about superior physical properties such as high hardness, tensile / compressive strength and strain, as well as elevated thermal and electrical conductivity [43].

It is generally considered that four distinct stages describe the compaction of powders [20], [44]. These are rearrangement of the particles, localised plastic deformation (primarily a function of particle geometry), homogeneous deformation, and consolidation where material properties play a greater role [44]. These stages each have associated rates of density increase with increasing compaction pressure, starting off very rapidly and tailing off until the theoretical density is reached. Under cold conditions, to begin with, elastic deformation occurs between particles where they make contact. Then, particles are arranged into a higher, more efficient, packing density until the maximum is reached due to particle rearrangement and sliding. This tap density is referred to as the upper limit of this rearrangement stage, and is a direct measure of the best possible packing fraction for any given powder.

The second stage is localised plastic deformation where any harsh features are flattened at points of particle contact. For ductile materials, when the stress increases above yield, material will flow into empty areas surrounding the particle resulting in uneven stress distributions. This flow does, however, remove the larger pore regions and only smaller pores remain unfilled. Brittle materials, on the other hand, fracture

early in this phase and particles are repacked as the smaller pieces get pushed into the unoccupied voids. Homogeneous deformation happens as pressures further increase and is characterised by deformation throughout the particle mass, increasing the properties of the bulk material. As the material strain hardens during the process, resistance to further deformation increases, and if sufficient pressures are reached surface layers can be breached, exposing the underlying metal previously protected by oxides. This can increase the interatomic forces and bonding potential increases dramatically between particles during the final consolidation stage.

2.5.2 Hot Consolidation

Most practical applications of sintering utilise increased temperatures to improve the speed, efficiency, and final density of the process as the sintering process usually occurs between 50% and 80% of the melting temperature, known as the homologous temperature. It has been stated in work by German et al. [45] that "Sintering is a thermal treatment for bonding particles into a coherent, predominantly solid structure via mass transport events that often occur on the atomic scale. The bonding leads to improved strength and a lower system energy". It is also known that sintering is driven by the fundamental push to reduce the total free energy of a system leading to the obvious conclusion that the addition of thermal energy is desirable where possible for the process.

The simplest model of sintering is a two sphere system, a basis which can be expanded into more complicated models, consisting of two identical spheres. A neck forms between the two which continues to expand until they have fully combined with 1.26x the diameter of the original, shown in Fig 2.9. This serves as a good model to understand the processes outlined in the previous section. However, with the addition of temperature to the system, the required pressures to achieve the energies necessary are lowered, increasing the formability of strong materials such as titanium. With this additional thermal energy in the process, the later stages now focus on grain growth, as well as increased mass transportation, as the mechanisms

primarily responsible for the final consolidation stages.

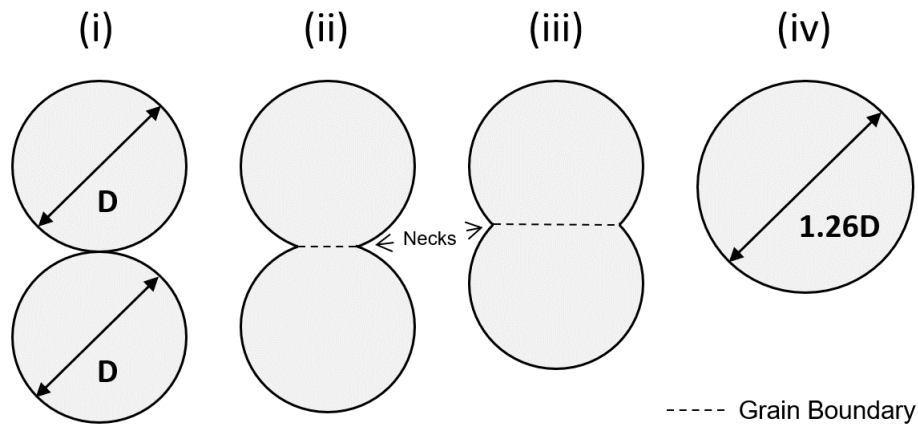


FIGURE 2.9: Schematic illustration of the stages of the necking process between two particles during sintering (i) Initial Contact (ii) Early Growth (iii) Late Stage Necking (iv) Fully Coalesced

Two mass transportation pathways contribute to bonding of particles during consolidation, surface and bulk transport. The first drives particle coarsening, and covers surface diffusion and evaporation/condensation while the latter primarily contributes to the densification of the sample through grain boundary and volume diffusion, as well as plastic flow. These two often compete during the sintering process and thus promoting the bulk transport is necessitated for efficient sintering. These mass transport mechanisms are displayed schematically below in Fig2.10. In certain material systems this temperature rise will cause a phase transition which may also affect the densification of the sample. Titanium's α - β phase transition for example reduces density between the two phases and there is additional space for diffusion to occur, leading to higher densification rates. Using higher temperatures is not without flaws however, as it is possible in some metals for liquid phase transformations to occur degrading the densification due to the de-wetting in certain metallic systems [46] or simply destroying the mould.

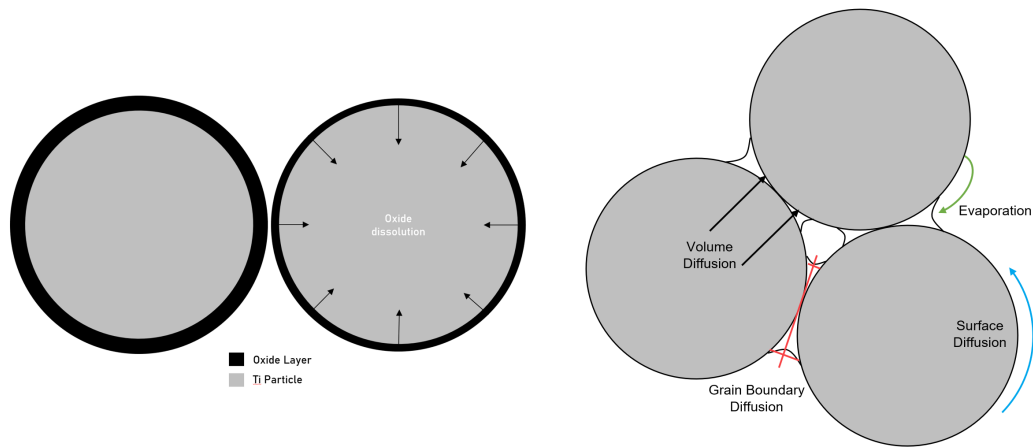


FIGURE 2.10: Schematic illustration of dissolution in the titanium oxide layer and common transport mechanisms available during the sintering process, adapted from [45]

2.5.3 Alternatively Available Sintering Techniques

Conventional Sintering

Conventional, free, or pressure-less sintering is the simplest application of these ideas involving the heating of a compact previously prepared at ambient conditions without the application of pressure. The benefits of this technique lie in its simplicity and ease of production, however, it does not produce highly dense samples, and is associated with low heating rates, commonly at around $10^{\circ}\text{C}/\text{min}$. For materials which sinter at higher temperatures such as titanium this also results in excessively long processing times, counteracting the benefits of simplicity and mass reproducibility in the concept.

In many systems the main reason for the low densities often seen in conventionally sintered parts is the lack of pressure. Whilst beneficial for potential complex geometry production through green bodies, this aspect of the process reduces, or removes, the particle rearrangement and plastic deformation common to pressure sintering techniques. It is, especially relevant to titanium alloys and MMCs where this plastic deformation is vital to achieving a good final density in the sintered component.

Hot Isostatic Pressing

Very similar in concept to conventional sintering, Hot Isostatic Pressing (HIP) is a solid state consolidation process that harnesses the application of temperature but with additional isostatic pressure to consolidate the powder to final theoretical density. Pressure is applied using an inert gas, commonly argon, and this technique is usually applied for wrought / cast products to finish removing internal porosity [47]. It has not historically been commonly used for pure powder consolidation due to the required canning and degassing processes along with post HIP removal [48]. It also suffers from low heating rates and long processing times but commonly produces good results in density with the added pressure from the gas. Here, similarly to the conventional sintering process, the added pressure from the external gas provides a uniform stress state in the powder. However, the increased pressure allows for more plastic deformation to cause pore collapse during the process, allowing the final consolidation of the parts to be much improved. HIPing has also been applied to metal matrix consolidation which can be difficult to conventionally process [37] for this reason, demonstrating some cases where the negatives can be accepted for potential gains.

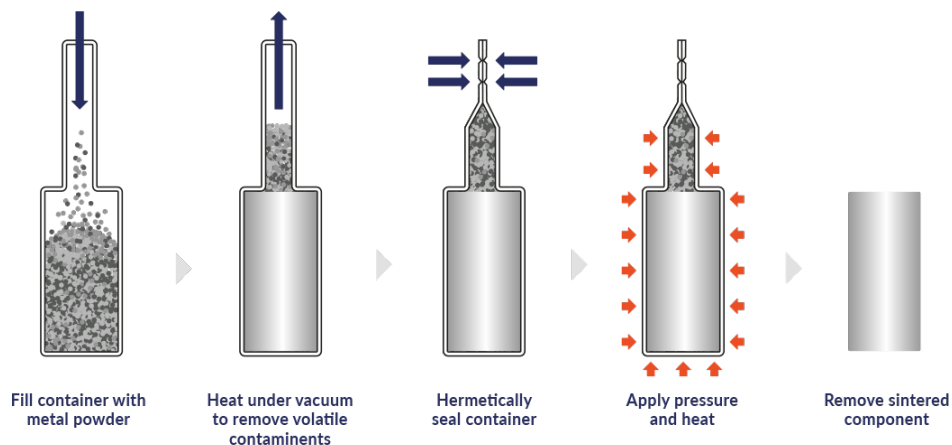


FIGURE 2.11: Diagram of the Powder Hot Isostatic Pressing process, from canning to final component, sourced from [49]

2.6 Field Assisted Sintering Technique

A step above these techniques in many regards, The Spark Plasma Sintering / Field Assisted Sintering Technique (SPS/FAST) is a low voltage, typically < 10 V, uniaxial pressure assisted process, which may be used to transform powders into near net shape component. There is a wide scope of variety in the technique, in that it may involve pulsed or direct current; and may be performed in vacuum, inert gas, or a reactive gas environment on a host of potential materials. This technique is similar, in essence, to Hot Isostatic Pressing (HIP) in that the densification of the powder components under compression is ensured through heating during the press. However, the way the heat is generated and transmitted into the sintering material is different. The generated current passes between the two pressing rams, typically formed from ISO graphite, through the sample and creates the required heat through internal resistance and joule heating. Review papers from Munir and Orru provide summaries of the surrounding research areas [50]–[52].

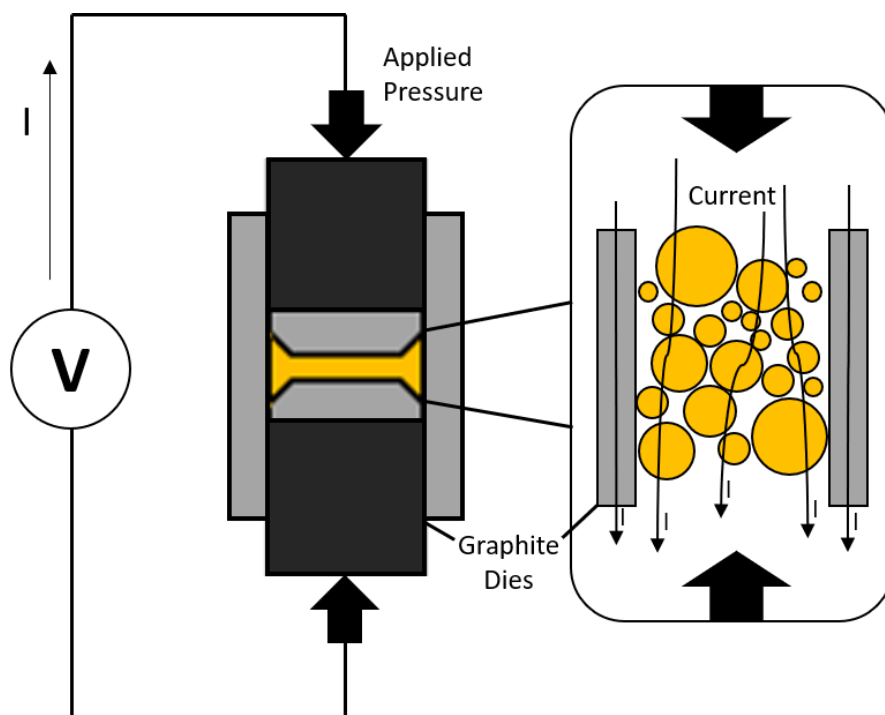


FIGURE 2.12: Schematic of a simplified FAST tooling layout highlighting the current driven nature of the process

The quasi-static compressive stress applied in FAST provides a better surface to

surface contact between particles, changing the quantity, and shape of the contacts in question whilst enhancing the existing densification mechanisms already present. It also activates new mechanisms, including plastic deformation, as well as grain boundary sliding [53]. However it is not so simple to describe the total behaviour of a porous powder under these conditions. Therefore, creep equations describing the deformation of dense materials at high temperature, have been adapted by Coble, and they primarily consider this porous aspect to the sintering sample. Although simplistic, this mechanical description is very useful in identifying the main mechanisms during FAST [54].

The amplitude of the applied stress is limited by the fracture strength of the ram tool at high temperatures (for ISO graphite, between 100 and 150 MPa) as well as the loading system. In addition, Salamon et al. [55] recorded punch vibrations correlating with pulsed current characteristics. It is possible therefore that an oscillating stress component can be imposed on top of the static component from the hydraulic system, possibly enhancing packing at the early stages of sintering. Many such complications exist within the system and these have resulted in many variations of the technique appearing in publication over the years.

2.6.1 Naming Schemes

Potentially due to marginal differences in operating parameters for the technique, up until 2014 there have been a total of 60 different naming conventions for SPS. It has been termed Pulsed Electric Current sintering (PECS), Plasma Activated Sintering (PAS), Electric Pulse Assisted Consolidation (EPAC), and Plasma Pressure Compaction (PPC) to name the most common. Most of these hold a solid connection to the process, however, to date no spark or plasma has been detected [56], [57] during sintering, despite the most common name being SPS. The plasma in the name referring to the discharges that were thought to occur between the particles theoretically providing a cleaning effect prior to consolidation. As such it will be referred to from here on using the FAST acronym used by machine manufacturers such as FCT systems. With all these different conventions comes a proportional horde of

publications, growing linearly from just 42 in 2000, through 472 in 2010, and now even reaching heights of 1408 in 2021 according to web of science, indicating a still growing and solid interest in the field. Additionally, with all this gathered information on the topic, novel features and applications of the FAST technique are being uncovered causing industrial interest in the field to be piqued. It is here that that this work commences.

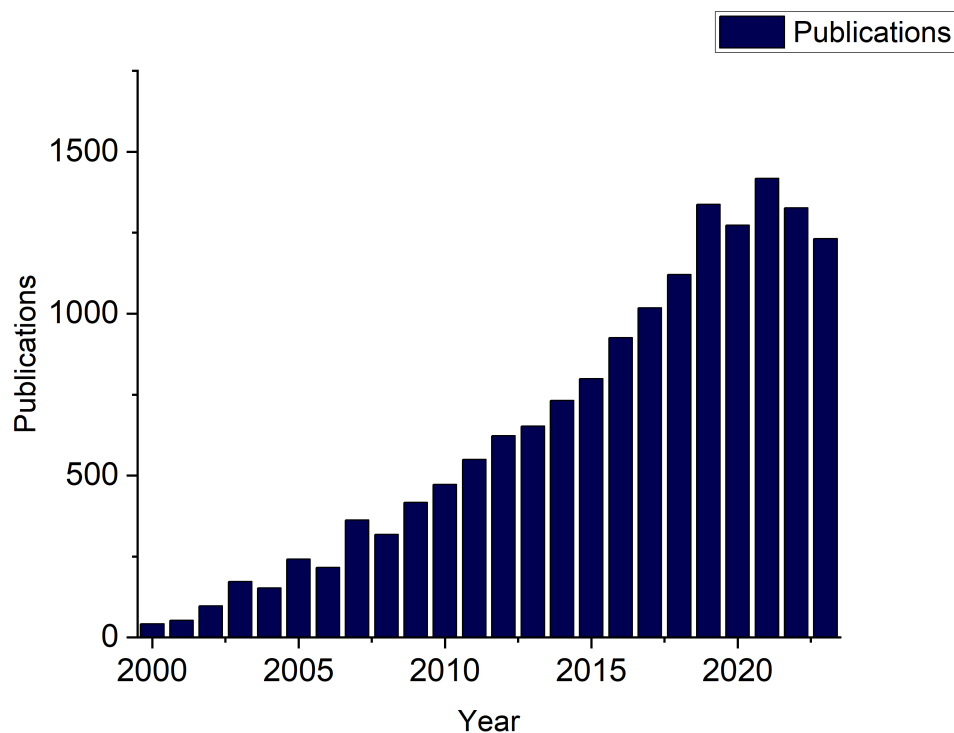


FIGURE 2.13: Number of publications for the process over the last 23 years labelled as Spark Plasma Sintering - from Web of Science

Whilst Fig 2.13 demonstrates a significant increase in publications on the technique in recent years, it also shows a mild stagnation over the last 5 years. It must be noted, however, that using the number of papers as a metric for interest in a field is subject to potential comparison with the increasing number of publications in all fields globally. In spite of these caveats, it is still believed that this is a positive indicator as to the wider uptake of this process, as well as its potential to grow further with new discoveries.

2.6.2 FAST Materials

FAST was initially developed for ceramic, composite, and metallic powders, however, the technique has been proven through these papers to be beneficial to a variety of fields with a broad scope of potential materials which can be processed successfully, including all classes of inorganic materials. Further explaining the continual growth of interest in the process and demonstrating a further potential in exploring the technique for more work to be carried out. One such avenue is the many composites and nano/micro architectures of great interest are achievable where conventional methods currently struggle to consolidate materials such as high temperature covalent solids or bulk nano-crystalline metals. One of the reasons for this is the ability to keep the grain sizes comparably small from powder to consolidated solid during sintering [58], [59] which can result in enhanced properties sometimes unobtainable otherwise.

Materials	Applications
Metals	Aerospace, Automotive, Shape-memory, Electronics, Thermoelectrics
Oxide ceramics	Sensors, Fuel cells, Lasers, Solar cells
Non-oxide ceramics	Biomedical, Abrasives, Cutting, Armor, Ultra-high temperature
Glasses	Biomedical, Optics, Upconversion devices, Thermoelectrics
Polymers	Composites, Aerospace, Electronics, Automotive

FAST uses [60] are not solely limited to these options however, as there is further potential to lay up material in such a way as to create functional gradients within a sample.

Functionally Graded Materials

The term Functionally Graded Materials (FGM) represents a gradient of composition, grain size, or porosity in 1,2, or 3 dimensions. The concept of these was introduced in 1972 [61], however, industry interest was not aroused until over 10 years later in the mid 1980s. The local variation of properties within these FGMs can fulfil

a vast range of applications across many fields.

Looking at Functionally Graded Materials from a processing point of view the gradients can be created from the powder itself or may be introduced during the sintering. There are numerous methods of powder processing which have been shown to successfully fabricate these graded compacts, however, when inhomogeneous powders are included the varied properties can lead to severe cracking problems. Superimposing an external pressure on the sinter helps to mitigate this issue and thus, FAST and HIP are therefore incredibly useful in consolidating FGMs such as Ti/TiB₂ systems [62]. It must be remembered however that the heating rates play an important role when required temperatures are high such as in this case, making FAST the ideal candidate for work in this area.

FAST is more than capable of this, and with the near net shaped die and insulation, opens new possibilities for the development of these materials based on the generation of a temperature gradient during the process. This can be obtained by modifying the heating elements cross sections or adding insulating material to the tooling, as when thermal energy is produced in the die this variation will result in a potentially desired gradient. A smaller cross section locally increases the resistance and current density, and thus the temperature from joule heating, allowing complex production in one single step.

2.6.3 FAST Equipment Development

The FAST process may have gathered much interest from industry but there are still many challenges left to overcome before it can fully realize its potential. Some of these challenges include near net shape and net shape formability, scalability and a design for high throughput system. Whilst this design still is yet to be perfected the other issues are addressed fairly comprehensively with FAST [63] and through the FAST-forge technique proposed by Weston et al. [64]. Between this and other work in the field, it has been shown to be a valid stand-alone process, as well as being an improvement over other currently existing techniques such as the hot pressing

mentioned previously. The reduced time and temperature for SPS/FAST when compared to Hot Pressing (HP) increases potential output and requires less energy per sample. For example, in work by Musa et al. the time required to obtain 99.9% dense Ti-Al₂O₃-TiC composites with a typical sintering cycle is 5 min for SPS/FAST compared to 5 hrs for HP with the energy consumed being less than 10% of the latter. [65]

Manufacturing From Powder

A primary driving force in many industries currently is the reduction of waste and cost in production. One solution to this challenge is to produce parts in near net shape to minimise the material required to be removed in machining and to reduce the material wasted in removal. This is true for industries such as aerospace, biomedical and tool development where by minimising finishing costs and timings, more components can be made in the same time frame with lower expenditure.

The production of these components however, is not an easy task for FAST and has historically been under explored. Recently though, more examples have been demonstrated with the advent of techniques such as the FAST-forging technique for titanium and the major challenge faced has been the fabrication of a suitable graphite tool/die which can provide the required uniform temperature distribution and the shaping. One geometrical issue is sharp corners in the design as these can easily become heat sinks from dominant heat losses near those regions.

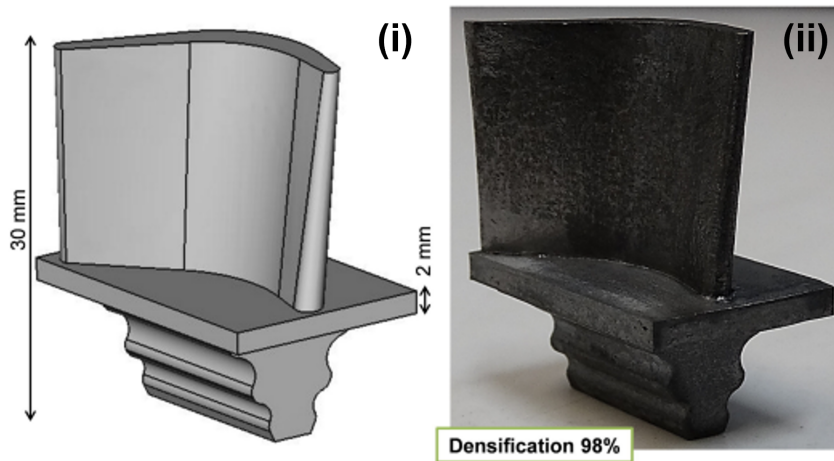


FIGURE 2.14: (i) A CAD model of the designed geometry (ii) Corresponding image of the sintered component from [66]

In addition, it must be noted the geometries possible are somewhat limited as FAST is a uniaxial compressive process, and as such undercuts and similarly complex features are currently impossible in a single step. Simple shapes, including bends and curves have been proved feasible and the resulting reduction of a significant percentage of required machining is still an improvement for material conservation over current techniques [66]. More complex shapes are also possible with more complicated die/punch systems, however full densification and other issues remain with more challenging geometries.

The largest limitation for taking the batch process sintering currently available to full industry scale is the reduction of total cycle time, specifically cooling to room temperature as this is the most time critical step for larger samples. One way of increasing the production rate is creating a separate cooling chamber where the hot tooling can be transferred after sintering such as in the FCT Systeme D 250. It may also be automated, first reported in 1999 [67] by Tokita, in a large-scale plant. For larger parts, > 400 mm in diameter, it is very challenging to implement a homogenous temperature distribution. This problem is not a simple one and specific tooling design is likely to be required to accurately perform this feat. It has also been suggested that an application of an additional induction heating source surrounding the die leads to this improved radial homogenous temperature distribution [63].

2.6.4 Temperature Control

This aspect of the process is a determining factor in the resulting properties of the material and as such is a critical factor. The main requirements for a reliable measurement of temperature are a short reaction time, low lag, and a high reproducibility in the temperature control of the system. An additional aim is to take the measurement as close to the sample itself as possible due to the differences in the spatial distribution of temperature over the equipment's scale. The temperature can be measured using a thermocouple drilled into the die, a radial pyrometer focusing on the outside of the die, or, as with the preferred method of controlling the temperature in most FAST machines, an internally drilled pyrometer taking readings from near to the sample region. A simplified diagram of the tooling stack in the machine is visible in Fig 2.12 and more detailed schematics in chapter 4 and 5.

Thermal Measurements

Devices in this process to measure the temperatures can be both optical, and non-optical (contact), and each has their own range of operation and limitations. Optical variants, such as pyrometers, are often used for higher temperature applications, such as in the FCT machines at the University of Sheffield. These are often incapable of measuring lower values close to room temperature due to limitations with emissivity. The equipment used in this thesis had a minimum temperature of approximately 400°C, though this has been lowered since the project began with recent improvements to 200°C. They also require the surface they are focused on to be clean and the emissivity of the material must be known. It can also be beneficial for the reading to be under vacuum conditions to prevent the thermal readings being impacted and corrected necessarily for the refractive index of air or inert gasses like argon. These limitations exist due to the underlying principle of these devices where they focus and detect the intensity of light thermally emitted from a body and calculate the temperature of the emitter using the Stefan-Boltzmann law. Given their position at a distance from the measurement, they are capable of measuring higher temperatures, though are subject to certain inaccuracies and other limitations

as mentioned previously.

Contact measuring devices, such as thermocouples (TC), can measure from lower temperatures and have an advantage in positional knowledge, able to determine values at multiple specific locations accurately. These devices fundamentally work using the Seebeck effect, where two dissimilar metals joined at two junctions held at different temperatures produce a measurable electromotive force. This can then be translated back to refer the temperature difference which caused it. However, at high temperatures the reactions between the TCs and the die material must be considered as well as potential melt. Large differences are often found between thermocouple values and those of the pyrometer and throughout the tooling due to the large thermal distributions created during heating. This has even been quantified previously in a paper by Voisin et al. [68] where they demonstrated the radial pyrometer underestimated the temperature by 50°C, and differences of over 200°C were observed under the same nominal conditions with temperature being measured at different locations. Wang and Fu have previously detected an undesirable temperature disparity of up to 450°C inside a sample at a high heating rate [69], and this is not by any means a cap on its potential.

Heating Rate / Dwell

The heating rate and duration of the sinter are two additional factors which have a great impact on the process. Heating rates, high or low, can have significant impacts on sintering, for example, increasing the heating rate results commonly in a higher rate of densification for many metallic systems, while reducing it can be beneficial in others. This is to reduce the potential formation of hotspots causing local melting from arcing, or dielectric breakdown, at initial stages as well as issues with overshooting desired temperatures during the heating phase. Immature necking [70] can also easily be caused by leading to the entrapment of porosities and a general lowering of the density attainable without longer dwell times. It has also been speculated that premature necking and resulting inhomogeneities may be created when

the higher heating rates allow only minimal time for neck formation [71]. An important variable to control during the process, the higher range of heating rates possible in FAST is a large factor in its favour and with PID control in FCT systems they are also very well controllable and reliable.

The higher heating rates are one significant factor that allow the FAST process to complete consolidation orders of magnitude quicker than alternative techniques but occasionally longer dwell times are also desirable for chemical or microstructural reactions to occur in certain systems. It has been shown that extended FAST dwell times generally enhance the densification of metals and alloys with improved mass transfer, greater inter particle bonding, reduced porosities, and enhanced heat flux. Many systems, especially those with metallic particles, are very sensitive to this energy imparted into the material during processing and, regardless of different initial size fractions, may form evenly coarse microstructures with extended dwell time bringing enhanced densification and expanded grains or greater atomic diffusion. However, for some systems, increases in FAST dwell time over 10 minutes have no noticeable effect on the densification of M2 steel [72] or nanostructured grade 2 Titanium [70]. In such systems the sintering can be seen to bring about maximum densification at early times and are key examples of the high heating rate benefits.

Temperature Effects/Gradients

One disadvantage of these hot sintering processes relates to the temperature and stress gradients which can form in the sample and apparatus itself. With the high heating rates of FAST, this can be more of an issue when compared with other sintering methods, especially within the die and punches which are under the greatest pressure [73]. These kinds of gradients and inhomogeneities also impact the densification and functional properties of the samples themselves when scaled up past lab sample size. Many of the negative thermal effects in FAST are related to high local temperature gradients, non-uniform temperature distributions across the sample, or macroscopic temperature fields which can all create thermal stresses [74]. As it is such a significant issue in the process, especially for real world applications,

resolving it is highly desirable. However, it is very difficult to control these experimentally, or record the values during the process, especially within the sample itself where measurements are challenging to record due to the 'black box' nature of the machine. This is to say that the thermal gradients and consolidation mechanisms of the sample during the process cannot be directly measured. They must instead be inferred, or simulated, then visualised. Gradients in the sample are therefore difficult to measure experimentally without impacting the resulting component through invasive tooling. As such, external techniques are required to envision and evaluate them, such as modelling and simulations.

On smaller scales, however, temperature gradients are known to provide an additional positive driving force for diffusion, known as Ludwig–Soret thermal diffusion. This effect, and these local maxima, may in some cases even induce local melting, though the formation and build-up of such small scale local thermal gradients is heavily dependent on the physical properties and size of the particles and grain boundaries involved [75]. A major goal of the field of modelling for FAST/SPS is to determine these temperature distributions and control microstructural variations to minimise, or maximise, them where required [76], [77].

It may also be noted that graphite is commonly used as a tooling material for its many beneficial properties, however, below 1000°C sintering temperatures, steel and refractory metals can be also used as tooling materials. But the choice is more limited for sintering processes where temperatures may reach above 1500°C intentionally or through such thermal gradients, such as titanium applications. In these cases, composite materials, titanium nitride or the classic graphite option lead, though double walled tooling concept with an inner ceramic die hand outer graphite mantle has also been proposed [78]. With these variations in tooling, for a hypothetical new geometry, or a novel material system, much trial and error would be needed to achieve the desired homogeneity in these gradients and an alternative solution would be preferable to achieve the ideal right first time approach.

Temperature and heating rate, as mentioned, also play a large role in consolidating the powders during FAST, in that the elevated grain growth at higher temperatures decreases the pores initially between metal particles and increase inter particle contacts [79], [80]. High temperatures may also assist in forming better necks between metallic and alloyed particles [72], increase the speed of diffusion processes and plastic flow rates [81] as well as decreasing the powder's strength and in turn enhancing the creep flow [82], though this can cause issues with entrapping the tooling and is the key reason for the inclusion of wear pads in tool design.

Thermal Distributions

The trend of temperature distributions in non-conductive sample materials depends on the experimental conditions, tool size and geometry. For example, Achenani et al. [83] have shown that for alumina, the temperature is maximum at the centre of the sample, however, Olevsky [84] demonstrated a different result and proposed that the distribution can be altered solely by adjusting the geometries of the tooling and sample. It was also seen that in a paper by Mondalek et al. [85] the temperature at the centre of the alumina specimen was lower for the first 80 seconds before reversing for the following 80 seconds due to the changing thermal conductivity of the graphite die and alumina sample itself with temperature. It is somewhat rare that work is performed to research the distribution in materials with high electrical resistance, mainly due to the fact that it is a difficult task to find a sample with both this feature and a high sensitivity to temperature. Much work of this kind has however been focused on ceramics to make up for difficulties with their electrical resistivity, however these features of the process have been thought to have potential for metallic systems examined in this thesis and other works referenced in later sections.

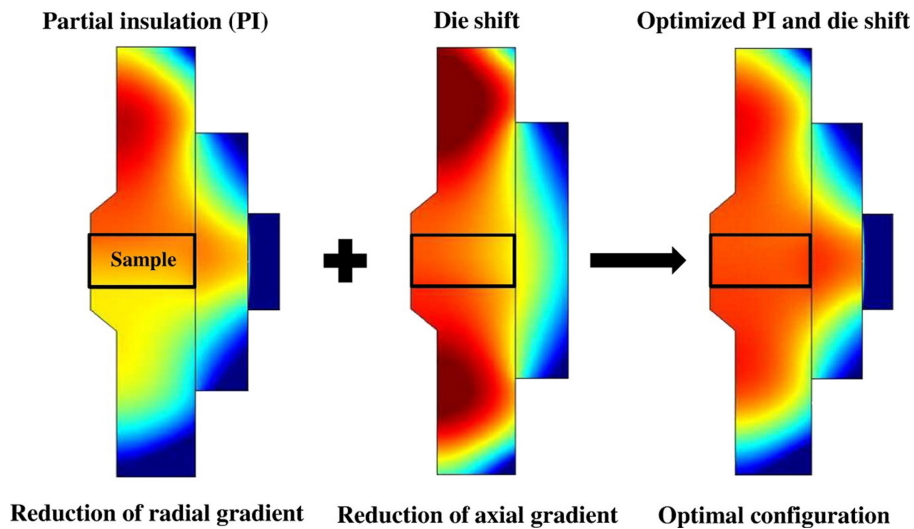


FIGURE 2.15: FEM model demonstrating the impacts of the impact of die design on thermal distribution within the tooling for Alumina samples from Achenani et al. [83]

2.6.5 Electrical Effects

One thing occasionally overlooked in the technique is that while the thermal effects play the greatest role in sintering material, for techniques like FAST it is the electrical current producing the heating and thus understanding and controlling this aspect provides a more fundamental solution. These electrical effects can be differentiated into field and current and they are dependant on the conductivity of the raw powder and tooling material. If the powder being processed is sufficiently electrically conductive, then high current densities will flow directly through the green body preferentially over the surrounding graphite tooling. In this situation certain possible interactions between the electric current and the microstructure formed during sintering become more prominent such as percolation effects [86] which reduce the net observable conductivity and result in potential super heating, the Peltier effect on the interfaces [87], and electrochemical reactions/electromigration. Due to this green sample body, meaning a body which is weakly bound and yet to be consolidated, being formed of powder metals it is neither completely homogenous nor dense, as such the current cannot flow through the material directly in straight pathways. Instead, a complex web of percolating current paths takes shape depending on the packing structure formed in the green body. The Joule heating effects then occur along these paths, which may shift over the course of the sintering process

as necking and plastic deformation begins to occur. Fluctuating hot spots may be formed along these paths as small internal sources of heating and can exceed the average temperature of the process significantly.

As a result, some sections can experience different heating effects as mentioned, such as partial melt and recrystallisation [88]. It is because of the prevalence of these effects that the local temperature variations dominate the microstructural development as densification sets in much faster in these current paths and hot spots during the early stages of sintering. During the ongoing compaction the conductivity of the material close to the current paths rises and these percolation patterns can occasionally 'burn' into the microstructure becoming visible on the scale of micrometres [89]. However it must be noted that this is not a common outcome and is rarely seen in the titanium alloy systems.

Joule Heating

This Joule Heating, also known as Ohmic Heating, responsible for the primary source of energetic input into the FAST system, originates from Joule's first law. This states that the power of heating generated by an electrical conductor is proportional to the product of its resistance and the square of the current:

$$P \propto I^2 R \quad (2.6)$$

where P is power, I is current, and R is resistance. On a small scale within the tooling this is caused when the potential difference between two points in a conductor, such as the graphite tooling, creates an electric field, accelerating charge carrying electrons in the direction of the field providing kinetic energy. When these electrons collide with the ions in the conductor, they are scattered randomly, providing the thermal kinetic motion observed in the heating effect. It differs in application marginally for the direct and alternating currents, with around 1-10 kA in magnitude, though the underlying theory remains the same.

Peltier Effect

This is another of these electric effects which is important to understand in the process. Peltier heating, or cooling, occurs when currents flow through a material interface due to an inconsistency between the two materials' Peltier coefficients. These are created when electrons which are carrying a different quantity of heat within them interact. The temperature change rate delivered to the interface is expressed as:

$$\dot{Q} = \Delta\Pi \cdot I \quad (2.7)$$

where Π represents the coefficient disparity. In FAST a high current is typically used of the order of kA and as such the Peltier can be significant where the material in question has a varying coefficient value to that of the graphite tooling such as semiconducting metals [90]. This can affect the heating by as much as 10% of the total heating power. It can be avoided by matching these values more specifically or by utilising AC over DC as it is directionally dependant, however both options are currently challenging to manufacture, though recent work by Xu et al. [91] has demonstrated their potential advantages.

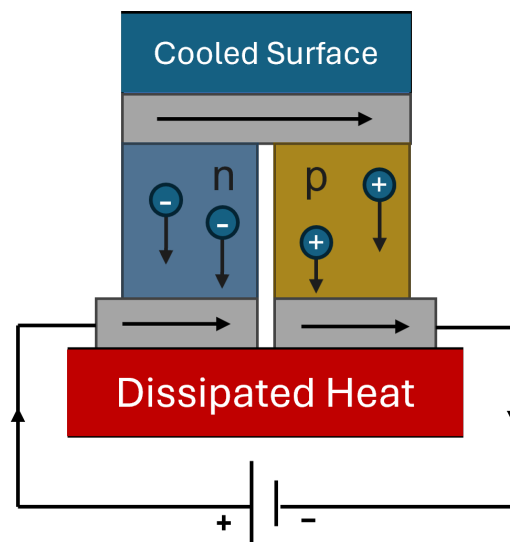


FIGURE 2.16: Diagram of the Peltier Effect creating a thermal gradient at the junction of dissimilar conductors

Atomic Diffusion

Another aspect of the FAST process impacted by the introduced electric current is an increase in the mass transportation by increasing point defects concentration, improving defects mobility, applying electromigration, and decreasing the activation energy for the migration of defects. [63] The effect of this mass transportation on the process can be explained by electromigration theory:

$$J_i = -\frac{D_i C_i}{RT} \left[\frac{RT \delta \ln C_i}{\delta x} + FZ * E \right] \quad (2.8)$$

where J , D , and C are the total flux of diffusing species, the species' diffusivity and concentration respectively. F , Z , E , R , and T are Faraday's constant, effective charge, electric field, gas constant, and temperature [92]. Though Joule heating has clearly been demonstrated to occur [93], the electric field has also been externally demonstrated to have a 'cleaning' effect on metal powders [94] as it breaks apart the oxide layers present on the particle surfaces, implying similar mechanisms inside the sample during sintering. There has historically also been a theory that the current may ionize the gas entrapped between particles, drastically heating these regions and enhancing neck formation [95]. However there has been little to no evidence for this practically since its inception and has been subject to much scepticism [56]. Under some extreme cases such as in Saunders et al. [96] demonstrated in situ observation of low temperature plasmas during ECAS with a voltage one order of magnitude greater than used in FAST, for a sample of less than 1 mm final height. Though this demonstrates the potential it also utilises such extreme conditions that it is unlikely to be a driving mechanism for standard FAST operation and may provide some micro scale support for early phase sintering.

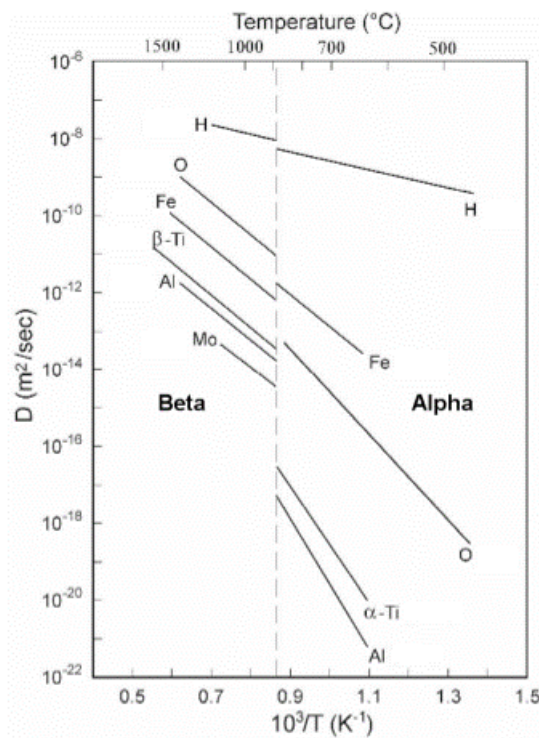


FIGURE 2.17: Arrhenius diagram of the diffusivities of alloying elements in titanium in both α and β phases, adapted from [4]

A common concern for titanium sintering in the FAST process is the diffusion of the carbon atoms from the graphite tooling into the samples to create carbides. This reaction is thermodynamically feasible and can proceed spontaneously at higher temperatures present during sintering and in addition the reaction is exothermic, encouraging further reactivity. This is typically not a concern for our work with low dwell times leading to insufficient diffusion to see a thick carbide layer build up in the sample edge. In addition the presence of borides in the composites prevent deep reaching of the atomic diffusion during longer dwells. This impact is often overlooked in this field due to the prevalence of further machining steps, skimming off this impacted layer, though it is important to mention here.

2.6.6 Atmospheric Effects

During sintering the atmosphere under which it is performed has a large impact on the eventual outputs from the process. Specifically, the composition of this sintering atmosphere and the partial pressure of its constituents impact both the defect

structure and diffusion/diffusivity in the sample material. As a knock on impact from this, the densification kinetics, grain growth, phase stability, oxidation number or stoichiometry are also known to be affected. Generally, it is the reduction in surface energy from the interactions between the sample and the atmosphere which must be considered when looking at atmospheric implications as this modifies the thermodynamic driving forces during the process. Schwarz et al. [97] observed an increased densification rate for zinc oxide and an improved consolidation at a lower temperature simply through the presence of moisture in the atmosphere during consolidation. This may also be observed to improve surface diffusion in magnesia or even titania [98] due to chemical interactions between the water in the atmosphere and the oxide surface resulting in diffusion of hydroxyl ions. These are unique cases though as they often have more demerits to their inclusion.

For titanium alloys, the presence of these reactants primarily has negative impacts on the final material properties [99] and many samples are sintered under inert atmospheres such as argon. Even in this case though, gases entrapped in closed pores are detrimental to densification and can lead to disintering and post consolidation cracking as a result of an internal pressure build up [100]. To avoid this, the use of a vacuum environment is beneficial, or a combination of the two as used by Weston et al. [64], where the chamber was evacuated and filled with argon twice before sintering to provide an atmosphere where few interstitials are picked up, though some impurities remain. Some typical values for sintering pressures would be low vacuum, range of 10^{-4} – 10^{-5} bar, or argon/nitrogen up to 1.3 bar. However, the conditions inside the tooling chamber can be very different from those of the wider chamber, even creating pressure differences capable of destroying the die. The tooling most commonly utilised for these dies is made of ISO graphite and at temperatures above 600°C residual oxygen can be absorbed by the tooling due to the formation of CO within the tool itself, resulting in a potential reduction of oxides which is beneficial for most processes, especially with titanium. It is also true that the evaporation of the sintering material itself as described by the Langmuir equation [101] can lead to a change in composition and the formation of defects in the sintered sample, though unlikely throughout metallic and ceramic samples. It may

also be noted that it is the use of these inert or vacuum conditions that allows the graphite tooling to operate as in the presence of oxygen it would be liable to combust.

2.7 Computational Techniques For FAST

Given the complex nature of these thermal distributions and their causes, as well as the difficulties in determining them in situ, computational techniques become an important avenue to utilise to further understanding. There are several potentially useful options at various scales such as, Molecular Dynamics, Kinetic Monte Carlo, and Phase Field simulation techniques which work at a range of time and length scales, however, these styles do come with their downsides. The MD and KMC styles are practically limited to scales much smaller than required to examine the sintering process effectively without an exceptional and unrealistic amount of computational power. The Phase Field system has benefits being based in thermodynamics and with no need to track interfaces in the systems, however it is difficult to validate and would be difficult to scale up to the tool sizes used on larger machines.

2.7.1 Atomistic Simulations

These simulations model the system as a constrained system of atoms to examine the collective behaviour and look for a minimization of the total energy. These can be useful for sintering to understand the fundamental reasons for observed behaviour, such as pore size reduction and volumetric changes [102]. Additionally, on a nano scale it is possible to model a sufficient number of atoms to observe local behaviours though computationally intense as demonstrated by Sestito et al.[103]. For this work however, as mentioned, the scale is much larger and as such the scope is prohibitive for these small scale techniques such as MD and KMC.

2.7.2 DEM

This Discrete Element Method is more practical than its atomistic counterpart, able to simulate thousands of particles and reproduce grain coarsening [104]. It can also handle temperatures appropriate for sintering using numerical models to observe the impacts of temperature dependant effects, such as surface diffusion, on densification [105]. However, this technique also requires a lot of computational power, even on modern machines. It can also be challenging to couple with larger scale simulation techniques such as FEM. With this in mind, the wider scope of the Finite Element Method, with timescales of ms-hrs, length scales from millimetres to meters, and a capability to deal with complex geometries was chosen to create the Digital Twin of the process for this thesis.

2.7.3 FEM

This Finite Element Analysis (FEA) or Finite Element Modelling (FEM) is one of the most important tools to predict the gradients at the meso and macro scales, as well as the temporal evolution of electric potential and current, dissipated energy, temperature stress and density of the sintered sample during a simulation. The basic idea can be found in the work of Courant in 1943 [106] and the first simulations were carried out in 1969 and then again in the early 1980s [107], [108]. This technique has advanced over the years with the rapid development of computer science and technologies and become vital for many fields and there are now many software developed from this concept such as COMSOL, ABAQUS, and the MOOSE platform. It has been used to model problems including heat transfer [109] using equations for heat flow and electrical systems using Maxwell's equations [110] with the micro and macro [111] equations.

The fundamental principle of FEM is to analyse a mathematical model with certain basic variable, equations, and boundary conditions and follows the following steps: 1. Divide a continuum domain into sub elements, connected to each other via nodes placed on their edge boundaries. 2. Unknown variables in this field are

represented by the approximate functions assumed in each element, expressed by the function value or its partial derivative at each node and a corresponding interpolation which is used to fill the matrix. 3. Establish algebraic Ordinary Differential Equations (O.D.Es) to solve these unknowns at the nodes using variational principles, or a weighted residual method. These steps and the reliable nature of the underlying theoretical basis are what provide FEM with the capacity to adapt to complex geometries with varying nodal mesh schemes, and high efficient calculative capacity providing potential for scale.

Meshing

As mentioned, FEM splits the problem into finite elements which are generated during the mesh generation step, this can be done with a vast variety of techniques as these mesh elements are arbitrarily formed. These elements most commonly consist of tetrahedra, pyramids, prisms or hexahedra in 3D systems and their 2D counterparts for simple problems or 2D-axisymmetric simplifications as in Fig 2.18. Some simple methods include algebraic methods using simple interpolation, and more complex mesh generation is exemplified by Vornoi tessellation which uses a bisection method to generate finite element geometries. In this technique a space is seeded with points which are then joined by straight lines and then bisected by a plane that is normal to the line. The planes are ended when they intersect another plane which forms finite polygons, allowing the whole shape to be meshed. The method to create these meshes changes from software to software and the best choice depends on the problem being modelled.

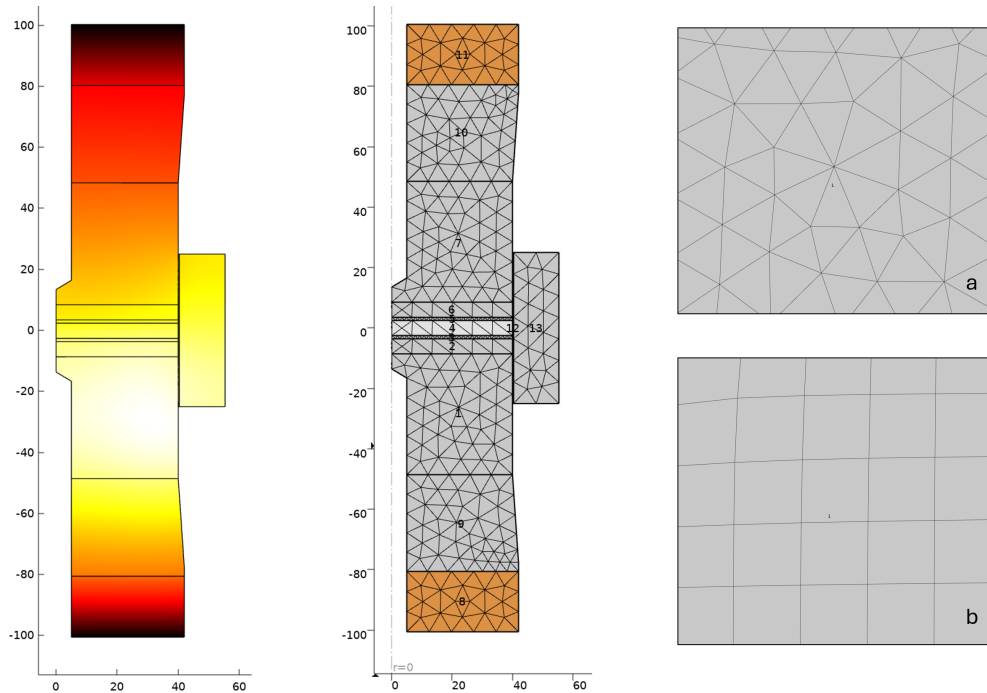


FIGURE 2.18: COMSOL 2D-axisymmetric slice showing the end result of the simulation (left), the variation in meshing within the FEM model to suit the geometry (centre), and a closer view of a.) the free triangular method used and b.) the free quad method (right)

To solve this problem with the other methods of variability in solution, adaptive grid method was created. At the point of mesh creation, the grid may or may not be the best for the simulation and it is difficult to know this in advance. Adaptive methods control either the mesh refinement or the number of grid points or the order of solution and use a feedback loop to determine the performance of a mesh before updating these parameters and refining the grid until a solution converges. There are difficulties in this method with the added complexities and it is useful primarily for steady flow and time-accurate flow calculations.

It is also possible to adjust the global element order while meshing, allowing control over mesh creation with mid-side nodes, quadratic elements, or without any nodes in the form of linear elements. The aim primarily being to more accurately define the boundaries of the system they are filling in more complex geometries, especially with curved edges. Increasing the number of these nodes increases the degrees of freedom allowing them to more accurately approximate these forms but

with an associated higher computational cost and potential instability. Mesh refinement as a process is the utilisation of these concepts to find the ideal form with the least computational power required and has been used in a variety of work even within FAST/SPS [112]–[115]

Boundary Conditions

An additional benefit to the technique is its ability to combine multiple physical systems in its iterative calculation steps though this potential often complicated the system requiring many inputs into the model to simulate the electrical-thermal-mechanical coupled responses in the system including: tool geometry, material properties and machine parameters. The work of Matsugi et al. in 2003 [116], [117] allowed SPS to become a better candidate for modelling prediction with a better correlation between calculated and experimental values of temperature and time has taken the field even further. Since then with the work of Olevsky in 2012 stretching to modelling both the chamber and the densification of the sample [84]. However, even in these works, the contact resistances generated by the presence of the carbon sheet are not considered. One of the more challenging properties to obtain, are the contact resistances, with their sensitivity to temperature and contact pressure which are vital to obtaining an accurate simulation as they contribute significantly to the Joule heating in the system [118]. There is also additional difficulty in determining the impact of vertical and horizontal contact resistances in the system.

There are some authors who have determined in situ Electrical Contact Resistance (ECR) measurements during SPS for their experiments [119] and some who have obtained the values through calibration [120]. But since these properties are temperature dependent and this experiment can range from room temperature to over 1200°C this makes it difficult to obtain good experimental agreement. Many other authors have also pointed out the variation and significance of this for these contacts [118], [121]–[123]. It has been suggested, for example, that the punch to sample ECR is negligible when the pressure is high while that of the punch to die contact is still important despite the similar pressure. This is difficult to study due to

being, in large part, dominated by the lateral pressure from the thermal expansion of the punch, any gaps in the interface, and possible compaction of the foil present.

Manière has previously used inverse analysis to identify these contact phenomena at all interfaces using thermal imaging and thermocouples [113]. It is also possible to perform this measurement via examining the overall column resistance in different configurations [124]. These two in situ approaches have the advantage of quickly allowing the establishment of these important properties, and thus, a heating model very close to the experimental values, however, their domain of validity is restricted to the experimental conditions of the model determination. In order to approach a more generalised model of the FAST heating, Manière et al. considered two main approaches [125]. In situ calibrations for varying geometries to extend the model and account for the scaling effect on the heating, and ex situ measurements of these variables in different pressure/temperature conditions to validate the in situ recorded values which provided good agreement.

The tooling geometry is also vital information for the model, however, it can also be created with much simplified 2D axisymmetric forms, due to the angular symmetry of the commonly cylindrical tooling. More recently, complex geometries have been surfacing in literature to look at larger sections of the die and punch [126] or for near net shaped tooling which would be difficult to simplify [66]. These simplifications are important however for these simulations to reduce the required computing power in order to balance the additional complications mentioned previously.

Another large simplification, which has been made previously in the literature, is that the sintering behaviour itself has been neglected. Instead the material is considered as a dense, elastic body at final height which is useful for approximations but can induce errors in terms of the stress level and current/temperature distribution if examining the early compaction phases. As a result, specific sintering powder laws have been implemented for FEM codes within the last 5-15 years [114], [127], [128]. Aspects such as a moving mesh to simulate the deformation and the addition of graphite foil to better account for the electrical anisotropy behaviour contributing

to the overall joule heating have also been considered. However, most simulations have taken temperature data from only one position and as such have not confirmed the experimental temperature profile in simulations across the apparatus. These become far more relevant and potentially troublesome, as FAST devices are scaled up for larger components such as aerospace parts or ballistic panels. The work in this thesis presents the option to use this technique for microstructural predictions as well based on FEM simulations and knowledge of the thermal and electrical distributions, providing a further and very interesting option for this process and the Digital Twin approach.

2.7.4 Powder Porosity In FEM

In powder compaction modelling, the powder can be represented by a micromechanical scale or through the basis of a continuum. The former allows for specific investigation on the powder size/shape/hardness and arrangement while the latter considers it as a continuum rather than an assemblage of individual particles. This allows us to obtain small scale interaction information and form a model allowing us to predict global behaviour of the powder mass and shape during compaction. [129] The compaction itself may be input into the simulation either through load applied to a boundary or a controlled displacement in the large scale continuum FEM in question. Loading is appropriate for non linear analysis like reinforced concrete components and structures, however it has issues with the ability to capture responses from the deforming material. Displacement however is effective for non linear plasticity analysis such as the compaction of powder materials due to the potential for large deformation with small load.

FEM has many of these powder modelling schemes which can be used depending on the material, including McMeeking and Rice's model based on Hill's principle for incremental deformations using an Eulerian Procedure where the physical quantities are expressed as a function of time and position vector. The alternative Lagrangian strategy determines the geometry changes of the mesh elements through

the deformation of the material boundaries. Modelled by Smit et al. [130], the original element mesh was sufficiently accurate for the small changes in physical alterations and material properties to be captured, however, instability may occur if the case is highly non linear. Potential variants for sintering compactions include FKM-GTN [131] Drucker Prager Cap and Norton Green Compaction. The DPC model, commonly used for cold compaction of tungsten carbide and other pharmaceutical powders [132]. This model is an elastic plastic continuum using phenomenological models such as Cam-Clay or Dimaggio-Sandler [133]–[135]. It consists of three stages; shear failure, cap segment, and transition segment, and can also be used to consider hardening, softening and inter particle friction for smaller scale FEM or DEM.

FKM-GTN is a macroscopic constitutive law developed for the plastic yielding of perfectly plastic spherical metal particles and has valid results between packing density and near full consolidation (60-99% of theoretical full density) due to the focus on inter particle interaction. For higher porosity, the FKM regime is used and for porosity lower than 10% the void interaction determine the rate of change and the model is not well suited to this region so the GTN regime is used. Between the two, a linear combination approximates the compaction process. Norton Green Compaction was observed by Manière [136] and is based on a creep power law formula defined for visco-plastic materials. It is useful in hot isostatic pressing but potentially lacks strong temperature dependence with higher heating rates common in FAST processing. Manière [136] used a series of creep experiments to determine the temperature effects and porous samples to validate the compaction law for porosity for Ti-6Al-4V and found good agreement for heating rates up to 100 K/min.

In order to overcome these problems an updated solution has been proposed where the coordinates of the mesh must refer to the previous calculation step, allowing for large but slow deformations to be accounted for. However, difficulties still arise in cases which involve large rapid displacements because the element shapes may become highly distorted leading to mesh degradation. As a further solution to this, the adaptive mesh method is often introduced, software such as COMSOL have

such options embedded into their interface due to the demand for these cases and this could be useful for preheated compaction in sintering simulations.

2.8 Summary

The literature review has covered a concise range of topics most closely related to the research aims. Relevant aspects of titanium metallurgy have been covered to ensure a good understanding of this material as well as related alloy and composite systems. The primary metallic-ceramic system of interest, Ti-TiB has been analysed in more detail and the reasons for its status as the primary candidate as titaniums composite partner explained. An overview of the production of titanium has been given, as well as a focus on the extraction techniques for conversion into powder material. The resulting morphology has been noted as well as the further mechanical alloying for composite systems, and the impact of this property on sintering and compaction researched to provide a better understanding of resulting processed microstructures. Various consolidation techniques have been discussed with increasing complexity and varying benefits with highlighted reasons for the benefits of choosing FAST processing for this powder.

A very detailed analysis has been carried out on the various fundamental aspects of the FAST process highlighting its most important aspects and their impacts for a greater understanding of the machine and process. This has then been used to explain the issues currently facing the technique and the necessity for the use of computational techniques to aid with analysis and prediction. These potential techniques have also been analysed and the most prominent option of FEM explained in more detail with examples of its use from literature. Finally some powder modelling theories have been explored to further increase the likeness of the computational analysis to that of the real world and potentially further improve the concept of the FAST 'digital twin'.

Overall, this review shows the reasoning behind the focus on the fundamental physics of the system during the sintering process and the importance of control over them. Highlighting a potential improvement in the system using finer control of the electrical field which is still a novel area of research within metallic systems. Titanium's clear temperature dependence allows visible determination of these impacts and will provide a solid system to prove the concept and benefits of current control within the FAST process.

Chapter 3

Experimental Techniques

3.1 Introduction

The aim of this chapter is to provide an overview of the experimental methods, analysis techniques, and modelling which was used in the upcoming chapters. Though additional detail can be found in the specific experimental sections, much of the generic and background details will be mentioned here.

First, the powder production methods will be explained in more detail regarding gas atomising, the HDH process, and cold milling as well as powder size distribution (PSD) analysis. Then the processing method for the powder, primarily the FAST process at both small and large scale. The methods required for the metallographic preparation of titanium samples for imaging, including scanning electron microscopy (SEM) and electron backscatter diffraction (EBSD) as well as standard optical imaging. X-ray energy dispersive spectroscopy (X-EDS) is also included as well as X-ray computational tomography (XCT) as attempted but low impact techniques on this thesis. A series of more practical mechanical property testing is also outlined, including Vickers micro-hardness testing, thermo-mechanical compression (TMC) testing, flexural strength testing, electrical and thermal conductivity testing, and specific heat capacity. A set of digital analysis methods are also laid out, finite element modelling (FEM) and image analysis using MIPAR software are finally introduced towards the end of this section.

3.2 Powders Studied

3.2.1 Gas Atomised and Hydride De-Hydride Powders

The hydride de-hydride (HDH) titanium alloy powder of both alloy systems used for this investigation was supplied by Phelly Materials Inc and the production route previously described in Section 2.2.1. Resulting secondary electron imaging (SEI) of the powder are shown below and demonstrate the rough, angular topography and angular morphology common to these powders, due to their fracturing along grain boundaries during production. The size and shape of these powders varies significantly due to the crushing process, as well as the morphologies which vary in size with some showing comparably finer grain structure, true for both Ti-6Al-4V and Ti-3Al-2.5V.

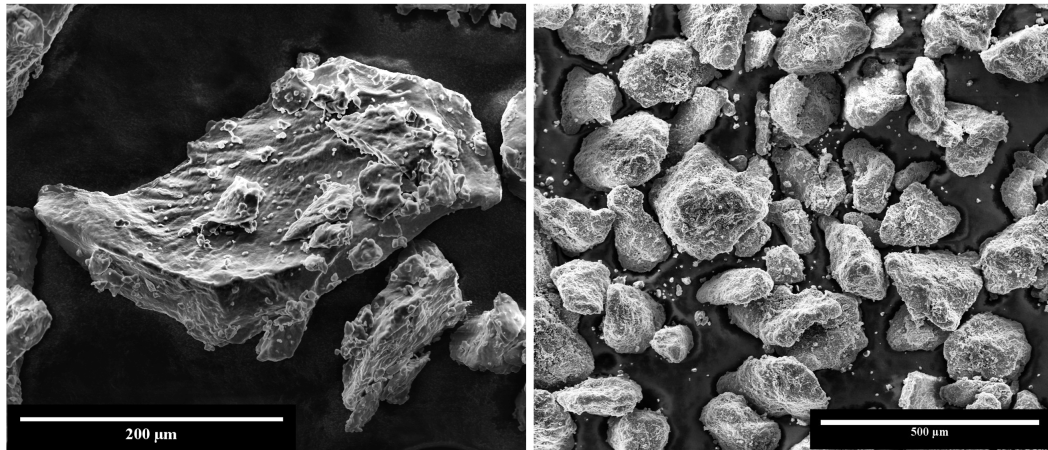


FIGURE 3.1: Secondary electron images of the HDH Ti-6Al-4V (left) and 9 wt.% TiB powders (right)

The powder size distribution of these powders was determined using laser diffraction with the Malvern Mastersizer 3000 with wet dispersion in distilled water. An average of 10 measurements was taken for both the rough HDH powders, as well as the spherical Puris LLC gas atomised (GA) powders pictured below in fig 3.2. These GA powders have good roundness with some small satellites observed as well as some internal porosity, though these features are expected with this processing technique. Internally, these powders show a martensitic acicular α lath microstructure

from the high cooling rates involved in production.

For further direct comparison, $Dx10$, $Dx50$, and $Dx90$ average statistical values, referring to the 10th, 50th, and 90th percentile in the distribution respectively, were recorded using calculation of a value called Span to quantify the spread of the PSD, calculated below:

$$Span = \frac{Dx90 - Dx10}{Dx50} \quad (3.1)$$

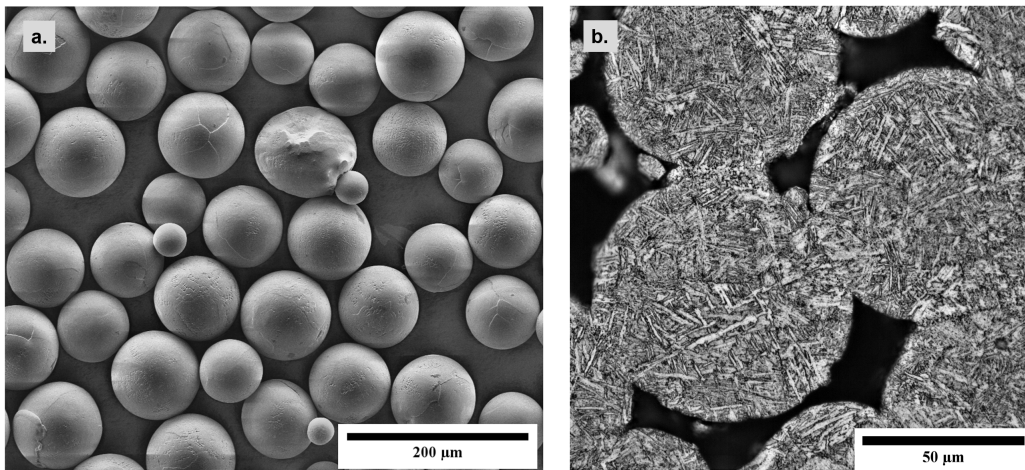


FIGURE 3.2: Gas atomised powder secondary electron surface image of Ti-6Al-4V powder (a) and BSE Microstructure (b)

Chemical analysis of these powders to determine accuracy to described commercial labels was performed previously using X-EDS, XRF (Bed Fusion) and LECOTM analysis for determining of oxygen and remaining hydrogen content. The chemical compositions of the powder alloys can be compared with the ASTM B348/B348M - 19. This standard is more commonly used for solid components, but it can be considered a good approximation for the powder state. The Ti-6Al-4V and Ti-3Al-2.5V did not comply with these standards due to excessive contaminant elements via greater than 0.25 wt.% Fe and 0.13 wt.% O levels discovered from production. However they do comply with the requirements for their relative grades 5 and 9 respectively.

Powder	Ti	Al	V	Sn	Zr	Mo	Cr	Fe	Si	C	S	O	N	H
Arcam Ti-6Al-4V*	Bal	6	4	-	-	-	-	0.1	-	-	-	0.15	0.01	0.003
Puris Ti-6Al-4V	Bal	6.1	3.8	-	-	-	-	0.26	-	0.028	0.01	0.163	0.019	0.0029
Eckart Ti-6Al-4V	Bal	6.0	3.6	-	-	-	-	0.16	-	0.023	0.01	0.181	0.003	0.0032
Eckart Ti-3Al-2.5V	Bal	3.3	2.2	-	-	-	-	<0.05	-	0.015	0.001	0.190	0.003	0.0105

TABLE 3.1: Powder chemistry determined prior to processing for titanium alloy powders used in this work. *Typical values that the powder supplier produces

3.2.2 Cold Milling

TiB_2 fine ($<44 \mu m$) ceramic powders from NewMet™ were sent to an external company, Materion™, for cold milling process with the GA Puris Ti-6Al-4V and Ti-3Al-2.5V powders. The powders were poured into a vessel with metallic balls and milled, see Fig 2.8, using their proprietary method. As mentioned the mechanical alloying in the process cold welded the titanium alloy particles together, trapping TiB_2 powder within, creating a fine distribution.

3.3 Powder Processing

3.3.1 FAST Sintering Machine HP D 25

For small lab scale testing at the University of Sheffield (UoS) an FCT Systeme GmbH SPS Furnace Type HP D 25 was used to produce all samples of diameters between 20 mm and 80 mm and is pictured in fig 3.3. To control the temperature during processing, this machine accommodates a top mounted optical pyrometer which measures the temperature approximately 3 mm away from the top powder surface within the graphite punch, separated only by the top wear pad and graphite foils. The key processing parameters used are sample diameter, heating rate, pressure, dwell temperature and time, and cooling rate though this depends primarily on the graphite mould volume. These parameters are planned and input into the machines onboard computer prior to the run in segmented sections, to more precisely control the entire process.



FIGURE 3.3: FCT HP D 25 FAST machine pictured (left) External view of the machine, (right) Internal view of the vacuum chamber with 20 mm graphite tooling

Two primary graphite tooling sets were utilised for these experiments. The first, had a 20 mm inner diameter and a 50 mm exterior diameter ring mould with two wear pads, two graphite rams, and two supports connecting the sample assembly to the copper electrodes within the machine. The latter had a 80 mm inner diameter and a 120 mm exterior and no wear pads within the ring mould, however, two 5 mm thick carbon fibre composite (CFC) plates were included between the supports and the electrodes for better confinement of the generated heat. The CFC plates also improve power efficiency and reduce temperature in the electrodes, beneficial for minimising stress on critical components.

The layout of the powders was either with a single material, or with layers normal to the compression direction and the quantity added was calculated and weighed in order to reach a desired final height using the following equations for volume, V , depending on the mould size, and then from this, the mass required, m :

$$V = \pi r^2 t \quad (3.2)$$

$$m = \rho V \quad (3.3)$$

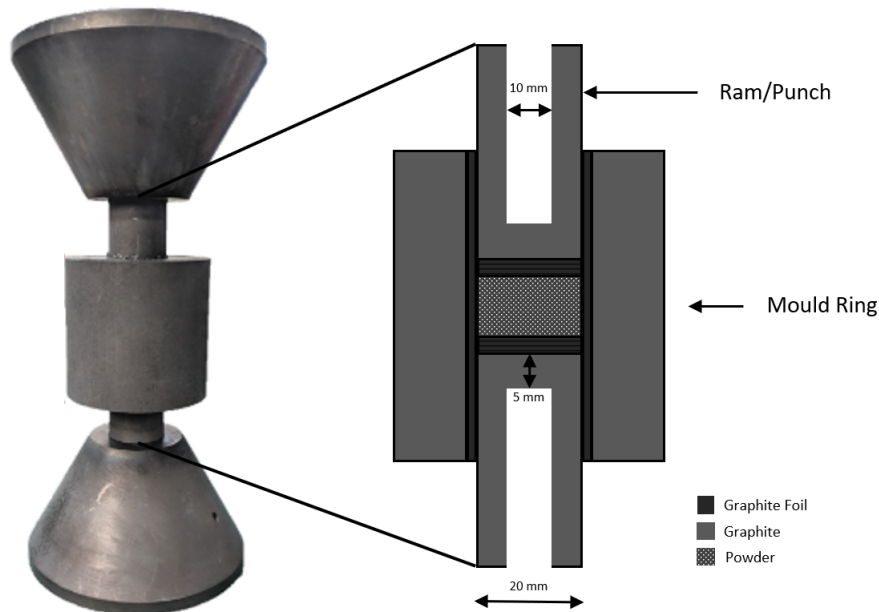


FIGURE 3.4: Image and Schematic cut away of the FAST graphite tooling at 20 mm scale demonstrating the internal lay up and symmetrical openings for the optical pyrometer

Here r is the sample radius, t is the theoretically consolidated final height, and ρ is the density of the powder. In addition to the graphite foil between the powder and the wear pads or rams, there is also a layer applied between the powder and ring mould to prevent adhesion of the powder to the tooling during processing, making extraction near impossible and reducing tool lifespan. This is inserted first into the 20 mm layup visible in Fig 3.4, followed by one wear pad and ram as well as three layers of graphite foil before powder is poured into the open end. The sample is then tapped to ensure level surface and the next three layers of foil, wear pad and ram are inserted to close the system and ensure no powder escapes. The sample was then pre-pressed to 20 MPa on a tabletop press to ensure a good connection and contact between the powder particles prior to processing resulting in more immediate effective heating. When specified on larger samples a carbon felt jacket was placed around the mould ring to further reduce heat loss before the supports were connected and the whole setup placed into the machine

The recipe mentioned earlier is then uploaded and is segmented into the following components:

1. Vacuum pump pulls out air to create a vacuum in the vessel
2. Sample is pressed to 20 MPa initially, followed by further pressing to desired limit
3. Uncontrolled heating occurs to 200°C where the pyro can begin recording values
4. Controlled heating to maximum temperature
5. Dwell is maintained at this temperature for a set time defined in the recipe
6. Power off resulting in uncontrolled cooling and return to minimum hold pressure of 20 MPa

The equipment uses real time temperature data from the optical pyrometer combined with a proportional-integral-derivative (PID) controller to feedback and control the input power into the system at all points of the run, depending on the temperature and the desired temperature in the recipe. Some other aspects were universal across the majority of runs on this system, the heating rate when controllable by the pyro above 450°C was 100°C/min and a 35 MPa final pressing force based on previous research [137]. The machine used a DC pulse pattern of 15 ms on and 5 ms off, for more direct comparison with previous work within the group where it was found to have improved densification for titanium. This topic was explored previously by researchers such as Chakraborty et al. [138] though the results are very dependant on the material being sintered.

This pulse waveform from this description seems akin to a top hat function where the current is either on or off. This is quite difficult to achieve on the scale of current used in the FCT machine used in this work due to overshoot and parasitic capacitance in the system. As such these waveforms may take on a much more fluctuating appearance averaging around the desired value. This could cause peaks and troughs in the power provided to the system and provide additional motivation to control the system constantly with a PID. However, this is beyond the scope of this project and as such it has been assumed to average to the ideal square top hat

function and further simplified in the modelling as a D.C current.

Post processing, the vessel is repressurised using atmospheric air and the tooling is removed once safely cool to touch. The tooling is disassembled and the now consolidated sample removed and cleaned of remaining foil before being taken for further processing, sectioning, or machining.

3.3.2 FAST Sintering Machine H-HP D 250

For the large scale testing, an FCT Systeme GmbH SPS Furnace Type H-HP D 250 was used in the Royce Discovery Centre (Sheffield, UK) shown in Fig 3.5. A 250 mm inner diameter ring mould with an outer diameter of 360 mm was used to create larger samples for the purposes of ballistic testing and scale up demonstration of the current control technique as well as the predictive capacity of the FEM simulation. An identical methodology was used to the small scale testing with the set up and processing, however pre-compaction is now performed on a hydraulic press next to the machine and there are additional CFC and ram supports placed in the tool stack. It may also be noted the pressing occurs from below in this machine rather than above as in the case of the smaller moulds. Additional care was also taken during powder layup to ensure fully flat layers for better connection and in the case of the FGM samples, more homogeneous results in thickness.



FIGURE 3.5: Photograph of the FAST Sintering Machine H-HP D 250 and accompanying 250 mm diameter graphite tooling

3.4 Metallographic Preparation and Imaging

This metallographic preparation is required in titanium to reveal the microstructures of the alloys. For consistency, the preparation steps have been kept consistent for all samples post sintering where required.

3.4.1 Sample Preparation

All of the small scale samples were sectioned using a Struers Secotom-50 with a silicon carbide, SiC, 10S20 cut-off wheel. Larger samples were first sectioned using the Struers Labotom-20 and similar SiC cut-off wheels before further machined on the Secotom-50. Samples, both powder and sectioned consolidated, were then hot mounted using a Buehler SimpliMet 3000 mounting press. Conductive Bakelite was used consistently so that scanning electron microscopy could later be used for imaging. Some powder samples were instead cold mounted in epoxy resin for optical microscopy, or stuck to carbon stubs for topographical imaging. Polishing was achieved using a Struers Tegramin-25, using a 2 minute grind on P400, P800, P1200, and P2500 SiC grit papers followed by further polishing with a mix of 9 parts colloidal silica and 1 part hydrogen peroxide H_2O_2 shown previously to have a positive impact on the process [139]. This chemical polishing step was performed for 10 minutes followed by cleansing of the surfaces with isopropyl alcohol and safe storage to prevent dust and scratching prior to imaging.

3.4.2 Optical, Scanning Electron Microscopy, and X-EDS

Both optical and electron microscopy were used to study microstructures, porosities, topographies of powders, and other features of the samples such as TiB needle growth. A Nikon Eclipse LV150 light microscope was used for the light microscopy, with cross polarised filters to reveal the orientation of atomic structure and therefore crystal grains of Ti alloys. For whole sample imaging, an Olympus BX51 optical microscope with a moving stage was utilised in combination with Clemex Vision software, allowing for high resolution mosaic images from a range of magnifications

by 'stitching' the images together digitally. These were used for porosity measurements of consolidated small scale samples, as well as grain size analysis on a range of samples. For porosity imaging, a threshold filter was applied and the percentage porosity measured via pixel count in ImageJ [140] or a simple Python 3.11.0 script for a good estimation.

SEM was performed using an FEI Inspect F50 with an acceleration voltage of 20 keV. Backscattered electron detector mode was used to analyse chemical distributions within the samples, brighter features corresponding to higher Z contrast. This has particular merit when observing titanium alloy microstructures as the α and β phases have different brightnesses in the images. Secondary electron detection was used for imaging topographical features and Energy-dispersive X-ray spectroscopy (X-EDS) was done on the same machine with an Oxford Instruments insert and AZtec software. Electron probe micro analysis (EPMA) is also possible on the machine using JEOL JXA-8530F+, which makes use of a combination of wavelength dispersive spectroscopy and X-EDS detectors to achieve high resolution elemental analysis, useful for local chemistry variations such as TiB needle growth.

Electron Backscatter Diffraction

For this the CMOS Symmetry S3 EBSD Detector was used in combination with AZtecHKL software from Oxford Instruments was used to obtain grain orientation indexing for examined samples. Firstly samples needed to be prepared through sectioning to a maximum thickness of 5mm, mounted and polished as described before being broken out of the Bakelite mount and glued to a stub using silver paint. This sample is then placed into the machine where the electron beam is scanned across the surface of the tilted sample; the diffracted electrons at each point form a pattern from transmission Kikuchi diffraction (TKD) that can be detected and analysed. The indexing provides information about the phase and the crystallographic orientation from which the microstructure can be reconstructed and texture examined.

3.4.3 Vickers Hardness Testing

Vickers hardness measurements were carried out using a ZwickRoell Durascan-80, with different forces used depending on the size of the features being tested, though the most common was 1 kgf, or 9.8N. The 'Hardness Vickers' (HV) values used is the number of kilograms of force applied by the diamond tipped indenter. This force was held for 15 s as per the ASTM E92.

3.5 Computational Techniques

3.5.1 FEM Software

For FEM simulations COMSOL Multiphysics 5.6 was used. This is a general-purpose finite element analysis, solver, and simulation software package for various physics and engineering applications, especially coupled phenomena. FEA simulation software based on advanced numerical methods with fully coupled multiphysics and single-physics modelling capabilities allows complete modeling workflow, from geometry to results evaluation.

In this work, it is used for the modelling of the resistive heating and electrical current density of the sample and tooling during sintering in the FAST process which has been demonstrated to be effective previously [84], [141]. The multiphysics capabilities of this software make it very effective at producing accurate results when combined with reasonable assumptions, if provided sufficiently accurate data on material properties and boundary conditions involved.

2D Axisymmetric

The simulations are performed in a simplified 2D axisymmetric way as demonstrated in Fig 3.6 assuming homogeneous rotational symmetry in the machine. The primary reason for this is the reduction in computational time requirements and simplification of setting up the simulations. The geometry was measured from the

experimental equipment and converted into this 2D slice format before being constructed in the model.

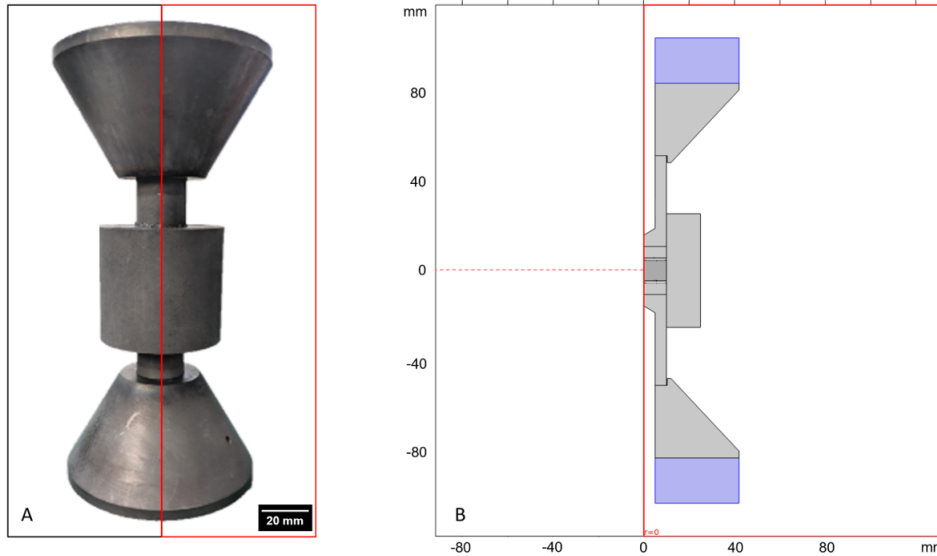


FIGURE 3.6: (A) Graphite tooling photograph (B) Simplified 2D Axisymmetric slice used in COMSOL simulations for computational efficiency

The contact conditions, for both the vertical and horizontal directions, between the workpieces were found from previous literature [142] and their impact confirmed through model comparison to experimental data during early sample production. The system was then meshed with free triangular meshing elements defined in COMSOL as between 'Extremely Coarse' and 'Extremely Fine' under general physics calibrations. This allowed a maximum element size as well as a minimum, a maximum growth rate, as well as a curvature factor and a resolution of narrow regions. These varied from tooling set up depending on scale and a table outlining these parameters is laid out in table 3.2 with around 1000 elements per mesh.

TABLE 3.2: Mesh refined simulation parameters for the reported models at all scales utilised later in chapters 4, 5, and 6.

COMSOL Mesh	20 mm	80 mm	250 mm
Maximum Element Size (mm)	2.01	7.44	19.1
Minimum Element Size (mm)	0.00402	0.0251	0.0855
Maximum Growth Rate	1.1	1.25	1.3
Curvature Factor	0.2	0.25	0.3
Resolution of Narrow Regions	1	1	1

These mesh parameters were determined through a mesh refinement process where various mesh parameters on the in-built COMSOL settings were parametrically swept and the results for thermal profiles across the sample were plotted on top of each other for stable configurations. The point at which the resulting thermal profiles converged was taken as the refined mesh for the simulation, without becoming excessively fine and unnecessarily increasing computational requirements. The details of the relevant numerical equations for calculations can be found later in the chapters where the results are discussed.

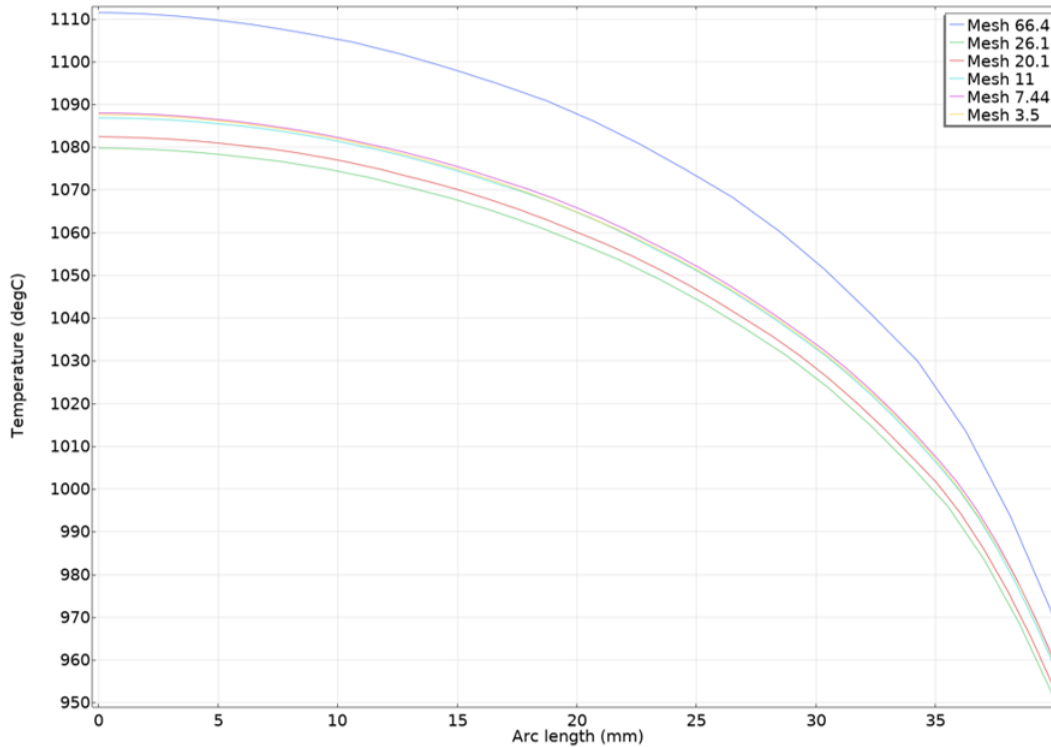


FIGURE 3.7: A plot of temperature vs distance from centre of the sample for varying mesh maximum element size on a 80 mm diameter simulation demonstrating convergence

3.5.2 MIPAR

The image analysis software MIPAR v4.4.0 is used in this work for its fully automated grain size detection and analysis. It is capable of analysing micrographs off of the optical microscopes mentioned as well as SEM images, and to run this analysis of the image sets in batch form. MIPAR generates a grain size distribution as well as data statistics which are very convenient for full surface analysis and comparison with simulated values.

Images were fed into the MIPAR Deep Learning Algorithm and for at least 50 images per magnification and microstructure, the prior β grain boundaries were drawn by hand and compared to train the model on recognising these features. The images were normalised for contrast and brightness through ImageJ software to further dial in the consistency. This trained Deep Learning Model was then checked on an additional image from the batch which had not been fed to the training by eye to confirm

the accuracy and to refine the recipe using image refinement with the full recipe outlined in the appendix.

Once this recipe had been refined and checked to accurately measure the grain boundaries, the batch mode of the software was used to process the remaining 1000s of micrographs into histogram data which can then be processed for averages and variance, as well as aspect ratios.

3.6 Graphite Physical Property Testing

All graphite tested here and used in our FAST tooling is isostatically moulded (ISO) graphite, a term which comes from the constant pressure on all sides applied during creation. It is a cold moulded petroleum based graphite composite which results in excellent properties uniformly distributed throughout the mass with no recognisable grain orientation. This allows it to provide the thermal and electrical, as well as mechanical properties required for the challenging task of sintering titanium. But specific data must be obtained for the simulation results to stand up to validation as mentioned.

Therefore eight grades of this isostatically moulded graphite were examined as part of work with Olmec Advanced Materials: TX1-6, Y542, and Y552, in their proprietary grading schemes. Data was collected for all grades and will be available in the appendix, though here the results for the two primary focus Y grades for sintering tooling will be demonstrated. The ASTM standards were followed wherever possible and results aligned closely with expected values from previous testing the company had performed.

3.6.1 Thermo-Mechanical Compression and Flexural testing

Compression Testing

This testing was carried out according to the ASTM standard - C695-15(2020) Standard Test Method for Compressive Strength of Carbon and Graphite. The UoS equipment used in this testing was the Servotest Thermomechanical Compression (TMC) Machine.

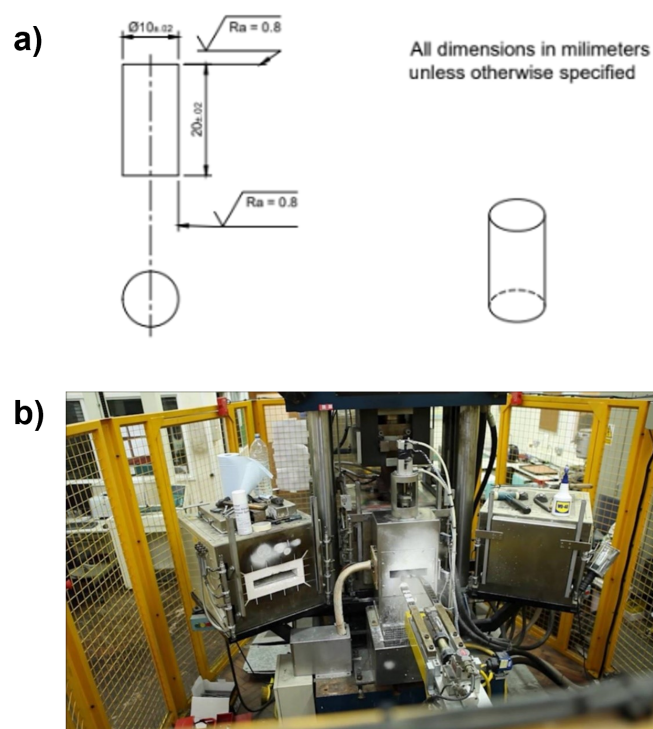


FIGURE 3.8: (a) Machine drawing of graphite sample geometry for TMC testing and (b) photograph of the machine the grades were tested on

Elevated temperature testing is possible on this machine, though not in an inert atmosphere and as such was not done here. Testing all 8 grades required shaped machining shown in Fig 3.8, and 3 repeats were carried out for each strain rate (0.1 s^{-1} and 0.01 s^{-1}) for each sample grade. These repeats were then averaged to find the reported value and a distribution relating to the repeatability of these values. After the machine had been calibrated and aligned, the machine noise was accounted for to remove inherent vibrations in the data. The samples were then placed centrally,

by hand, between the plates and the machine was remotely activated following the set profile for strain rate. As the sample's strength limits were easily within the machine's capabilities, an initial guess was set at 20 kN max load and the machine stiffness calibrated earlier included. The loads at which the samples failed were then converted using the surface area of the samples into compression strength in MPa using Python Script and presented below. It was discovered that there seemed to be some slight dependence on strain rate, however, when this varied significantly, as in the case of TDX 6, much of it was accounted for in the errors from averaging results and potential outliers.

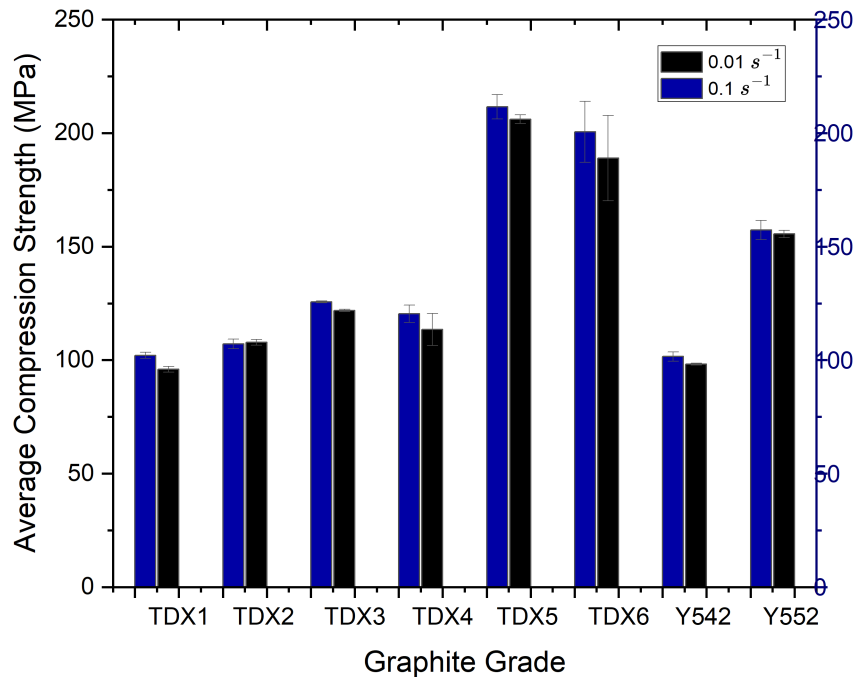


FIGURE 3.9: Compression strength results from the TMC graphite testing, showing particularly high strength on the Y552 grade in use

Flexural Strength Testing

This testing was carried out according to the ASTM Standard – C651-20 Standard Test Method for Flexural Strength of Manufactured Carbon and Graphite Articles Using Four-Point Loading at Room Temperature. The equipment used here is the

Nene 12 kN Servohydraulic Universal Test Machine.

Elevated temperature testing is not possible on this equipment so only room temperature measurements were recorded. For the 6 TDX grades 3 repeats were carried out and for the Y552 and Y542 grades, 5 repeats were performed for additional accuracy due to the importance of flexural strength in mould stability. The tooling was fitted into the framework of the machine and the positions of the loading points calibrated to the sample shape according to ASTM standards. Then the lower section holding the sample was moved until contact was made at 0 load.

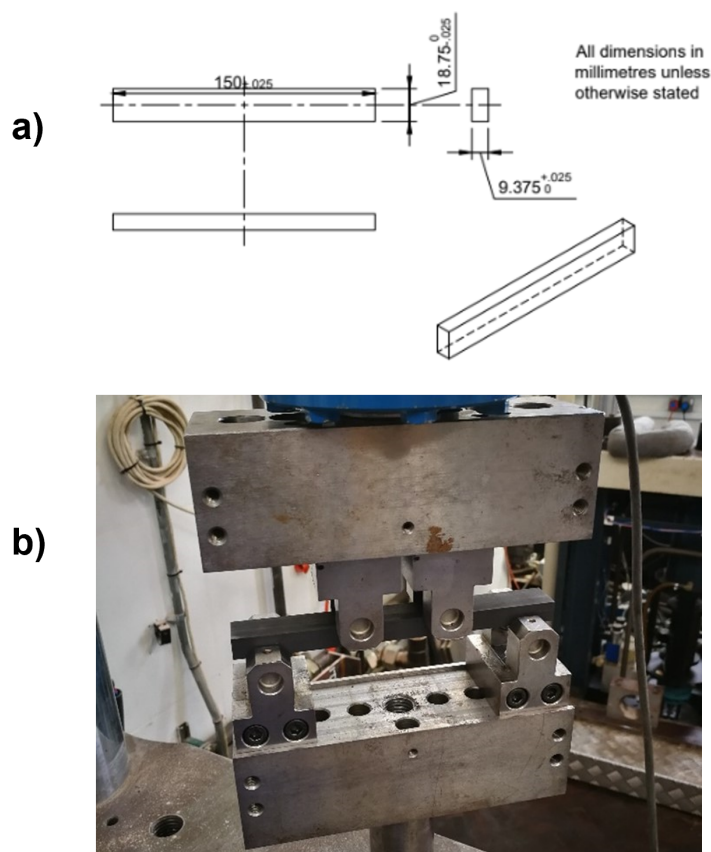


FIGURE 3.10: (a) Machine Drawing of the sample geometry for 4 point bend testing and (b) photograph of the set up used

The machine was provided an initial guess to the force required to fracture the samples and a loading rate applied such that the breakage occurs after a minimum of 5 s according to the standard. These initial estimates were determined through an additional sacrificial sample prior to testing. The force at failure readings were

recorded manually from the monitor attached to the machine and averaged before being converted to Flexural Strength simply as:

$$\sigma_f = \frac{3 FL}{4 bd^2} \quad (3.4)$$

where σ_f is flexural stress, F is force, L is length, b is width, and d is thickness. It was seen that here were large differences in strength between the samples but very little in the forces at failure resulting in very low errors in the measurements.

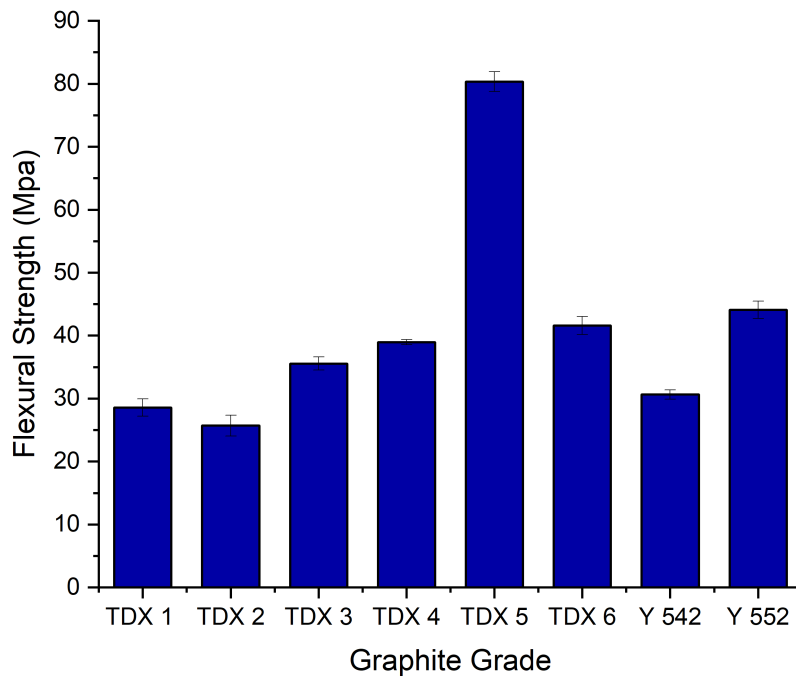


FIGURE 3.11: Flexural Strength results from the graphite testing in MPa

3.6.2 Conductivity Testing

Electrical

This testing was carried out according to the "C611-98 (2016) Standard Test Method for Electrical Resistivity of Manufactured Carbon and Graphite Articles at Room Temperature" and at several elevated temperatures. The equipment which was used here was the Netzsch SBA 458 Nemesis and for all eight grades of Graphite in this

report three repeat measurements were recorded and are reported.

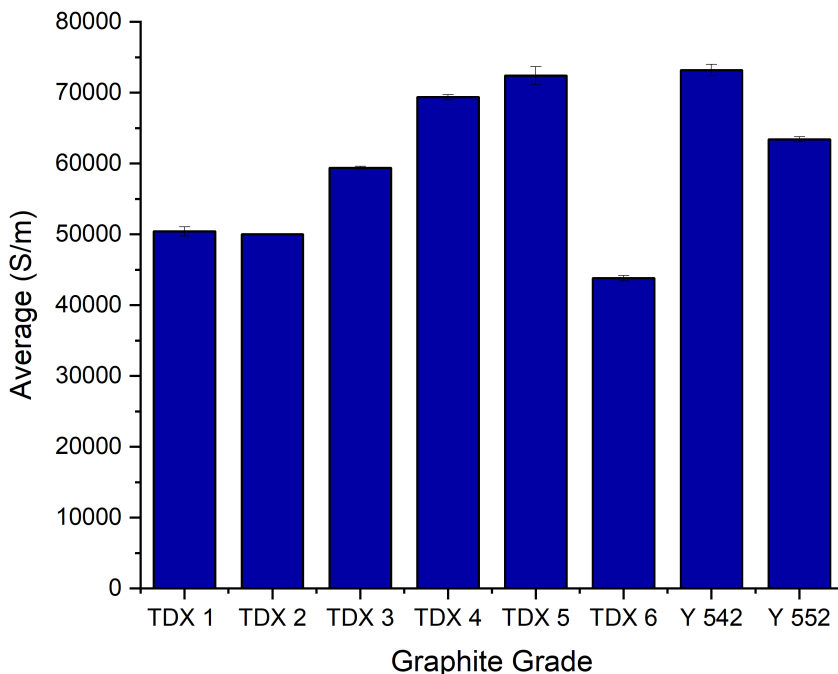


FIGURE 3.12: Electrical Conductivity results for the graphite grades highlighting the excellent conductivity of the material

Thermal

This testing was carried out according to the "C714-17 Standard Test Method for Thermal Diffusivity of Carbon and Graphite by Thermal Pulse Method". The equipment used was the Light Flash Analysis on the NETZSCH-LFA 467 Hyperflash with limits between -90°C and 1500°C , reduced due to safety operating limits to 1200°C for tests conducted. For all eight grades of Graphite three repeat measurements were recorded for the purposes of ensuring the results were consistent. These results will be included but only averaged results are displayed here.

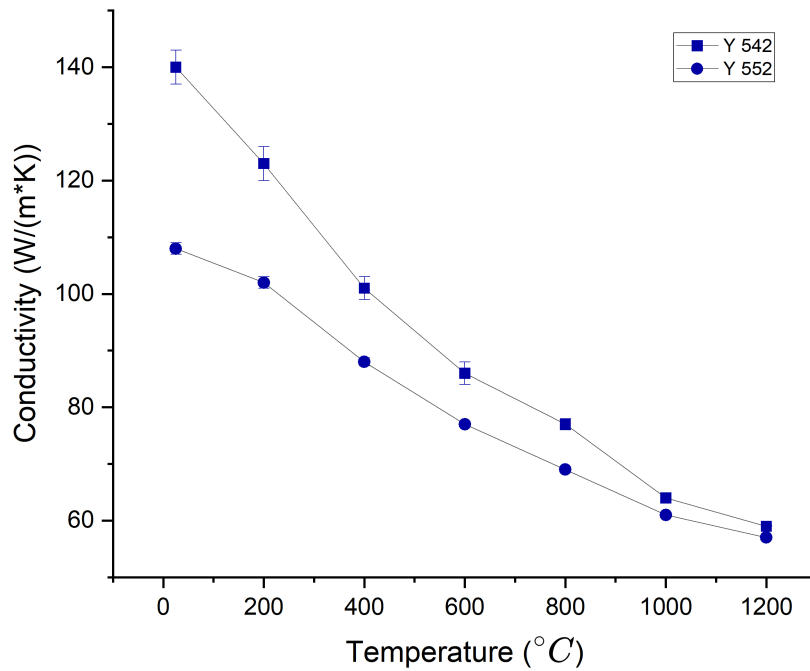


FIGURE 3.13: Thermal Conductivity results displayed for the relevant graphite grades tested Y-552 and Y-542 due to the additional size of the dataset from testing at temperature

Specific Heat Capacity

A measurement obtained as part of the thermal conductivity testing on the NETZSCH-LFA 467 Hyperflash was also recorded for all eight grades according to the C1470-20 ASTM standard. A graphite contact spray was used to better connect the samples with the machine as without it, the heat capacities reported were excessively large compared to expected values. Repeats were performed similarly to other tests, however, some did not use the graphite spray and are therefore excluded from the reported results.

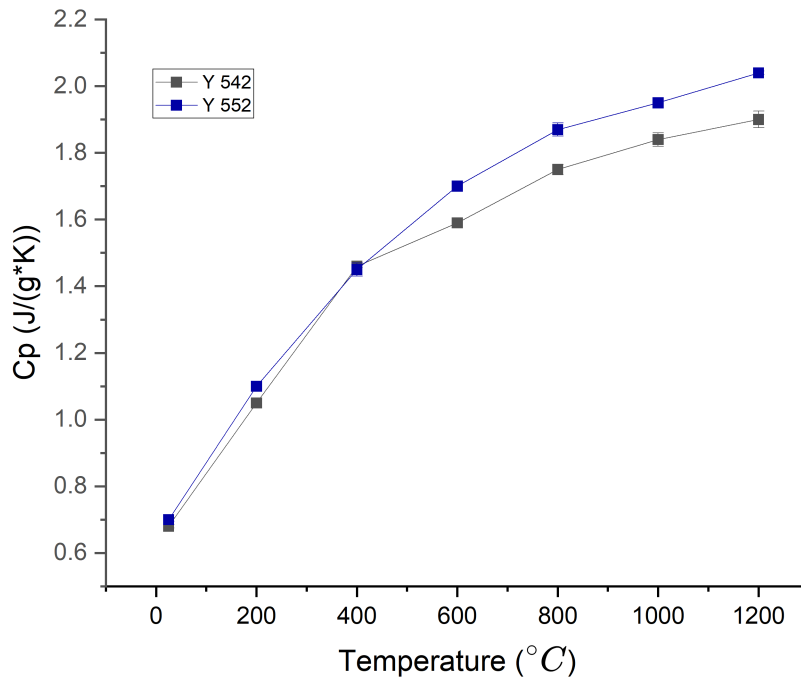


FIGURE 3.14: Heat Capacity results displayed for the relevant graphite grades tested Y-552 and Y-542

3.6.3 Coefficient of Thermal Expansion Testing

This was performed according to the "C1470-20 Standard Guide for Testing the Thermal Properties of Advanced Ceramics AND E228-17 Standard Test Method for Linear Thermal Expansion of Solid Materials with a Push-Rod Dilatometer". The equipment used here was the NETZSCH- DIL 402 Expedis Dilatometer and when carrying out these tests all eight grades were tested with three repeats at each condition to check for any inconsistencies, as most runs resolved with some discrepancies at low temperatures. These results were then converted to Thermal Expansion Coefficients via the following equation:

$$\alpha_l = \frac{1}{L} \frac{dL}{dT} \quad (3.5)$$

where α is the CTE, L is length, and T is temperature. The results seem to follow the same pattern, with some deviation at the initial stages of the heating, followed by a dip and then a plateaued rise to a converging point around 700°C. Discrepancies at

low temperatures can be somewhat explained by the low values and potential fluctuations in conditions pre-heating as well as mild surface roughness of the samples from machining and handling. As mentioned, full data can be found in the appendix to prevent excessive clutter.

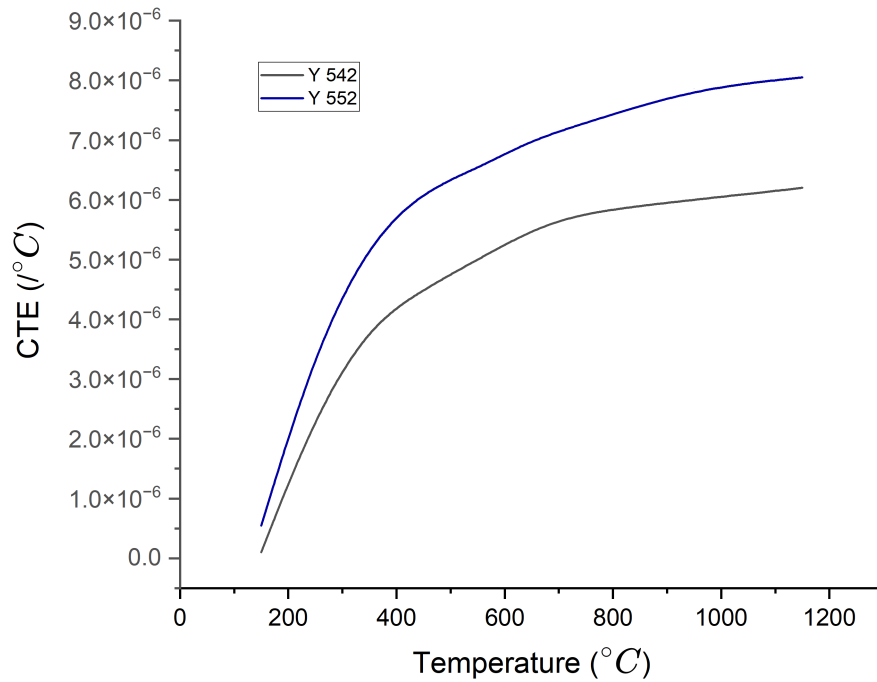


FIGURE 3.15: Thermally dependent Coefficient of Thermal Expansion for grades Y-542 and T-552

Chapter 4

Current Control Trials

4.1 Introduction

With the practical data acquired for the graphite tooling the FEM simulation may be provided data using a solid foundation. As mentioned in section 3.5.1, COM-SOL Multiphysics was used to create a 2D axisymmetric slice of the 20 mm diameter graphite tooling and created boundary conditions to recreate the conditions inside the sintering machine. This 2D slice can subsequently be rotated in the software to provide visual direct comparisons to the tooling if required, though no new data is created during this process.

The temperature is initially set to be globally ambient at 20°C, and recorded temperatures to compare against experimental results are measured from a point equivalent to the location of the pyrometer measurement. This is located at the mirror point where $r = 0$ within the hollow ram section of the graphite tooling. A boundary condition (BC) is then applied at a fixed time onto the edge of the tool stack to create an influx of normal current from one copper electrode whilst the other is 'grounded' to remain fixed to 0V to replicate the circuit of the FAST machine. The BC for normal current flow is defined as follows:

$$\frac{Cond * HeatingState * limPower}{(v_{fast} * ElectrodeR^2 * \pi)} + \frac{Cond_2 * HeatingState * Uctrl * limPower}{(v_{fast} * ElectrodeR^2 * \pi)} \quad (4.1)$$

Here $Cond$ and $Cond_2$ refer to the heating condition that the machine uses to define 'uncontrolled heating' early in the process for maximum heating rate, until the minimum pyrometer measurement temperature is reached so the machine may regulate its input using the robotic control system using this value. This was 450°C when the work began but has since been improved to 250°C through equipment upgrades and has been similarly updated in the model. $Uctrl$ refers to the parameter for control over the level of potential normal current flow defined using output from the proportional–integral–derivative (PID) robotic controller based on the machine's operation. For both conditions, the current is calculated using the radius of the electrodes and the FAST voltage, v_{fast} referring to the voltage reading reported by the machine and this value is adjusted based on the recipe limiting power ($limpower$) and PID controller ($Uctrl$). After defining this input BC and the contact resistances between each component based on literature from Maniere et al. [123], [143] a control simulation with a graphite spacer was performed to represent a calibration experiment done during maintenance. Thermal readings at the pyrometer and thermocouple measurement points in the simulation agreed with the recipe to within a few degrees during controlled heating and dwell in measured output from the experimental data, showing good alignment of the PID control. The electrical properties recorded by the system matched qualitatively also, providing initial validation for the model. More accurate quantitative validations are performed and discussed later in this work where they are performed.

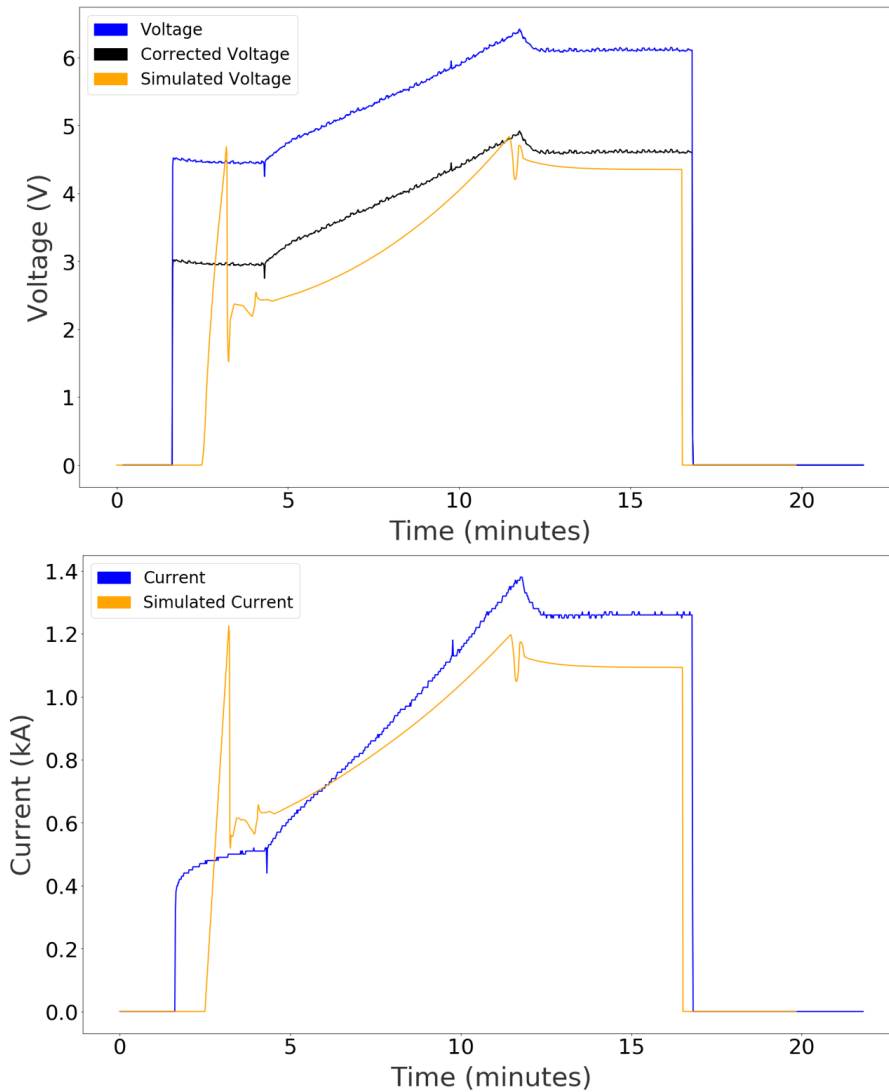


FIGURE 4.1: Initial current and voltage plots against sintering time for both experimental and simulated results demonstrating good qualitative matches, though with a disparity in voltage from simulated direct current simplification without adjustment

The discrepancy between the simulated voltage and recorded voltage in the Figure 4.1 was practically analysed using a digital oscilloscope attached to the machine between each electrode externally which recorded the output during the calibrated run. It was noted that the peak value during the pulsed sintering was in fact 3.5 V. This suggests additional circuitry within the machine is responsible for the remaining voltage discrepancy, though proving which elements cause this is challenging in a closed system. However, for this work it provides a sufficient explanation for why the machine reports 5V or greater during sintering while the analytical calculations show it to be significantly lower. This additional 1.5V is accounted for in the rest of

the machines electronics and not within the tooling stack which is solely considered within the simulation. It is therefore this 3.5 V, or more specifically the 1.5 V drop, which was included moving forward. Additionally, the pulsing of current has been removed for computational simplicity and any other discrepancies may likely be attributed to this simplification of the simulation. It may be noted though that some aspects of this were improved or included as the work continued into chapter 5 and 6.

It was initially noticed how significant the impact of the boundary conditions, especially conductivity, was here during the creation of the simulation and boundary conditions. From this, the concept of applying some external electrically or thermally insulating material would allow us to alter the sintering results purely from adjusting sample preparation. A thermal jacket is already commonly utilised to prevent radiative heat losses, however it was noticed that a majority of electrical manipulation was relatively simplistic. The aim of this work was to demonstrate that more complex manipulations were possible and effective, and initial 20 mm samples were created to probe this hypothesis. Some concept layouts were created and are visible in Fig 4.2 for how practical confirmation of the electrically created thermal gradients potential could be determined. Some resistivity testing on the material used to insulate the tooling graphite (boron nitride) was then required before further simulation work could be carried out. It was targeted at discovering the exact values for resistivity of the chosen BN sprayed onto the graphite foils already used in sample preparation for varying thicknesses and surface coverages. Boron nitride was selected as the insulation material for its easy availability as a cheap non interactive and temperature resistant coating already commonly used in industry which may be simply applied in designed shapes onto the foils used in FAST.

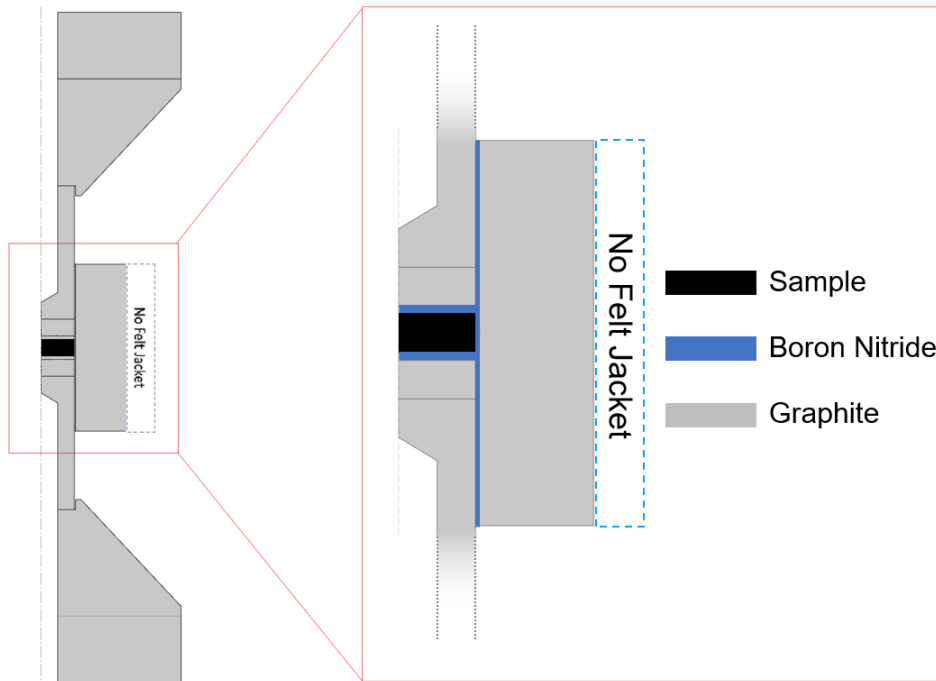


FIGURE 4.2: Schematics of the 2D axial slice view of the graphite tooling stack with focused schematics (right) demonstrating the Full BN spray concept pattern for testing and simulation.

It may also be noted that the spray contained not just the boron nitride, but a blend of solvents and resins with butane/propane propellant. Whilst some of the solvents and propellants likely evaporate during the drying of the layers, as could be detected through the odours, the resins remain. During sintering these have the potential to react and bond to the surface of the titanium samples, or potentially diffuse into the sample. This may be the subject of future analysis, however, in the work as a whole no evidence of this diffusion was observed through EDX SEM testing and in fact a resistance to the carbon diffusion seen from the graphite foils may prove an additional benefit of this material for titanium FAST processing.

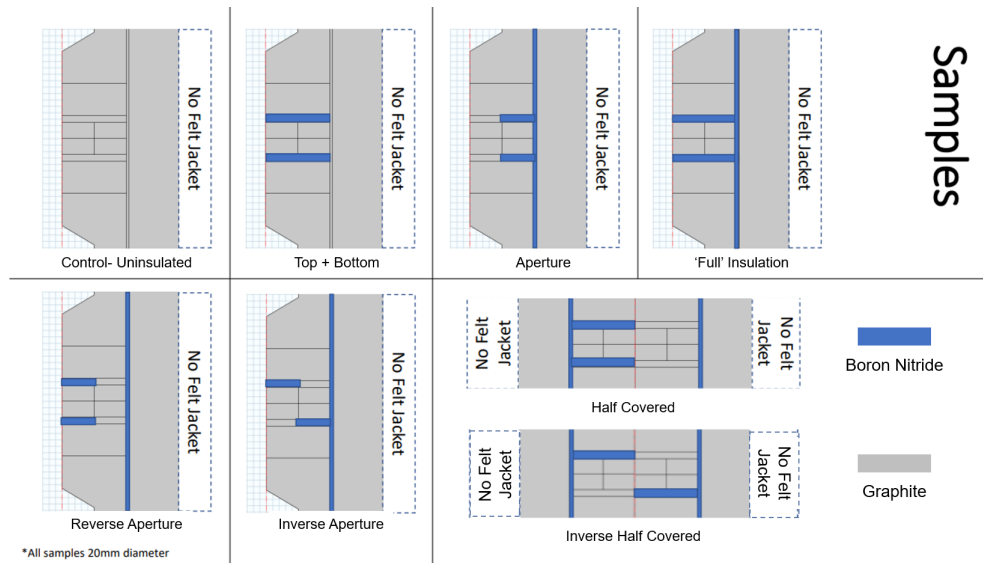


FIGURE 4.3: Schematics of all the 2D axial slice views of the focused schematics demonstrating the initial BN spray concept patterns for testing and simulation.

4.1.1 FEM 'Twin'

Initially a total of 8 BN spray patterns were designed as shown in Fig 4.3, however, through early stage testing and using the simulation the effectiveness of this FEM simulation as a 'digital twin' was seen for this technique. The FEM simulation allowed the resistance profiles to be included and run a parallel simulation to act as an explicative tool for the effects seen in the samples created, or even as a predictive tool for the impacts of adjusting the BN layups or recipes. With the assistance of this simulation, the initial eight patterns were reduced to a final four to be tested in more detail practically. The primary variable used for this selection criteria was the radial thermal gradient created within the sample region, with the target of producing varying degrees of consolidation which could be examined optically.

2D Axisymmetric Restrictions

As mentioned the 2D axisymmetric approach was required to reduce computational requirements and simulated run times, however, whilst normally not a concern, with patterns that do not also conform to the axial rotational symmetry, it was not possible to utilise this technique. As such, the half and half layups were examined using

a primarily practical approach with a simplified 180° rotational slice in the finite element model. It may be noted that these demonstrated little impact on a 20 mm diameter scale and were discarded for practicality, though there is greater potential at greater length scales for the sintering of dissimilar materials through generation of non-symmetrical radial thermal gradients.

4.2 Methods

Testing was carried out to investigate the impact of the application of varying thicknesses of BN spray on the consistency and the resistance noted. This extended to examining the relationship between the resistivity of the foil and the surface % covered by the insulating spray. As the designed layups often did not cover the full surface, it was important to know any limits on current restriction for the refinement of sample design for experimental testing. It could be expected that reducing the conductive area through the BN application would result in a net reduction to the current passing through the system with increasing resistance. That said, this was demonstrated to not be the case until a significant area had been covered, determined by the material and energy input. With an increase in current it will initially reduce the resistance slightly, with constant voltage, from Ohm's law. However, this rise in energy will also cause joule heating, described through Joule's law where $P = I^2R$ providing a limiting factor on current passing through a conductive 'hole', or aperture, in the foils. The result of this is seen in the resistivity testing where a series of samples, sprayed with boron nitride and surfaces scraped until the graphite was exposed to a range of percentages of surface area coverage, were analysed and the data can be seen in Fig 4.5. It was noticed that with a surface covering of less than 75% the net resistance of the surface was near to equivalent to no covering. This strongly implied that the current was then travelling at a higher density through the exposed region with no visible change to the voltage or resistance but a lower area of conductive material. This is the desired outcome, resulting in more localised Joule heating during sintering. This data allowed the final specifications for the boron nitride spraying and cut out masks to be created for more precise measurements and

layups of insulation for repeatability and comparison to simulation.

The initial measures of resistance were taken from manually prepared samples removing the BN layer by hand, resulting in some imprecise surface coverage. To counteract this and create a level of quantitative certainty, the foil discs were photographed and the images analysed to more accurately calculate the surface coverage and associated resistances. The photographs were converted to black and white in ImageJ software before a threshold was applied to clearly define regions which had remaining coating (white) and those that did not (black). This threshold process chose a limiting point in the pixel value and set all pixels lighter than this to white and lower to black as seen in Fig 4.4. Once this alteration had been made, comparing the pixel counts from the known initial size of the foil cut-outs allowed a surface coverage to be determined and compared to the resistances.

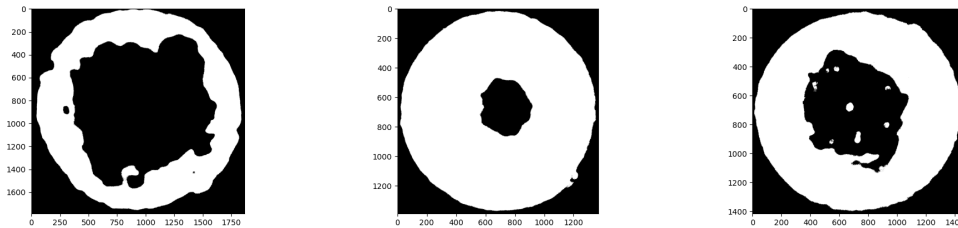


FIGURE 4.4: Threshold images of the sprayed graphite foils for resistivity testing

The resistance from the machine was calibrated against a copper plastic coupon of known 1 Ohm. The resistance data was taken over a period of time to allow for an equilibrium to be reached, and averaged over the five tests. To later transfer this information to the simulation it would be converted to resistivity using the following:

$$\rho = \frac{RA}{l} \quad (4.2)$$

where ρ is resistivity, R is the measured resistance, A is cross sectional area, and l is length over which the current is being measured. This resistivity can then be converted to conductivity with a simple inverse proportionality and reported in siemens

per meter S/m which is the term utilised in COMSOL for inputting this material property.

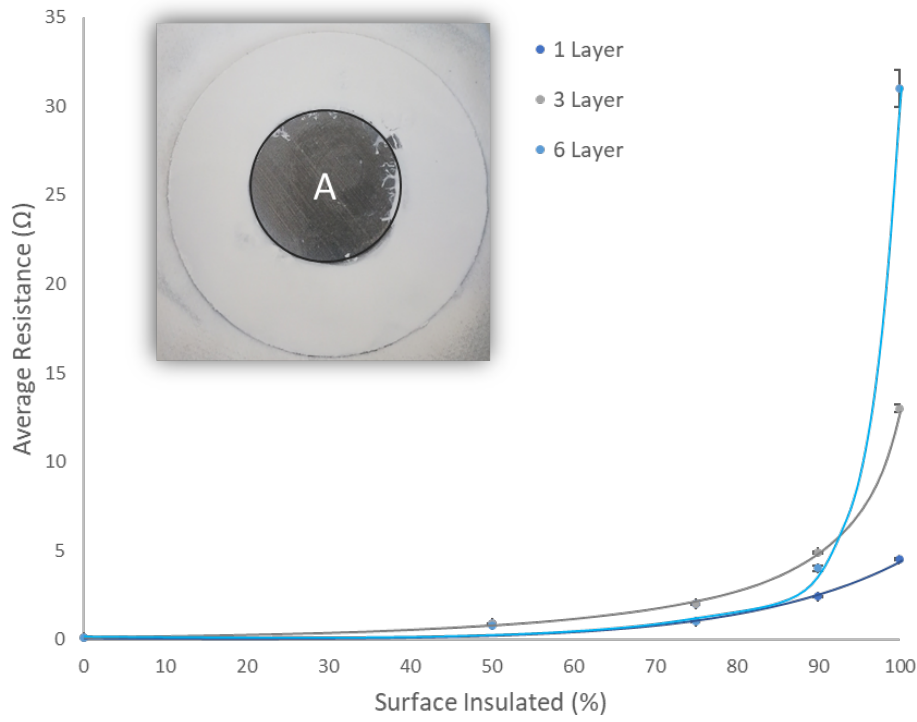


FIGURE 4.5: Plots demonstrating the rise in resistance to the normal flowing current as the surface % of graphite foil coated with Boron Nitride (A) increases. For circles with approximately 85 % or higher coverage, there was a sharp increase in total resistance.

The testing foils used to obtain Fig.4.5 were primarily aperture in shape, as seen in Fig.4.4. This was as they were the easiest to prepare to specified surface coverage, though additional configurations, such as reverse aperture were also included as comparisons and showed little variation.

4.2.1 Practical Sintering

Initially the specimens were sintered at temperatures slightly below the β transus temperature for the Ti-6Al-4V alloy, targeting the possibility of overshooting the target temperature due to the increased localised heating. The runs were performed at 975°C for the Ti-6Al-4V grade 5 ASTM powder with 0s dwell time, with a heating

rate of $200^{\circ}\text{C}/\text{min}$, a 16 kN max pressing load, and 12 g of powder for final height of 10 mm with 20 mm diameter. It must be noted that there was no insulating carbon heat retention jacket, common in sintering, to facilitate comparison to the simulation which did not include this feature.

The most seemingly impactful four layups after an initial visual inspection under optical microscopy were then repeated at 995°C , 1015°C , and 1075° to be examined both at, around, and above, the β transus line. There had been an expectation that this would have been primarily visible under cross polarised light through the resulting microstructure of the samples, however, a much more prominent impact was the resulting densities. The 0 s dwell period, cautiously decided upon to avoid degradation of the insulating properties of the BN spray, was the cause of this lack of consolidation. This resulted in insufficient energy at such a high heating rate, and lacking time, for the powder particles to complete their deformation. Therefore all initial determinations of impact were from porosity distributions observed in Fig 4.7, improved throughout testing and described in detail in the results section 4.3.

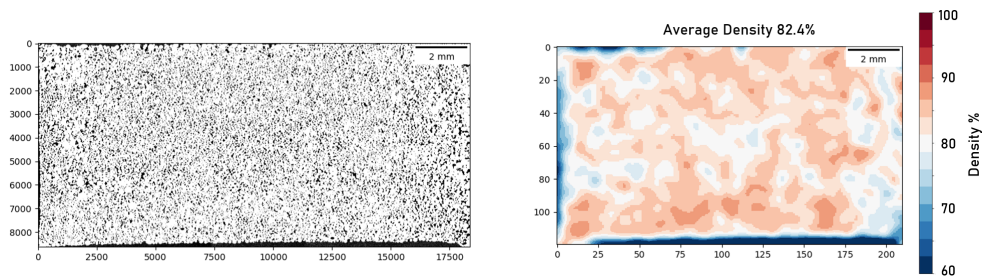


FIGURE 4.6: A mosaic micrograph of the control sample which has been cropped and processed (left) and the python output density heat map (right) with calculated average density

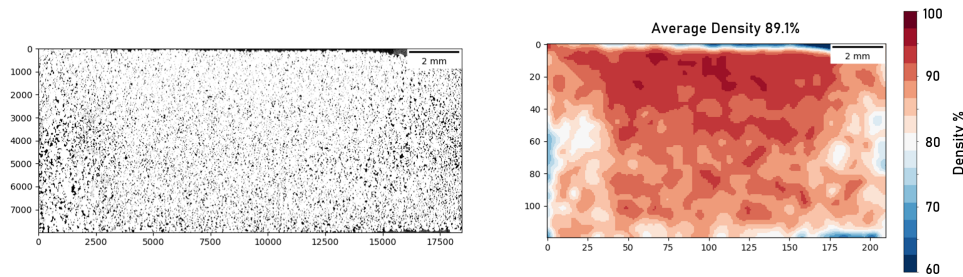


FIGURE 4.7: A mosaic micrograph of the aperture sample which has been cropped and processed (left) and the python output density heat map (right) with calculated average density demonstrating impact on consolidation of current control

These four layups were sintered again, at least once each, to confirm the effects witnessed before being metallographically prepared, as described in sections 3.4.1 and 3.4.2 for imaging on the Olympus microscope and Clemex software to obtain 'mosaic' images of the cut surface. Here 'mosaic' refers to large optical micrographs composed of many smaller higher magnification images which have been taken through pre-programmed moving of the sample stage and refocusing of the microscope lenses before being 'stitched' together in the Clemex software. These larger images were then processed using the image threshold method described in section 4.2 using ImageJ to determine the porosity, setting the threshold to turn surface metal white and the remaining porosity black. Thus, the resulting electrical and thermal impact on the consolidation of the samples was recorded from this channelling of current during the FAST process. A small script was then written in Python, to section the image into small sections and locationally determine the density of metal, through the white pixel count. This allowed the plotting of density heat maps for this value, highlighting trends in the macroscopic behaviour of the titanium alloy during sintering. For the final averages of the densities reported, the sampling was ensured to be within the material, with any edge anomalies excluded from the measurements, though they remain visually in the maps for identification. It may be noticed that for the sintering runs of 995°C in Fig 4.10, though at the β transus, the microstructure was not seen to dramatically change due to the samples only remaining above the β transus temperature for a few seconds, including overshooting from the PID control, which was not long enough to result in significant prior β grain growth, especially with the lacking degree of consolidation.

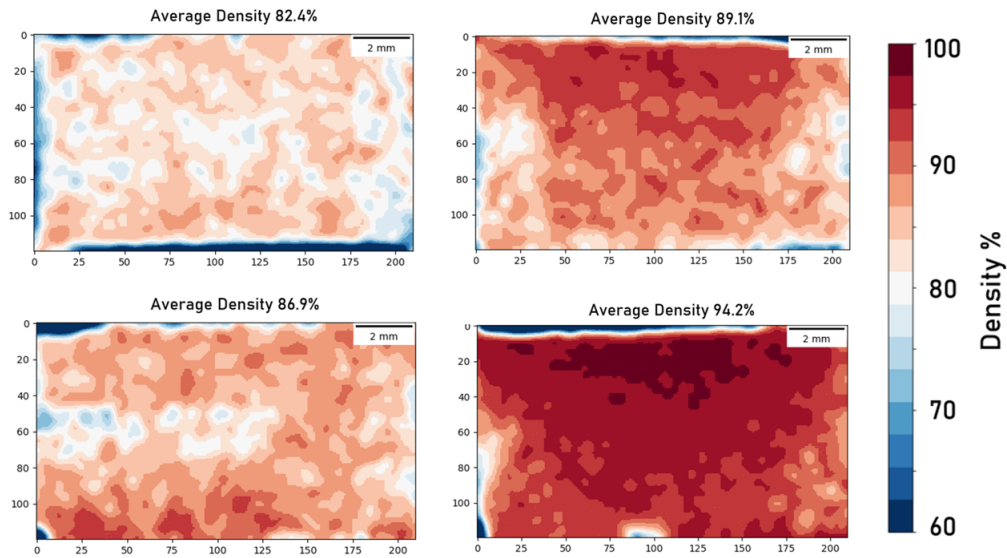


FIGURE 4.8: The resulting density heat maps from the 20 mm diameter 975°C processed samples for the Control (top left), Aperture (top right), Reverse Aperture (bottom left), and Full (bottom left) showing increase in overall density.

As clearly visible in these density maps, there was a dramatic change in the overall density, as the quantity of insulation increased as well as the pattern of consolidation. Before discussing any other aspect, it is important to mention that it seems that this was achieved with less overall power for the runs reported in Fig 4.9 calculated as the area under the power plotted against time for the run. This density increase also seems, in Aperture and Full samples, to provide an axial density gradient. There are several potential explanations for this such as a temperature gradient in the cooling rams, though the machine data demonstrates this not to be significant in these runs. It could also be positioning of the samples within the mould placing one face closer to the heating rams than the other, or some early densification effect from the axial pressure at these processing conditions similar to forging effects. It is also understood, through comparison with the simulation, that the BN can act directly, or indirectly, as a heating source or CFC plate when positioned in the tool stack with high enough insulating spray coverage to increase the net electrical resistance of the stack. This is what we believe caused these distributions based on information from the simulations, and it may prove useful for the FAST process to provide a means of reducing energy consumption when the samples increase in scale and thermal, and

therefore energy requirements.

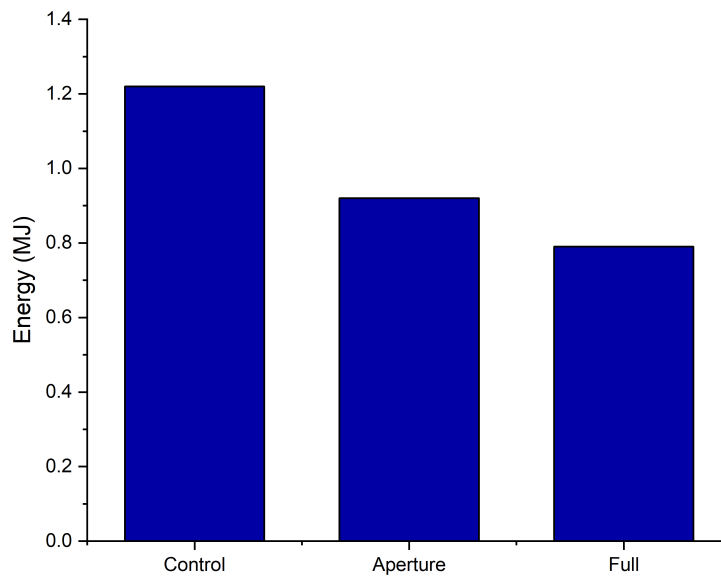


FIGURE 4.9: Bar graph displaying the impact of increasing the electrical insulation reducing the required energy to reach dwell temperature.

It can also be seen that for this processing temperature in the full insulation sample, but more prominently in the aperture, Fig 4.8, that there is a band of higher density through the centre of the sample. This increase of 5-10% density is indicative of higher temperatures during processing, meaning that there was in fact a thermal gradient created over only 10 mm, purely from this BN application controlling the current. This is a significant indicator of the potential of this technique at larger sample scales and a positive aspect for the technique as a whole. While here it is demonstrated that the capabilities to improve consolidation and potentially produce inhomogeneous thermal gradients, it also demonstrates a strong potential to do the opposite and tackle the thermal gradient issue common with processing using this technique at greater scales.

4.3 Results

Previously discussed, the four most impactful layups from 975°C were repeated at three higher temperatures, 995°C, 1015°C, and 1075°C with no dwell time again for consistency and ease of comparison. However, even 20°C above the β transus in the 1015°C tests there was not sufficient time, or consolidation, to experience a significant variation in prior β grain growth across the sample, leaving this aspect to the final higher temperature option of 1075°C. This microstructural impact is examined in much more detail and at greater scales of 80 and 250 mm in chapters 5 and 6, so this section will focus primarily on the increases in consolidation seen from these 20 mm trials.

The densities were then also processed for 995°C and 1015°C, seen to be much closer to full consolidation in Fig 4.10 and Fig 4.11 respectively, reducing the impact on total averaged density. However, the patterns in the consolidation trends seen before were once again demonstrated, showing them to be consistent through the whole sintering process and suggesting they would remain so at longer dwell times. However, while there was significant alteration in microstructure, predicted to be from the rise in temperature gradient, it was not as conclusive as expected without the microstructural 'thermal marker' forming. Regardless, the density maps are presented below and do add more evidence to support the hypothesis of thermal gradients from electrical manipulation being possible and spatially predictable and designable.

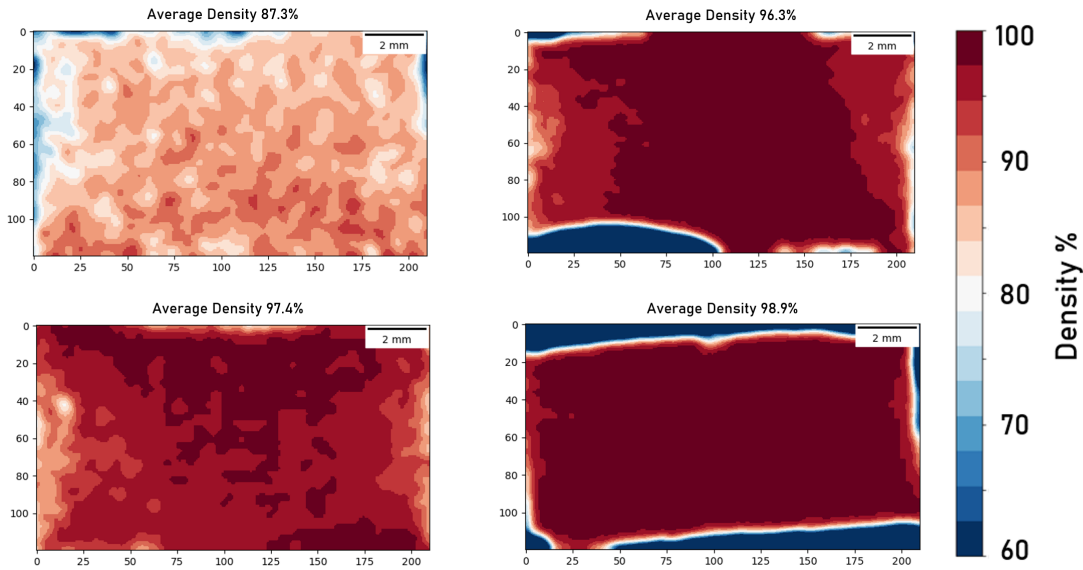


FIGURE 4.10: The resulting density heat maps from the 20 mm diameter 995°C processed samples for the Control (top left), Aperture (top right), Reverse Aperture (bottom left), and Full (bottom left) showing increase in overall density.

The darker blue regions visible in Aperture and Full, and to a lesser extent in Control, represent the Bakelite surrounding the mounted samples and was removed prior to average density measurements through data cropping for more accurate readings.

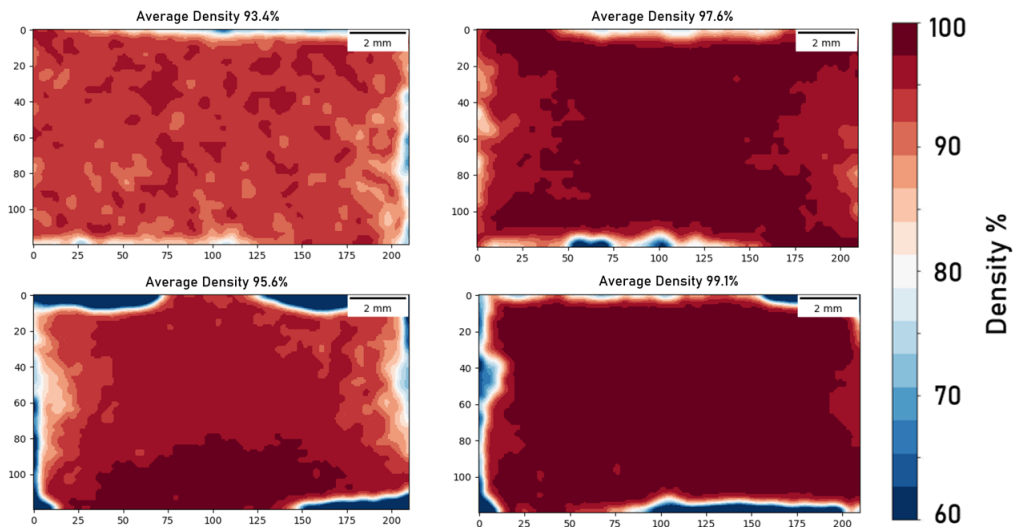


FIGURE 4.11: The resulting density heat maps from the 20 mm diameter 1015°C processed samples for the Control (top left), Aperture (top right), Reverse Aperture (bottom left), and Full (bottom left) showing increase in overall density.

In Figs 4.10 and 4.11, near identical trends can be seen to each other and to those seen initially in Fig 4.8. The control sample is relatively inhomogeneous and contains the lowest average density, from the lower concentration of localised heating meaning the energy was absorbed more into the graphite tooling and less reached the powder in this small timescale. It has been seen previously that these temperatures are more than sufficient to fully consolidate this material with even 5 mins of dwell, highlighting the reasons for an initial choice of 0s dwell. These control samples can then be used as reference for the baseline performance at these conditions and the full insulation sample, reaching full consolidation at 995°C provides a limit to the processing window, showing a much quicker full consolidation and the theoretical limit of rapid consolidation.

The pieces of greatest interest for this work lie in the aperture and reverse aperture sample and their density patterns in these heat maps. The reverse aperture samples were expected to consolidate preferentially towards the edges of the samples, however, as is clear from the density profiles this is not the case. It seems that primarily these samples experience some preferential surface densification, resulting in 'knock on' consolidation in a wave through the sample. The surface effect stems from the impact of the higher resistive BN spray central region, acting as a localised heating source in the direction of the flow of current. The reason that this occurs for the reverse sample but the opposite occurs for the aperture sample is not yet well understood, but it is thought to be a result of a combination of improved contact with the conductive foils in the aperture sample and the diameter of the available space for current to flow through.

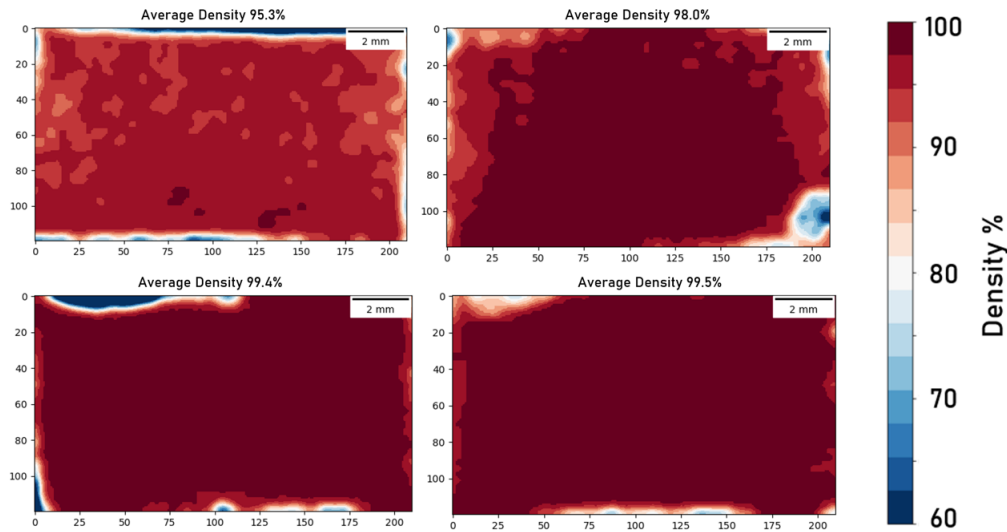


FIGURE 4.12: The resulting density heat maps from the 20 mm diameter 1075°C processed samples for the Control (top left), Aperture (top right), Reverse Aperture (bottom left), and Full (bottom left) showing increase in overall density.

At the final set of tests performed at 1075°C, Fig 4.12, there was a much less significant change in consolidation visible due to reaching full density, but some trends in the microstructure features were noticed. The three micrographs in Fig 4.13 were taken from the samples shown in the density maps in Fig 4.12 and demonstrate the variations in final microstructure in the Ti-6Al-4V samples. Where sufficient porosity is seen, below approximately 90-95% density, sub-transus microstructure is observed with no prior β grains similar to Fig 4.13 (a) above. Between 95 and 99% final density the consolidation approaches completion and the grains are no longer restricted by the powder boundaries, allowing the initial transformation and growth of small β grain structures to occur Fig 4.13 (b). Some pinning from voids is still visible and the energy input from the local temperature field is only slightly above the transformation temperature, in the aperture samples.

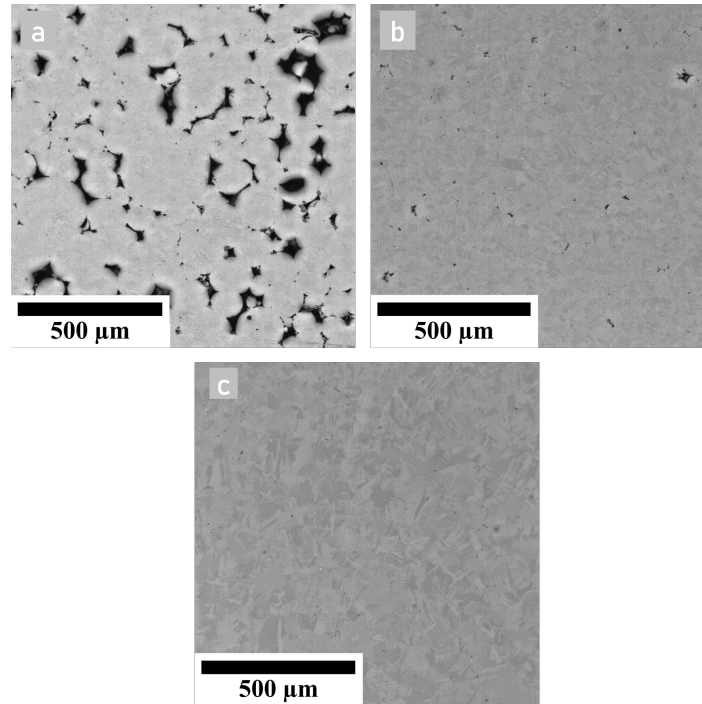


FIGURE 4.13: Cross polarised micrographs taken at 100x magnification of (a) the 1075°C control sample, (b) the 1075°C aperture sample, and (c) the 1075°C full microstructure.

It may also be slightly lower than the recipe suggests due to the gradients produced from current control. The micrograph in Fig 4.13 (c) is the clearest depiction of super-transus microstructure visible in regions above 99% final density and confirms the thermal impact through the inherent microstructural 'thermometer' in this titanium alloy. With this information it can be said that the final density variations through the samples were in fact from the thermal gradients predicted from the initial simulations rather than any potential electrical effects and may be significantly altered and improved simply by applying surface insulation to the tooling stack.

4.4 Discussion

What has been determined here is that the inclusion and spatially resolved location of the BN spray application has demonstrated a definite impact on the densification of the 20 mm samples during FAST. It can strongly be inferred that this was due to the increase in current densities from the insulation profiles leading to a focused

heating effect, either in the sample region or the BN foils. In the case of the aperture sample, the model predicts that happens in a channel through the centre of the sample, and the findings seem to confirm this. Whereas, with the Rev Ap and Full samples, the BN spray acts more like a CFC plate, or heating pad, adjacent to the powder in the sample region, providing more direct and localised heating from the technique and increasing the efficiency of power transfer for densification with overall reduced power input. This is primarily an effect for the controlled heating phase of the sintering process and does not directly affect the dwell profile. Though it may be suggested that the location of heating may cause heat lag to appear depending on the pyrometer measurement location and this is discussed in chapter 5 in greater detail.

Using the microstructures of the samples at peak temperatures of 1075°C the inherent thermometer of Ti-6Al-4V's β transus temperature was used to determine that this increased and targeted densification was a result of thermal impacts and not directly caused by any specific electrical effects or atomic mobility, though it is possible they were marginally increased. The multi-physics simulation predicted this effect, and has agreed with the qualitative results thus far, however it had not been quantitatively validated at this point of the work and as such the results cannot be compared numerically in this chapter as they are in chapter 5.

Overall in this chapter it was demonstrated that the current control technique has a real and repeatable impact comparable to the simulations' prediction of thermal trends and resulting microstructures. This result strongly influenced the subsequent work where the scale of the samples was increased to 80 mm to intensify these effects and make them more relatable to a real world setting where components may be produced at similar scales. The model validation was carried out from practical data and provided further retrospective evidence of the causes and relevant nature of this effect.

This evidence points to a novel capacity within the FAST process to not only

focus the current within or without the sample region, but to spatially resolve it further within the sample to create varying and tailored heating profiles. These could be utilised to homogenise larger samples or design gradients for intentional microstructural differences for multifunctional parts.

Chapter 5

Predictive Sintering

This chapter consists primarily of content from a paper which has been published in the Journal of Materials Science, titled "Channelling electric current during the Field-Assisted Sintering Technique (FAST) to control microstructural evolution in Ti-6Al-4V" accessible through the DOI - <https://doi.org/10.1007/s10853-023-08884-8>. Some modifications have been made to fit the style of the thesis, however, this is a self-contained publication, and is mostly unmodified in content from the currently published version. There will therefore be some inevitable overlap in content with other sections which discuss similar topics and methods.

5.1 Introduction

Perhaps the most defining feature of Field Assisted Sintering Technology (FAST) is the application of a current, in addition to the uniaxial pressure, to create resistive heating in and around the sample region. However, with a few exceptions, most research takes this as an unchangeable part of the process. Here, this current flow is directed to specific regions within the toolset using boron nitride as electrically insulating material. This caused the heating to occur in differing regions within the Ti-6Al-4V sample and mould over four insulating configurations, with the shift in current density resulting in an extreme disparity in the final microstructures. The samples were imaged and analysed with Deep Learning in MIPAR, alongside comparisons with Finite Element Analysis (FEA) Models for 20 s and 5 min dwell times, to provide the technique with predictive capabilities for grain size and microstructure. The results gathered imply significant potential for this concept to improve the

flexibility of FAST, and potentially reduce negative effects such as undesirable temperature profiles in size scaling sintering for industry.

Powder consolidation is a diverse field, full of potential. However, with this potential comes a slew of problems and limitations associated with each of the varied techniques. Currently, one of the most promising solid-state process variants is Field Assisted Sintering Technology (FAST), also known as Spark Plasma Sintering (SPS). FAST is capable of consolidating a wide variety of powder materials from ceramics [144], [145] to composites [146], as well as many metallic systems [147]–[149]. Through resistive heating, this process can generate fully dense samples at a range of temperatures allowing for some degree of control in microstructural evolution, and thus, mechanical properties. Additionally, FAST performs this process many times faster than other alternative techniques used for similar purposes such as Hot Isostatic Pressing (HIP) [150]. This increase in speed and efficiency comes from the simultaneous application of high uniaxial pressure and temperature via Joule resistive heating from pulsed current passing through the graphite tools and materials to be sintered. The technique is also capable of much higher heating rates than other high pressure methods at 200 °C per min for our machine, or up to 600 °C per min in some cases [151].

This low voltage, DC activated synthesis and sintering technique has used uniaxial pressure, in conjunction with resistive heating, to consolidate a wide variety of materials since its inception. Though it has a relatively short history, with much of the work since its patenting in the 1960s focusing on its ability to rapidly sinter materials which are otherwise challenging to consolidate, such as ceramics or refractory materials. Over the last decade, it has gained popularity as a technique, becoming the sintering method of choice in several of these fields. However, until recently very little work has investigated the potential to spatially fine tune the most unique factor of this process, the electric current and resulting heating. Zapatas [152], and Geuntak et al. [153] used alumina fibres, borosilicate, and boron nitride respectively as insulators to completely isolate the sample from current, as well as ensuring that nearly all of the current flows through the sample in their work. Additionally, Manière et al.

used an expansion of this in his work on nickel alloys [143], [154] in a “controllable interface method” in an attempt to channel the current through more conductive graphite foil regions for shaped production.

In this work, it is attempted to further advance this concept using high strength, lightweight aerospace titanium. Ti-6Al-4V powder was chosen here, due to its excellent properties [11], [155], [156] for real world applications such as aerospace engines medical implants or tools. It is these diverse and impactful uses driving the recent rising popularity in the field [137]. Titanium alloys also commonly possess a microstructural sensitivity at specific temperatures which aids in analysing the resulting temperature profiles. This change falls between the two allotropes of titanium, the α phase of hexagonal close packed structure, and the β phase above 994°C for Ti-6Al-4V which is body centred cubic. Although much of this structural change reverts upon cooling to the α phase, it leaves prior β regions which experience much greater grain growth during heating than their α stable counterparts. It is with these larger prior β grains that attempts are made to quantitatively determine the impact of the thermal gradients along with the more qualitative ‘ β transus line’, where the boundary between grains which did and did not experience this allotropic change can be seen.

These alloys are also currently expensive and difficult to produce, making the flexibility and control FAST offers incredibly appealing [63], [157], with large potential reduction in costs and little loss in component complexity appealing even further. Current limitations in the production cost for titanium components [6] have driven a wave of interest for a ‘right first time’ approach where the component is created in the minimum number of steps possible to reduce the price and the number of costly machining steps. With the ideal for FAST processing of titanium being this aim for a ‘right first time’ approach, the flexibility and control of the technique become more important to improve as each further machining or thermomechanical processing step required will reduce the benefits provided by the technique.

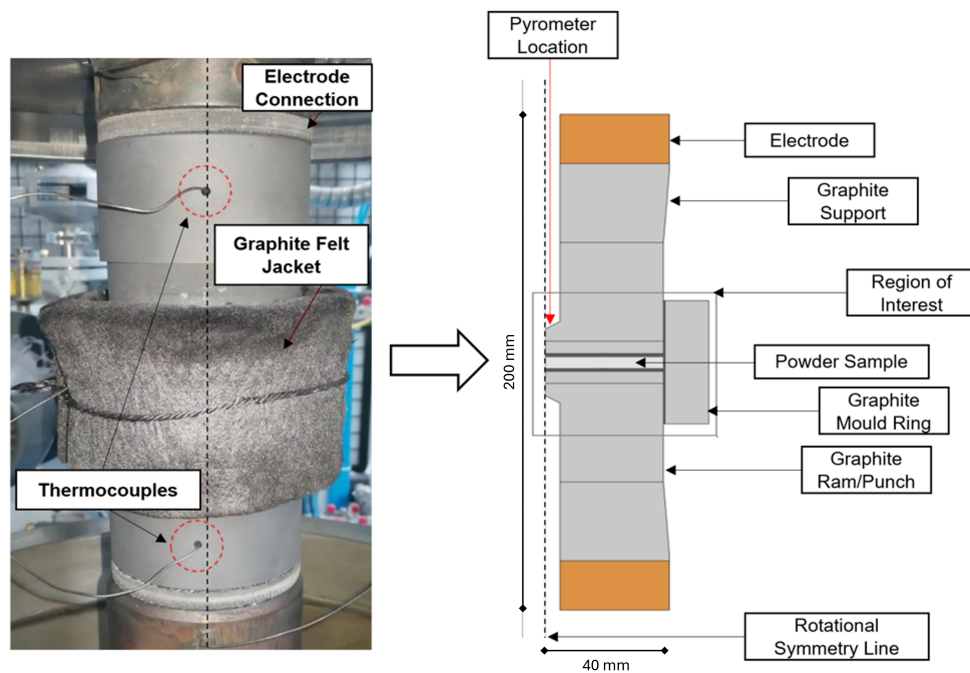


FIGURE 5.1: Left: Photograph of 80 mm graphite tooling in the FAST vacuum chamber / Right: Labeled Schematic of the 2D uniaxial slice of the FAST tooling stack.

Our primary goal is to investigate the potential of further shaping the current profile with tailored boron nitride (BN) shapes applied to the graphite foils connecting a sample to the wear pads, demonstrated in Figure 5.2. Boron nitride was chosen due to its nature as a cheap and readily available material providing good potential for industry use. It is also capable of maintaining the insulating properties required at the high temperatures present in the titanium sintering process. The current is an important aspect of the FAST process, with the direct pulsed current providing the control and exceptional heating rate which make it unique amongst similar techniques, such as HIP. However, there are still aspects of this mechanism whose impact on the process is less well understood, such as surface cleaning [158] and potential arcing or plasma sparking between particles [159] during the early stages of sintering. It is hoped that by furthering our understanding of this current channelling approach that it will provide more control of microstructural properties thus leading to more efficient use of material. With this, new options will become available to the industry and the accompanying analytical process may also prove beneficial to other fields.

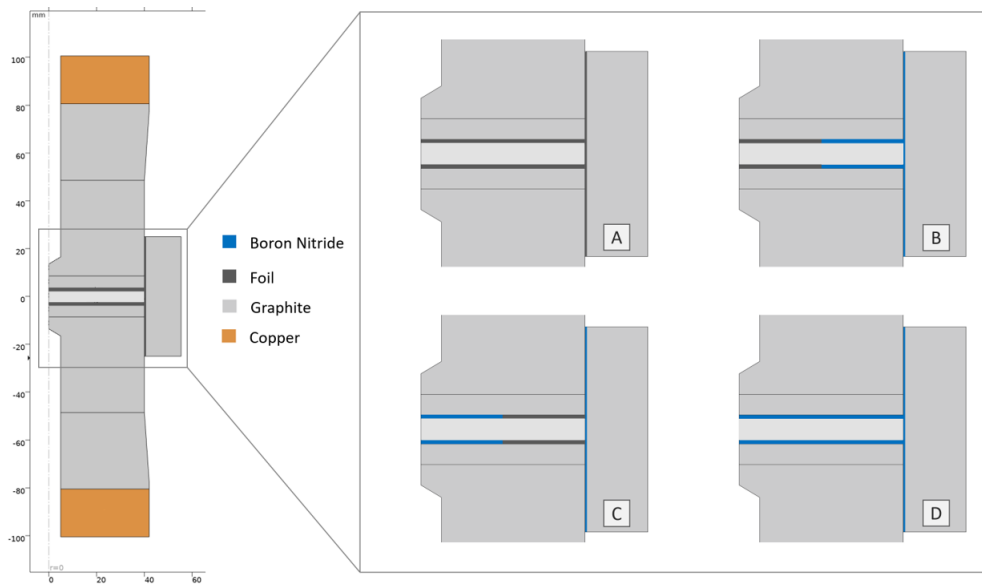


FIGURE 5.2: Left: Simplified 2D uniaxial slice of the simulated 80 mm graphite tooling stack. Right: The primary region of interest highlighted and enlarged, showing A - Control | B - Aperture | C - Reverse Aperture | D - Full Insulation

In all samples where BN is involved, highlighted in blue above in Fig 5.2, the connection to the mould is insulated to ensure that the path of least resistance available to the current will be created where possible. A fully insulated design was also included to determine another end parameter to this design process and any parallel vs perpendicular effects in this additional resistance to the foils [142]. These designs were formulated using a Finite Element Analysis (FEA) model to predict the current density and how this in turn would impact the temperature profile during the sintering process. Designs were chosen based on two major factors, firstly that they produced a temperature profile which was sufficiently intense to be perceived practically, and secondly that the resolution of the design was large enough to allow current to pass through the uninsulated spaces unimpeded where desired. Figure 4.5 in the previous chapter demonstrated this effect from experimentally covering a 20 mm diameter circle of this material with BN, providing a framework to experiment within.

The reason for turning to this FEA technique is that the physical system within the FAST machine is a complicated 'black box' system which may only be indirectly

measured without impacting the results. This is to say that although many macro and micro mechanisms have been proposed to explain the densification process of the powder [160], [161], the state of the sintered sample cannot easily be observed directly during the process. In terms of the sintering densification, many studies and models have been proposed to probe into this 'black box' within the process [162], [163]. These primarily discuss the correlations of shrinkage behaviour, densification mechanism, and atomic diffusivity and linking these to theoretical frameworks and thus models of the process.

Multiple of these physical models have been proposed to discuss the densification process and many have been backed by calibrated experimental results [164], though the complexities and variations between powders and machines provide additional complications. For titanium alloys such as Ti-6Al-4V investigated here, necking from grain boundary, volume and surface diffusion, is the primary early consolidation process and the high temperatures involved in FAST provide more kinetic energy for these processes to occur [165], depending on powder morphology. Combining bulk and surface atomic mobility on the micro scale with void evolution and shrinkage on the macro scale at later sintering stages is a multi-scale computational challenge facing the field to this day. Because of this, the densification mechanisms of multi-physics field sintering processes are not thoroughly understood, and the simulations, as well as deep learning image analysis concept proposed in this work become more relevant and impactful in exploring them.

As an additional complexity, the sample temperature may only be measured using an external pyrometer or thermocouple, which has potential to be a different temperature due to the thermal profiles or heat lag in the system. As such, it would be challenging to design a surface insulation pattern to direct the current to achieve the desired result without much trial and error, reducing the 'right first time' impact of the concept. Therefore a Finite Element Model (FEM) was chosen to be used in parallel to the sample creations to act as a pseudo digital twin of the FAST process through COMSOL [159], [166], allowing us to understand the impacts of the insulation on the current and therefore the temperature profiles. From this knowledge it is

also hoped to be able to predict the eventual microstructures and densities based on understanding of the alloys in question.

It is our hypothesis here that this targeted current channelling technique will provide a greater concentration of current in these 80 mm samples and therefore a more significant temperature increase in regions left uninsulated, resulting in greater densification and grain growth for short dwell FAST processing. Longer dwell processing is also possible and will be examined in future works when specific tooling can be designed and tested for purpose.

5.2 Methods

5.2.1 FEM Simulation

Details of the FEM simulations and modelling can be found in section 3.5 of the Experimental Techniques chapter, and specifics or changes will be highlighted here. All FEM simulations were performed in COMSOL Multiphysics software Ver 5.6 [167], [168] and used a 2D – axisymmetric approach to further simplify the computational requirements [169], commonly used in similar work [170]–[172] (demonstrated in Figure 5.2). These simulations used the resistance results from Figure 4.5 as boundary conditions to input the effect of BN insulation on current flow and density. Remaining contact boundary conditions were defined using data presented in work from Manière et al. [173] and graphite-titanium boundaries are assumed as ideal graphite-graphite contact due to the addition of foil in the sample creation. Our dataset for the graphite tooling materials collected for Olmec Advanced Materials grades Y-552 and Y-542 was utilised to generate a more accurate set of insulation profiles for the machine in this study, though literature values were used for the titanium sample. Surface effects are assumed entirely radiative with an emissivity of 0.8 approximating the near vacuum state in the machine. This heat loss is accounted for in COMSOL as follows:

$$q_r = v\zeta(T_w^4 - T_0^4) \quad (5.1)$$

where q is the heat flux per area v is emissivity and ζ is the Stefan-Boltzmann constant. All physical Partial Differential Equation (PDE) calculations were handled within the simulation using COMSOL's Multiphysics package, allowing for the efficient generation of data for design and prediction of samples. Dynamic elastic motion and electrical potential can reach the equilibrium state in a much shorter time frame with the heat transfer, so mechanical and electric factors are considered to be quasi-static to further reduce the models complex nature. The DC current is set to be unpulsed for the purposes of simplicity, and the resulting electromagnetic heating is governed by the following PDE within the package:

$$\rho c_p \frac{\delta T}{\delta t} + \rho c_p u \cdot \nabla T = \nabla \cdot (k \nabla T) + Q_e \quad (5.2)$$

where ρ is resistivity, c_p is heat capacity, T is temperature, t is time, k is the Boltzmann constant, and Q_e is the electric charge. The current providing this heating in the model is determined using a Proportional-Integral-Derivative (PID) controller similar to the physical machine with feedback from the previous iterations. Impact on current delivery is dependant on the desired heating profile and pyrometer temperature readings, and is inputted as a normal current density through the face of an electrode. Edge temperatures of these electrodes were fixed at room temperature to emulate the efficient liquid cooling they experience, although the practical temperatures vary by a few degrees depending on power load. Finally, while the solid mechanics in the simulation are included as a pressing force through the top ram, they have relatively little impact on the heating profiles of interest. This is due to our primary focus being the near consolidated dwell region of the sintering runs with a focus on final height microstructure.

5.2.2 Resistance Measurements

Before the samples were created, an accurate series of measurements were taken using a sample resistivity test unit from the *Lotus Engineering Instrumentation Department* to gain an understanding of the resistivity of the graphite foils when coated with layers of BN. Details of this testing can be found in chapter 3, as can the resulting resistance measurements. It was noted that the effectiveness of insulation falls rapidly as the surface is exposed, losing 90% of its total effect after exposing only 15-20% of the surface. With an exposed circle of graphite foil 10 mm diameter centred on the foil, 75% coverage was achieved. At this level of coating, there was a significant increase in conductivity when compared with full surface covering, clear in Figure 4.5, and not much lower than the base conductivity of the foil itself. This implies that a majority of the current is now being channelled through the exposed aperture rather than evenly across the surface, a theoretical fourfold increase of current density for a 25% aperture in the central region of the sample. This would make for very efficient heating for targeted regions within a sample.

5.2.3 Sample Creation

To create the samples to compare with simulated results, commercially available Ti-6Al-4V Puris™blend Bl-067 powder, within ASTM grade 5 specifications, with reported particle D50 of 163 μm was used. However, a more specific size was determined using a Malvern Mastersizer 3000 laser diffraction particle size analyzer with a wet dispersion method. A total of 3 repetitions were conducted to confirm previous results where this powder had been previously tested [174]. The D10-D90 scale was shown to be between 92-297 μm , within error of the previously recorded results. The powder was poured into moulds of Y-552 graphite from Olmec Advanced Materials for sintering by hand after weighing a fixed quantity to achieve a predetermined final height of 11-12 mm.

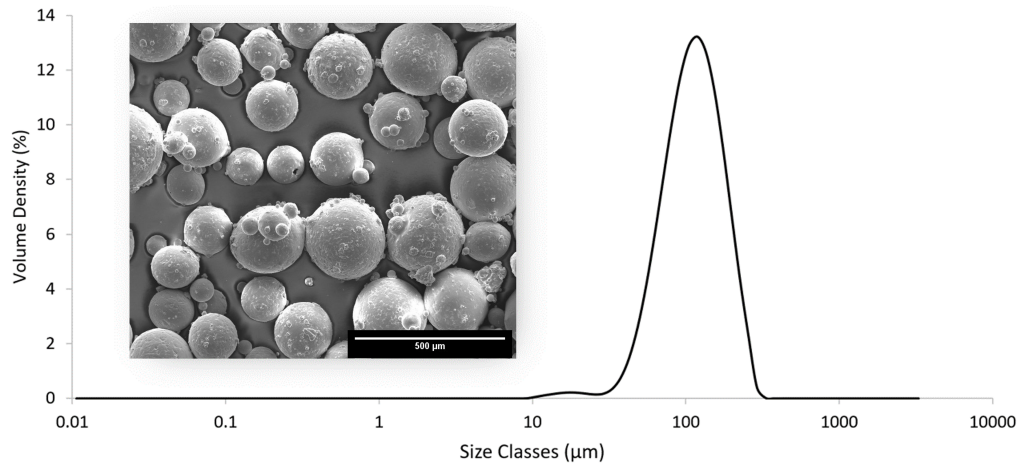


FIGURE 5.3: Ti-6Al-4V Puris Powder Size Distribution (PSD), averaged over several runs. Insert - Secondary electron micrograph image (20 kV accelerating voltage) of the powder's topography

For the preparation of the samples for sintering, six layers of BN spray were applied to 0.35 mm thick graphite foils, three per side. The primary use of this foil is to create electrically conductive contacts between the sample and tooling material. However, these foils were sprayed with BN through templates to block the spray for prescribed regions, shaping the resulting coating. A control was implemented with no insulation, and one sample which had all graphite foils coated to 100%, with the aim of exemplifying extreme insulation effects. For the intermediate, partially insulated designs, it was decided to focus the heating at the centre and edge respectively by attempting to direct current through these regions of the sample. All samples were then assembled with the graphite tooling and powders and pre-pressed at 0.6 kN before being pressed to 16 kN (32.5 MPa) over 5 minutes and only subsequently heated at a rate of 200°C per minute to 1015°C. This temperature was chosen to allow for sufficient time above the β transus of the titanium alloy with short dwell times to allow noticeable prior β grain growth whilst remaining low enough for the differences in grain size and α/β morphology to be determined visually. The FAST sintering machine used a pulsed current application of 15 ms on and 5 ms off DC current for easier comparison with previous work performed and for better consolidation. To prevent unnecessary oxidation of the Ti-6Al-4V powder, the process is carried out under vacuum, which is confirmed and controlled with an internal system to 10^{-3} bar. When at temperature they were held for 0 seconds, and 5 minutes

of dwell for each insulating pattern. They were then allowed to cool freely under the same vacuum and removed from the graphite moulds.

The sintering itself was performed in a *FCT Systeme GmbH Spark Plasma Sintering Furnace type HP D 25* and monitored with a pyrometer monitoring the temperature within a hollow ram. The internal diameter of the graphite ring was 80 mm and no external thermal insulating material was included. Samples were then sectioned, mounted in conductive carbon filled PolyFast™ Bakelite, ground, polished, and etched in Kroll's reagent (*HF 2%, HNO 6%, H₂O 92%*) for 15-20 seconds before cleaning to check and reveal the grain structure. A Struers Tegramin-25 was used for grinding/polishing, and the surfaces were ground for 2 minutes using P800, P1200 and P2500 *SiC* grit papers, followed by polishing with a 9 part 0.06 μm colloidal silica and 1 part hydrogen peroxide suspension for 10 minutes.

Using the *Olympus™ BX51* microscope, optical micrograph mosaics were taken from two slices of half the surface at 100x magnification with a compensated overlap. Focusing was determined using a plane of focus created prior to imaging, which was performed with a spatial resolution of 1.094 $\mu\text{m}/\text{pixel}$. This imaging was performed using *Clemex™* software and an automated stage to acquire images across the whole sample surface.

5.2.4 Image Analysis

These micrographs were analysed in Materials Image Processing and Automated Reconstruction software (MIPAR™) [175]–[177] to determine both the average grain size and the distribution to be related to the processing temperature. To perform the analysis of these grains in the software, grain boundaries were drawn manually on top of 50 reference images, taken from the samples in question, and used to train a 'Deep Learning' algorithm to recognise these grain boundaries under the lighting and magnification conditions used to capture sample micrographs. This was used as part of a recipe to then identify grains within further micrographs, the first step of which is the deep learning model using techniques such as semantic segmentation

to identify the prior β grain boundaries and improved with a variety of other inbuilt commands. Any which did not have a complete boundary due to a connection with the image edge were then discounted to minimise errors in under-measuring as well as over counting, and an average was taken for each image.

5.3 Results

The findings must first be discussed with reference to the electro-thermal-mechanical simulations used to design them. These, as with most simulations, required validation through comparison to experimental results. The first aspect of the FEA technique which needed thorough analysis was the mesh used. This was put through a refinement process where a series of stable mesh configurations within the COMSOL software were parametrically swept while all other parameters were kept constant for each simulation. It was found that this can have as much as a 5% potential impact on temperature readings if not optimised, with values dependant on the mesh scale in the sample region relative to the convergence point. However, using the smallest possible mesh to reach this convergence point exactly is wasteful computationally and this value was reasonably reached with a maximum element size of 11 for our models. To optimise performance, increasing the computational requirements by further refining this mesh was seen as irrelevant and so these were the parameters used.

When the simulation was compared thermally at the pyrometer location, and electrically through both the current (I rms) and voltage across the simulated section of tooling the accuracy was very good. These results from Table 2 show a strong correlation with the practically acquired results, with low average % deviation in the region of interest. It was expected that the temperature recorded at the pyrometer location follows the planned profile for heating as this was the PID feedback condition for the model and as such has not been included having a maximum error of 0.5 % in this region. However, the current and voltage also showed good agreement and thermocouple data also previously demonstrated a qualitatively strong connection.

It is believed that this is sufficient to have demonstrated the validity and accuracy of the simulation for obtaining the thermal profiles desired.

	I (kA)	I Sim (kA)	Diff %	V (V)	V Sim (V)	Diff %	Res (k Ω)	Res Sim (k Ω)	Diff %
Control	5.24	5.55	5.92	5.22	5.50	5.31	0.997	0.991	0.57
Aperture	3.71	3.50	5.79	5.49	5.20	5.28	1.478	1.486	0.53
Reverse	4.33	4.50	4.02	5.04	5.14	2.04	1.164	1.142	1.91
Full	3.68	3.45	6.27	5.47	5.15	5.77	1.485	1.493	0.53

TABLE 5.1: Data comparison between experimental runs and associated models demonstrating a 2-6% match on the current and voltages with a remarkable 1-2% match for the resistances.

The simulated predictions for the thermal distributions which can be seen in Figure 5.4 (A-D) demonstrate the impact of current density redistribution at the otherwise stable sintering dwell phase. With temperature differences of greater than 100°C over the radius of some samples, 40 mm across, processing at temperatures around the β transus point, as is done here, could have a single sample demonstrate the full transition from sub to super-transus microstructure. It is also clear from the results that whilst there is some small change in the thermal profile early in the dwell, it does not change the overall profile significantly. It is however, likely that at these temperatures the BN's loss of resistivity with extended exposure to heat would have some significant impact on runs with longer dwell times. For cases such as these, a potentially different method of insulation would be recommended, such as alumina tooling or similarly electrically insulating materials.

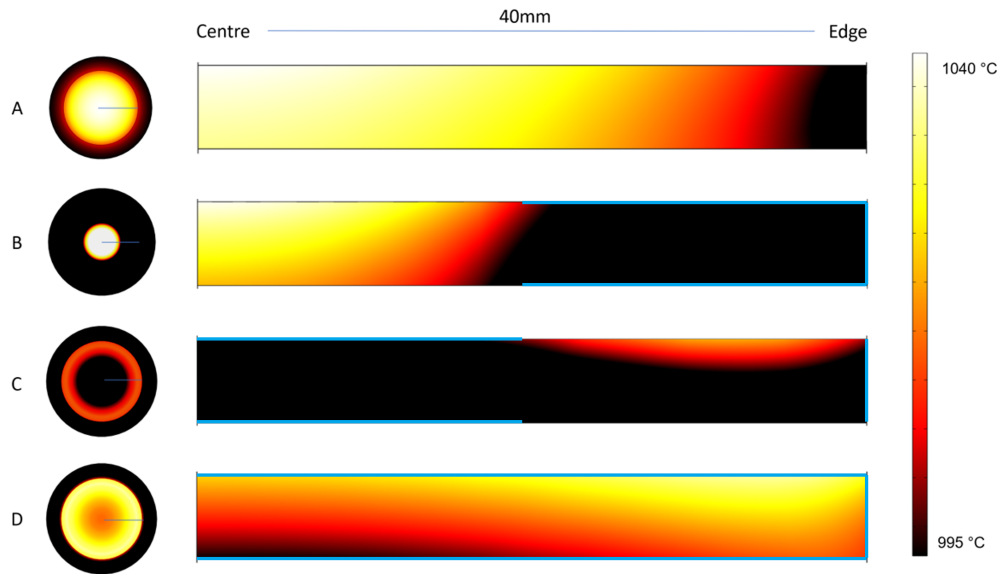


FIGURE 5.4: Left - Temperature cross sections of simulated region of interest at maximum temperature for BN insulation (blue) configurations. Right - 2D axisymmetric display of the sample regions thermal distributions in both Z and R for A - Control, B - Aperture, C - Reverse Aperture, D - Full samples

5.3.1 Characterisation

The samples with a dwell time of 20 s were a snapshot of the very early process with regions of sub, and super transus clearly visible upon etching certain samples, (see Figure 5.5). However, after later processing with MIPAR, we found that there was no major region where the prior β average grain diameter was differentiated by more than $20 \mu m$. This was expected to some degree as there was not enough time above the β transus for the grains to grow significantly. Though now with this quantitative knowledge a timeline to the growth of these super transus grains can be provided in relation to their applied temperature. Given the size of grains that were observed, there was some correlation to that of the initial powder size, demonstrating that with limited time post consolidation, the microstructure is 'penned in' by the initial powder size in the early stages of sintering and must be considered in future trials.

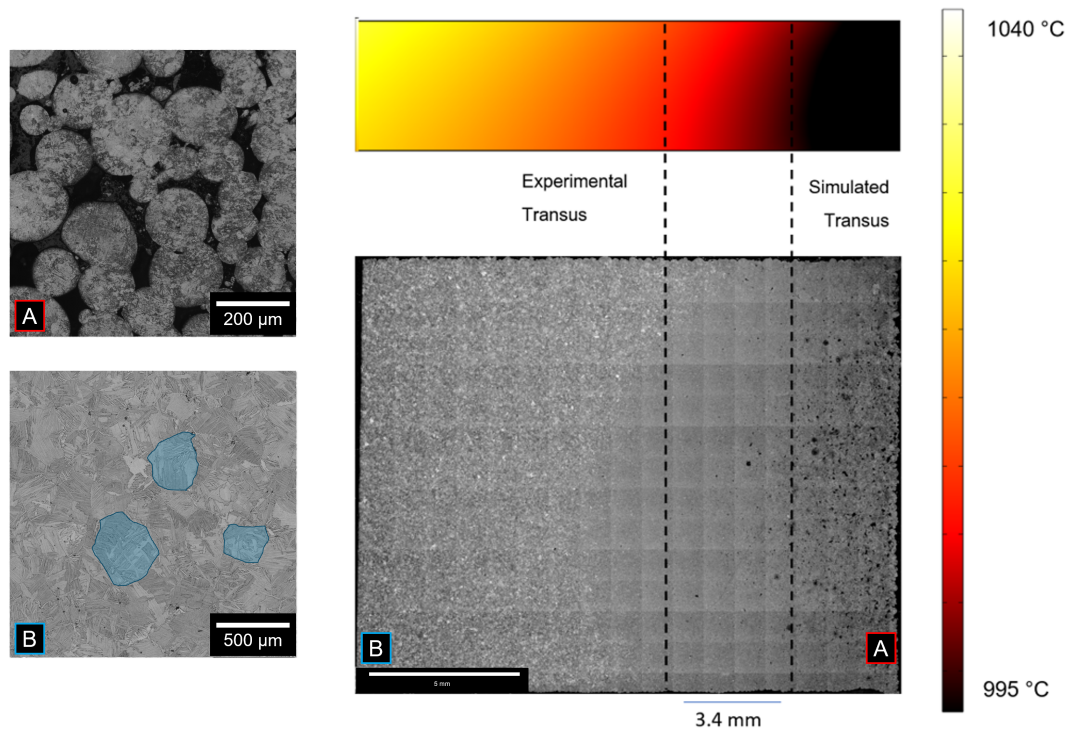


FIGURE 5.5: Right: Sample transus line separating equiaxed α particles (A) and prior β regions (B). Right: grain structure visible on the etched Aperture sample (examples highlighted) with a qualitatively similar angle in simulation.

In some samples, once etched, a clear boundary exists between regions of the sample that were above the β transus during processing and regions below the β transus. Regions that experienced temperatures above the β transus exhibit large β grains due to the reduction in surrounding α phase to restrict grain growth due to the transformation from α to β that occurs at and above this processing temperature. For the Aperture sample, the simulation predicted this feature at 19.5 mm from the edge, and in reality it was measured to be 21 mm. A spatially resolved error range of $\pm 7\%$ in this case, which is remarkably precise for this kind of application, especially as most industry applications would be this size or larger. This would imply that the expected 50 degrees gradient over the 20 mm length of the sample is also accurate, providing significant potential for control and prediction in future work. The relative homogeneity in the Full sample when compared to the Control samples also leaves much promise for the potential to reduce the issue of existing temperature gradients in large scale production, maximising potential yield and minimising subsequent machining operations for a 'right first time' approach.

For the samples with 5 min of dwell¹, a significant increase in this average grain diameter was seen from the samples at 20 s dwell. With variations of over 100 μm average grain diameter within a sample the more subtle transitions in grain size due to temperature have become far clearer and may now be compared to the simulated values for more detailed validation of the predicted temperature profiles. For this analysis the OlympusTM microscope and ClemexTM software were used to generate micrograph mosaics with individual images of increased magnification to examine the grains in more detail. These were run through a 'recipe' generated in MIPAR which determined mean grain size through pixel count, and the resolution of images from the microscope. This 'recipe' was a series of image refining steps attached to the tail end of the deep learning algorithm that were trained on other sample images from the same material system.

¹Considered here to be a minimum for the practical use of this material to ensure full consolidation and grain growth

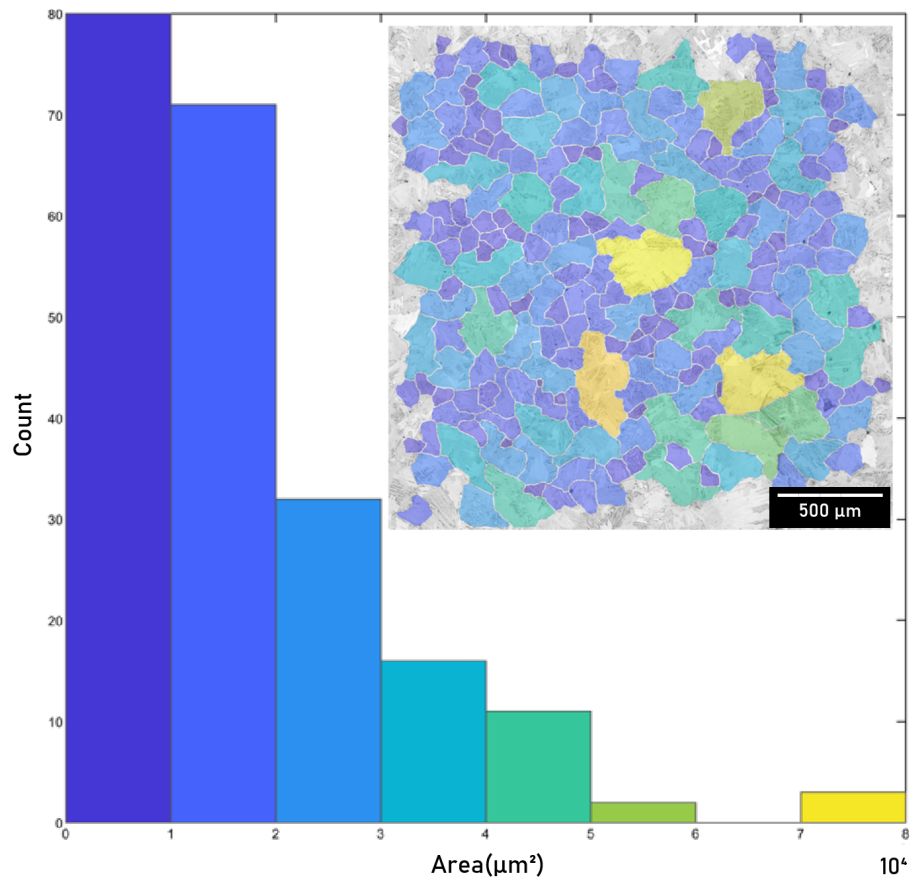


FIGURE 5.6: Insert: Overlay of the detected grains from MIPAR onto the original image (Top Right). Main: The associated histogram of output data from the measurements of the insert image, creating an average value and a range.

This histogram data was averaged and the results plotted graphically for each micrograph in a grid with 1:1 representation to the fully imaged sample's mosaic structure. A script written in Python was then employed to plot the data and visually determine any trends and likenesses to predicted patterns from simulation.

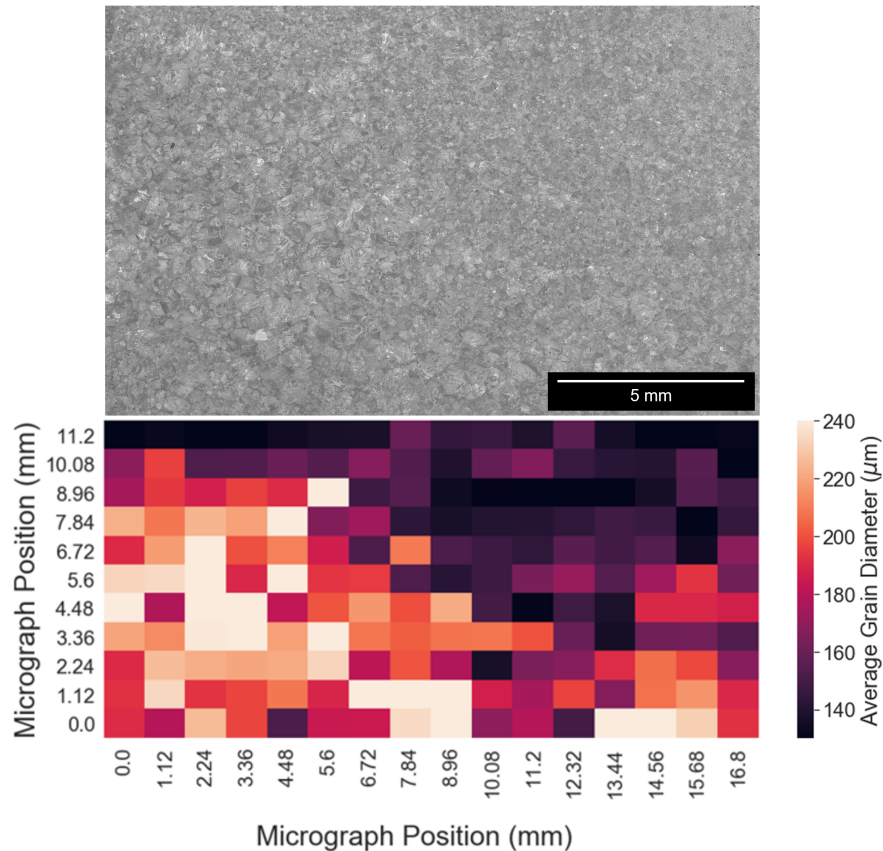


FIGURE 5.7: Top: A cropped mosaic micrograph of higher resolution images from the Aperture Sample 5min Dwell. Bottom: MIPAR results plotted as raw data. Each square displays the average diameter of the grains detected within that micrograph from the mosaic above.

We assumed spherical grains for calculation purposes knowing that this would average out statistically for a large number of grains, though the compaction process deforms the initial spherical powder, visible in Figure 5.6. Then an average grain diameter was obtained for comparison to our previous PSD where the particles were shown to be initially spherical as well as the sintered samples. As visible in Figure 5.7, the raw data is difficult to visually parse through the noise. We believe this noise to be a statistical effect from the combination of slicing through randomly distributed planes of each 3 dimensional grain, in addition to non uniform grain growth during the sintering process. Therefore, a moderate Gaussian blur effect of $\sigma^2 = 2$ within Python was also applied to more clearly define trends for direct visual comparison with simulated data. Further to this, the data was interpolated to a set of 1000 by 1000 points for smoothing of the resulting image. This trend analysis technique has not been carried forwards in any quantitative work however (as

found in the previously cited work) the Gaussian blur has significant impact on the quantitative numerical outputs. It is in essence, a useful false colour image used for comparisons/validations with our temperature distributions.

5.4 Discussion

As mentioned, during sample preparation the 80 mm samples were cut into sections, resulting in some material loss, represented below with the white space between the samples. Additionally, during image analysis, part of these micrographs were cropped to avoid edge effects, accounting for the differences in scale. As such, in the qualitative comparison images of the 4 samples the thermal distributions have also been appropriately cropped to match their practical counterparts. Figures 5.8-5.11 show the raw values of average grain diameter determined through the MIPAR deep learning above the processed images for comparison with the thermal distributions below. This allows us to qualitatively compare the effect of varying temperatures spatially on the resulting grain growth of the β phase. It is expected that with greater available energy above the β transus temperature, grains will show a corresponding increase in size. Some statistical variation is expected from two factors; the first being the distribution of grain sizes which naturally exist across a sample, and secondly, the influence of the cut depth. This references the location sectioned, and material ground during preparation, affecting the plane of the individual grain being sampled. The quantity of grains analysed has minimised some of this statistical variation, and for the purposes of qualitative inspection, the image processing further reduces this factor.

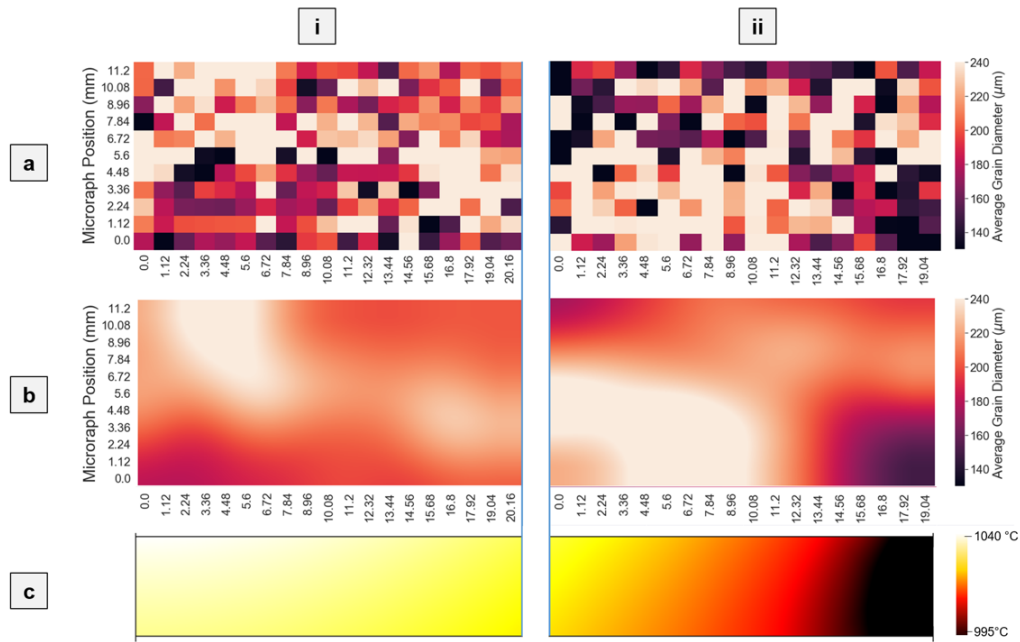


FIGURE 5.8: Control (Sample centre left (i) and edge right (ii)) - Raw (a) and processed (b) grain size distributions compared to the predicted temperature profiles (c) from Figure 5.4 demonstrating the correlation between heating and resulting grain size. Unexpected spots of grain size variance approximately $30 \mu\text{m}$ in scale.

This sample, prepared without any insulation, demonstrates a reasonably homogeneous outcome both in simulation and measured grain size. However, there is a region close to the edge (ii) where a lower grain size region is noticeable. Predicted to a very accurate degree by the simulated thermal profile (c), this region contains grains which are not significantly larger than the initial powder size distribution similarly to the 0s dwell samples mentioned. This implies that the region only reached the transus temperature of 994°C for a brief period in the 5 minute dwell, possibly due to thermal overshooting caused by the high heating rate. Figure 5.8 also demonstrates the statistical variation discussed, especially in respect to the noise in the raw data (a) and the 'hot spots' noticeable in the processed images as well as the original micrographs. This could be the result of some localised chemistry, potentially with a lower oxygen content reducing the β transus slightly as oxygen is an α stabilising element and increases the β transus. Additionally it could be due to localised heating during early stages of the sinter causing early compaction, allowing more time for the grains to grow, unpinned by the particle boundaries. Overall, however, the trends show a remarkable degree of correlation and likely causation, demonstrating

the predictive capabilities of the model.

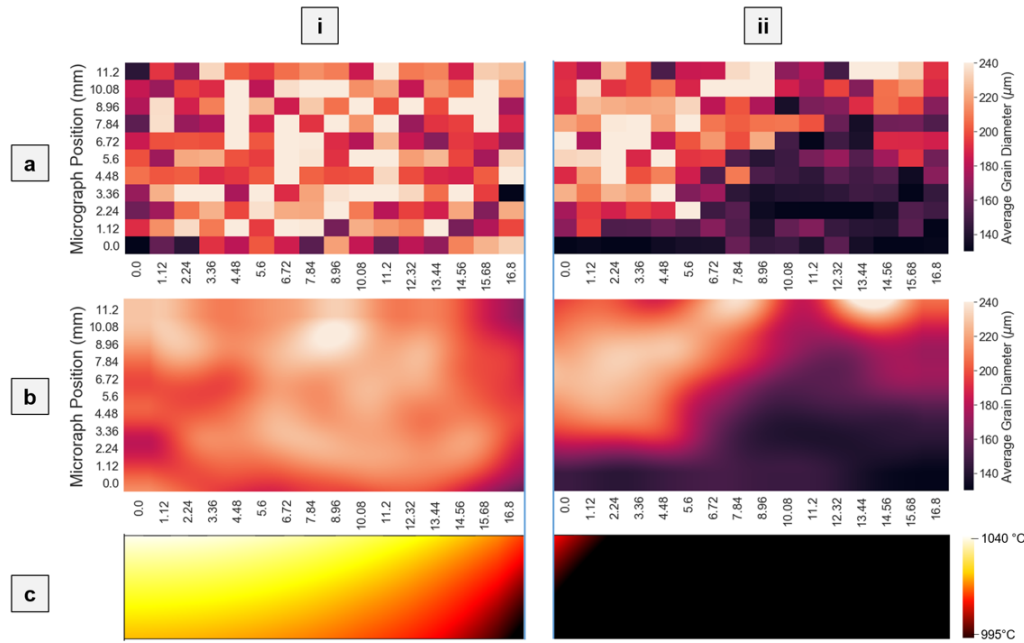


FIGURE 5.9: Aperture (Sample centre left (i) and edge right (ii) - Raw (a) and processed (b) grain size distributions compared to the predicted temperature profiles (C) from Figure 5.4 demonstrating the correlation between heating and resulting grain size. This shows a very accurate overall trend, though the expected line of transus falls 7 mm short of its predicted location.

When compared to the Control sample above, the Aperture sample, with insulation around the edge of the sample (ii) region depicted with insert B in Figure 5.2 has a much more severe thermal gradient (c). This is caused when the insulation forces the current path to shift preferentially through the centre of the sample (i). Potentially increasing the current density in this region by up to a factor of four depending on the permeability of the BN layer. With this additional current, further Joule heating is expected and localised in the central region and with the pyrometer measuring from a point closer to this area than the edge, the distribution becomes more severe. There are fewer 'hot spot' regions in this sample, implying a greater degree of homogeneity in this central heated region than the uninsulated sample provides from the concentrating of heating.

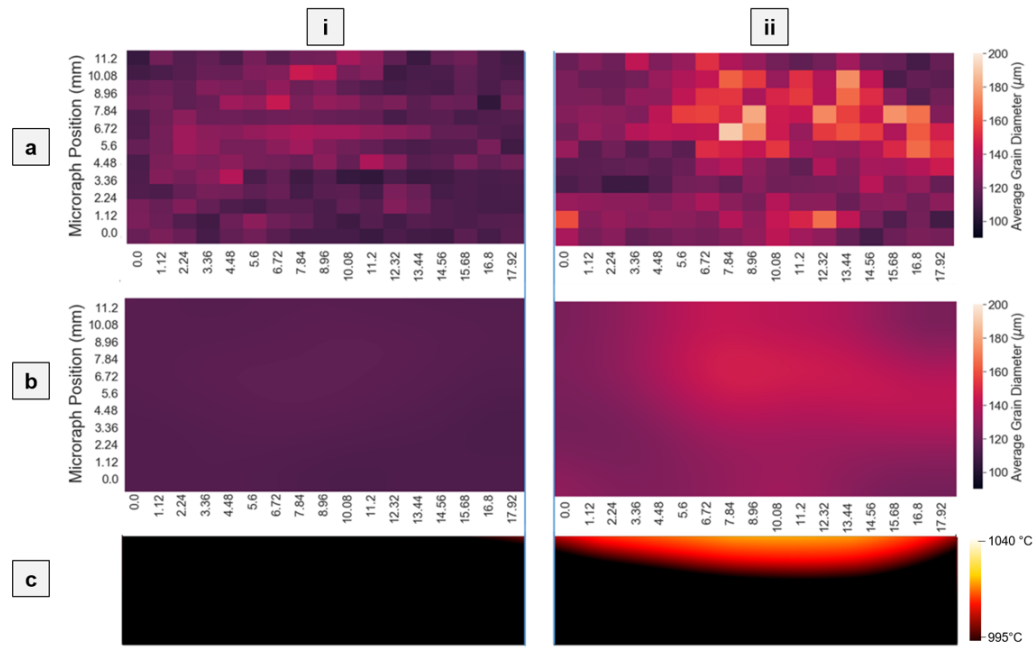


FIGURE 5.10: Reverse Aperture (Sample centre left (i) and edge right (ii) - Raw (a) and processed (b) grain size distributions compared to the predicted temperature profiles (c) from Figure 5.4 demonstrating correlation between heating and grain size. This accurately predicted the temperatures being too low to cause significant grain growth in the majority of the sample.

The reverse of the Aperture sample shows an interesting result that was initially unexpected. It is much colder than the other models and shows it with an average grain diameter 40-60 μm lower even in the higher temperature areas. This is somewhat unintuitive as it was thought that it would appear as an inverse of the Aperture result. However, from the simulation, it appears that the heating occurs primarily in the tooling on the side of the pyrometer. This heat travels through the tooling to the sample edge and pyrometer similarly quickly, and therefore, the heating will slow, or even stop when the desired temperature reaches both points. This will lower the sample's experienced temperature for an equivalent pyrometer reading to the other models as seen in the experimental results in Figure 5.10. It demonstrates the importance of pyrometer location in relation to the direction of current flow and reveals interesting possibilities for this new variable using these insulation profiles.

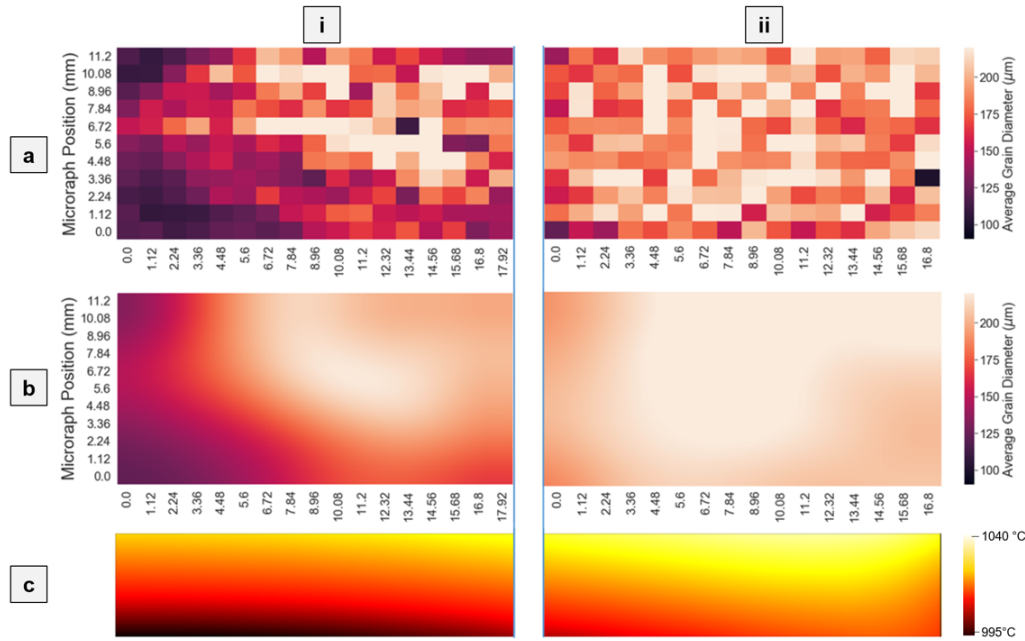


FIGURE 5.11: Full (Sample centre left (i) and edge right (ii) - Raw (a) and processed (b) grain size distributions compared to the predicted temperature profiles (c) from Figure 5.4 demonstrating the correlation between heating and resulting grain size. The trend again appears to fit the profile very well with the most homogenous large grain growth at the sample edges.

For the final insulation profile the overall temperature profile has completely reversed, with the centre (i) being at a lower heat than the edge (ii). It also seems the most homogeneous with respect to grain growth of the 4 samples even visible through the noise of the raw data (a). As visible here and in the other samples, the trends seen in the MIPAR data have a strong spatial correlation to the predicted thermal gradients across the samples with positional accuracy greater than initially hoped for on this 80 mm scale. These average grain sizes and their respective simulated temperatures can then be sampled to produce a quantitative graph of this correlation at these conditions. Looking at these values, we can compare them to previous studies by Semiatin et al. [178] where for powder with initial diameter of $40\ \mu\text{m}$, prior β grain diameters of between 200 and $300\ \mu\text{m}$ were found for peak times and temperatures only 20°C higher than those reported here. Although no lower temperatures were examined in these works this quantitative match provides additional support for our findings. It should be noted though that this graph is limited to this material system, processed under super transus conditions with similar $\alpha - \beta$ chemistry. Although this limits the broader impact, it still maintains great

utility for further work and for similar systems. It also demonstrates possibilities for its application in an industrial setting where similar materials systems are used regularly, and optimisations are impactful.

Although it was most obvious in the Reverse sample, all the samples also demonstrated some sensitivity to the direction of current flow and pyrometer position with the upwards facing gradient of their β transus angle, red to black transition. This is as thermal equilibrium of the system varies depending on the insulation profile, the actual temperatures reached within the sample depend on the recipe, controlled by the pyrometer. If the pyrometer is measuring from a region where the thermal distribution is colder then the average temperature in the hotter regions will be higher and vice versa; this is an issue with both thermocouple control and surface pyrometers which may be remedied with some simulated knowledge of the internal system. This correlation is important, as with different geometries it could lead to unexpected gradients at the process scales in complexity. This will be important to consider going forwards as a qualitative observation, but more quantitative results are possible here too.

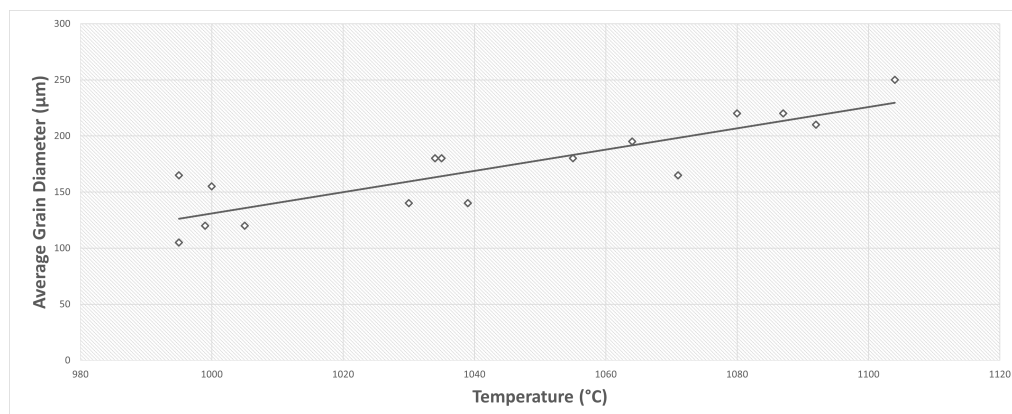


FIGURE 5.12: Ti-6Al-4V sintered super transus grain growth plotted as average grain size against highest predicted temperature for a 5 minute Dwell. The sampling was done pseudo randomly and shows a good fit linear trend.

The plot above is simply generated from a direct quantitative comparison of pseudo randomly sampled points from all 4 tests (Figures 9-12), and shows strong predictability using this technique. It can certainly be said that it has a clear visible

correlation, and with an R^2 value of 0.75 it shows a quantifiable trend within this dwelling period. It also makes an obvious case for this analysis route to be tested further on other systems, and through other processing/sintering conditions. In future work this process can be further tuned, and a solid predictive tool generated to advance the 'right first time' approach which has recently become so sought after in powder processing, and specifically SPS/FAST. For example, with a different sample size, or insulation profile, a new thermal gradient can be simulated. Then in advance of creating the sample this gradient can be adjusted such that the temperatures, and thus grain size distributions, fit the desired outcomes.

One such example is with the scaling of the technique, not only in diameter but also in height. As is visible even in these samples of 20 mm thickness there is some thermal gradient in the Z axis in addition to that in R. This is an issue which scales problematically with size requiring significantly more energy than previously to reach desired temperatures and occasionally causing undesirable microstructures to form. It is hoped that with simulations like this and a database of grain growth information it will be possible to minimise, or even remove these gradients in some cases, before the sample is even created. This would result in the saving of significant quantities of material, time, and energy at scales larger than that of a laboratory.

It is likely that for this purpose, an energy map, in addition to this temperature plot in Figure 5.12, based on the power and time used in the dwell period of the sinter, could be of sufficiently broad use but was not within the scope of the work here. Certainly if a larger range of sizes and temperatures is investigated in future to ascertain a more definitively widely applicable grain size prediction tool, a map of this nature would be invaluable. Additionally, some small scale particle simulation or a grain growth model could be created for further validation and predictive capability, and both ideas are strongly recommended for future efforts.

5.5 Conclusions

An expansion on a previously under explored technique for FAST processing has been tested on a common titanium alloy to examine the potential for impact and control over the final microstructure in a single step process. It has been shown that, with the help of an accompanying FEM simulation, remarkable thermal gradients of over 100°C are possible and designable, even within the relatively small scale of an 80 mm test sample. The analysis of this revealed that prediction and spatial control of the final microstructure is resolved down to a few millimetres, with the size of grains produced being predictable within a defined error range provided some previous knowledge for the material system. With this technique it may also be possible to sinter dissimilar materials more easily with varying consolidation points, or perhaps design and create non-homogeneous microstructures to suit a pre specified function. Perhaps more simply, and excitingly for the industry which has recently shown more interest in this technique it also holds great potential to balance any concerns with thermal gradients and increase homogeneity in samples greater in scale. With minimal addition to the existing process, increasing the yield efficiency of the powder to create useful material prior to further processing is possible.

Additionally, with the Reverse sample, an important feature of the process, in the location of a pyrometer in relation to the flow of current, was highlighted for its impact on resulting thermal gradients. It has been noted from the model that this is likely to become significantly more prevalent for larger scale samples in future.

Finally, the use of MIPAR for the purpose of analysing titanium super-transus prior β grains has been demonstrated, along with its utility for obtaining information of this kind on a large scale. This allows for potential further scaling of this analytical technique for spatial resolution to the largest samples we are currently able to produce, at 250mm diameter, with much less effort than a manual approach would require. It also will allow for the measurement and therefore potential control of the Ti-6Al-4V α microstructures which are the most sought after for operational components in aerospace, provided sufficient resolution on the mosaic micrography.

There is also potential for this technique and the level of control it can provide to be useful for material systems without solid state transformations such as seen here or those of mixed composites. Some examples provided here include, the Ti-TiB system for ballistic applications or for the creation of designed porosity for functionally graded properties in metal or ceramic systems.

Chapter 6

Current Control At Scale

This chapter consists of content from a conference paper under review for World Ti 2023, titled "Titanium / Titanium Boride Composite Field-Assisted Sintering Technology (FAST) Process Mapping For Potential Armour Production", and a paper which has been published in the Journal of Materials Science and Technology, titled "Microstructural Examination and Ballistic Testing of Field Assisted Sintering Technology (FAST) produced Ti-TiB₂ FGM composite armour plates". Some modifications have been made to fit the style of the thesis, however these self-contained publications will be mostly unmodified from versions currently published. There is therefore some inevitable overlap in content within this thesis which cover similar methods and conclusions.

6.1 Introduction

A demonstration of this techniques effectiveness on another material system would prove beneficial to its validity, and as such a titanium based MMC was chosen here for its additional practical demonstration capabilities in a real world setting. Additional background and material characterisation is included to better understand the resulting microstructures and their reliance on the thermal gradients simulated and generated in the process.

There is an increasing use of armour piercing projectiles globally constituting a significant threat to life. This is most concerning for wearers of body armour and to lightly armoured vehicles and new materials must be developed. These must have high hardness, fracture toughness, elastic modulus, as well as the highly desirable multi hit capacity. This is to say that the material must be able to withstand multiple

impacts without too great of a loss in these important properties [179], [180]. In such materials, the high hardness of ceramics is combined with the ductility of metals to produce a balance suited for purpose.

The previous candidates in this category include several ceramic systems, including B_4C , SiC , Al_2O_3 , and TiB_2 / TiB . These materials remain high on the list for light armour applications due to their low density, reliability, superior hardness, and energy absorption capacity. However, despite their high impact velocity and deformation induced hardening increasing their resistance to the initial shot, they shatter on impact [180]. This shattering can in fact further aid in increasing the impact resistance of the material by abrading the projectile, though it does make the multi-hit capability challenging to obtain. One solution to this over the years which has displayed greater protective capabilities has been the introduction of metal matrix composites (MMCs) which contain both ceramics and metals, specifically in the form of a composite material with fibres or particles dispersed throughout a metallic matrix. Many of these such systems have been studied and one of the most promising is the Ti / TiB MMC [181], [182].

TiB as a ceramic offers many of the required properties as an armour material, however, full consolidation of this material requires dwell times of 20-30 mins at sintering temperatures of 1500-1900°C under pressures of 40-70 MPa [183]. However, it was discovered during this work that for lower compaction pressures, temperatures in excess of 2000°C were required to achieve similar densities. Conditions that currently would cause melting in the combined metal matrix, or at least adversely affect the mechanical properties from microstructural effects and interfacial reactions. This is especially true for titanium which experiences large grain growth above the β transus temperature of 1000°C [184]. This has previously been attempted to positive effect in work by Gupta et al. [185] where it can be noted that this explosive grain growth has been avoided at 1500-1600°C, from a grain pinning effect of TiB inclusion. Titanium has, in spite of this concern, been chosen by many for this system as the metal partner as it does provide significant toughness to the system whilst, most importantly, having a similar density and coefficient of thermal expansion to

TiB₂ and is therefore thermomechanically compatible with minimal separation on cooling with no internal cracking. It additionally provides more titanium for the ceramic to react with to form the desired TiB needles, further strengthening the system.

In this work, fully dense 20 mm and 80 mm diameter Ti-3Al-2.5V discs were initially produced using field assisted sintering technology (FAST) with stepped functional grading. Testing used 0, 6, and 9 wt.% TiB₂ powder, for material testing and process mapping between 900°C and 1400°C for up to 6 hours. Subsequently, 250 mm diameter Ti-6Al-4V discs were produced using FAST with the same stepped functional grading using the previously acquired data for prospective application in armour plating. The in-situ generation of a significant quantity of high strength, ceramic TiB needles was confirmed for the samples and the plates were ballistically tested to attain indicative V₅₀ values, in addition to a microstructural examination. The ballistic results indicate a superior behaviour to the monolithic titanium alloy plates without TiB₂ additions. This is encouraging as hot isostatically pressed Ti-TiB composite systems have previously been tested and demonstrated poorer performance.

Current control, which involved the implementation of a boron nitride mask to direct the flow of current, described in the previous chapters, was also utilised for one sample as a final test of the technique and model at scale. A predicted thermal profile was also generated using finite element modelling (FEM) to demonstrate the thermal sensitivity of the plates, ability to scale the simulation accurately, and the importance of the digital twin simulations. The technique has a significant spatially resolved impact, which has been demonstrated to be from the resulting thermal gradient. The billets were consolidated using field assisted sintering technology (FAST) to demonstrate the capability to generate unique microstructural solutions to real world issues. A previously unmentioned benefit of the technique is the ability to combine similar and dissimilar materials in a single step, and this is taken advantage of here to layer specific depths of the three TiB₂ powder concentrations for a potential purpose as an armour material. This work has been focused on the TiB [186] and titanium system created from this layering as a type of Metal Matrix Composite

(MMC) armour ceramic in the form of a Functionally Graded Material (FGMs).

A FGM may be visualised as a stack of these metal matrix composite layers with varying concentrations of the ceramic particulate. The differing mechanical properties of each layer may be decided upon in advance to create a bulk performance suited to the needs of the task. In this case the high hardness of the ceramic elements may provide impact protection on the surface, while the relative ductility of the titanium alloy matrix allows for the absorption of the incoming energy and material on the rear face. This has been examined in several previous works [187], [188], and progressed in this work using previously cold milled powder allowing the combining of these elements on a much more refined scale, allowing for a homogeneous structure to be formed in a single sintering step akin to the work by Singh et al. [189]. In addition, only low percentage ceramic inclusions are used with the intent of reducing fabrication difficulties from high temperature requirements and promoting the growth of TiB needles through the TiB_2 + titanium reaction in situ [190] to increase fracture toughness resistance [191]. The growth of such needles has been demonstrated before using an annealing process, over a period of up to 50 hours [192], [193]. They possess no obvious preferential orientation from the FAST process and a hardness multiple times that of the underlying titanium substrate. As such it is expected that their presence will provide several additional barriers and hard/soft interfaces for the projectile and resulting cracks to encounter, further increasing the ballistic performance.

The generation of these needles has been demonstrated before in this material composite [194] and using an annealing process, commonly over a period of 5-50 hr [195], as well as through in-situ spark plasma sintering (SPS) [196]. They possess no preferential orientation determined in this work, and previously noted by Feng et al. [188] from elemental generation, and a hardness multiple times that of the underlying titanium alloy substrate. As such it is expected that their presence will provide several additional barriers and hard/soft interfaces for the projectile to encounter, increasing the ballistic resistance performance further. This has been mentioned in previous work [197], which also postulated that the presence of non needle form TiB

would in fact weaken the strength and fracture resistance, a potential target of this work is to provide a more quantitative relationship, or practical demonstration for this. Mechanistically, these needle shaped TiB grains increase this fracture toughness through the crack deflection, pull-out and the micro-fracture of the TiB seen and discussed in [198].

This system has previously been tested in either a bilayer design [185], though with significantly less impact from any needle generation due to the much larger concentrations of TiB₂ at 80-90 wt.%, or in other works with much higher percentages of ceramic inclusions up to 95 wt.% [199]. In both cases the benefits of using FAST remain, with the shorter sintering times and temperatures to produce the same, or improved, effects as other techniques such as HIP. It also assists in reducing the generation of large residual stresses and pores in the material which negatively impact the ballistic properties [200]. The study also suggested that low magnitude residual stresses can enhance the anti penetration performance making FAST even more promising for armour production. The current control technique has been utilised here to push the gradients to an extreme in one sample so as to examine the thermal sensitivity impacts on this more complicated microstructure and its ballistic feasibility. It is hoped that with this, in addition to testing the effect of ball milling lower percentages of ceramic for this purpose at scale, the thermal gradient impact can also be examined here which will prove to be an interesting challenge moving forward to using systems like this.

6.2 Methods

Additional methods and relevant data from these papers has been included here as more specific to the chapter, whilst general information and methodologies can be found in the previous chapter 3.

6.2.1 Powder Production

Initially the base titanium powder, Ti-6Al-4V and TiB₂ ceramic were chosen due to their compatibility with each other and complimentary properties for the task as mentioned previously. In addition, the TiB₂ titanium reaction providing TiB needle growth is expected to be very beneficial if homogeneously dispersed throughout the microstructure. To achieve this the powders were processed at Materion (Farnborough, UK), producing 3 wt.%, 6 wt.%, and 9 wt.% TiB₂ powders using a proprietary ball milling process using both the grade 5 ASTM standard titanium alloy powders and TiB₂ with example BSE images of the resulting blend pictured in Fig 6.2.

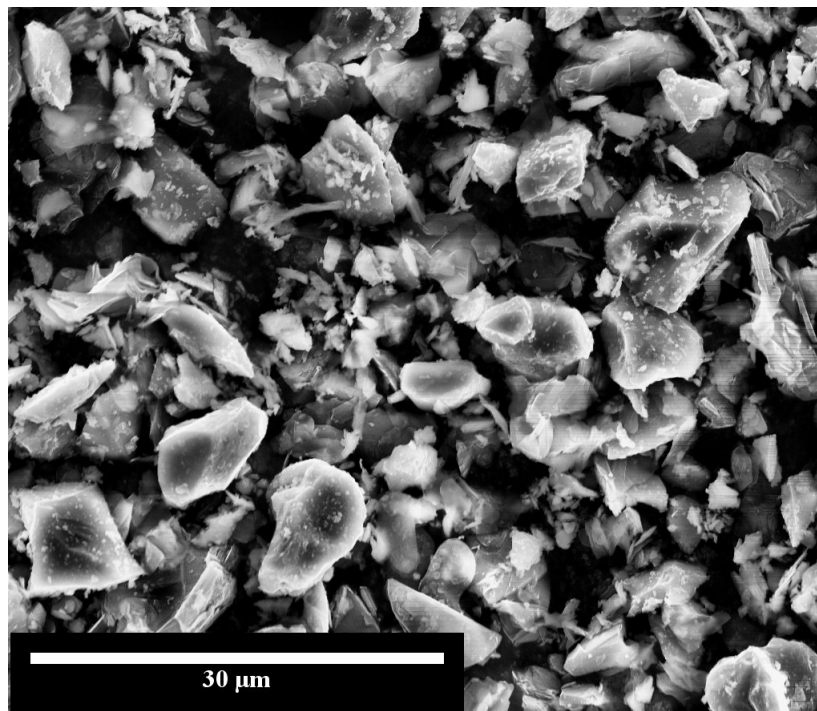


FIGURE 6.1: Secondary Electron SEM image of the TiB₂ un-milled powder.

The microstructure and morphology of the initial hydride-dehydride (HDH) Ti-3Al-2.5V powder which was cold milled with 6 wt.% of TiB₂ is shown in Fig 6.2 and Fig 6.1. A portion of the particles have been very well seeded (a.ii) while other HDH particles seem to be almost entirely untouched (a.i). It is believed that this is due to trapping of the TiB₂ between the titanium powders via a cold welding mechanism during the milling process. This is especially visible in the larger particles like those pictured in Fig 6.2(a).

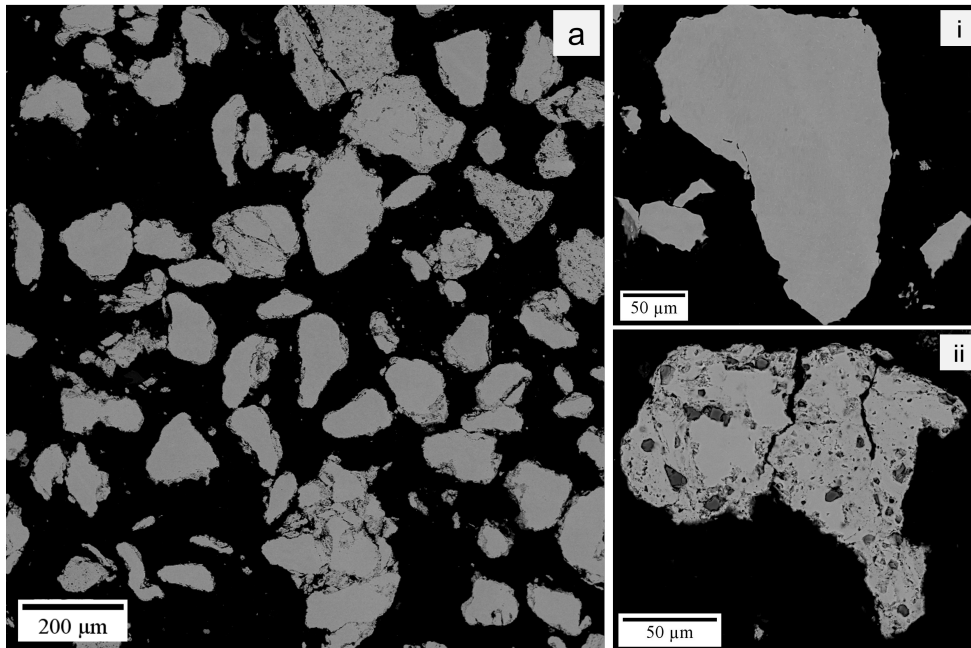


FIGURE 6.2: BSE image of (a) the HDH Ti-3Al-2.5V with 6 wt.% TiB₂ milled powder; (i) HDH Ti-3Al-2.5V particle unseeded and; (ii) HDH Ti-3Al-2.5V particle seeded with TiB₂

The powder size analysis was performed using a Malvern Mastersizer 3000 laser diffraction particle size analyser with a wet dispersion method. A total of 3 repetitions were conducted to confirm results and the D10-D90 scale was found and displayed below.

TABLE 6.1: PSD results of the analysed powders for sample creation demonstrating large variance in size and oversized nature of the rough topography powders

Powder	D10	D50	D90
Average of Ti-6Al-4V	60.4	112	191
Average of Ti-6Al-4V 3 wt.%	73.4	213	542
Average of Ti-6Al-4V 6 wt.%	83.4	240	612
Average of Ti-6Al-4V 9 wt.%	62.6	157	378

6.2.2 Sample Sintering

These samples were initially laid up in 20 mm discs split into two equal layers, pressed to 35 MPa and heated at a rate of 100°C/min to dwell temperature in the

FCT Systeme GmbH Spark Plasma Sintering Furnace type HP D 25. A range of temperatures (900, 1000, 1200, 1300, 1400°C) and times (10 min, 30 min, 1 hr, 2 hrs, 6hrs) for this dwell period were tested where deemed productive for additional consolidation and needle growth. They were then laid up in functionally graded stages from 0 to 9 wt.% TiB₂ inclusion with the aim to generate a high hardness - high ductility interface depicted in Fig 6.3 before being sintered.

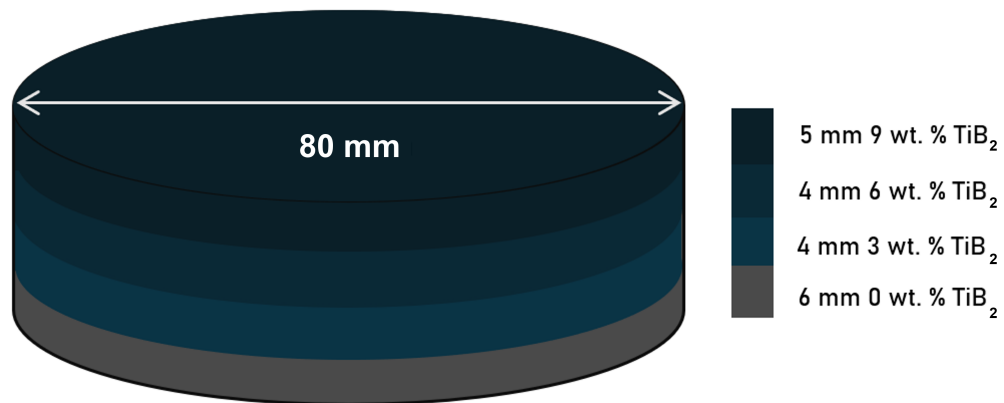


FIGURE 6.3: Diagram schematic of the as sintered layers of the FGM Ti-3Al-2.5V + TiB₂ system powders in this 80 mm diameter sample with a final height of 12.5mm.

An 80 mm sample was then also produced under the previously determined conditions from this process mapping for needle growth using the same parameters. However this had been produced with five layers (9 / 6 / 0 / 6 / 9 wt.%) to test for any potential directionality in the process from the flow of current, as well as testing the scalability of the material system to the size limits of this machine.

The hardnesses of the samples were then finally tested using the Vickers method at a pressing force of 1 kgf in each of the layers as well as each of the bonding zones. There were several repeats for each of these tests to average out the presence of differing quantities of needles and TiB in each. Ranges were presented with the data to represent this variability.

6.3 Microstructure Optimisation

Initially, 20 mm samples were processed according to previous work by Singh et al. at 1200°C for 2 hrs to demonstrate the materials would in fact create the needles under FAST conditions. Fig 6.4 shows an example of these needles grown in situ during the sintering process of “significant length” at differing magnifications. This term refers to needles longer than 20 μm in length as the milled TiB_2 powder would have needed to react and grow to achieve this scale. It may also be noted that these are only the needles which fell in the plane of the cut used for sample prep and many of the shorter examples are likely at an angle to this plane, thus not showing their full scale.

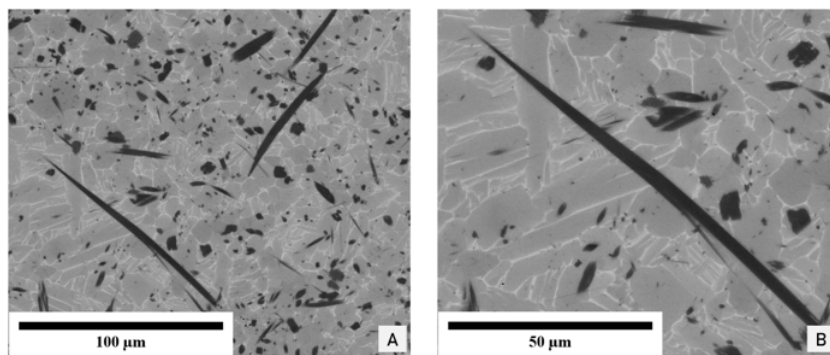


FIGURE 6.4: (Backscattered electron images of TiB needles produced at 1200°C in the 6 wt. % TiB_2 milled powder with the HDH Ti-3Al-2.5V alloy, close to the boundary layer

Several examples of needles were observed under BSE imaging at these conditions; however, it is important to sample the surrounding temperatures to generate a full process map. This map will help with both deciding the most efficient conditions to produce a certain microstructure without waste energy, and to analyse thermal history of further samples.

6.3.1 Process Mapping

The samples for this map were sintered between 900°C 10 min to 1400°C for 6 hrs, at 20 mm diameter, and imaged using SEM. Average needle length, if any were produced, and visual determinations of needle count were recorded within a fixed area.

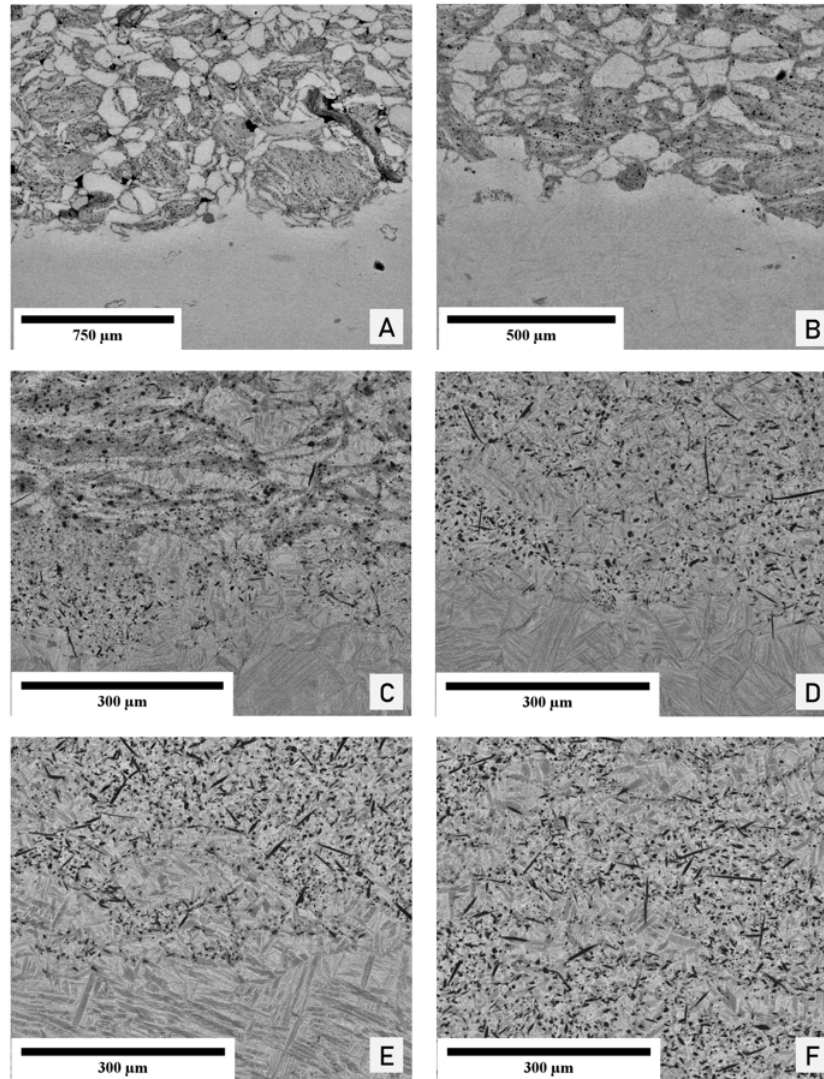


FIGURE 6.5: Backscattered electron images of the 0-6 wt.% TiB_2 boundary layer with increasing energy conditions.

Fig 6.5 shows the 0-6 wt.% TiB_2 boundary layer, with A-900°C 10 min / B-1000°C 10 min / C-1200°C 30 min / D-1200°C 60 min / E-1400°C 60 min). F additionally shows the boundary between the 6-9 wt.% TiB_2 boundary for the 1400°C 6 hr condition. The lack of needle growth at 900°C was expected as, from literature, the lowest temperature noted for the TiB reaction to occur at is approximately 1050°C [201] explaining why no needle production was observed in at 1000°C (B) as well, though with a slight increase in homogeneity. C shows the first production of needles of significant ($>20 \mu\text{m}$) size, primarily on the boundary with the Ti-3Al-2.5V layer, likely due to the more abundantly available titanium to fuel the reaction. However, this

seems to be a thin layer, approximately $100\ \mu\text{m}$ deep and much of the inhomogeneity remains with discolouration in the MMC layer. In D the end of this region of clearly bounded layers in the MMC material can be observed, as well as the first needles of approximately $100\ \mu\text{m}$ length. These needle growths also penetrated far deeper into the material as desired. Fig 6.5 E and F both show notable increases again in both needle density and average length, though it may be noted that this is a significant increase in dwell time and temperature and this level of increase may be considered a diminishing return at this point with very little un-reacted TiB_2 remaining to form or grow additional needles. Overall, the figures demonstrate the increasing homogeneity and needle growth, though at a diminishing rate, as the energy of the system increases. This is demonstrated more clearly by the quantified length and number of needles plotted in Fig 6.6.

It may be noted that the count, whilst dependent on the image in question, seems to plateau earlier than the size, suggesting that almost all of the TiB_2 in the samples has reacted to form TiB at 1300°C 1 hr, but the increase in energy can allow for further growth and penetration of these needles. Small enclaves of un-infused titanium alloy remain even at these high energy processing conditions, as expected when comparing to the powder images from Fig 6.2, and these are potential areas for further homogenisation. However, increasing the processing temperature much further leads to potential risk of partial melting at temperatures of approximately 1700°C with localised hot spots or contaminants from the milling process. It is also possible to increase the dwell time further, but the energy intense nature of this approach would potentially make it impractical for many uses.

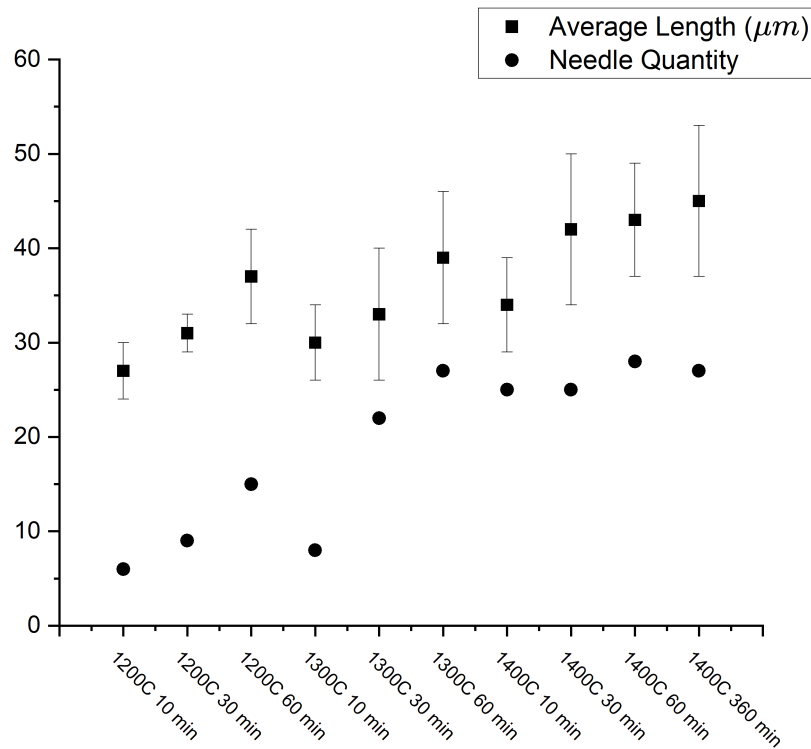


FIGURE 6.6: Graph of needle growth for the process mapping of the Ti-3Al-2.5V + TiB₂ powder system, demonstrating the limited increase in these features with additional processing.

The needle production can be seen to increase consistently past the point at which the energy available is sufficient to start the reaction but slows to plateau at around 1400°C, above 30 min in dwell time. Previous efforts with higher concentrations of TiB₂ have shown increasing results for longer dwell times however, aside from the energy concerns mentioned above, this is impractical with the equipment accessible, and excessive as a relative peak in needle production for these concentrations of ceramic inclusion has already been reached.

6.3.2 Scaled Sample Profiling

Once the process had been mapped at a smaller 20 mm scale, an 80 mm diameter sample was produced on the same machine at parameters which had been determined to produce reasonable needle growth to check feasibility of scale, 1200°C for 10 min. In addition, this sample was laid up as a true functionally graded material, as visible in Fig 6.3, tamping each layer to ensure straight bonds. The 9 wt.% layer

is external as for ballistic purposes this would need to be the attack face for ballistic testing.

Layer Boundary Microstructures

These processing conditions were chosen with the explosive grain growth of titanium alloys in mind once the allotropic transus temperature (β transus) is reached. The intent was to find conditions at which the needles could be grown successfully and homogeneously whilst retaining a reasonably super transus grain structure for the pure titanium alloy layer to retain desired properties such as ductility and strength. However, initial trials with this design demonstrated the microstructure of samples processed at significantly lower temperatures with very little needle growth and very anisotropic distribution in the ceramic doped layers visible in Fig 6.7 A-B.

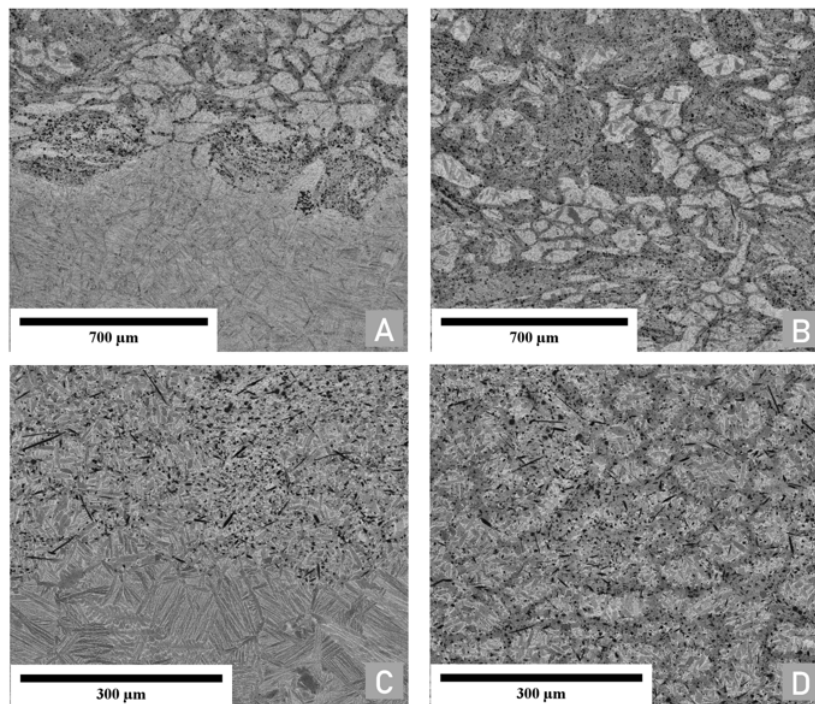


FIGURE 6.7: Backscatter electron images of the 80 mm microstructure at the 0 / 6 wt.% TiB₂ and the 6 / 9 wt.% TiB₂ boundary regions for the 1200°C 10-minute sample (A,B) and the sample produced at 1300°C for 1 hour (C,D).

It is also observed that the increase in energy input has demonstrably improved the homogeneity of the microstructure, though further improvement is possible based

on previous mapping. With this knowledge of a increased energy requirement to achieve the same microstructural results with larger volume samples a condition was selected further along the energy scale of the process mapping. An additional sample was then sintered at 1300°C for 1 hour to ensure the desired needle growth. This adjustment dramatically improved the microstructure at the boundary with the titanium alloy and there was also a significant increase in the isotropic nature of the layers of higher concentration on the faces of the sample. These are displayed in Fig 6.7 and provide strong suggestions that this technique may be used to produce materials within this system on a larger scale for real world applications. It may also be noted that no variation was noticed on either side of the layers, strongly suggesting no directionality to this growth process or diffusion direction dependency on current flow during the sintering process.

6.3.3 Layer Microhardness

The initial 20 mm diameter process mapping test samples were used to check for needle growth, bonding of the layers, and noticeable diffusion during processing. While no diffusion was observed in the bonds visually, the 0-6 wt. % layers, when tested for hardness showed that some had in fact occurred. Fig 6.8 shows for all processing conditions there was a gradient in hardness from the inclusion of the TiB₂ powders. It also demonstrates the variance observed in this diffusion depending on local concentrations and the initial observation of the impact of processing temperature on variance. This variance and diffusion lead directly to the performance in ballistic trials and are important to take note of. This is especially true for the current control sample where thermal variance will be pushed to an extreme.

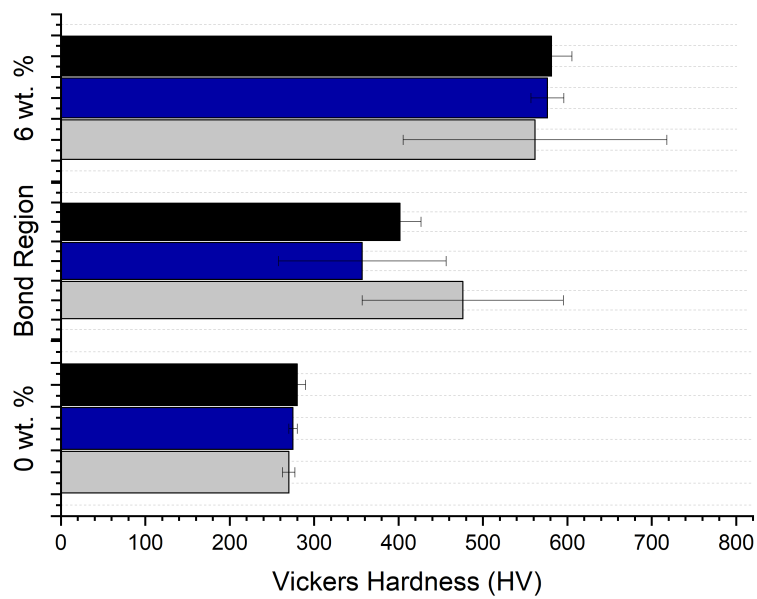


FIGURE 6.8: Grouped bar plots of the microhardness measured from 3 Ti-3Al-2.5V + 0-6 wt.% TiB₂ samples at 900°C (grey), 1200°C (blue), and 1400°C (black)

The larger 80 mm samples were then also tested using the microhardness indenter for quantitative comparison and further validation of the connection between variance in hardness and inhomogeneity in microstructure. The hardness readings were measured, not in a grid pattern within the layers, as previously, but in a diagonal line across the full height of the samples including all layers. These have then been displayed from edge to centre in such a way as to make both centre-edge transitions comparable.

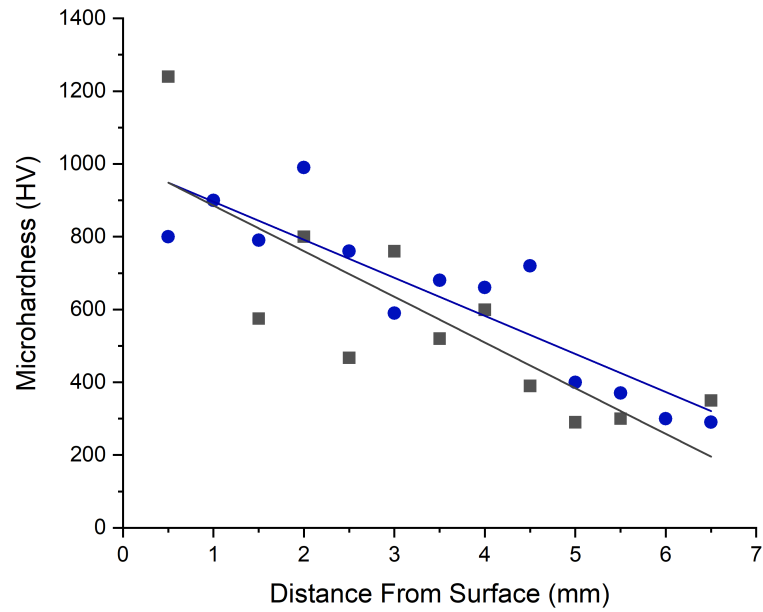


FIGURE 6.9: Microhardness plot of the 1200°C 10 min sample from the 9 wt.% TiB₂ edge to the Ti-3Al-2.5V layer of the 80 mm sample (Fig 6.3).

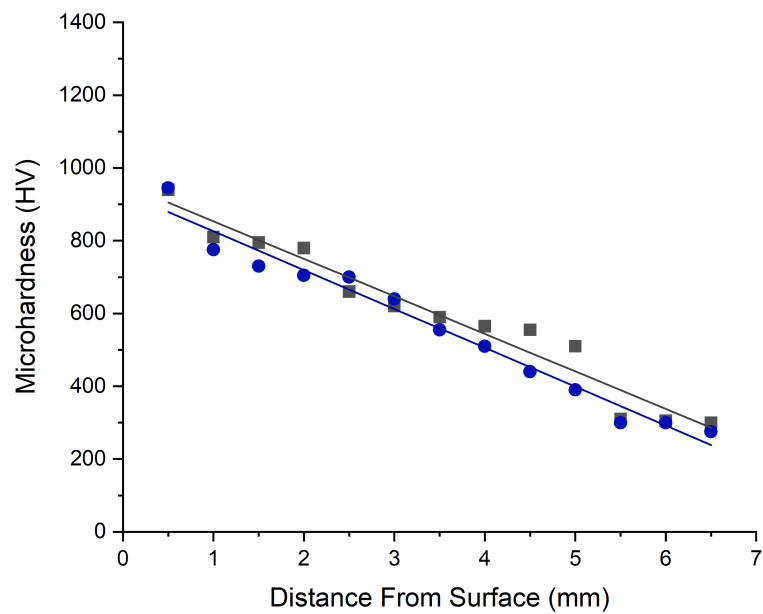


FIGURE 6.10: Microhardness plot of the 1300°C 1 hr sample from the hard 9 wt.% TiB₂ edge to the Ti-3Al-2.5V layer of the 80 mm sample with a marked improvement in consistency from Fig 6.9

Figs 6.9 and 6.10 above clearly demonstrate the inhomogeneity from the microstructure impacting the properties, in this case, the microhardness (HV). As the indenter perceives unreacted, enriched regions of relatively soft titanium alloy or much harder TiB/TiB₂ this results in the high degree of variance noted here in the hardness results. There is a second point to note in these graphs also, that the diagonals were taken from as close to the centre of the sample as possible in both cases. This is important as the radial edges of both samples displayed an average hardness of 10-30 HV lower for the ceramic doped layers at the edge of the samples compared to their centres. This is likely from some small thermal gradients within the samples over the 40 mm distance but could also be some degree of remaining variability inherent in an MMC system like this. More generally, these results are very impressive for only 9 wt.% TiB₂ inclusion given the hardness of the pure sintered TiB₂ system was found to be 2527 HV \pm 50 HV when consolidated at above 2000°C in the same machine.

Discussion

These results, like in previous work, demonstrate in situ growth of these TiB needles but with greater size and distribution than seen previously at these concentrations due to alterations to the processing conditions. Mapping these conditions has allowed us to find optimal processing routes and a larger scale 80 mm sample has been successfully produced, imaged, and tested, demonstrating the scalability of generating this microstructure using FAST. The bonded regions between the 0 wt.%, 6 wt.%, and 9 wt.% regions has also demonstrated a very good level of bonding, allowing for the creation of functionally graded material parts with a reasonable homogeneity throughout each layer. The hardness values also provide good insight into the great potential of this concept for ballistic success at low wt.% TiB₂ infusion through FAST.

Scalability of the process to 250 mm will hopefully allow for further testing, ballistically and from machined coupons. However, it is predicted that the thermal gradients from scale up, seen on a small level at 80 mm, could have an impact on the performance as microstructures from lower temperatures are clearly different

with reduced degrees of strength. This region responsible within the ceramic infused layers of discoloured material is chemically very similar under X-EDS and as is assumed to be caused by minor variations in diffused boron content or other inclusions from the milling process impacting the matrix.

6.3.4 Scaled Plates

These larger plates were made with the same layer design as previously, with knowledge gathered from the analysis of the smaller 20 and 80 mm samples. Due to limitations on powder quantity, two plates were created, one without any current channelling and one with. The goal of the addition of the channelled current here was to create a more homogenous microstructure in the centre and a more inhomogeneous one at the edge. This would allow the thermal sensitivity of the system to be probed, the larger scale simulation to be validated, and the resolution of the CC technique to be examined at scale.

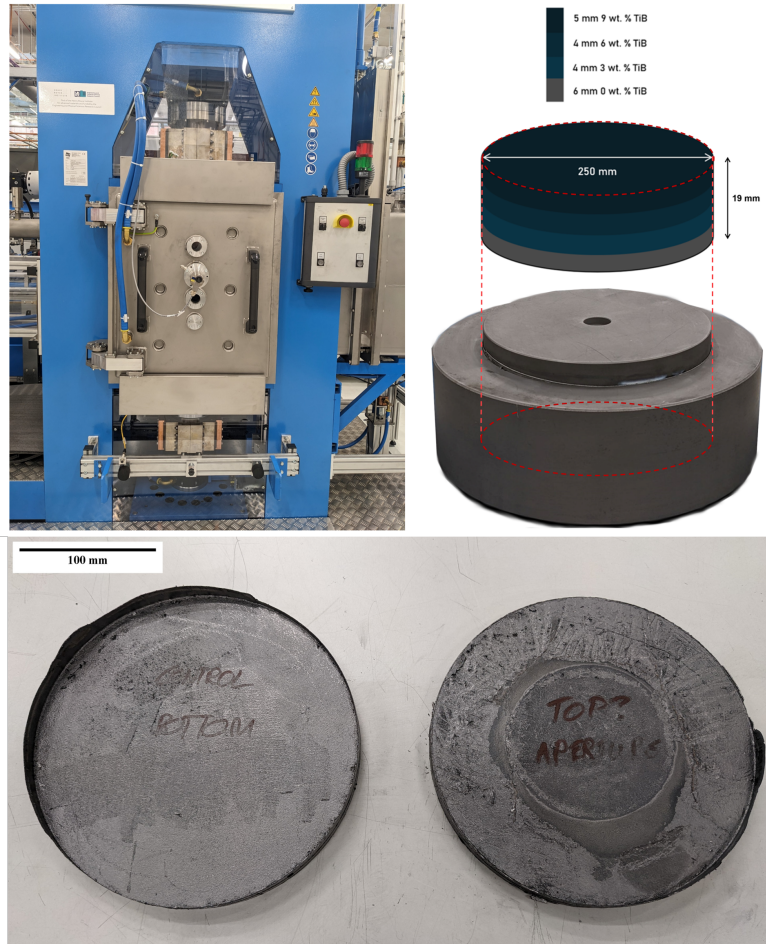


FIGURE 6.11: Top: Schematic of the design for the powder grading in the 250 mm samples. Bottom: Photograph of both plates produced post sinter with Control (Left) and Aperture (Right). Faces were labelled to ensure correct attack face tested

A clear difference between the surfaces of the plates could already be seen, Fig 6.11, and once cleaned of residual graphite foil, this remained apparent. On the surface it was primarily due to the discolouration from contact with the BN spray, however, the FEM simulations demonstrated that this boundary continued through the plate thickness.

6.3.5 FEM Simulation

The earliest result came from the FEM simulations. These had previously been validated through the work in chapter 5, and the ability to manipulate spatial heating through current demonstrated. When applied to the larger 250 mm diameter samples the impact was discovered to have a similarly significant impact on the radial

thermal gradient with only 55% of the diameter of the sample reaching the desired temperatures for microstructural transformation as opposed to 90% in the control sample. With the known thermal sensitivity of the material, combined with an observed limit to the growth of needles and homogenisation at raised processing temperatures, the model predicted that the centre of the aperture sample will exhibit similar or greater properties compared to that of the control plate. The microstructural change towards the edges, however, will be significant and quantifiable as temperatures fall significantly. This is as the sample will not have sufficient energy input to grow its needles and diffuse the boron evenly through the microstructure, resulting in a weaker structure as postulated by Radhakrishna et al. [197].

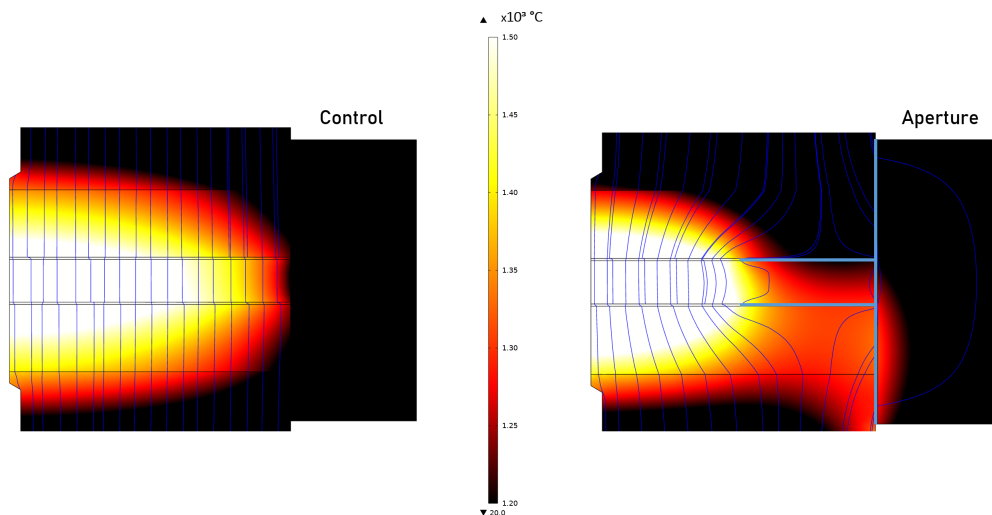


FIGURE 6.12: FEM simulations of the thermal gradients at dwell for the 250 mm diameter plates during sintering demonstrating the differing thermal gradients created

The next practical step, once the plate was successfully consolidated in one step using the FAST process and subsequently sandblasted to remove any residual graphite foil was to section and examine the microstructure in the aperture plate. On the surface the difference was primarily due to the discolouration from contact with the BN spray, however, within the sample the thermal history becomes apparent, as can be seen in Fig 6.13.

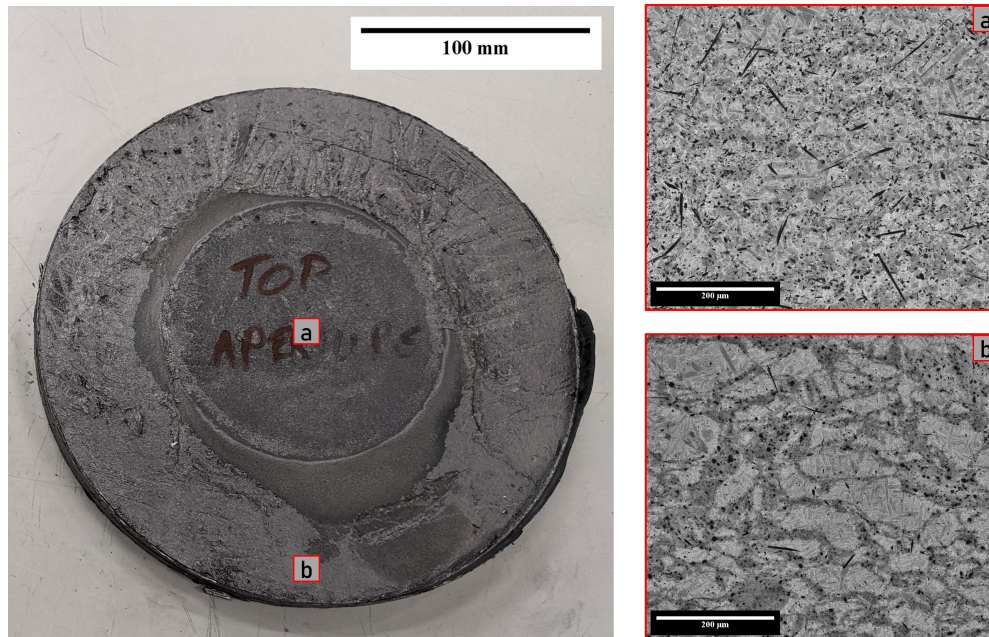


FIGURE 6.13: A 250 mm diameter aperture plate produced (Left), and backscattered electron images of internal microstructures of the 6 wt.% layer demonstrating microstructural variation.

Here the impact of the current channelling shifting the heating profile is obvious with the edge suffering from an inhomogeneous and unreacted microstructure. This is in line with the expected temperatures from simulation and the previously witnessed low temperature samples produced. The thermal simulation created in chapters 4 and 5 were expanded in scale, as mentioned, and demonstrated that this boundary would continue through the full thickness of the material as seen here, producing a weaker ballistic response, observed later in this chapter.

6.3.6 Microstructure Analysis

The variation in microstructures qualitatively matched the expected variations from the simulated sintering steps and aligned with the outcomes of the ballistic trials. The microstructural variation is shown in Fig 6.14.

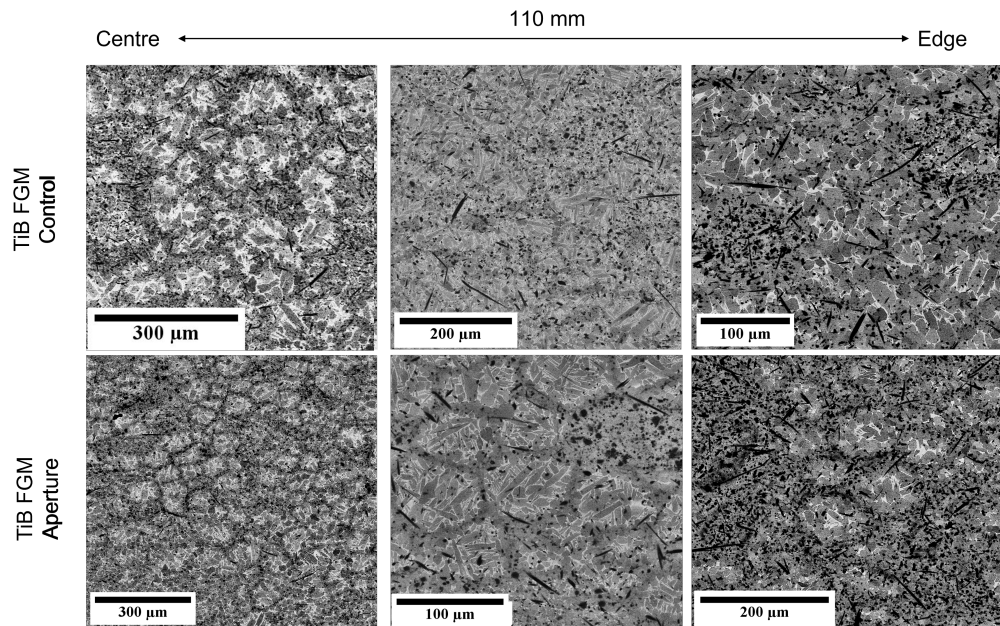


FIGURE 6.14: Backscattered electron images of the microstructure at increasing radial distances from the centre of both TiB FGM (Control) and TiB FGM (Aperture) samples post firing

The most easily noticeable trend within the micrographs noticed is the quantity and concentration of remaining clusters of un-reacted TiB_2 in particulate form. These are most visible in the edge regions of the aperture sample, conforming to what the simulation would suggest, with large clusters on the left and the bottom right of the micrograph. These large quantities of untransformed TiB_2 resulting from the lower thermal exposure cause a lower strength and lower fracture toughness in the resulting plate. Some of these clusters, though fewer in number, remain in the central regions of the aperture sample and more TiB needles have homogeneously spread along the prior beta grain boundaries with very few remaining in the centre providing higher, though still not optimal, strength. For the control sample, the trend also matches the simulation's prediction, with the spread and generation of TiB needles being homogeneous until 20-30 mm from the edge where a number of the weakening TiB_2 remnant clusters remain.

The thermal profiles from the simulation indicate a thermal gradient of up to $250^\circ C$ from centre to the plate edge over 125 mm for the control sample and the aperture sample. All FEM 'digital twin' simulations, visible in Fig 6.12, are adapted from work previously validated against experimental data to be accurate to within

5%. In the control sample this transition region dropping below the minimum desired processing window occurs only 10 mm from the edge, whereas the aperture plate experiences this 50-60 mm from the edge, causing significant differences in the resulting final microstructure. This is demonstrated in the improved homogenisation towards the middle and edge of the control over the aperture visible in Fig 6.14. This microstructural variance and dependency on processing temperature has been confirmed through the small scale testing and related to microhardness such that the decrease in isotropic microstructure leaves a slight drop in hardness but with a much larger variation in the value. This is expected, and seen to produce an easier pathway for cracks to propagate, either through the interconnectivity of harder material in brittle fracture, or through the softer underlying titanium alloy.

In the case of the aperture sample, the greater spatial thermal gradient can be seen in the model output from the centre to the plate edge, and the microstructure from this cooler edge region resembles 20 mm test samples produced in previous work at temperatures $>100^{\circ}\text{C}$ lower than the 1350°C processing temperature for the plate. This implies that this was the temperature reached at this location as the 20 mm samples are known to be accurate to the expected thermal conditions. It must also be noted that this thermal gradient has apparently been mitigated to some degree by the distance from the sample region at which the pyrometer measures and controls the temperature. This distance causes thermal lag in the processing, allowing more heat to be generated within the sample region before it can conduct to the surface where it can be measured, resulting in potential overshooting of temperatures during processing. This was originally thought to be a feature of the early process before temperatures can reach equilibrium throughout the tooling. However, it was noticed when the simulation was allowed to run for the full 2 hr dwell used in the physical twin that this did not occur, and the gradient did not change by more than a few millimetres once the dwell temperature was reached. This is an important aspect to note for future work, as scale and demonstrated further the importance of the simulation digital twin for the process, as well as being able to control the current accurately.

Between the simulation showing an increased spatial thermal gradient of over the same 125 mm distance, and the micrographs in Figure 6.14, these plates provide additional validation to the accuracy of these models at the larger scale. It may be noted, however, that even at the hottest expected section some inhomogeneity can still be observed on a large enough scale. This is also expected in the regions of higher wt.% TiB due to the increased volume fraction of reacted TiB and quantity of Boron to diffuse within the sample. In previous work by Gorsse et al. [195] heat treatments were performed up to 50 hr for improved results with larger quantities of TiB₂. However, this is not feasible for this process and would also cause increased issues for the titanium alloy substrate layer, with rapid grain growth increasing with energy input. From these microstructures and the V_{50} values, it is clear that this is a composite material sensitive to temperature and provides a strong case for the use of comparative or predictive simulations for the creation of novel components in real settings by demonstrating how much of an impact unexpected thermal gradients can have.

Microhardness

The results previously showed the 9 wt.% layer has a Vickers hardness of between 750 and 900 HV, confirmed here, with greater than two times that of the underlying Ti-6Al-4V layer. The variance in these MMC layers is significant when processed at low temperatures causing the poor ballistic performance seen in the aperture sample, though this variance disappears when properly homogenised, leaving well distributed needles through the matrix. For these values, multiple points were tested and averaged to account for the not totally dispersed TiB within the region. This may be significantly lower than pure TiB₂, however it was decided that on this scale the required conditions which would allow us to fully sinter a TiB₂ layer on the surface would cause significant problems for the predominantly titanium layers below, leading to melt and failure to process.

These results can be seen in figure 6.15 and little difference can be observed in the values compared to the previously recorded values that is not accounted for

with the positioning of the test lines within the layers and boron diffusion, implying that the material doped with TiB does not experience much stress hardening. However, it may be possible that during the sectioning and grinding some of the residual stresses were released from within the material as some fragmentation and cracking was noted during this process.

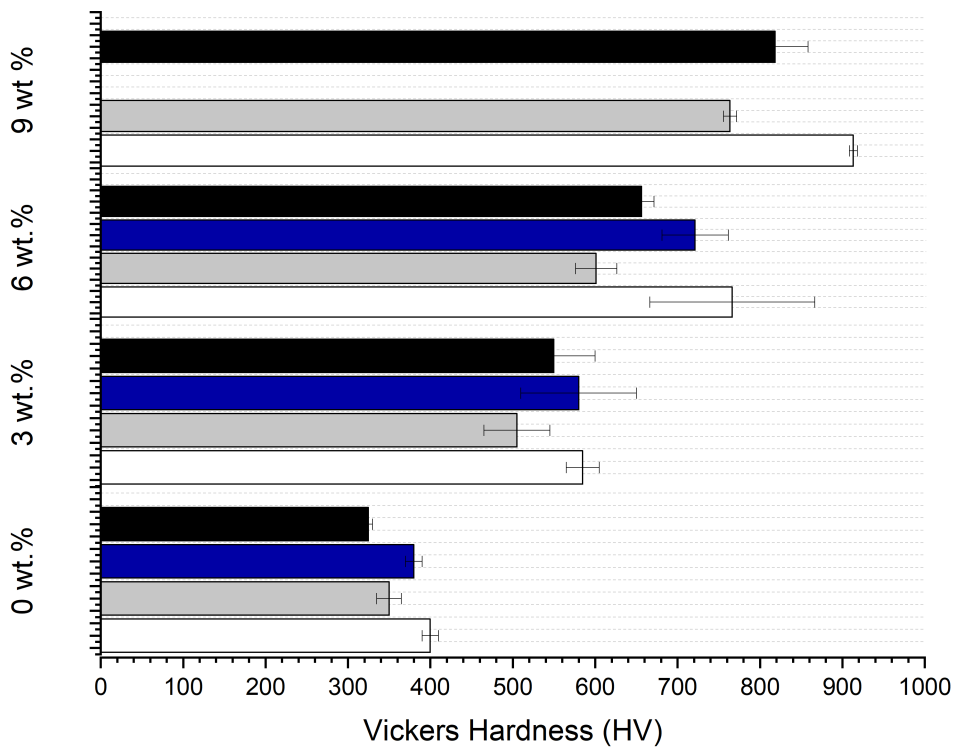


FIGURE 6.15: Micro-hardness of each layer at diagonally spaced points on a line from the attack face to the rear face of both Aperture (grey / white) and Control (black / blue) samples

Two main features common to both plates can be observed, in that the centre of the sample (blue / white) consistently out performs the edge (black / grey) in terms of hardness and that the control plate is a little less hard than the aperture equivalent for each layer tested. The first point is further confirmation for the initial hypothesis that the thermal gradients in producing samples on this scale has a significant impact on the generation of optimised microstructures for this MMC system, backed up by the micrographs from Figure 6.14. The second, however, is slightly unexpected with the variance not being consistent between the samples to allow for this to be error. It is expected that this lower hardness in the control sample is in fact also due to the

higher average processing temperatures across the surface. As the TiB_2 reacts with the titanium matrix and forms the TiB needles, homogenising the microstructure the harder regions of concentrated TiB_2 into a more ductile combination of needles and matrix providing benefits to the desired multi hit capacity. There is also a potential element of survivor bias, as the materials were tested post ballistic firing it is possible that some of the regions which were too brittle or too soft were destroyed more easily and the remaining microstructures and hardnesses survived due to their strengths.

Looking at the impact of this visual difference on the hardness at various points was then carried out. The results are shown in Fig 6.8 and seem to suggest little difference within the layers themselves with respect to hardness. There is a seeming increase in the value when examining the bond between the two layers, however when looking at the data further, it can be seen that this is dependent on the locations measured. The hardness increases with the increased inclusion of the TiB_2 ceramic and the temperature impacts this minimally. While the variance in the values is much more strongly tied to this variable. The standard deviation of the points relates to this variation and the colour variation, from boron inclusion, in the micrographs, seen in Fig 6.5 A-C. The lower temperature samples at 900°C show high variation at all points where the ceramic is present, while with enough energy the 1200°C sample enables sufficient diffusion to even out the distribution and thus the resulting hardness. The 1400°C sample allows for an improvement even within the bond region.

The TiB FGM aperture sample was successful in demonstrating very clearly that this material is sensitive to processing temperatures for its mechanical properties as well as its microstructure. This demonstration of the thermal sensitivity of the material's performance, and the ability of the current control technique to produce tailored thermal gradients and unique microstructures in a single step, at these scales was a success in itself. There is, however, further potential to utilise the current control technique for the homogenisation of these thermal gradients instead of pushing them to an extreme on larger scale samples as in this paper.

6.4 Ballistic Trials

The ballistic testing was conducted at Radnor Range in collaboration with RBSL and DSTL. During testing the plates created using FAST with diameter 250 mm and thickness 19 mm were further sandblasted to remove any remnant graphite foil from the process and ground down where edge creep occurred to aid clamping. An armour piercing 30-06 AP M2 hardened steel round was used as test projectile, as pictured and shown in schematic form in Fig 6.16 and Fig 6.21. The bullet was aligned and fired at the target directly with 0 intended yaw and pitch, and the speed was measured as it passed through two infra red light gates. This was required as the bullets were live fired with precisely measured powder weight for desired speed and could vary within an expected range when tested.

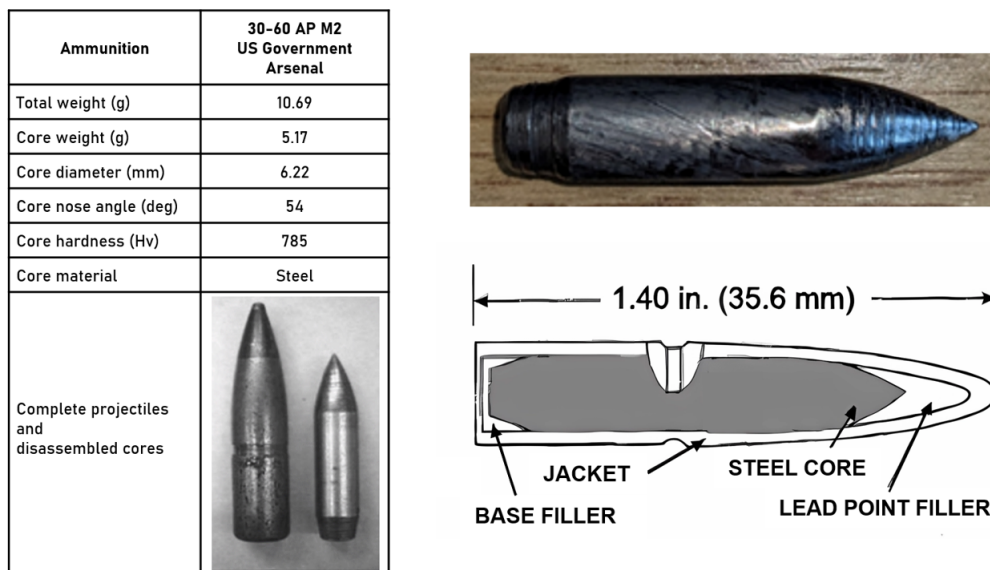


FIGURE 6.16: 30-60 AP M2 hardened steel slug data sheet (left), photograph of the core, and full schematic (right) images, adapted from RBSL documentation

The V_{50} was determined using two passes and two failures at as narrow a range of velocities as possible with the material available, where a failure is determined by whether the 5 mm thick aluminium alloy witness sheet, placed behind the plate during the test as depicted in Fig 6.17, had been perforated sufficiently to let light

pass through. Three outcomes are possible for the test; complete perforation (CP), partial perforation (PP), no perforation (NP) with NP and PP counting as passes and CP as failure. Usually, with enough shots, a narrow range for this V_{50} value can be obtained and then further testing may improve the precision of this measurement. However, for these plates, the MMC/ceramic nature of the impacts minimises the number of potential shots per surface area. It must be noted however, that this repeatability of impact testing is not usually possible for dense ceramic targets [202] and this multi-impact tolerance is a large positive for this system.

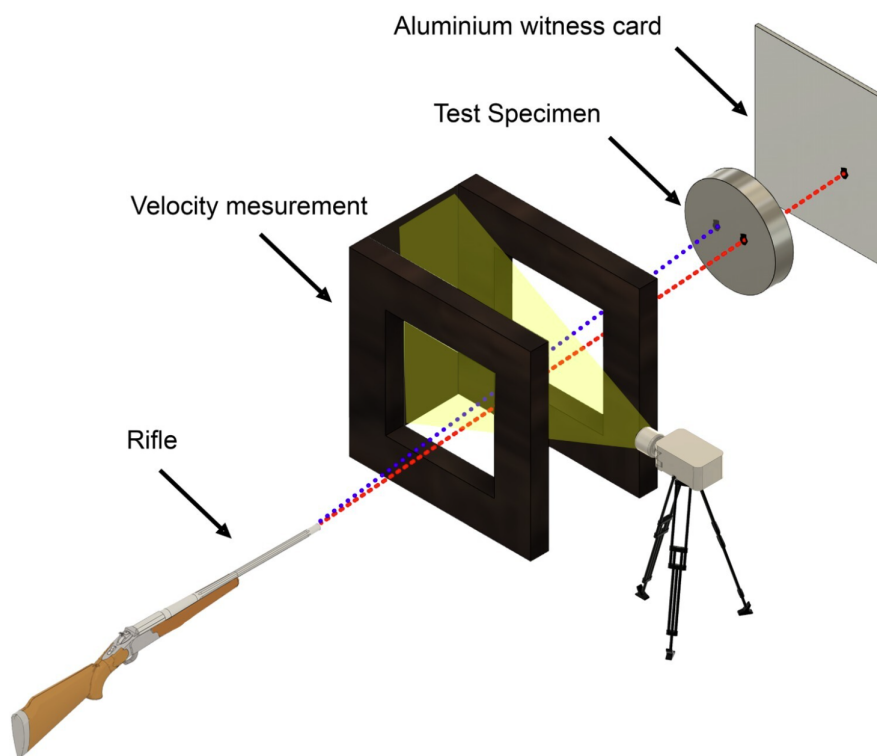


FIGURE 6.17: A visual schematic of the equipment used for the ballistic test, referenced with permission from [203]

The plates were photographed each time a test firing occurred to document the impact and locations of impact on the attack face as well as how the plate held up to multi-hit testing. Once firing was completed, a rear face photograph was also taken to examine the scale and mechanisms of failure for the shots if the sample had maintained its form.

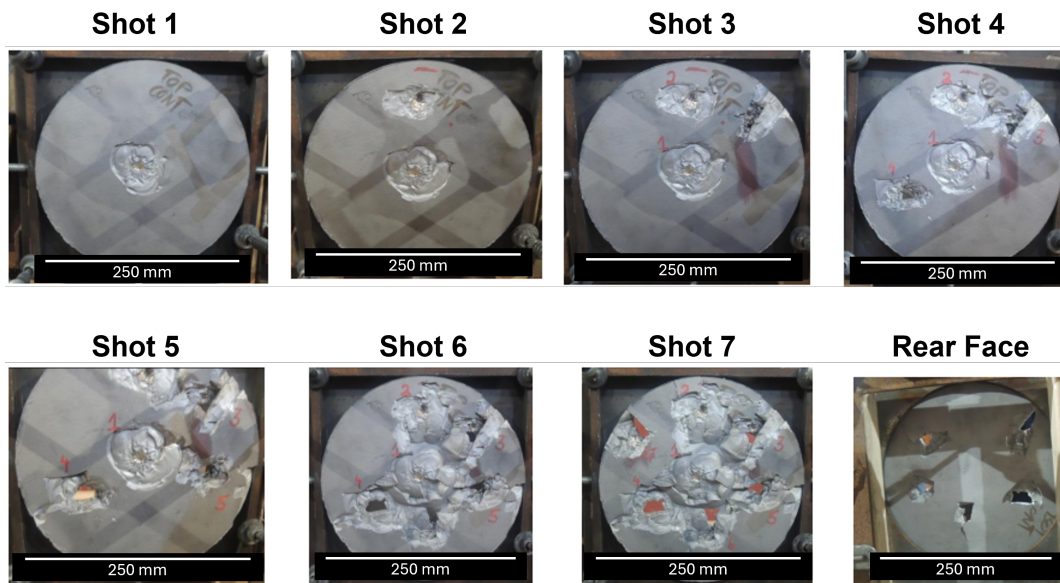


FIGURE 6.18: Photographs of the impact faces taken after each shot into the 250 mm diameter control plate, as well as the final shot rear face demonstrating the scabbing failure mechanisms

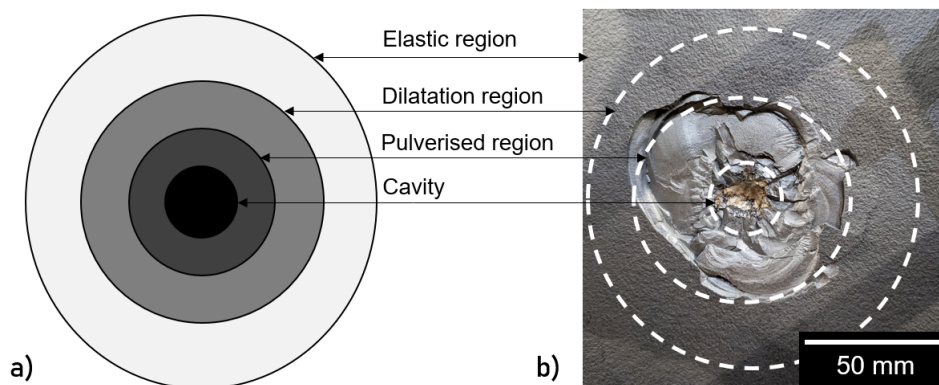


FIGURE 6.19: Galanov's model diagram adapted from Zhang et al. [204] (a) and an overlaid photograph of the impact of Shot 1 from Fig 6.18(b) displaying the impact cavity region, as well as the visible pulverised area of front spallation.

In shot 1, with a velocity of 795 m/s, the clearest example of impact can be seen, with a deeper central impact area (approximately 10 mm diameter and 3 mm depth) corresponding to the penetration of the projectile tip. Surrounding this is a much larger area of front spallation which is estimated to be around 80 mm diameter and 2 mm in depth, all of which is within the hardest layer of 9 wt. % TiB. According to work by Zhang et al. [204] Galanov's model can be expanded for ballistic applications and suggests there are multiple zones to an impact, pictured in Fig 6.19(a)

moving from the cavity, through the pulverised region, dilatation and pore formation region, to the elastic region. These match very well, qualitatively, to the shot profiles seen with the overlaid profile visible in Fig 6.19 (b). The dilatation region is not visible on the surface but was later seen as the region containing the internal stress cracking and voids from the impact seen during analysis in section 3.2.1. A similar shot with a deeper penetration from shot 2 is understandable with a velocity of 844 m/s, indicates very good multi-hit capacity with a separation of less than 100 mm from the edge of the previous shot, and a high likelihood of overlapping elastic regions. Shots 6 and 7 then demonstrate the failure modes for this system, characterised by large regions of front spallation again, but with scabbing failure on the rear face, clearly observed in Fig 6.18. This is likely in part due to the high temperatures the titanium alloy was exposed to during processing resulting in excessive β grain growth and reduced ductility leading to brittle failure modes. It must be noted however, that the plates structural integrity survived and fully held together even after 7 shots and large amounts of damage and material loss, once again demonstrating the importance of FGMs for their multi-hit potential for real world armour applications.

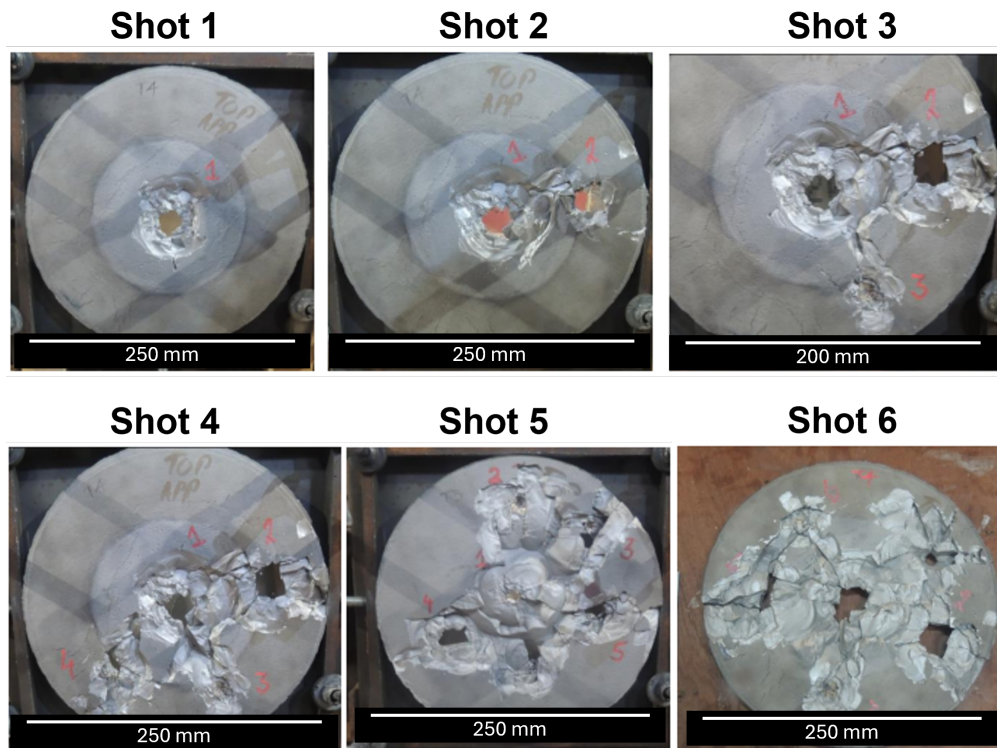


FIGURE 6.20: Photographs of the impact face taken after each shot into the 250 mm diameter aperture plate, with shot 6 demonstrating critical failure of the plate.

The largest observable difference between this and the previous plate with respect to shot characteristics is the increased area of spallation. In part this was due to variation in the bullet speed from the live fire approach, and an initially high speed probing shot at 889 m/s resulting in the damage to the face in shot 1. The spallation in this shot is estimated to be around 100 mm in diameter and the elastic/plastic zones have clearly resulted in some impact on shots 2 (CP) and 4 (CP). Shot 3 (NP) displays the expected pass result similarly to shot 1 from the control sample, though with greater spallation than expected for the speed of shot at 714.4 m/s and with some directionality due to the previous shots. It is believed that this was specifically due to the stress impact from the initial high speed shots and potential internal residual stress and cracks. The overall V_{50} for this sample was significantly worse than the previous sample, as expected, though the extent of the variation will be discussed later, and the multi-hit capacity was reduced also, with the sample collapsing after the sixth shot.

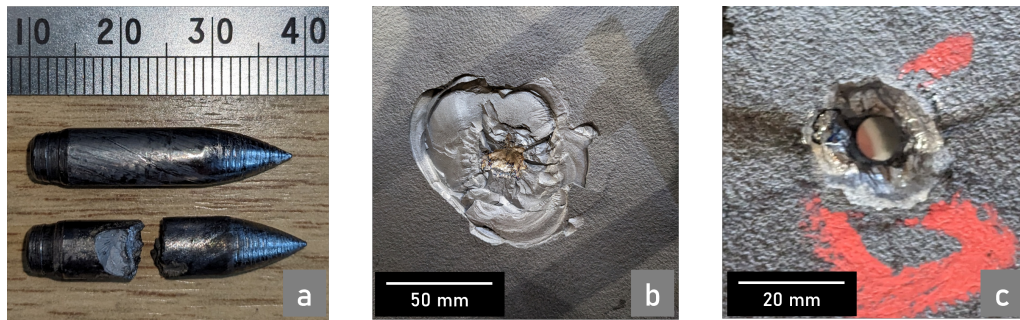


FIGURE 6.21: (a) Photograph of the hardened steel slugs fired at the metallic target plate (top) and the ceramic plates (bottom). (b) Impact (pass) on ceramic attack face. (c) Impact (fail) on metallic face

Fig 6.21 shows the differences in the impact on the ceramic and metallic layers for both the bullet and the plate. The fired cores are displayed in (a) displaying the effect of contact with the reference plate (top) and the FGM control plate (bottom). This clearly demonstrates the increased abrasion and fracture of the bullet resulting from making contact with a harder surface, solely from the 9 wt.% TiB₂ to the layer. The resulting critical failure and fractures in the steel core of the bullet during contact with attack face of the plate, with this TiB inclusion, is due to the plate becoming harder than the bullet if properly processed, seen in Fig 6.15. Whilst this provides more protection, it also results in higher degrees of damage to the sample, as seen earlier in the rear faces of the TiB plates. In addition, Fig 6.21 (c) shows the impact of a shot into the rear face of the plates, testing for the effect of the orientation of the FGM layers vs bulk properties. This matched identically to the pattern noticed on the attack faces of the Ti-6Al-4V reference plate, though the rear face failure differed with additional spallation. It can also be seen with this rear face shot failure at the low shot speed of 740 m/s that the directionality of the layering does have a significant effect, even in the lower performing plate. Also, it may be noted that the spallation of the ceramic rear face for this shot experienced severe spallation, potentially causing more damage to the test sheet than a clean metallic penetration. Therefore, these composite materials have been shown to have severe directionality in their fracture toughness and ballistic properties and must be handled with care to prevent misorientation during production and transport.

TABLE 6.2: Ballistic results from range firing using hardened steel slugs. Indicative V_{50} (*) noted where insufficient shots for a more accurate determination were possible due to impact ablation and structural damage.

Sample	V_{50}	Std Dev
Titanium Mil Spec	833 m/s	N/A
Ti-6Al-4V 1350°C	799.2 m/s	6.3 m/s
TiB FGM Control	*860.3 m/s	10.5 m/s
TiB FGM Aperture	*733.0 m/s	24.2 m/s

The final values present an excellent case for this material system, with the TiB inclusion to the surface attack layers for the control sample providing a 30 m/s increase in ballistic performance over mil spec titanium currently used for purpose. It also demonstrates the real world impacts and importance of the current control technique, with the variation in thermal profile solely from directing the current resulting in the aperture sample failing to equal the performance of even the Ti-6Al-4V reference sample made under the same conditions, and with greater spatial variance. This is fundamentally due to the thermal gradient in the large machine resulting in weaker microstructures for this temperature sensitive material system. The impact for the Ti-TiB MMC is discussed in section 3.2 and visible in Fig 6.14, however, this aspect is also clearly observed in titanium alloys such as Ti-6Al-4V due to their microstructural sensitivity to temperatures close to the β transus.

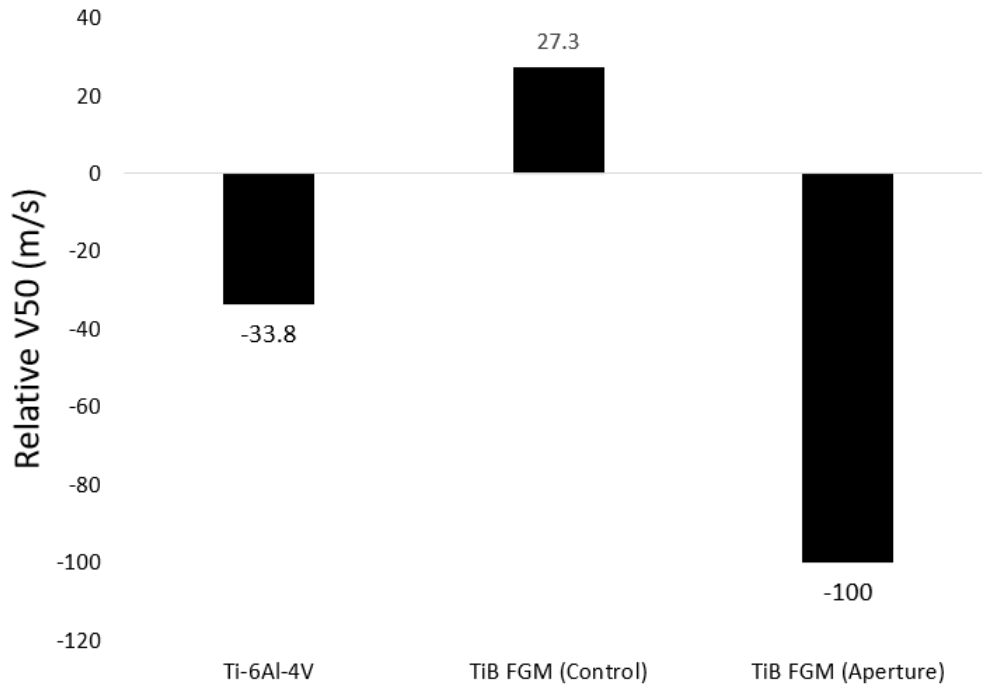


FIGURE 6.22: Relative V_{50} , results normalised to military specification (Mil Spec) titanium alloys for the same thickness and firing conditions

TiB FGM Aperture & *733.0 m/s & 24.2 m/s

6.4.1 Microstructure Analysis

Once the plates had been ballistically tested in the as FAST condition they were sectioned, mounted in conductive carbon filled PolyFast™ Bakelite, and ground and polished using a Struers Tegramin-25. Grinding was performed for 2 min using P800, P1200 and P2500 SiC grit papers, followed by polishing with a 9 part 0.06 μm colloidal silica and 1 part hydrogen peroxide suspension for 10 min. After having been prepared the samples were analysed using light and electron microscopy. The initial optical micrographs were taken using the Olympus™BX51 microscope, to identify features of interest for more focused imaging on the Inspect F50 Secondary Electron Micrograph image with 20 kV accelerating voltage. The variation in microstructures qualitatively matched the expected variations from the simulated sintering steps and aligned with the outcomes of the ballistic trials. The microstructural

variation is shown in Fig 6.14.

The most easily noticeable trend within the micrographs noticed is the quantity and concentration of remaining clusters of un-reacted TiB_2 in particulate form. These are most visible in the edge regions of the aperture sample as the simulation would suggest, with large clusters on the left and the bottom right of the image with large quantities of untransformed TiB_2 which results from the lower thermal exposer and causes a lower strength and lower fracture toughness in the resulting plate. Some of these clusters, though fewer in number, remain in the central regions of the aperture sample and more TiB needles have homogeneously spread along the prior beta grain boundaries with very few remaining in the centre. For the control sample, the trend also matches the simulations prediction, with the spread and generation of TiB needles being homogeneous until close to the edge region where a number of the TiB_2 remnant clusters remain.

The thermal profiles from the simulation indicate a thermal gradient of up to 250°C from centre to the plate edge over 125 mm for the control sample and the aperture sample. However, in the control sample this transition region dropping below the minimum desired processing window occurs only 10 mm from the edge, whereas the aperture plate experiences this 50-60 mm from the edge, causing significant differences in the resulting final microstructure. This is demonstrated in the improved homogenisation towards the middle and edge of the control over the aperture visible in Fig 6.14. This microstructural variance and dependency on processing temperature has been confirmed previously through the smaller scale samples, and related to microhardness such that the decrease in isotropic microstructure leaves a slight drop in hardness but with a much larger variation in the value. This is expected, and seen to produce an easier pathway for cracks to propagate, either through the interconnectivity of harder material in brittle fracture, or through the softer underlying titanium alloy. The FEM twin simulations, seen earlier in Fig 6.12, from the model in chapter 5 were confirmed to be accurate to within 5%.

In the case of the aperture sample, the greater spatial gradient can be seen in

the model output from the centre to the plate edge, and the microstructure from this cooler edge region resembles 20 mm test samples produced in previous work at temperatures 100°C lower than the 1350°C processing temperature for the plate. It must also be noted that this thermal gradient has apparently been mitigated to some degree by the distance from the sample region at which the pyrometer measures and controls the temperature. This distance causes thermal lag in the processing, allowing more heat to be generated within the sample region before it can conduct to the surface where it can be measured, resulting in potential overshooting of temperatures during processing. This was originally thought to be a feature of the early process before temperatures can reach equilibrium throughout the tooling. However, it was noticed when the simulation was allowed to run for the full 2 hr dwell used in the physical twin that this did not occur, and the gradient did not change by more than a few millimetres once the dwell temperature was reached. This is an important aspect to note for future work, as scale and demonstrated further the importance of the simulation digital twin for the process, as well as being able to control the current accurately. A caveat to this is that it is known that the BN spray's effectiveness at insulating the current decays when processed for long periods at high temperatures, meaning it is likely that the gradient would slowly shift towards the control model over the course of the sintering process. Further work using more permanent insulating tooling materials may be recommended, however, the effect is still strongly demonstrated here and there are advantages to using easily available, cheap, relatively unreactive materials which are simple to control and apply, such as BN spray.

Between the simulation showing an increased spatial thermal gradient of over the same 125 mm distance, and the micrographs in Fig 6.14, these plates provide additional validation to the accuracy of these models at the larger scale. It may be noted, however, that even at the hottest expected section some inhomogeneity can still be observed on a large enough scale. This is also expected in the regions of higher wt.% TiB due to the increased volume fraction of reacted TiB and quantity of boron to diffuse within the sample. In previous work by Gorsse et al. [195] heat treatments were performed up to 50 hr for improved results with larger quantities

of TiB₂. However, this is not feasible for this process and would also cause increased issues for the titanium alloy substrate layer, with rapid grain growth increasing with energy input. From these microstructures and the V_{50} values, it is clear that this is a composite material sensitive to temperature and provides a strong case for the use of comparative or predictive simulations for the creation of novel components in real settings by demonstrating how much of an impact unexpected thermal gradients can have.

Crack Propagation Mechanisms

Some of the underlying mechanisms for the improvement in ballistic performance seen from these plates are investigated in more detail here, accounting for both the insertion of the ceramic itself, and the desired reaction with the alloy to create the TiB needle structure. Four primary mechanisms for crack propagation have been observed in the series of primary cracks propagating through the FGM layers, crack face bridging, particle de-bonding or cracking, crack-tip deflection, and crack branching. Evidence for these mechanisms has been seen previously in work by Sahragard-Monfared et al. [205], and due to their positive impact on fracture toughening, observing them is a positive indicator for the use of FAST for the production of this MMC. Beyond this, it can be noticed that the commonly observed straight fracture is typical of a brittle material in the previous work [205] when TiB wt.% reached higher concentrations with little impact from the TiB needles as predicted, providing more motivation to understand these lower concentration MMC systems. With the lower concentrations the increase in ductility is sufficient for the primary mechanisms to begin to occur and improve the fracture toughness.

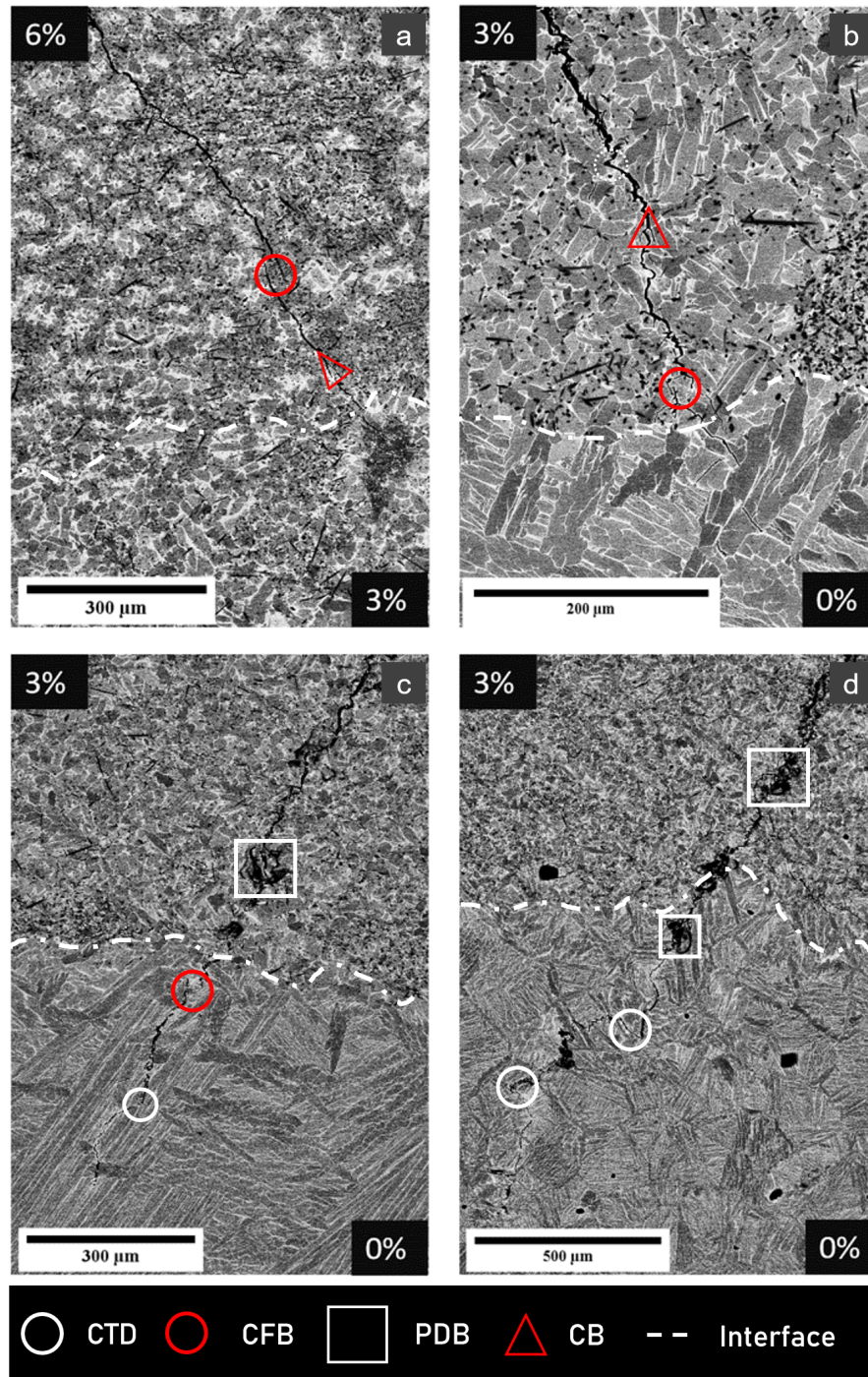


FIGURE 6.23: Backscatter electron images of ballistically induced cracks in 1350°C 2 hr processed Ti-TiB MMC plates, arresting at the interfaces of the functionally graded Ti-6Al-4V + TiB layers with features highlighted in white: crack tip deflection (CTD) in c and d, crack face bridging (CFB) in a, b and c, particle de-bonding (PDB) in c and d, and crack branching (CB) in a and b.

The most obvious macroscopic feature of the samples sectioned from near the impact locations was that almost all of the residual cracks terminated within a few hundred microns of a layer boundary. Four examples of this can be seen in Fig 6.23,

with the majority of the arrested cracks seen in sectioned samples being between the 3 wt.% TiB layer and the Ti-6Al-4V layer, processed at 1350°C for 2 hrs. This is due to the increasing ductility in the unreinforced Ti-6Al-4V allowing more plastic deformation to occur as the matrix absorbs more energy during crack propagation, slowing and eventually halting the crack progression. The consistent scabbing failure mechanism producing shrapnel on the rear face, or 'scabbing', of the samples likely stems from this conical crack propagation through the hard surfaces. When the impact energy is sufficient to penetrate the final ductile layer, this results in the back face ejecting larger pieces of material. It must also be noted that due to the high temperatures required for full consolidation, the grain sizes of the ductile back face will be much larger than ideal fine grain titanium, of an order of magnitude difference at >1mm in diameter, compared to desirable grain diameters of approximately 100 μm . This increase in size decreases the ductility, likely a primary mechanism in exaggerating this scabbing feature.

The crack features can each be seen in Fig 6.23, with the crack path becoming strongly affected by the presence of the TiB particles in front of the advancing crack tip. Crack branching and crack deflection can be seen in the 3 wt.% regions of Fig 6.23 (a) and (b), as the cracks are redirected on a small scale around the TiB needles, with the highlighted deflections in the titanium alloy matrix occurring primarily from following larger grain boundary pathways. Crack bridging is also seen occurring primarily in regions of higher TiB or TiB₂ concentration, due to the higher hardness and brittleness in those regions, though in (b) an example can be seen of grain boundaries aligning for a similar feature to occur. Delamination, or particle debonding is also visible in both Fig 6.23 (c), (d) and in Fig 6.24 (c), however, the crack face bridging has been the primary observed feature on a larger scale. The delamination has been seen less often than expected due to better consolidation around the needles from FAST than expected. This is likely due to the heat making the titanium alloy matrix more ductile during processing, allowing the needles to expand without external cracking. In this primary mechanism of crack face bridging, the crack can 'bridge' the more ductile titanium matrix through the strain field surrounding the crack front, seen near the interface in Fig 6.23 (b) and (c). This causes microcracks

ahead of the propagation, and these 'sealed' bridges due to plastic deformation and stored energy pressing the material together behind the crack as it passes through. It has also been seen to occur closer to the attack face in (a), where sufficient driving forces can bridging through regions of higher TiB or TiB₂ concentration, though with other destructive features present at the impact locations these can be more difficult to distinguish and can be more easily attributed to spallation.

In Fig 6.24 (b) and (d) it can be seen that when the orientation of the needles is perpendicular to the direction of the propagation, the strain field around the crack tip cracked them or more rarely resulted in deflection when the approach was angular (a). Those more in line with the crack suffered delamination or lesser deflections observed in (a), and (c). Some microcracking is also visible in some of the needles along the crack's path (d) which could have been a result of the propagation, absorbing more energy. However, it is also possible that these micro cracks occurred during the cooling process of production, providing early nucleation points for voids which also slow the advance of the fracture. Therefore, regardless of the creation mechanism, their presence in these images is seen as a further positive for the needles presence in low wt.% TiB MMCs.

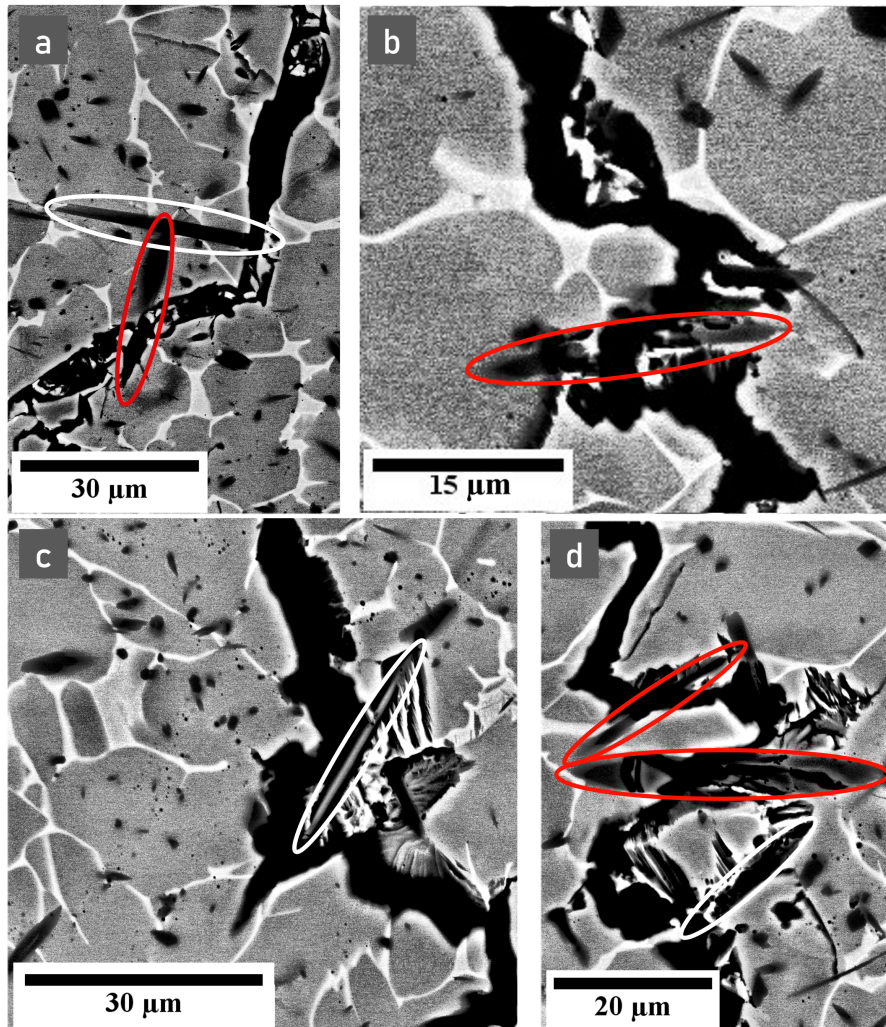


FIGURE 6.24: Backscatter electron imaging of cracks interacting with individual TiB needles during propagation showing de-bonding and deflection in white with examples of needle cracking in red. Images a and c are taken from the control, and b and d from the aperture Ti-TiB MMC plate, processed at 1350°C for 2 hr

With a closer look at the propagation of these cracks two effects these needles have on a micro scale can be seen. In Fig 6.24 a and c it can clearly be seen that the crack is deviating from its path to circumvent a needle in the plane of the sectioning cut, clearly de-bonding it in c. Mechanistically this is due to the crack propagating along the α - β interface to follow the lowest energy pathway. A convoluted crack path requires higher energy for fracture, i.e. higher fracture toughness, which is why this property is beneficial in ballistic applications. It is, as mentioned previously in this section, seen that the alternative in regions closer to the surface attack face, with higher ceramic wt.%, Fig6.24 b and d, where the crack seems to propagate across,

or through the TiB needles, cracking them and following the prior β grain boundaries. The needles in these images are occasionally deeper into the sample, and less clearly resolved, so there is some potential that the crack has indeed circumvented them in the direction normal to the sectioning cut, curving over them. However, it is believed that close to the impact points there is simply sufficient energy for the crack to shear through them following the shock-wave in an overall more energy efficient path, at the potential cost of smaller energy losses from avoiding needles in the 9 wt.% layer.

6.5 Further Analysis

Another set of post ballistic testing in the as produced state was chemical and texture analysis using the Inspect F50 Scanning Electron Microscope, as well as the JEOL JSM-7900F Microscope with AZtekHKL software. The Inspect machine came equipped with an X-EDS module which allowed us to chemically analyse and map the material to further improve the findings, and determine the TiB transition had in fact occurred as expected.

X-ray Energy Dispersive Spectroscopy

SEM image (left) in Fig 6.25 shows a region of poor homogenisation close to the edge of the aperture sample from Fig 6.14, this was the region with one of the lowest expected processing temperature and the highest variance in hardness. What can be seen in the element maps is that the regions richer in boron (purple), slightly lacking in titanium (red), and much more significantly lacking in aluminium (blue), are where the needles are present. The vanadium (green) scan appears to have no issues with the presence of the needles but from point scans it is known that this not the case, meaning the lower level green values may be taken as background, or 0 content. As expected with this alloy, most of the vanadium will be trapped in the β phase within the microstructure. The TiB needles that do grow then react more aggressively with the titanium atoms in their TiB_2 phase when temperatures are

reached, pushing the alloying elements out, and increasing their concentrations in islands until a longer dwell and more energy is imbued. What can be inferred from this is that in areas with less exposure to high temperatures during the sintering phase, the boron has had less ability to diffuse throughout the surrounding titanium alloy powders, seeming to trap them in islands of microstructure and providing brittle pathways for cracks to potentially propagate through. For some of these TiB_2 concentrations, hardnesses were observed of up to 1300 HV, which is approaching fully consolidated TiB_2 hardness values in excess of 2200 HV. This is incredibly brittle relative to the Ti-6Al-4V particles with almost one eighth of this value at 300 HV, resulting in the mechanisms and resulting poorer performance discussed previously.

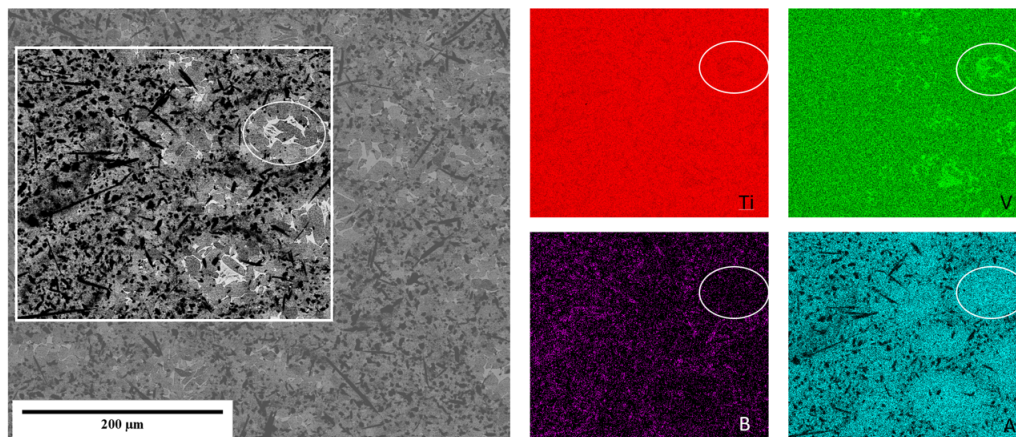


FIGURE 6.25: X-ray Energy Dispersive Spectroscopy (X-EDS) showing displacement of Al from needles and distribution of elements in the edge aperture sample, displaying the inhomogeneous effect of poor processing

Electron Backscatter Diffraction

This testing was performed to check for the presence of any potential compressive texture that may have resulted in the needles preferentially growing along the prior β grain boundaries during FAST processing. However, as visible in Fig 6.27 there is little visible compression texture in this sample and this has also since been demonstrated in a paper by Fernandez Silva et al. [206]. What was observed from this technique, in addition to this knowledge of a lack of preferential growth direction for the needles, is an excellent demonstration of another improvement to the microstructure the TiB inclusions provide in their severe grain pinning. This huge refinement

in grain structure, of over an order of magnitude, provides additional strengthening to the material in these MMC layers through the Hall-Petch effect with additional fracture toughness, potentially significantly adding to the resulting improved ballistic properties seen in this work. It may also be noted that this was in spite of the high temperatures these plates were sintered at, meaning that the grain pinning occurs without sensitivity to temperature, at least demonstrated up to 1300-1400°C. This could potentially allow for the base layer to contain a low concentration of TiB_2 to refine the grain structure at these higher temperatures, or the application of this concept in other fields for high working temperature titanium applications.

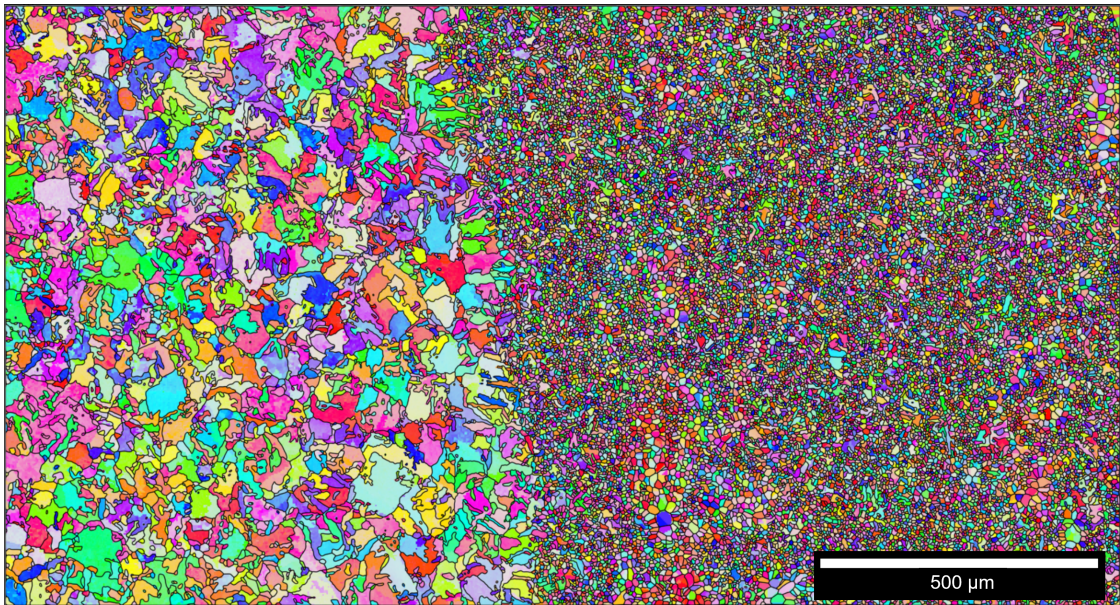


FIGURE 6.26: Electron Back Scatter Diffraction (EBSD) of the Ti-6Al-4V + 3 wt.% TiB_2 interface demonstrating extreme grain pinning from the TiB_2 and TiB ceramic particles on the growth of the titanium alloy prior β grains

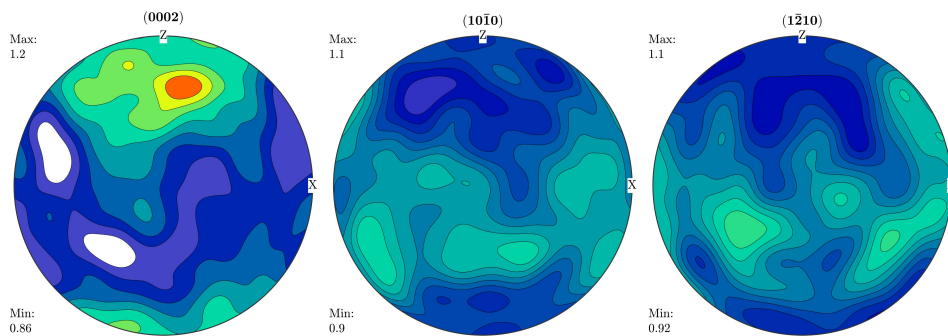


FIGURE 6.27: Pole figures showing the lack of texture discovered in Fig 6.26 above, consistent through both regions

Given the temperatures used for processing required to provide the desired TiB needle structure, it is unsurprising that the Ti-6Al-4V layer (left) demonstrates large alpha colonies, with noticeable prior beta grains of above 1 mm diameter under cross polarised microscopy. However, as visible in Fig 6.26, the layered powder provides a stark contrast, with the alpha colonies being an order of magnitude smaller than their immediate neighbours with only 3 wt.% TiB₂ milled inclusion. There are even regions visible in the EBSD image where colonies have grown within this layer due to mild inhomogeneities in the boron distribution.

6.6 Conclusions

The main observation is that the TiB FGM control plate out-performed both the reference Ti-6Al-4V plate, and the military specification value for the sample dimensions tested. This demonstrated the overall superiority in performance provided by the functionally graded inclusion of TiB into the titanium alloy matrix for ballistic performance, and the plate's multi-hit capacity targeted in this work was shown through the absorbing of between 5 and 7 shots at the required velocity whilst maintaining structural integrity. The TiB FGM aperture sample was also successful in demonstrating very clearly that this material is sensitive to processing temperatures. Significantly reduced ballistic properties were observed solely from the channelling of the electric current resulting in exaggerated thermal gradients. This thermal sensitivity of the material's ballistic performance and the ability of the current control technique to produce tailored thermal gradients to create specific microstructures in a single step, even at scale was a success in itself. There is, however, further potential to also utilise the current control technique for the homogenisation of these thermal gradient on larger scale samples, which will be a target of future work.

The unique crack mechanisms resulting from TiB needle inclusion have been investigated and their positive impact on the fracture toughness was connected through the micro-hardness to their ballistic results. These mechanisms, as well as the remarkable grain pinning, revealed through microstructural analysis, provided

additional resistance to crack propagation and added to the strength of this material system, explaining the material's ballistic success. It was, however, noticed that the high temperature processing required likely resulted in the exaggerated scabbing of the rear face on penetrating shot failures. It was discovered that this was likely due to excessive prior β grain growth within the titanium alloy layer, reducing the ductility of the rear face and its ability to dissipate the energy, resulting in brittle failures.

Chapter 7

Conclusions and Further Work

7.1 Conclusions

This thesis presents important findings from the development of an auxiliary technique for field assisted sintering technology. Through the current control approach, the generation of predictable unique microstructures has been simulated and practically demonstrated. The primary focus of this work has been on use of boron nitride as an electrical insulator for the directing of electric current, and finite element models as predictive design tools for the resulting thermal gradients. Two primary material systems were utilised, Ti-6Al-4V and a Ti-TiB metal matrix composite, examined using a novel deep learning image analysis method to categorise the resulting microstructure, proposed in chapter 5. The real world impacts of the technique have also been practically demonstrated through ballistic trials, reported in chapter 6, fulfilling the targets of the initial research question.

7.1.1 FEM digital twin production

The creation of the finite element model allowed for the internal examination of the tool stack and highlighted the remarkable effect on thermal profiles from the addition of insulating BN layers. It also demonstrated the requirement for accuracy of the model for the purposes of predicting these outcomes and controlling them to generate tailored microstructures. Gathering the graphite tooling material property data, reported in chapter 3 was incredibly beneficial in arriving at this required accurate model, providing real data to output practically useful results. The inerrant

thermal transformation in Ti-6Al-4V acts as a processing thermometer in that its β transus temperature allowed us to confirm the existence of these predicted thermal gradients and further validate the simulation. The predicted impact on thermal gradients from this technique was then observed through the density profiles in chapter 4 and in the microstructures of 1075°C processed samples, qualitatively confirming our theory. This simulation was then further validated in chapter 5 against the electrical and thermal output data from the FAST machine to within a 5% range of error, as well as more in depth microstructural evidence. The model was then also proven to have a solid predictive capacity with resulting ballistic and microstructural properties matching expected results from the model in the previously untested large 250 mm diameter samples of thermally sensitive Ti-TiB MMC.

7.1.2 Current Control Thermal Gradients

The initial consolidation findings of chapter 4 are expanded through chapter 5 with the four primary boron nitride designs demonstrating huge differences in the microstructures of the Ti-6Al-4V samples with no changes to processing except the addition of insulation foil inserts. Temperature gradients of over 100°C were predicted in the model over 40 mm from the centre of the samples to the edges. Cross sectional, as well as, top down views are visible in Fig 5.4 to better visualise this impact on localised heating which was shown to commonly be spatially accurate down to a few millimetres. Additionally the size of the prior β grains could now be predictable within a defined error range, provided previous knowledge of the system through the analysis route presented in chapter 5. This could allow for component microstructural design in a single FAST step which could be assist significantly in enhancing FAST as a disruptive process for industry. Additionally a less well explored variable, the location of the pyrometer, was shown to be an important factor in determining the thermal profiles within the technique and process as a whole from heat lag, carrying potential impact for the design of new FAST machines and tooling to combat or cause thermal gradient formation.

Microstructural Validation

A novel image analysis route proposed for batch microstructural examination of an entire sample face using MIPAR deep learning algorithms for comparison of Ti-6Al-4V samples with simulation has been demonstrated. This route allows for potential scaling comparison to any degree where sufficient scale microscopy is possible with significantly less effort than a manual approach. It also provides a potential to analyse the more common and desirable α microstructures in Ti-6Al-4V, as well as more complex material systems, provided sufficient optical resolution during the mosaic micrography. This work however, demonstrated its use to compare the localised prior β grain growth to predicted thermal conditions and generate a grain size relationship which may then be used either as a predictive tool to further the technique, or to assist in validating further simulations which may then be used to similar effect.

7.1.3 TiB System And Ballistic Trials

Finally, in chapter 6, the validated current control technique was trialled on a different Ti-TiB MMC material system. The model provided a predicted microstructural outcome which was achieved and tested ballistically and further examined through microstructural examination, hardness testing and EBSD. It was demonstrated that the current control technique can be used at scale to tailor an outcome for practical effect in this manner as long as sufficient information exists about the sintering of the material system. The 250 mm plates also show that the current control technique provides the desired impact at a scale more practical for industry. In addition, the control plate is evidence for the challenge presented through thermal gradients existing at these scales naturally which this technique has potential to resolve through locationally specific heating. This would be the primary aspect of further work recommended here in this thesis.

Overall, the research in this thesis presents important developments in the FAST processing to provide additional flexibility, control, and understanding of the technique. By combining this technique with other FAST techniques and mould designs

there is potential for full control over locational heating during the process, allowing for absolute control over thermal profile and thus sintering and microstructural results. This has incredible potential for the process, and combined with the simulation in the FEA model's predictive capacity it may be possible to design, in advance, the final component to be produced in a single step from powder, or other waste materials.

7.2 Further Works

The demonstration of the impact and repeatability of the current control technique allows for opens up a huge variety of material systems and applications to future work, building on the results presented here. Initially this would focus on individual material systems but with a view to expanding into the sintering of dissimilar metals and materials through the focused channelling of these heating and electrical profiles.

7.2.1 Further Ti-6Al-4V Work

As mentioned, the primary avenue for further work would be the reduction of pre-existing thermal gradients in samples at scale. This would most simply be done using the most well understood system of Ti-6Al-4V. There is interest in producing thicker 80 and 250 mm diameter plates with reverse aperture insulation profiles for this purpose. The primary focus for this avenue would be using the MIPAR image analysis route from chapter 5 to examine samples of greater final height with 2 axes of thermal gradients to attempt to reduce using a combination of this technique and mould design. This would provide a solid impetus for industry to move towards the FAST process demonstrating it can generate homogeneous billets of known microstructure at any scale in a single step from powder.

7.2.2 Dissimilar Materials

The secondary avenue of potential is to utilise the predictable inhomogeneous distributions of temperature and current possible to sinter dissimilar materials that may otherwise be challenging to combine due to thermal incompatibilities or electrical differences in conductivity. The possibilities for research in this channel are extensive, however, it is recommended here to focus on the metallic ceramic systems as much is already known about the sintering of these materials. It may also be possible on a shorter timescale to utilise this inhomogeneous designable thermal gradient to generate differences in microstructure in temperature sensitive alloys such as Ti-6Al-4V to provide different properties throughout a produced sample for practical purposes such as connecting rods for engine production.

7.2.3 Additional TiB MMC V₅₀ Optimisation

The final direction of recommended further work is to continue the ballistic testing in chapter 6 to produce improved plates for armour purposes. There is much room for improvement including parametric studies for a rigorous analysis of the effect of both layer thickness and ceramic wt.% impact. This could potentially be carried out in combination with the thermal gradient work to reduce the those found impacting the resulting microstructure and improving the fracture toughness and strength of the plates. Two other aspects where these improvements could be focused would be the separate sintering of the titanium alloy rear face and TiB included layers with subsequent bonding to avoid excessive prior β grain growth, or the the addition of further surface TiB or TiB₂ plates to the attack face. Aiming primarily to provide more extreme hardness to ductile layering for the FGM to provide a processing window to test the remaining combinations within and aim for optimal combinations.

The successful demonstration of this technique and the simulations accurate predictive capacities have opened a wide variety of potential future work and exciting processing additions to the FAST technique, broadening the scope and providing more tools for manufacturers to reach their desired component in fewer steps using

less energy and more cost effective materials.

Appendix A

Appendix

A.1 Graphite Data

A.1.1 Thermal Conductivity

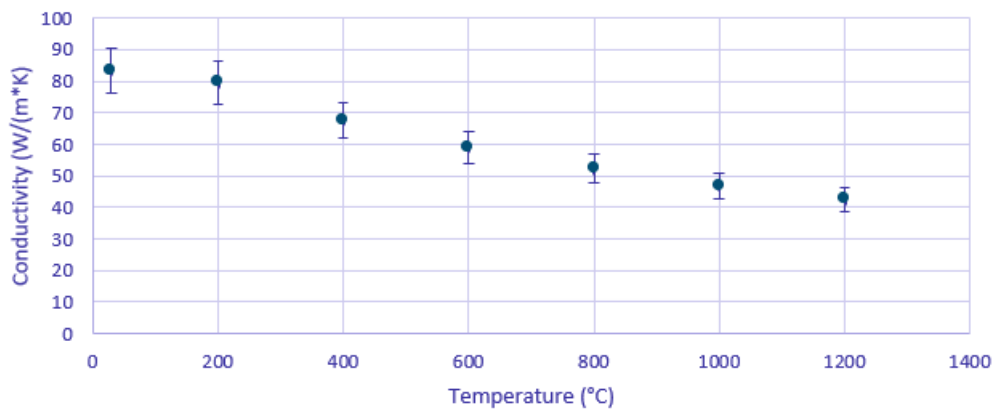


FIGURE A.1: Thermal Conductivity of TDX-1 grade ISO Graphite

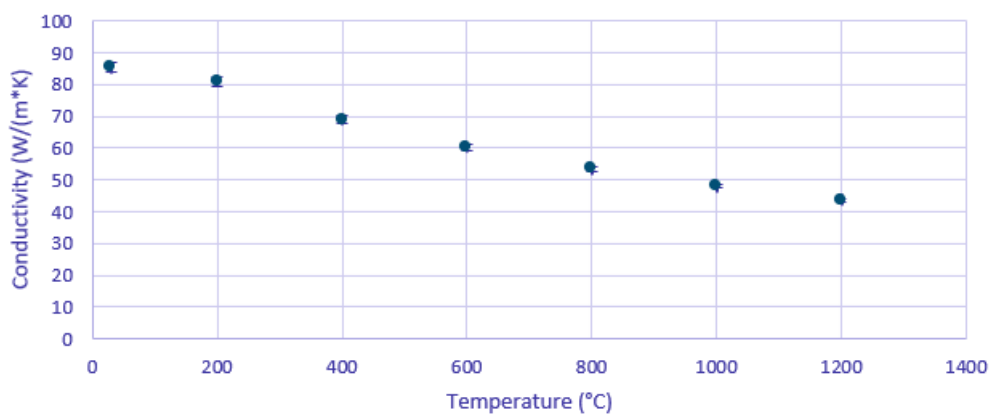


FIGURE A.2: Thermal Conductivity of TDX-2 grade ISO Graphite

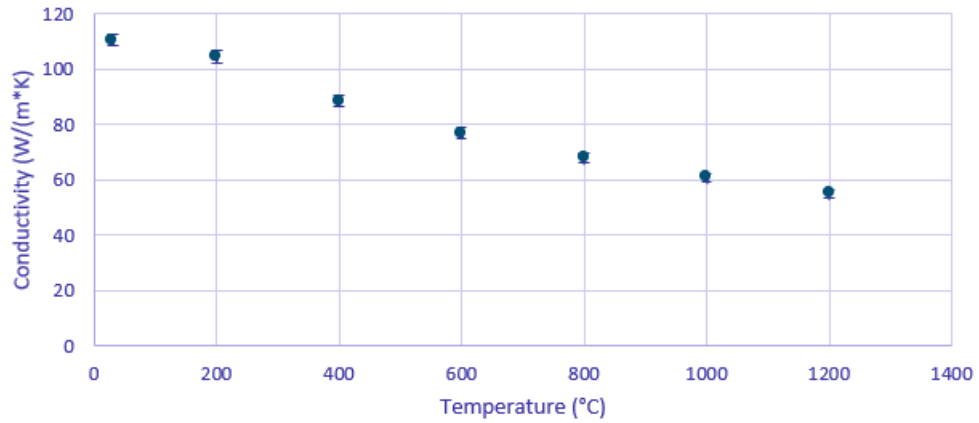


FIGURE A.3: Thermal Conductivity of TDX-3 grade ISO Graphite

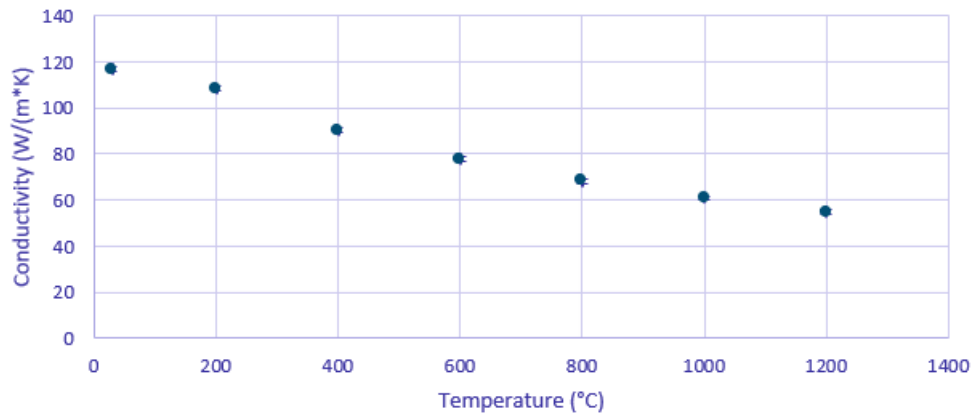


FIGURE A.4: Thermal Conductivity of TDX-4 grade ISO Graphite

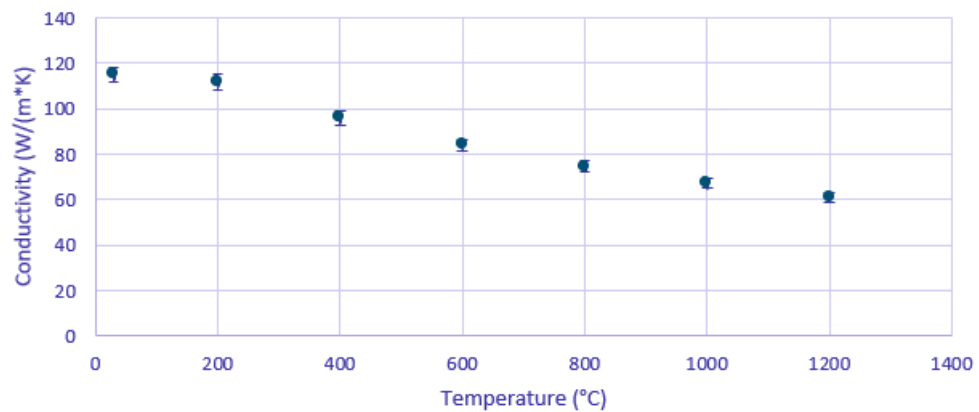


FIGURE A.5: Thermal Conductivity of TDX-5 grade ISO Graphite

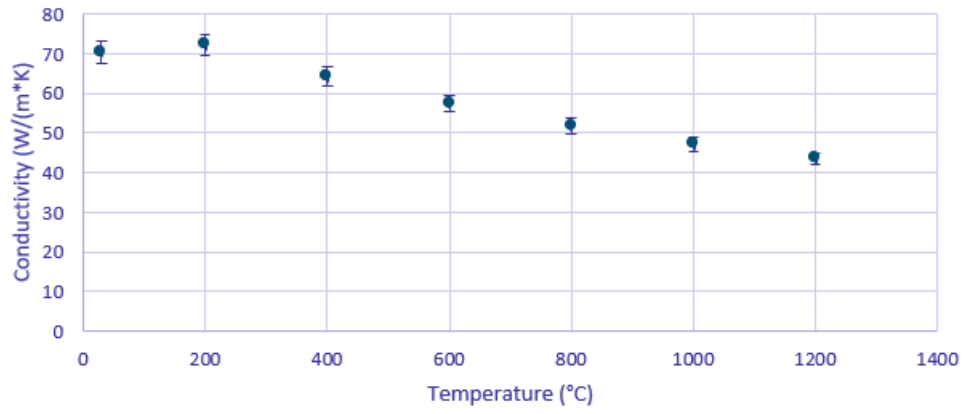


FIGURE A.6: Thermal Conductivity of TDX-6 grade ISO Graphite

Appendix B

Appendix

B.1 MIPAR Recipe

The MIPAR recipe for processing these 100x magnification etched micrographs at a scale factor of $0.5486 \mu\text{m}/\text{px}$ is as follows:

- **Apply Deep Learning:** DL Model Complete
- **Smart Cluster:** 2 10 Class 1 Dark to Bright
- **Basic Threshold:** 62 Bright Percentage
- **Reject Features:** Area 5000 px^2 Objects
- **Manual Edit:** Interruptible - *Removed for batch processing*
- **Invert**
- **Separate Features:** 10.00 Low 10 300 1
- **Reject Features:** Area 20 px^2 Objects
- **Invert**
- **Clean Boundaries:** 5
- **Reject Features:** Area 10000 px^2 Objects
- **Manual Edit:** Interruptible - *Removed for batch processing*
- **Clean Boundaries:** 4

- **Set Memory Image: #1**
- **TOTAL GRAINS:** Reject Features
- **COMPLETE GRAINS:** Remove Edges
- **Call Memory Image #1**
- **Invert**
- **Grain Boundary DL:** Uniform Dilation 20.0 px

B.2 Python Scripts

In this section the script used to process the MIPAR data in Python is included. # lines are 'commented' out meaning they have no impact on the code beyond explaining impacts.

B.2.1 MIPAR grain size heat map processing

```

8 import csv
9 import math
10 import numpy as np
11 import matplotlib.pyplot as plt
12 import pandas as pd
13 import seaborn as sns
14 import scipy as scp
15 from scipy.ndimage.filters import gaussian_filter
16 #from scipy import interpolate
17
18 imy=11
19 y = 1.12*np.linspace(0,imy-1,imy)
20 y = [round(num,2)for num in y]
21 y.reverse()
22 #Required Dimensions of image
22 imx=16
23 x = 1.12*np.linspace(0,imx-1,imx)
24 x = [round(num,2)for num in x]
25 #x= np.reshape(x,(imx,1))
26
27 #df = pd.read_csv('Full_5_Centre.csv')
28 df = pd.read_csv('Full_5_Edge.csv')
29 #df = pd.read_csv('Full_5_Centre.csv')
30 #df = pd.read_csv('A_5_Centre.csv')
31 #df = pd.read_csv('A_5_Edge.csv')
32 #df = pd.read_csv('C_5_Centre.csv')
33 #df = pd.read_csv('C_5_Edge.csv')
34
35 #-----
36
37 #df = pd.read_csv('Full_0_Centre.csv')
38 #df = pd.read_csv('Full_0_Edge.csv')
39 #df = pd.read_csv('C_0_Centre.csv')
40 #df = pd.read_csv('C_0_Edge.csv')
41 #df = pd.read_csv('RApp_0_Centre.csv')
42 #df = pd.read_csv('RApp_0_Edge.csv')
43 #df = pd.read_csv('A_0_Centre.csv')
44
45 Images = pd.unique(df['Image'])
46 #print(Images)
47 myDict = {}
48 AreaList = []
49
50
51 for im in Images:
52
53     Balthazar = df[df['Image']==im]
54     Dayta = Balthazar.to_numpy()[1:,2,3]
55     myDict[im] = Dayta
56     Area=list(myDict[im][:,1])
57     AVA=2*np.sqrt((np.average(Area))/math.pi)
58     AreaList.append(AVA)
59
60 newAreaList = np.array(AreaList).reshape(imy,imx)
61 #print(newAreaList)
62 newAreaList[1::2, :] = newAreaList[1::2, :-1]
63 types = type(newAreaList)
64 print(types)
65 #-----Plotting Section-----
66
67 GaussAreaArray = gaussian_filter(newAreaList, sigma=0)
68 #print(GaussAreaArray)
69 newAreaList2 = np.ndarray.tolist(newAreaList)
70 newGaussAreaArray = np.ndarray.tolist(GaussAreaArray)
71
72 newfunc = scp.interpolate.interp2d(x,y,newAreaList2, kind='cubic')
73 newfuncG = scp.interpolate.interp2d(x,y,newGaussAreaArray, kind='cubic')
74
75 xn = imx*1.12
76 xtotal = 1000
77 xnew = np.linspace(0,xn,xtotal)
78
79 yn = imy*1.12
80 ytotal = 1000
81 ynew = np.linspace(0,yn,ytotal)
82
83 fnew = newfuncG(xnew,ynew)
84
85
86 fig, axes = plt.subplots(2,1)
87
88 #fig.suptitle('Full Ins Av Grain size and Distributions')
89 p = sns.heatmap(GaussAreaArray,ax=axes[0],vmin=90, vmax=220, cbar_kws={'label':'Average Grain Diameter ($\mu$m)'},xticklabels = x,yticklabels = y)
90 #p = sns.heatmap(fnew,ax=axes[0],vmin=140, vmax=220, cbar_kws={'label':'Average Grain Diameter ($\mu$m)'},xticklabels = x,yticklabels = y)
91 #axes.set_yticklabels(y.astype(int))
92 #Plots the heatmap
93 sns.set(rc = {'figure.figsize':(16,14)})
94 sns.set(font_scale = 2)
95 #plt.legend()
96 p.set_xlabel('Micrograph Position (mm)', fontsize = 30)
97 p.set_ylabel('Micrograph Position (mm)', fontsize = 30)
98
99 plt.show()

```

FIGURE B.1: Python script for generation of grain size heat maps in chapter 5

Bibliography

- [1] W. Kroll, "The production of ductile titanium," *Transactions of the Electrochemical Society*, vol. 78, no. 1, p. 35, 1940.
- [2] J.-P. Monchoux, A. Couret, L. Durand, T. Voisin, Z. Trzaska, and M. Thomas, "Elaboration of metallic materials by sps: Processing, microstructures, properties, and shaping," *Metals*, vol. 11, no. 2, 2021, ISSN: 2075-4701.
- [3] M. Stuer, P. Bowen, and Z. Zhao, "Spark plasma sintering of ceramics: From modeling to practice," *Ceramics*, vol. 3, no. 4, pp. 476–493, 2020, ISSN: 2571-6131.
- [4] G. Ltjering and J. Williams, *Titanium, engineering materials and processes*, 2007.
- [5] M. Hunter, "Metallic titanium.," *Journal of the American Chemical Society*, vol. 32, no. 3, pp. 330–336, 1910.
- [6] N. S. Weston and M. Jackson, "Fast-forge of titanium alloy swarf: A solid-state closed-loop recycling approach for aerospace machining waste," *Metals*, vol. 10, no. 2, p. 296, 2020.
- [7] J. J. Pope, E. L. Calvert, N. S. Weston, and M. Jackson, "Fast-db: A novel solid-state approach for diffusion bonding dissimilar titanium alloy powders for next generation critical components," *Journal of Materials Processing Technology*, vol. 269, pp. 200–207, 2019.
- [8] H. Flower, "Microstructural development in relation to hot working of titanium alloys," *Materials Science and Technology*, vol. 6, no. 11, pp. 1082–1092, 1990.
- [9] C. Leyens and M. Peters, *Titanium and titanium alloys: fundamentals and applications*. Wiley Online Library, 2006.

- [10] W. D. Callister, D. G. Rethwisch, *et al.*, *Materials science and engineering: an introduction*. John Wiley & Sons New York, 2007, vol. 7.
- [11] G. Lütjering and J. C. Williams, *Titanium matrix composites*. Springer, 2007.
- [12] G. Welsch, R. Boyer, and E. Collings, *Materials properties handbook: titanium alloys*. ASM international, 1993.
- [13] G. Lütjering, "Influence of processing on microstructure and mechanical properties of (α + β) titanium alloys," *Materials Science and Engineering: A*, vol. 243, no. 1-2, pp. 32–45, 1998.
- [14] A. Attanasio, M. Gelfi, A. Pola, E. Ceretti, and C. Giardini, "Influence of material microstructures in micromilling of ti6al4v alloy," *Materials*, vol. 6, no. 9, pp. 4268–4283, 2013, ISSN: 1996-1944.
- [15] L. Bolzoni, E. M. Ruiz-Navas, and E Gordo, "Influence of sintering parameters on the properties of powder metallurgy ti-3al-2.5 v alloy," *Materials characterization*, vol. 84, pp. 48–57, 2013.
- [16] L Bolzoni, E. Ruiz-Navas, and E Gordo, "On the microstructure and properties of the ti-3al-2.5 v alloy obtained by powder metallurgy," in *TMS 2014: 143 rd Annual Meeting & Exhibition: Annual Meeting Supplemental Proceedings*, Springer, 2016, pp. 121–128.
- [17] M. I. Bal'shin, M. J. Bal'shin, M. I. Bal'shin, and S. Kiparisov, *General principles of powder metallurgy*.
- [18] S. Tsukerman, *Chapter iii—metal powders*, 1965.
- [19] C. G. McCracken, C. Motchenbacher, and D. P. Barbis, "Review of titanium-powder-production methods.," *International journal of powder metallurgy*, vol. 46, no. 5, 2010.
- [20] R. M. German, "Powder metallurgy science," *Metal Powder Industries Federation*, 105 College Rd. E, Princeton, N. J. 08540, U. S. A, 279, 1984.
- [21] C. A. W. Paper, *Comparison of plasma and electrode inert gas atomized powder*, <https://www.carpenteradditive.com/eiga-titanium-powder-whitepaper>, Accessed: 2023-04-07, 2020.

- [22] T. Saito, "A cost-effective p/m titanium matrix composite for automobile use," *Advanced Performance Materials*, vol. 2, pp. 121–144, 1995.
- [23] T. Clyne and P. J. Withers, *An introduction to metal matrix composites*. Cambridge university press, 1993.
- [24] J. L. Murray, "Phase diagram of titanium alloys," *ASM*, vol. 182, 1987.
- [25] W. Gooch and M. Burkins, "Development and ballistic testing of a functionally gradient ceramic-metal applique," May 2001.
- [26] S. Tamirisa and D Miracle, "An overview of titanium alloys modified with boron," *Ti-2007 Science and Technology*, p. 737, 2007.
- [27] Z. Ma, S. Tjong, and L Gen, "In-situ ti-tib metal–matrix composite prepared by a reactive pressing process," *Scripta materialia*, vol. 42, no. 4, pp. 367–373, 2000.
- [28] J Brandstötter and W Lengauer, "Multiphase reaction diffusion in transition metal-boron systems," *Journal of Alloys and compounds*, vol. 262, pp. 390–396, 1997.
- [29] B. Decker and J. Kasper, "The crystal structure of tib," *Acta Crystallographica*, vol. 7, no. 1, pp. 77–80, 1954.
- [30] J. Otte, "Investigating the formation and growth of in situ tib in titanium matrix composites," 2022.
- [31] M. Hyman, C McCullough, J. Valencia, C. Levi, and R Mehrabian, "Microstructure evolution in TiAl alloys with b additions: Conventional solidification," *Metallurgical Transactions A*, vol. 20, pp. 1847–1859, 1989.
- [32] S. H. Whang, "Rapidly solidified titanium alloys for high-temperature applications," *Journal of materials science*, vol. 21, pp. 2224–2238, 1986.
- [33] S Tamirisakandala, R. Bhat, D. Miracle, *et al.*, "Effect of boron on the beta transus of ti–6al–4v alloy," *Scripta Materialia*, vol. 53, no. 2, pp. 217–222, 2005.
- [34] L. Shufeng, K. Kondoh, H. Imai, B. Chen, L. Jia, and J. Umeda, "Microstructure and mechanical properties of p/m titanium matrix composites reinforced by in-situ synthesized tic–tib," *Materials Science and Engineering: A*, vol. 628, pp. 75–83, 2015.

- [35] V. Chandravanshi, R Sarkar, P Ghosal, S. Kamat, and T. Nandy, "Effect of minor additions of boron on microstructure and mechanical properties of as-cast near α titanium alloy," *Metallurgical and Materials Transactions A*, vol. 41, pp. 936–946, 2010.
- [36] J. Wang, X. Guo, J. Qin, D. Zhang, and W. Lu, "Microstructure and mechanical properties of investment casted titanium matrix composites with b4c additions," *Materials Science and Engineering: A*, vol. 628, pp. 366–373, 2015.
- [37] Z Fan, A. Miodownik, L Chandrasekaran, and M Ward-Close, "The young's moduli of in situ ti/tib composites obtained by rapid solidification processing," *Journal of Materials Science*, vol. 29, pp. 1127–1134, 1994.
- [38] T. M. T. Godfrey, "Production, microstructure and tensile properties of mechanically milled titanium-boron alloys," 2001.
- [39] T. Godfrey, P. Goodwin, and C. WardClose, "Production of titanium particulate metal matrix composite by mechanical milling," *Materials science and technology*, vol. 16, no. 7-8, pp. 753–758, 2000.
- [40] R. Gardiner, P. Goodwin, S. Dodd, and B. Viney, "Non-equilibrium synthesis of new materials," *Advanced Performance Materials*, vol. 3, pp. 343–364, 1996.
- [41] J. R. Silk, "The influence of secondary processing conditions on the mechanical properties and microstructure of a particle reinforced aluminium metal matrix composite," Ph.D. dissertation, Imperial College London, 2008.
- [42] T Sheppard and P. Chare, "The extrusion of atomized aluminium powders," *Powder Metallurgy*, vol. 15, no. 29, pp. 17–41, 1972.
- [43] H. Wen, Y. Zhao, Z. Zhang, O. Ertorer, S. Dong, and E. J. Lavernia, "The influence of oxygen and nitrogen contamination on the densification behavior of cryomilled copper powders during spark plasma sintering," *Journal of materials science*, vol. 46, pp. 3006–3012, 2011.
- [44] R. Heckel, "An analysis of powder compaction phenomena," *Trans. Metall. Soc. AIME*, vol. 221, pp. 1001–1008, 1961.
- [45] R. German, "Sintering theory and practice, edited by john wiley & sons," *Inc, Canada*, 1996.

- [46] A. S. Sharma, K. Biswas, B. Basu, and D. Chakravarty, "Spark plasma sintering of nanocrystalline Cu and Cu-10 wt Pct Pb alloy," *Metallurgical and Materials Transactions A*, vol. 42, pp. 2072–2084, 2011.
- [47] H. Atkinson and S Davies, "Fundamental aspects of hot isostatic pressing: An overview," *Metallurgical and materials transactions A*, vol. 31, pp. 2981–3000, 2000.
- [48] A. S. M. Handbook, "Volume 1," *Properties and Selection: Irons, Steels, and High Performance Alloys*, vol. 1, 2005.
- [49] R. Blackburns, *Hot isostatic pressing (hip)*, <https://www.rightonblackburns.co.uk/powder-metals/markets/hot-isostatic-pressing-hip>, Accessed: 2023-06-07.
- [50] Z. A. Munir, D. V. Quach, and M. Ohyanagi, "Electric current activation of sintering: A review of the pulsed electric current sintering process," *Journal of the American Ceramic Society*, vol. 94, no. 1, pp. 1–19, 2011.
- [51] Z. A. Munir, U. Anselmi-Tamburini, and M. Ohyanagi, "The effect of electric field and pressure on the synthesis and consolidation of materials: A review of the spark plasma sintering method," *Journal of materials science*, vol. 41, pp. 763–777, 2006.
- [52] R. Orru, R. Licheri, A. M. Locci, A. Cincotti, and G. Cao, "Consolidation/synthesis of materials by electric current activated/assisted sintering," *Materials Science and Engineering: R: Reports*, vol. 63, no. 4-6, pp. 127–287, 2009.
- [53] M. Rahaman, "Grain growth and microstructure control," *Ceramic processing and sintering*, pp. 541–620, 2003.
- [54] R. Castro and K. Van Benthem, *Sintering: mechanisms of convention nanodensification and field assisted processes*. Springer Science & Business Media, 2012, vol. 35.
- [55] D. Salamon, M. Eriksson, M. Nygren, and Z. Shen, "Can the use of pulsed direct current induce oscillation in the applied pressure during spark plasma sintering?" *Science and Technology of Advanced Materials*, 2012.

- [56] D. M. Hulbert, A. Anders, D. V. Dudina, *et al.*, "The absence of plasma in "spark plasma sintering"," *Journal of Applied Physics*, vol. 104, no. 3, p. 033 305, 2008.
- [57] D. Hulbert, A Anders, and J Andersson, "Ej lavernia, ak mukherjee," *Scr. Mater*, vol. 60, p. 835, 2009.
- [58] O. A. Graeve, H. Singh, and A. Clifton, "Synthesis and consolidation of zirconia nanopowders via a unique reverse micelle synthesis process and spark plasma sintering," *Ceramic Transactions*, vol. 194, p. 209, 2006.
- [59] K. Sinha, B. Pearson, S. R. Casolco, J. E. Garay, and O. A. Graeve, "Synthesis and consolidation of baal2si2o8: Eu: Development of an integrated process for luminescent smart ceramic materials," *Journal of the American Ceramic Society*, vol. 92, no. 11, pp. 2504–2511, 2009.
- [60] J. P. Kelly and O. A. Graeve, "Spark plasma sintering as an approach to manufacture bulk materials: Feasibility and cost savings," *Jom*, vol. 67, pp. 29–33, 2015.
- [61] M. Bever and P. Duwez, "Gradients in composite materials," *Materials Science and Engineering*, vol. 10, pp. 1–8, 1972.
- [62] H. Feng, Q. Meng, Y. Zhou, and D. Jia, "Spark plasma sintering of functionally graded material in the ti–tib2–b system," *Materials Science and Engineering: A*, vol. 397, no. 1-2, pp. 92–97, 2005.
- [63] O. Guillon, J. Gonzalez-Julian, B. Dargatz, *et al.*, "Field-assisted sintering technology/spark plasma sintering: Mechanisms, materials, and technology developments," *Advanced Engineering Materials*, vol. 16, no. 7, pp. 830–849, 2014.
- [64] N. Weston and M Jackson, "Fast-forge- a new cost-effective hybrid processing route for consolidating titanium powder into near net shape forged components," *Journal of Materials Processing Technology*, vol. 243, pp. 335–346, 2017.
- [65] C. Musa, R. Licheri, A. M. Locci, *et al.*, "Energy efficiency during conventional and novel sintering processes: The case of ti–al2o3–tic composites," *Journal of Cleaner Production*, vol. 17, no. 9, pp. 877–882, 2009.

- [66] C. Manière, E. Nigito, L. Durand, A. Weibel, Y. Beynet, and C. Estournes, "Spark plasma sintering and complex shapes: The deformed interfaces approach," *Powder technology*, vol. 320, pp. 340–345, 2017.
- [67] M. Tokita, "Development of large-size ceramic/metal bulk fgm fabricated by spark plasma sintering," in *Materials science forum*, Trans Tech Publ, vol. 308, 1999, pp. 83–88.
- [68] T. Voisin, L. Durand, N. Karnatak, *et al.*, "Temperature control during spark plasma sintering and application to up-scaling and complex shaping," *Journal of Materials Processing Technology*, vol. 213, no. 2, pp. 269–278, 2013.
- [69] W. Yucheng and F. Zhengyi, "Study of temperature field in spark plasma sintering," *Materials Science and Engineering: B*, vol. 90, no. 1-2, pp. 34–37, 2002.
- [70] O. Ertorer, T. D. Topping, Y. Li, W. Moss, and E. J. Lavernia, "Nanostructured ti consolidated via spark plasma sintering," *Metallurgical and Materials Transactions A*, vol. 42, pp. 964–973, 2011.
- [71] M. Shongwe, M. M. Ramakokovhu, S Diouf, *et al.*, "Effect of starting powder particle size and heating rate on spark plasma sintering of feni alloys," *Journal of Alloys and compounds*, vol. 678, pp. 241–248, 2016.
- [72] M Pellizzari, A Fedrizzi, and M Zadra, "Influence of processing parameters and particle size on the properties of hot work and high speed tool steels by spark plasma sintering," *Materials & Design*, vol. 32, no. 4, pp. 1796–1805, 2011.
- [73] Y. Kim, C. Shin, T. Kim, and S.-W. Kang, "Inhomogeneity in thermoelectrics caused by peltier effect-induced temperature gradient during spark plasma sintering," *Scripta Materialia*, vol. 158, pp. 46–49, 2019.
- [74] E. A. Olevsky and L. Froyen, "Impact of thermal diffusion on densification during sps," *Journal of the American Ceramic Society*, vol. 92, S122–S132, 2009.
- [75] T. B. Holland, U. Anselmi-Tamburini, D. V. Quach, T. B. Tran, and A. K. Mukherjee, "Effects of local joule heating during the field assisted sintering of ionic ceramics," *Journal of the European Ceramic Society*, vol. 32, no. 14, pp. 3667–3674, 2012.

- [76] G Molénat, L Durand, J Galy, and A Couret, "Temperature control in spark plasma sintering: An fem approach," *Journal of Metallurgy*, vol. 2010, 2010.
- [77] A. Pavia, L. Durand, F. Ajustron, *et al.*, "Electro-thermal measurements and finite element method simulations of a spark plasma sintering device," *Journal of Materials Processing Technology*, vol. 213, no. 8, pp. 1327–1336, 2013.
- [78] S. Grasso, H. Yoshida, H. Porwal, Y. Sakka, and M. Reece, "Highly transparent α -alumina obtained by low cost high pressure sps," *Ceramics International*, vol. 39, no. 3, pp. 3243–3248, 2013.
- [79] G. Marnier, C. Keller, J. Noudem, and E. Hug, "Functional properties of a spark plasma sintered ultrafine-grained 316l steel," *Materials & Design*, vol. 63, pp. 633–640, 2014.
- [80] C. B. Danisman, B. Yavas, O. Yucel, F. Sahin, and G. Goller, "Processing and characterization of spark plasma sintered tzm alloy," *Journal of Alloys and Compounds*, vol. 685, pp. 860–868, 2016.
- [81] D. Liu, Y. Xiong, T. D. Topping, *et al.*, "Spark plasma sintering of cryomilled nanocrystalline al alloy-part ii: Influence of processing conditions on densification and properties," *Metallurgical and Materials Transactions A*, vol. 43, pp. 340–350, 2012.
- [82] D. Guan, W. M. Rainforth, J. Sharp, J. Gao, and I. Todd, "On the use of cryomilling and spark plasma sintering to achieve high strength in a magnesium alloy," *Journal of Alloys and Compounds*, vol. 688, pp. 1141–1150, 2016.
- [83] Y. Achenani, M. Saâdaoui, A. Cheddadi, G. Bonnefont, and G. Fantozzi, "Finite element modeling of spark plasma sintering: Application to the reduction of temperature inhomogeneities, case of alumina," *Materials & Design*, vol. 116, pp. 504–514, 2017.
- [84] E. A. Olevsky, C. Garcia-Cardona, W. L. Bradbury, C. D. Haines, D. G. Martin, and D. Kapoor, "Fundamental aspects of spark plasma sintering: Ii. finite element analysis of scalability," *Journal of the American Ceramic Society*, vol. 95, no. 8, pp. 2414–2422, 2012.

- [85] P. Mondalek, L. Silva, L. Durand, and M. Bellet, "Numerical modelling of thermal-electrical phenomena in spark plasma sintering," in *AIP Conference Proceedings*, American Institute of Physics, vol. 1252, 2010, pp. 697–704.
- [86] B. McWilliams and A. Zavaliangos, "Multi-phenomena simulation of electric field assisted sintering," *Journal of Materials Science*, vol. 43, pp. 5031–5035, 2008.
- [87] A. Becker, S. Angst, A. Schmitz, *et al.*, "The effect of peltier heat during current activated densification," *Applied Physics Letters*, vol. 101, no. 1, p. 013 113, 2012.
- [88] Z.-H. Zhang, Z.-F. Liu, J.-F. Lu, X.-B. Shen, F.-C. Wang, and Y.-D. Wang, "The sintering mechanism in spark plasma sintering—proof of the occurrence of spark discharge," *Scripta materialia*, vol. 81, pp. 56–59, 2014.
- [89] D. Schwesig, G. Schierning, R. Theissmann, *et al.*, "From nanoparticles to nanocrystalline bulk: Percolation effects in field assisted sintering of silicon nanoparticles," *Nanotechnology*, vol. 22, no. 13, p. 135 601, 2011.
- [90] G. Maizza, G. D. Mastrorillo, S. Grasso, H. Ning, and M. J. Reece, "Peltier effect during spark plasma sintering (sps) of thermoelectric materials," *Journal of Materials Science*, vol. 52, pp. 10 341–10 352, 2017.
- [91] J. Xu, J. Lang, D. An, J. Liu, Z. Hu, and Z. Xie, "A novel alternating current-assisted sintering method for rapid densification of Al_2O_3 ceramics with ultrahigh flexural strength," *Ceramics International*, vol. 46, no. 4, pp. 5484–5488, 2020.
- [92] A. S. Nowick, "Diffusion in solids: Recent developments," 2012.
- [93] N. Chawake, L. D. Pinto, A. K. Srivastav, K. Akkiraju, B. Murty, and R. S. Kottada, "On joule heating during spark plasma sintering of metal powders," *Scripta Materialia*, vol. 93, pp. 52–55, 2014.
- [94] C. S. Bonifacio, T. B. Holland, and K. van Benthem, "Evidence of surface cleaning during electric field assisted sintering," *Scripta Materialia*, vol. 69, no. 11-12, pp. 769–772, 2013.

- [95] V Mamedov, "Spark plasma sintering as advanced pm sintering method," *Powder Metallurgy*, vol. 45, no. 4, pp. 322–328, 2002.
- [96] T. Saunders, S. Grasso, and M. J. Reece, "Plasma formation during electric discharge (50 v) through conductive powder compacts," *Journal of the European Ceramic Society*, vol. 35, no. 3, pp. 871–877, 2015.
- [97] S. Schwarz, A. M. Thron, J. Rufner, K. van Benthem, and O. Guillon, "Low temperature sintering of nanocrystalline zinc oxide: Effect of heating rate achieved by field assisted sintering/spark plasma sintering," *Journal of the American Ceramic Society*, vol. 95, no. 8, pp. 2451–2457, 2012.
- [98] J.-L. Hébrard, P. Nortier, M. Pijolat, and M. Soustelle, "Initial sintering of sub-micrometer titania anatase powder," *Journal of the American Ceramic Society*, vol. 73, no. 1, pp. 79–84, 1990.
- [99] C. Yu, P. Cao, and M. I. Jones, "Titanium powder sintering in a graphite furnace and mechanical properties of sintered parts," *Metals*, vol. 7, no. 2, p. 67, 2017.
- [100] B.-K. Yoon, E.-Y. Chin, and S.-J. L. Kang, "Dedensification during sintering of BaTiO_3 caused by the decomposition of residual BaCO_3 ," *Journal of the American Ceramic Society*, vol. 91, no. 12, pp. 4121–4124, 2008.
- [101] Z. Z. Fang, *Sintering of advanced materials*. Elsevier, 2010.
- [102] Y. Zhu, N. Li, W. Li, L. Niu, and Z. Li, "Atomistic study on the sintering process and the strengthening mechanism of al-graphene system," *Materials*, vol. 15, no. 7, 2022, ISSN: 1996-1944.
- [103] J. M. Sestito, F. Abdeljawad, T. A. Harris, Y. Wang, and A. Roach, "An atomistic simulation study of nanoscale sintering: The role of grain boundary misorientation," *Computational Materials Science*, vol. 165, pp. 180–189, 2019, ISSN: 0927-0256.
- [104] L. Engelke, L. Brendel, and D. E. Wolf, "Microstructure evolution during sintering: Discrete element method approach," *Journal of the American Ceramic Society*, vol. 106, no. 8, pp. 5022–5032, 2023.

- [105] T. Matsuda, "Development of a dem taking account of neck increments caused by surface diffusion for sintering and application to analysis of the initial stage of sintering," *Computational Materials Science*, vol. 196, p. 110 525, 2021.
- [106] R. Courant, "Variational methods for the solution of problems of equilibrium and vibrations," 1943.
- [107] A. Vidoz and W. Rothwell, "Research report–lockheed palo alto research laboratory," *Materials Science Lab., Palo Alto, CA, USA*, 1969.
- [108] A. Raichenko, G. Burenkov, and V. Leshchinsky, "Theoretical analysis of the elementary act of electric discharge sintering," *Physics Sinter.*, vol. 5, pp. 2–2, 1973.
- [109] J. Daurelle, R Ocelli, and R Martin, "Finite-element modeling of radiation heat transfer coupled with conduction in an adaptive method," *Numerical Heat Transfer, Part B Fundamentals*, vol. 25, no. 1, pp. 61–73, 1994.
- [110] J. C. Maxwell, *A treatise on electricity and magnetism: Pt. III. Magnetism. pt. IV. Electromagnetism*. Clarendon press, 1881, vol. 2.
- [111] J. S. Dean, J. H. Harding, and D. C. Sinclair, "Simulation of impedance spectra for a full three-dimensional ceramic microstructure using a finite element model," *Journal of the American Ceramic Society*, vol. 97, no. 3, pp. 885–891, 2014.
- [112] A. D. Preston, "Understanding and utilization of thermal gradients in spark plasma sintering for graded microstructure and mechanical properties," Ph.D. dissertation, Colorado State University, 2022.
- [113] C. Manière, A. Pavia, L. Durand, G. Chevallier, K. Afanga, and C. Estournès, "Finite-element modeling of the electro-thermal contacts in the spark plasma sintering process," *Journal of the European Ceramic Society*, vol. 36, no. 3, pp. 741–748, 2016.
- [114] C. Wolff, S. Mercier, H. Couque, and A. Molinari, "Modeling of conventional hot compaction and spark plasma sintering based on modified micromechanical models of porous materials," *Mechanics of Materials*, vol. 49, pp. 72–91, 2012.

- [115] C. Wolff, S. Mercier, H. Couque, A. Molinari, F. Bernard, and F. Naimi, "Thermal-electrical-mechanical simulation of the nickel densification by spark plasma sintering. comparison with experiments," *Mechanics of Materials*, vol. 100, pp. 126–147, 2016.
- [116] K Matsugi, H Kuramoto, T Hatayama, and O Yanagisawa, "Temperature distribution at steady state under constant current discharge in spark sintering process of ti and al₂o₃ powders," *Journal of Materials Processing Technology*, vol. 134, no. 2, pp. 225–232, 2003.
- [117] K Matsugi, H Kuramoto, O Yanagisawa, and M Kiritani, "A case study for production of perfectly sintered complex compacts in rapid consolidation by spark sintering," *Materials Science and Engineering: A*, vol. 354, no. 1-2, pp. 234–242, 2003.
- [118] A. Zavaliangos, J. Zhang, M. Krammer, and J. R. Groza, "Temperature evolution during field activated sintering," *Materials Science and Engineering: A*, vol. 379, no. 1-2, pp. 218–228, 2004.
- [119] J. Zhang, *Numerical simulation of thermoelectric phenomena in field activated sintering*. Drexel University, 2004.
- [120] K. Vanmeensel, A. Laptev, J Hennicke, J. Vleugels, and O. Van der Biest, "Modelling of the temperature distribution during field assisted sintering," *Acta Materialia*, vol. 53, no. 16, pp. 4379–4388, 2005.
- [121] G Maizza, S Grasso, and Y Sakka, "Moving finite-element mesh model for aiding spark plasma sintering in current control mode of pure ultrafine wc powder," *Journal of Materials Science*, vol. 44, pp. 1219–1236, 2009.
- [122] K. Vanmeensel, A. Laptev, O. Van der Biest, and J. Vleugels, "Field assisted sintering of electro-conductive ZrO₂ based composites," *Journal of the European Ceramic Society*, vol. 27, no. 2-3, pp. 979–985, 2007.
- [123] C. Manière, A. Pavia, L. Durand, *et al.*, "Pulse analysis and electric contact measurements in spark plasma sintering," *Electric Power Systems Research*, vol. 127, pp. 307–313, 2015.

- [124] X. Wei, D. Giuntini, A. L. Maximenko, C. D. Haines, and E. A. Olevsky, "Experimental investigation of electric contact resistance in spark plasma sintering tooling setup," *Journal of the American Ceramic Society*, vol. 98, no. 11, pp. 3553–3560, 2015.
- [125] C. Manière, L. Durand, E. Brisson, *et al.*, "Contact resistances in spark plasma sintering: From in-situ and ex-situ determinations to an extended model for the scale up of the process," *Journal of the European Ceramic Society*, vol. 37, no. 4, pp. 1593–1605, 2017.
- [126] B. McWilliams, A. Zavaliangos, K. C. Cho, and R. J. Dowding, "The modeling of electric-current-assisted sintering to produce bulk nanocrystalline tungsten," *Jom*, vol. 58, pp. 67–71, 2006.
- [127] E. A. Olevsky, S. Kandukuri, and L. Froyen, "Consolidation enhancement in spark-plasma sintering: Impact of high heating rates," *Journal of Applied Physics*, vol. 102, no. 11, p. 114913, 2007.
- [128] P. Mondalek, L. Silva, and M. Bellet, "A numerical model for powder densification by sps technique," *Advanced Engineering Materials*, vol. 13, no. 7, pp. 587–593, 2011.
- [129] M. M. Rahman, A. Ariffin, and S. Nor, "Development of a finite element model of metal powder compaction process at elevated temperature," *Applied Mathematical Modelling*, vol. 33, no. 11, pp. 4031–4048, 2009.
- [130] R. J. Smit, W. M. Brekelmans, and H. E. Meijer, "Prediction of the mechanical behavior of nonlinear heterogeneous systems by multi-level finite element modeling," *Computer methods in applied mechanics and engineering*, vol. 155, no. 1-2, pp. 181–192, 1998.
- [131] S. Galen and A. Zavaliangos, "Strength anisotropy in cold compacted ductile and brittle powders," *Acta Materialia*, vol. 53, no. 18, pp. 4801–4815, 2005.
- [132] A. Zavaliangos, "A numerical study of the development of tensile principal stresses during die compaction," *Particulate Science and Technology*, vol. 21, no. 2, pp. 105–115, 2003.

- [133] C.-y. Wu, A. C. Cocks, and O. T. Gillia, "Die filling and powder transfer," *International journal of powder metallurgy*, vol. 39, no. 4, 2003.
- [134] D. TRAIN, "Transmission forces through a powder mass during the process of pelleting," *Trans. Inst. Chem. Eng.*, vol. 35, pp. 258–266, 1957.
- [135] H. S. Kim, "Densification modelling for nanocrystalline metallic powders," *Journal of Materials Processing Technology*, vol. 140, no. 1-3, pp. 401–406, 2003.
- [136] C. Manière, U. Kus, L. Durand, *et al.*, "Identification of the Norton-Green compaction model for the prediction of the Ti-6Al-4V densification during the spark plasma sintering process," *Advanced Engineering Materials*, vol. 18, no. 10, pp. 1720–1727, 2016.
- [137] N. S. Weston, F Derguti, A Tudball, and M Jackson, "Spark plasma sintering of commercial and development titanium alloy powders," *Journal of Materials Science*, pp. 4860–4878, 2015, ISSN: 1573-4803.
- [138] S. Chakraborty, A. Mallick, D. Debnath, and P. Das, "Densification, mechanical and tribological properties of ZrB_2 by sps: Effect of pulsed current," *International Journal of Refractory Metals and Hard Materials*, vol. 48, pp. 150–156, 2015, ISSN: 0263-4368.
- [139] S. OKAWA and K. WATANABE, "Chemical mechanical polishing of titanium with colloidal silica containing hydrogen peroxide and mirror polishing and surface properties," *Dental Materials Journal*, vol. 28, no. 1, pp. 68–74, 2009. DOI: 10.4012/dmj.28.68.
- [140] C. A. Schneider, W. S. Rasband, and K. W. Eliceiri, "Nih image to imagej: 25 years of image analysis," *Nature methods*, vol. 9, no. 7, pp. 671–675, 2012.
- [141] C. Wang, L. Cheng, and Z. Zhao, "FEM analysis of the temperature and stress distribution in spark plasma sintering: Modelling and experimental validation," *Computational materials science*, vol. 49, no. 2, pp. 351–362, 2010.
- [142] C. Manière, L. Durand, E. Brisson, *et al.*, "Contact resistances in spark plasma sintering: From in-situ and ex-situ determinations to an extended model for the scale up of the process," *Journal of the European Ceramic Society*, vol. 37, no. 4, pp. 1593–1605, 2017, ISSN: 1873619X.

- [143] C. Manière, E. Nigito, L. Durand, A. Weibel, Y. Beynet, and C. Estournès, "Spark plasma sintering and complex shapes: The deformed interfaces approach," *Powder Technology*, vol. 320, pp. 340–345, 2017.
- [144] M. Shahedi Asl, Z. Ahmadi, A. Sabahi Namini, A. Babapoor, and A. Motallebzadeh, "Spark plasma sintering of tic–sicw ceramics," *Ceramics International*, vol. 45, no. 16, pp. 19 808–19 821, 2019, ISSN: 0272-8842.
- [145] B. Niu, F. Zhang, J. Zhang, W. Ji, W. Wang, and Z. Fu, "Ultra-fast densification of boron carbide by flash spark plasma sintering," *Scripta Materialia*, vol. 116, pp. 127–130, 2016, ISSN: 1359-6462.
- [146] E. Calvert, A. Knowles, J. Pope, D. Dye, and M. Jackson, "Novel high strength titanium-titanium composites produced using field-assisted sintering technology (fast)," *Scripta Materialia*, vol. 159, pp. 51–57, 2019, ISSN: 1359-6462.
- [147] Z. Trzaska, C. Collard, L. Durand, *et al.*, "Spark plasma sintering microscopic mechanisms of metallic systems: Experiments and simulations," *Journal of the American Ceramic Society*, vol. 102, no. 2, pp. 654–661, 2019.
- [148] M. Abedi, S. Sovizi, A. Azarniya, *et al.*, "An analytical review on spark plasma sintering of metals and alloys: From processing window, phase transformation, and property perspective," *Critical Reviews in Solid State and Materials Sciences*, vol. 0, no. 0, pp. 1–46, 2022.
- [149] T. Voisin, J.-P. Monchoux, L. Durand, N. Karnatak, M. Thomas, and A. Couret, "An Innovative Way to Produce γ -TiAl Blades: Spark Plasma Sintering," *Advanced Engineering Materials*, vol. 17, no. 10, pp. 1408–1413, 2015.
- [150] G. Delaizir, G. Bernard-Granger, J. Monnier, *et al.*, "A comparative study of spark plasma sintering (sps), hot isostatic pressing (hip) and microwaves sintering techniques on p-type Bi_2Te_3 thermoelectric properties," *Materials Research Bulletin*, vol. 47, no. 8, pp. 1954–1960, 2012, ISSN: 0025-5408.
- [151] E. Macía, A. García-Junceda, M. Serrano, M. Hernández-Mayoral, L. Diaz, and M. Campos, "Effect of the heating rate on the microstructure of a ferritic odds steel with four oxide formers (y-ti-al-zr) consolidated by spark plasma

- sintering (sps)," *Journal of Nuclear Materials*, vol. 518, pp. 190–201, 2019, ISSN: 0022-3115.
- [152] E. Zapata-Solvas, D. Gómez-García, A. Domínguez-Rodríguez, and R. I. Todd, "Ultra-fast and energy-efficient sintering of ceramics by electric current concentration," *Scientific Reports*, vol. 5, pp. 1–7, 2015, ISSN: 20452322.
- [153] G. Lee, C. Manière, J. McKittrick, and E. A. Olevsky, "Electric current effects in spark plasma sintering: From the evidence of physical phenomenon to constitutive equation formulation," *Scripta Materialia*, vol. 170, pp. 90–94, 2019, ISSN: 13596462.
- [154] C. Manière, E. Torresani, and E. A. Olevsky, "Simultaneous spark plasma sintering of multiple complex shapes," *Materials*, vol. 12, no. 2, pp. 1–14, 2019, ISSN: 19961944.
- [155] A. P. Mouritz, *Introduction to aerospace materials*. Elsevier, 2012.
- [156] C. Leyens and M. Peters, *Titanium and titanium alloys: fundamentals and applications*. John Wiley & Sons, 2003.
- [157] Z.-Y. Hu, Z.-H. Zhang, X.-W. Cheng, F.-C. Wang, Y.-F. Zhang, and S.-L. Li, "A review of multi-physical fields induced phenomena and effects in spark plasma sintering: Fundamentals and applications," *Materials & Design*, vol. 191, p. 108662, 2020.
- [158] J. E. Garay, "Current-activated, pressure-assisted densification of materials," *Annual Review of Materials Research*, vol. 40, pp. 445–468, 2010, ISSN: 15317331.
- [159] J. P. Kelly and O. A. Graeve, "Spark Plasma Sintering as an Approach to Manufacture Bulk Materials: Feasibility and Cost Savings," *Jom*, vol. 67, no. 1, pp. 29–33, 2015, ISSN: 15431851.
- [160] M. Eriksson, Z.-z. Shen, and M. Nygren, "Fast densification and deformation of titanium powder," *Powder Metallurgy*, vol. 48, pp. 231–236, Sep. 2005.
- [161] D. Wang, H. Yuan, and J. Qiang, "The microstructure evolution, mechanical properties and densification mechanism of TiAl-based alloys prepared by spark plasma sintering," *Metals*, vol. 7, no. 6, 2017, ISSN: 2075-4701.

- [162] X. Li, C. Yang, H. Lu, X. Luo, Y. Li, and O. Ivasishin, "Correlation between atomic diffusivity and densification mechanism during spark plasma sintering of titanium alloy powders," *Journal of Alloys and Compounds*, vol. 787, pp. 112–122, 2019, ISSN: 0925-8388.
- [163] S. Xie, R. Li, T. Yuan, *et al.*, "Viscous flow activation energy adaptation by isothermal spark plasma sintering applied with different current mode," *Scripta Materialia*, vol. 149, pp. 125–128, 2018, ISSN: 1359-6462.
- [164] Z. Trzaska, G. Bonnefont, G. Fantozzi, and J.-P. Monchoux, "Comparison of densification kinetics of a tial powder by spark plasma sintering and hot pressing," *Acta Materialia*, vol. 135, pp. 1–13, 2017, ISSN: 1359-6454.
- [165] C. Yang, M. Zhu, X. Luo, *et al.*, "Influence of powder properties on densification mechanism during spark plasma sintering," *Scripta Materialia*, vol. 139, pp. 96–99, 2017, ISSN: 1359-6462.
- [166] K. Vanmeensel, A. Laptev, J. Hennicke, J. Vleugels, and O. Van der Biest, "Modelling of the temperature distribution during field assisted sintering," *Acta Materialia*, vol. 53, no. 16, pp. 4379–4388, 2005, ISSN: 1359-6454.
- [167] C. Multiphysics, "Introduction to comsol multiphysics®," *COMSOL Multiphysics*, Burlington, MA, accessed Feb, vol. 9, no. 2018, p. 32, 1998.
- [168] E. J. Dickinson, H. Ekström, and E. Fontes, "Comsol multiphysics®: Finite element software for electrochemical analysis. a mini-review," *Electrochemistry Communications*, vol. 40, pp. 71–74, 2014, ISSN: 1388-2481.
- [169] S. Li, Y. Liu, F. Sun, and H. Fang, "Multi-particle molecular dynamics simulation: Shell thickness effects on sintering process of Cu-Ag core-shell nanoparticles," *Journal of Nanoparticle Research*, 2021.
- [170] C. Wang, L. Cheng, and Z. Zhao, "Fem analysis of the temperature and stress distribution in spark plasma sintering: Modelling and experimental validation," *Computational materials science*, vol. 49, no. 2, pp. 351–362, 2010.
- [171] E. A. Olevsky, V. Tikare, and T. Garino, "Multi-scale study of sintering: A review," *Journal of the American Ceramic Society*, vol. 89, no. 6, pp. 1914–1922, 2006.

- [172] E. A. Olevsky, C. Garcia-Cardona, W. L. Bradbury, C. D. Haines, D. G. Martin, and D. Kapoor, "Fundamental aspects of spark plasma sintering: II. Finite element analysis of scalability," *Journal of the American Ceramic Society*, vol. 95, no. 8, pp. 2414–2422, 2012, ISSN: 00027820.
- [173] C. Manière, A. Pavia, L. Durand, G. Chevallier, K. Afanga, and C. Estournès, "Finite-element modeling of the electro-thermal contacts in the spark plasma sintering process," *Journal of the European Ceramic Society*, vol. 36, no. 3, pp. 741–748, 2016.
- [174] O. Levano Blanch, D. Lunt, G. J. Baxter, and M. Jackson, "Deformation behaviour of a fast diffusion bond processed from dissimilar titanium alloy powders," *Metallurgical and Materials Transactions A*, vol. 52, no. 7, pp. 3064–3082, 2021.
- [175] J. Sosa, D. Huber, B. Welk, and H. Fraser, "Mipar™: 2d and 3d image analysis software designed by materials scientists, for all scientists," *Microscopy and Microanalysis*, vol. 23, no. S1, 230–231, 2017.
- [176] Z. Fu, M. Freihart, L. Wahl, T. Fey, P. Greil, and N. Travitzky, "Micro-and macroscopic design of alumina ceramics by robocasting," *Journal of the European Ceramic Society*, vol. 37, no. 9, pp. 3115–3124, 2017.
- [177] H. Zhang, J. Xiong, Z. Guo, T. Yang, J. Liu, and T. Hua, "Microstructure, mechanical properties, and cutting performances of wc-co cemented carbides with ru additions," *Ceramics International*, vol. 47, no. 18, pp. 26 050–26 062, 2021.
- [178] S. Semiatin, J. Soper, and I. Sukonnik, "Short-time beta grain growth kinetics for a conventional titanium alloy," *Acta Materialia*, vol. 44, no. 5, pp. 1979–1986, 1996, ISSN: 1359-6454.
- [179] Y. Shen, Y. Wang, S. Du, Z. Yang, H. Cheng, and F. Wang, "Effects of the adhesive layer on the multi-hit ballistic performance of ceramic/metal composite armors," *Journal of Materials Research and Technology*, vol. 13, pp. 1496–1508, 2021, ISSN: 2238-7854.

- [180] J. Broos and R Gunters, "Study on the ballistic performance of monolithic ceramic plates," in *Proceedings of the 23 rd International Symposium on Ballistics, Tarragona, Spain, 2007*, pp. 16–20.
- [181] M. Chouhan, P. Kumar, L. Thakur, and S. K. Verma, "A comparative study on the ballistic performance of multilayered sic/aa7075 functionally graded armor materials," *Journal of Materials Engineering and Performance*, pp. 1–22, 2023.
- [182] B. Zhang, Z. Zhong, J. Ye, *et al.*, "Microstructure and anti-penetration performance of continuous gradient ti/tib–tib₂ composite fabricated by spark plasma sintering combined with tape casting," *Ceramics International*, vol. 46, no. 7, pp. 9957–9961, 2020, ISSN: 0272-8842.
- [183] S. Failla, S. Fu, D. Sciti, and S. Grasso, "Flash spark plasma sintering of pure tib₂," *Open Ceramics*, vol. 5, p. 100 075, 2021, ISSN: 2666-5395.
- [184] N. Weston, F Derguti, A Tudball, and M Jackson, "Spark plasma sintering of commercial and development titanium alloy powders," *Journal of Materials Science*, vol. 50, pp. 4860–4878, 2015.
- [185] N. Gupta, V. Prasad, V Madhu, and B. Basu, "Ballistic studies on tib 2-ti functionally graded armor ceramics.," *Defence Science Journal*, vol. 62, no. 6, 2012.
- [186] J. Schmidt, M. Boehling, U. Burkhardt, and Y. Grin, "Preparation of titanium diboride tib₂ by spark plasma sintering at slow heating rate," *Science and Technology of Advanced Materials*, vol. 8, no. 5, p. 376, 2007.
- [187] Z. Zhong, B. Zhang, Y. Jin, *et al.*, "Design and anti-penetration performance of tib/ti system functionally graded material armor fabricated by sps combined with tape casting," *Ceramics International*, vol. 46, no. 18, Part A, pp. 28 244–28 249, 2020, ISSN: 0272-8842.
- [188] H. Feng, Y. Zhou, D. Jia, and Q. Meng, "Rapid synthesis of ti alloy with b addition by spark plasma sintering," *Materials Science and Engineering: A*, vol. 390, no. 1-2, pp. 344–349, 2005.

- [189] N. Singh, V. Edachery, M. Rajput, K. Chatterjee, S. V. Kailas, and K. Prashanth, "Ti6Al7Nb-tib nanocomposites for ortho-implant applications," *Journal of Materials Research*, vol. 37, no. 16, pp. 2525–2535, 2022.
- [190] F. Ma, P. Liu, W. Li, *et al.*, "The mechanical behavior dependence on the tib whisker realignment during hot-working in titanium matrix composites," *Scientific Reports*, vol. 6, no. 1, p. 36 126, 2016.
- [191] B. Radhakrishna Bhat, J. Subramanyam, and V. Bhanu Prasad, "Preparation of ti-tib-tic & ti-tib composites by in-situ reaction hot pressing," *Materials Science and Engineering: A*, vol. 325, no. 1, pp. 126–130, 2002, ISSN: 0921-5093.
- [192] S Gorse and D. Miracle, "Mechanical properties of ti-6al-4v/tib composites with randomly oriented and aligned tib reinforcements," *Acta Materialia*, vol. 51, no. 9, pp. 2427–2442, 2003.
- [193] S Gorse, J. Chaminade, and Y Le Petitcorps, "In situ preparation of titanium base composites reinforced by tib single crystals using a powder metallurgy technique," *Composites Part A: Applied Science and Manufacturing*, vol. 29, no. 9-10, pp. 1229–1234, 1998.
- [194] L. Ropars, M. Dehmas, S. Gourdet, J. Delfosse, D. Tricker, and E. Aeby-Gautier, "Structure evolutions in a ti-6al-4v matrix composite reinforced with tib, characterised using high energy x-ray diffraction," *Journal of Alloys and Compounds*, vol. 624, pp. 179–188, 2015, ISSN: 0925-8388.
- [195] S Gorse and D. Miracle, "Mechanical properties of ti-6al-4v/tib composites with randomly oriented and aligned tib reinforcements," *Acta Materialia*, vol. 51, no. 9, pp. 2427–2442, 2003, ISSN: 1359-6454.
- [196] X. Shen, Z. Zhang, S. Wei, F. Wang, and S. Lee, "Microstructures and mechanical properties of the in situ tib-ti metal-matrix composites synthesized by spark plasma sintering process," *Journal of Alloys and Compounds*, vol. 509, no. 29, pp. 7692–7696, 2011, ISSN: 0925-8388.
- [197] B. Radhakrishna Bhat, J. Subramanyam, and V. Bhanu Prasad, "Preparation of ti-tib-tic and ti-tib composites by in-situ reaction hot pressing," *Materials Science and Engineering: A*, vol. 325, no. 1, pp. 126–130, 2002, ISSN: 0921-5093.

- [198] P. E. Markovsky, D. G. Savvakina, O. M. Ivasishin, V. I. Bondarchuk, and S. V. Prikhodko, "Mechanical behavior of titanium-based layered structures fabricated using blended elemental powder metallurgy," *Journal of Materials Engineering and Performance*, vol. 28, pp. 5772–5792, 2019.
- [199] A. Pettersson, P. Magnusson, P. Lundberg, and M. Nygren, "Titanium–titanium diboride composites as part of a gradient armour material," *International Journal of Impact Engineering*, vol. 32, no. 1, pp. 387–399, 2005, Fifth International Symposium on Impact Engineering, ISSN: 0734-743X.
- [200] L. Xin, M. Yuan, Y. Yao, L. Yao, and F. Han, "Numerical study the effects of defects on the anti-penetration performance of ti6al4v–al3ti laminated composites," *Materials Research Express*, vol. 6, no. 8, 0865f8, 2019.
- [201] A. S. Namini, S. A. A. Dilawary, A. Motallebzadeh, and M. S. Asl, "Effect of tib2 addition on the elevated temperature tribological behavior of spark plasma sintered ti matrix composite," *Composites Part B: Engineering*, vol. 172, pp. 271–280, 2019.
- [202] E. Medvedovski, "Ballistic performance of armour ceramics: Influence of design and structure. part 2," *Ceramics International*, vol. 36, no. 7, pp. 2117–2127, 2010, ISSN: 0272-8842.
- [203] B. F. Silva, O. L. Blanch, K. Sagoo, and M. Jackson, "Effect of processing route on ballistic performance of ti-6al-4v armour plate," *Materials Science and Technology*, vol. 0, no. 0, pp. 1–11, 2023.
- [204] X. Zhang and Y. Li, "On the comparison of the ballistic performance of 10% zirconia toughened alumina and 95% alumina ceramic target," *Materials & Design*, vol. 31, no. 4, pp. 1945–1952, 2010, Design of Nanomaterials and Nanostructures, ISSN: 0261-3069.
- [205] G Sahragard-Monfared, C. Smudde, R. Carpenter, Z. Munir, and J. Gibeling, "Fracture resistance and crack growth mechanisms in functionally graded ti–tib," *Metallurgical and Materials Transactions A*, pp. 1–9, 2023.
- [206] B Fernandez-Silva, B. Wynne, M Jackson, M Bodie, and K Fox, "Preliminary investigation of billet processing route on microstructure, texture and fatigue

response of ti834 forged disc products,” in *MATEC Web of Conferences*, EDP Sciences, vol. 321, 2020, p. 11 031.